Delft University of Technology

A bird's-eye view on infrasound
High-resolution methods to unravel the ambient microbarom wavefield

den Ouden, O.F.C.

DOI
10.4233/uuid:c44f8490-da62-4f7c-9945-3cdb6fe0a7a4

Publication date
2022

Document Version
Final published version

Citation (APA)
den Ouden, O. F. C. (2022). *A bird's-eye view on infrasound: High-resolution methods to unravel the ambient microbarom wavefield*. [Dissertation (TU Delft), Delft University of Technology]. https://doi.org/10.4233/uuid:c44f8490-da62-4f7c-9945-3cdb6fe0a7a4

A bird's-eye view on infrasound

High-resolution methods to unravel the ambient microbarom wavefield

A bird's-eye view on infrasound

High-resolution methods to unravel the ambient microbarom wavefield

Dissertation

for the purpose of obtaining the degree of doctor
at Delft University of Technology,
by the authority of the Rector Magnificus, prof. dr. ir. T.H.J.J. van der Hagen,
chair of the Board for Doctorates,
to be defended publicly on
Friday, 29 April 2022 at 12:30

by

Olivier Frederik Constantinus DEN OUDEN

Master of Science in Applied Geophysics, IDEA League
(TU Delft, ETH Zurich, RWTH Aachen)
born in Wythenshaw, Manchester, UK

This dissertation has been approved by the promotor.

promotor: Prof. dr. L.G. Evers
copromotor: Dr. ir. P. S. M. Smets

Composition of the doctoral committee:

Rector Magnificus	chairman
Prof. dr. L. G. Evers	Delft University of Technology
Dr. ir. P. S. M. Smets	Delft University of Technology

Independent members:

Prof. dr. ir. C. P. A. Wapenaar	Delft University of Technology
Prof. dr. M. van der Meijde	University of Twente
Prof. dr. R. M. Waxler	University of Mississippi, United States
Dr. D. N. Green	AWE Blacknest, United Kingdom
Prof. dr. ir. E. C. Slob	Delft University of Technology, reserve member

Other member:

Dr. J. D. Assink	Royal Netherlands Meteorological Institute

Dr. J.D. Assink heeft als begeleider in belangrijke mate aan de totstandkoming van het proefschrift bijgedragen.

TU Delft

Royal Netherlands
Meteorological Institute
Ministry of Infrastructure
and Water Management

Keywords: infrasound, microbaroms, sensor technology, array processing, soundscapes

Cover illustration: Marilou Maas (Persoonlijk Proefschrift) i.s.m. Julia Aartsen

ISBN 978-94-6366-487-5

Typesetting system: LaTeX.
Printed by Ridderprint, Alblasserdam, The Netherlands.

MIX
Paper from
responsible sources
FSC
www.fsc.org

An electronic version of this dissertation is available at
`http://repository.tudelft.nl/`.

Voor Julia
Aan Mama en Papa

Preface

> *“I am more and more convinced that our happiness depends more on the way we meet the events of life than on the nature of those events themselves.”*
>
> Alexander von Humboldt

In front of you is my PhD dissertation, something of which I am excessively grateful and proud but never intended to create. During my scientific career, I have met brilliant people. Doing a PhD, not mentioning finishing, was initially not a realistic perspective.

My scientific journey started in 2012 at the Delft University of Technology (TU Delft) while doing the BSc. Applied Earth Science, or in Dutch: *Mijnbouw*. In combination with my visit to the TU Vienna (AT), I discovered the joy of technology. The MSc. of Applied Geophysics, hosted by the IDEA League, was an explainable next step. The IDEA League is a joint master’s degree by three of the leading technical universities in Europe. The first semester is in Delft, the second in Zürich (CH), the third in Aachen (GE), and the final semester is hosted by one of these three universities. My thesis was with the Royal Netherlands Meteorological Institute (KNMI). Together with Dr.ir. Pieter Smets and Prof.dr. Läslo Evers (copromoter and promoter, respectively, of my MSc and PhD dissertation), we intended to localise deep ocean seismic noise sources.

During my MSc thesis, I met many exciting colleagues at the KNMI, particularly Dr. Jelle Assink. Jelle is always up for an excellent scientific discussion and was therefore also heavily involved in my MSc project. At the end of the MSc project, after a colleague’s wedding, it was on the bike home to Utrecht when Jelle told me about his bird project. Waving goodbye at the train station Jelle spoke the famous last words; *"Come work with me on birds and infrasound. Let’s put some sensors on birds!"*

The idea for the bird project, the SeabirdSound project, arose in 2015 when two scientific worlds got in contact. During the austral summer of 2015, biologists of Liverpool University (Dr. Samantha Patrick) were studying the wildlife of Crozet Islands, while physicists of the Comprehensive Nuclear-Test-Ban Treaty Organisation (CTBTO) (Dr. Mario Zampolli) were generating a new hydroacoustic array near Crozet. The discussions between both worlds resulted in a research proposal. SeabirdSound became an interdisciplinary project funded by the Young Researchers grant of the Human Frontier Science Program (HFSP). The project address one of the fundamental questions in biology: how species navigate in a featureless landscape. The species of study is the Wandering Albatross, the largest seabird of the Southern Ocean. Within this search, various navigational cues are discussed, especially the use of infrasound. To answer this question, the project is built up with behavioural ecologists (Liverpool University, UK), statisticians (Florida University, US), physiologists (Stellenbosch University, ZA), and physicists (KNMI/TU Delft, NL). Projects like SeabirdSound are unique. It is not often that four different scientific communities collaborate. The journey was bumpy, especially at the beginning. We had to learn to communicate between disciplines to discover what was already done, what needed to be done, and how it should have been done. Together we have experienced the pure joy of technology and pushed each other into new and intently impossible studies. We are currently at the end of our project, answering the main question of our research; does the albatross use infrasound as a navigational cue?

As my father wrote in the preface of his dissertation: *"Promoveren doe je niet alleen"* (accomplishing a doctoral dissertation is not an individual result). Therefore I would like to thank those who have supported and helped me during this journey. First of all, Julia, I could not have achieved this without you or your support. Sorry for the endless noise of the 3D printer and to bother you with infrasound over the years; at least you are (partly) an expert now! Recently, you graduated from Tilburg University in the faculty of Social and Behavioural Sciences while combining a semi-professional sailing career. I am proud of you and fortuitous to have you by my side. Thanks for your understanding, helpful advice, and the magnificent cover of my thesis. You helped to create an enjoyable representation of my dissertation through your eyes. This dissertation is a team effort, and you are one of the critical members.

Thank you, Mama, Papa, and Carleyn. You have always believed in me. Thanks for everything, especially your eternal love. Thanks for the heated discussions at the kitchen table, based on love, passion, and support. A special note to Oma *Prik*, who has been strong and enjoys this journey with me. And a note to Opa & Oma *Beesd* and Opa *Prik*, who have unfortunately passed away but would have been excessively proud.

Jelle, thank you for this journey! You gave me this life-changing opportunity and have taught me everything about infrasound. Together we have experienced ups and downs. We have been a great team, good colleagues, friends. Thanks for your patience, unwavering support, and critical internal reviews (which were crueller than the external reviews!). Together, we have addressed and solved the most complex issues, but we wrote them down in an easy way! I would lie when I say this journey was always fun. It was a learning process for both, and we have always attempted to achieve the best. I dare to say we will have a lifetime 'in-build' connection! Thank you!

Many thanks to Läslo. Our meetings always started and ended with a smile. I felt welcome and appreciated, which I am thankful for. Often you tell me; that many things in the world are fascinating, but most of it is relative, so focus and finish your tasks before moving on to the next!

Also, many thanks to Pieter. Together with Jelle, you are the very few people I know with whom I can talk mathematical formulas. Discuss why a code on a specific line is not working. Or how to tweak our WiFi home network to have the best access in every corner of the house. Thank you for being my supervisor during my MSc thesis, copromoter during my PhD, and colleague/friend! I am proud and happy we worked together on the Multi-EAR. You truly improved the project enormously!

Many thanks to my colleagues at the KNMI and TU Delft. Especially Dr. Auke Barnhoorn, thank you for your advice, help, and confidence! I am grateful to the SeabirdSound project for making this dissertation possible. Thanks to Samatha Patrick, Mathieu Basille, and Susanna Clusella-Trullas for hosting the HFSP meetings and being Pi in the project. Thanks to my colleagues in the project; Tommy, Lucia, Natasha, Rocio, and Jeff. Moreover, many thanks to Corné Oudshoorn, Jens van den Berg and Dominique Filippi, who have taught me the world of electrical engineering. Thanks for your patience and experience. Thank you, David Green, David Fee, Roger Waxler, and Daniel Bowman, for the inspirational discussions about infrasound and the highly valued reviews. And thank you, Machteld, Gerard, and Bobbie, for letting me stay in Langweer to finish the dissertation.

Many thanks to my friends from Erasmus, the IDEA League, Delft, Hilversum, and sailing. Without you, there were no adventures or stories. A special thanks to Frans Ligui Lung and Coen de Vries, the paronyms of my dissertation. Frans, you have been my friend since day one at the TU Delft. We share a passion for technology, physics, nerd books, and surfing. You have been awarded as TU Delft's best graduate of the faculty of Civil Engineering and Geoscience in 2020 and were granted a PhD project at the University of Melbourne (AU). Moments to be proud of. Thank you and Floor for being my friend. Coen, we go back a long way. The first picture of us together is (of course) in a sailing boot, made in 2009. We have sailed against each other, with each other, and learned to the youth how beautiful sailing is. We share some great stories. You have graduated cum laude at the TU Delft Faculty of Architecture, with a 10 out of 10 as the final mark. Again, proud moments - thank you that I could celebrate with you. Thank you and Jurriënne for our friendship.

This work was performed during the SeabirdSound project, which was founded by the Young Scientist Award of the Human Frontier Science Program (RGY0072/2017). Jelle Assink's contribution is partly funded through the HFSP SeabirdSound grant. The contributions of Läslo Evers, Shahar Shani-Kadmiel and Pieter Smets are financed through a VIDI project from the Netherlands Organisation of Scientific Research (NWO), project number 864.14.005. The Marie Curie Actions WAVES funded Gil Averbuch's contributions from the European Union with H2020, grant number 641943.

The development of the Multi-EAR (Section 2.2) has been established by the nomination for the 'Digitaliserings-fonds en Ontwikkeling' research grand of the Netherlands Ministry of Infrastructure and Water Management awarded by Gijs van Schouwenburg and the 'Innovation' grand by the Delft University of Technology awarded by Auke Barnhoorn.

The CTBTO and station operators are thanked for guaranteeing the high quality of the IMS data and products. The ECMWF ERA5 are thanked for assuring high-quality atmospheric reanalyses data of the global climate. Most graphs in this thesis have been made with the Generic Mapping Tools [Wessel *et al.*, 2019].

Throughout this dissertation, various quotes are assigned to the different chapters. These quotations are from Alexander von Humboldt (1769-1859) and Richard P. Feynman (1918-1988). Both scientists have changed my vision of physics and science while working on this dissertation. Alexander von Humboldt was the first scientist to perform comparisons studies based on Europe and South American observations. His view of biological and physical phenomena has changed the scientific community. Charles Darwin, one of the most famous natural scientists in history, could perform his studies thanks to the ideas of Alexander von Humboldt. Richard Feynman received the Nobel prize in physics thanks to his contributions to the development of quantum electrodynamics. He was a theoretical physicist and known for being a pioneer in quantum computing and introducing the concept of nanotechnology. He shared his passion for physics through various lectures and books, affecting my vision on multiple topics.

Olivier den Ouden, 2022

Summary

A bird’s-eye view on infrasound: High-resolution method to unravel the ambient microbarom wavefield

Infrasound is low-frequency inaudible sound ($<$ 20 hertz (Hz)) which propagates efficiently over long distances. The propagation path of infrasonic signals is influenced by atmospheric conditions, while the attenuation is relatively small. Therefore infrasound is used as a verification technique for the verification of the Comprehensive Nuclear-Test-Ban Treaty (CTBT). The International Monitoring System (IMS) globally monitors the infrasonic wavefield thanks to the sparse network of infrasound monitoring arrays. Therefore, the IMS has played a central role in the characterisation of the global low-frequency wavefield and the localisation of infrasound sources [Campus and Christie, 2010; Marty, 2019].

Deep oceanic ambient noise is globally the most omnipresent infrasound source. The driving force of the ambient atmospheric noise (i.e., microbaroms) is the sea state, which describes the energy of the travelling ocean surface waves. Non-linear interaction of counter travelling ocean surface waves results in standing ocean waves, causing the radiation of acoustic energy and resonance within the water column [Longuet-Higgins, 1950; Hasselmann, 1963]. At the upper interfaces of the water column, acoustic energy is radiated into the atmosphere resulting in microbaroms [Brekovskikh, 1973]. The spectral peak of microbaroms is typically found around 0.2 Hz, with a characteristic amplitude range of 55-110 decibel (dB) [Campus and Christie, 2010]. Earlier studies have shown the dominance of microbarom signals within the infrasonic wavefield [Donn and Rind, 1972; McKee *et al.*, 2021]. Microbarom signals can, therefore, potentially mask other infrasonic signals of interest (e.g., seismo-acoustic signals of explosions [Assink *et al.*, 2018; Averbuch *et al.*, 2020], earthquakes [Shani-Kadmiel *et al.*, 2018], and volcanoes [Green *et al.*, 2012]). Characterising microbaroms is essential for the understanding of the infrasonic wavefield.

The fundamental challenge within this dissertation is to create high-resolution methods to characterise individual ambient infrasonic source contributions. In particular, the methods are applied to microbarom signals. Accomplishing this challenge forms the basis of this thesis and can be subdivided into four objectives:

- The design, development, construction, and calibration of a mobile multidisciplinary sensor platform for monitoring geophysical parameters. The platform is based on the latest sensor technology (i.e., cost-efficient MEMS sensors (Microelectromechanical systems)) and complements existing high-fidelity equipment.

- The development of high-resolution array processing techniques. The infrasonic wavefield is complex. Various signals may interfere with each other or mask other signals of interest. High-resolution data processing techniques are required to resolve spatially distributed infrasound which are concurrently active.

- The development of a reconstruction method for infrasonic soundscapes. The method is modular and can, in principle, be used with any infrasonic source and propagation model to resolve multiple spatially distributed infrasound sources. In this dissertation, the method is applied to reconstruct microbarom soundscapes in absolute numbers.

- The creation of a workflow for the reconstruction of infrasonic climatology studies. The method helps to improve the knowledge of the global infrasonic background noise by comparing microbarometer array observations with infrasonic soundscape simulations. This new knowledge contributes to a better verification of the CTBT and better applicability of infrasound as a remote sensing technique of the upper atmosphere, by enabling a better understanding of the recorded infrasonic wavefield and its decomposition into contributions from separate sources.

Within this thesis, two multidisciplinary sensor platforms (the INFRA- and Multi-EAR) are introduced (Chapter 2). It is demonstrated how to design, develop, and calibrate individual sensors to monitor geophysical parameters. Due to the digital design, the sensor platforms can readily be integrated with existing geophysical data infrastructures and be embedded in geophysical data analysis. The small dimensions and cost-efficient price per unit allow for unconventional, experimental designs, for example, high-density spatial sampling or deployment on moving measurement platforms. Moreover, such deployments can complement existing high-fidelity geophysical sensor networks.

In addition to developing the mobile infrasonic sensor platform, the dissertation also addresses high-resolution array processing algorithms (Chapter 3). Conventional beamforming algorithms can only confidently detect the most dominant signal in each processing window and cannot distinguish concurrent infrasound signals with side lobes. This can hamper the detection and identification of infrasound sources

in the vicinity of dominant noise sources, such as microbaroms. Various beamforming methods have been introduced in scientific literature to identify multiple sources which are simultaneously active. This dissertation presents the CLEAN beamforming algorithm for the enhanced detection of multiple infrasonic source signals within overlapping time and frequency segments. CLEAN is a post-processing method applied to conventional frequency-wavenumber (f/k) beamform techniques introduced by Bartlett and Capon. Sub-dominant sources can be identified because contributions to the total f/k spectrum are iteratively removed in this procedure. Moreover, a sharper f/k spectrum is obtained because the array response is deconvolved in the process. The enhanced beamforming resolution of CLEAN improves the capabilities of infrasound as a monitoring technique. This comes to the benefit of infrasonic monitoring of nuclear tests and natural hazards, such as volcanoes, earthquakes and hurricanes, because such signals may be masked when the ambient noise levels are high.

The application of the INFRA-EAR as biologger, attached to the Wandering Albatross (*Diomedea exulans*), has led to new insights into the ambient infrasonic wavefield. Thanks to the INFRA-EAR, a method has been introduced for the reconstruction of microbarom soundscapes (Chapter 4). Within this dissertation, soundscapes are defined as 4D infrasonic landscapes based on oceanic and atmospheric reanalysis models. Soundscapes provide time and frequency dependent 2D spatial insights into the various infrasonic source contributions. In particular, the method accounts for multiple microbarom source contributions in an infrasonic sensor's vicinity ($\sim$ 5000 km). It follows that the observations on the biologger can be identified as evanescent and propagating microbaroms. While the latter corresponds to the field typically observed at larger distances, the evanescent microbarom can only be observed directly overhead the sea surface. The soundscape method can generate synthetic spectra in absolute numbers, which agree with infrasound recordings on the INFRA-EAR, deployed in the middle of the Southern Ocean and the nearest IMS microbarometer array on Kerguelen Island (I23FR). The presented soundscapes rely on several approximations related to (1) the source model and (2) the assumptions made in the propagation modelling. However, the methodology is modular and supports different microbarom models, ocean wave models, and propagation models. The application of this reconstruction is essential in understanding the infrasonic wavefield, the ambient noise field, and remote sensing of the atmosphere. The analysis leads to a better understanding of microbaroms contributions to array recordings.

Using the methodologies that have been developed in this dissertation and building on the knowledge from the other chapters, an infrasonic climatology study is presented in the penultimate chapter (Chapter 5). This study analyses five years of continuous data recorded at IMS microbarometer array I23FR (Kerguelen Islands). The climatology analysis addresses the differences between microbarom soundscapes and observations, which is essential for future detection algorithms and microbarom studies. Moreover, the combination of observations and soundscape may enhance the filtering of microbarom source contributions within the infrasonic wavefield.

In conclusion, this dissertation adds to new knowledge of monitoring, dataprocessing, and modelling of infrasound. This knowledge contributes to a better verification of the CTBT and better applicability of infrasound as a remote sensing technique for the upper atmosphere [Donn and Rind, 1972; Smets, 2018]. The analysis is modular and can be applied to any infrasound station or place on earth. Moreover, the analysis could play a role in the installation of future infrasound arrays. The soundscapes provide insights into the expected microbarom exposure at (future) infrasound arrays. In addition, the presented high-resolution tools can potentially be used in concert to filter ambient noise contributions from the infrasonic wavefield (Chapter 6).

Samenvatting

Een panoramisch overzicht over infrageluid: hoge-resolutie methodes om infrasone omgevingsruis in kaart te brengen

Infrageluid is laag-frequent geluid ($<$ 20 hertz (Hz)) en onhoorbaar voor de mens. De propagatiepaden van infrageluidgolven worden beïnvloed door atmosferische condities. Door de lage frequenties kunnen infrageluidgolven effectief propageren over grote afstanden en verliezen deze relatief langzaam hun energie. Mede door deze eigenschappen wordt infrageluid gebruikt voor de verificatie van het kernstopverdrag, Comprehensive Nuclear-Test-Ban Treaty (CTBT). Het internationaal monitoring systeem (IMS) is hiervoor opgezet, en in staat om over de gehele wereld het infrageluidsveld te meten dankzij een sensornetwerk. Hierdoor heeft het IMS een belangrijke rol gespeeld in het karakteriseren van het globale laag-frequente geluidspectrum, en het lokaliseren van individuele infrageluidsbronnen [Campus and Christie, 2010; Marty, 2019].

De diepe oceanen genereren ook infrageluid dat wordt gemeten door het IMS en wordt geclassificeerd als ruis (omgevingsruis). Deze omgevingsruis, ook wel microbaromen genoemd, wordt gegenereerd door de energie in de oceanen. Non-lineaire interacties tussen in tegenovergestelde richting reizende oceaangolven resulteren in staande golven. Deze staande golven in de waterkolom resoneren tussen de oceaanbodem en het atmosferisch raakvlak met de oceaan [Longuet-Higgins, 1950; Hasselmann, 1963]. Op dit scheidingsvlak tussen oceaan en atmosfeer wordt laag-frequente akoestische energie uitgestraald (microbaromen, Brekovskikh [1973]).

Microbaromen hebben een spectrale piek rond 0.2 Hz, met daarbij een karakteristieke amplitude tussen 55-110 decibel (dB) [Campus and Christie, 2010]. In de literatuur is bekend dat microbaromen dominant aanwezig zijn in het infrageluidspectrum en zo andere, relevante, infrageluidsbronnen kunnen maskeren [Donn and Rind, 1972; McKee *et al.*, 2021]. De karakterisering van microbaromen is daarom essentieel voor een volledig begrip van het infrageluidspectrum, en zal zo ook bijdragen aan een betere verificatie van het kernstopverdrag en monitoring van relevante natuurverschijnselen (seismo-acoustic signalen van explosies [Assink *et al.*, 2018; Averbuch *et al.*, 2020], aardbevingen [Shani-Kadmiel *et al.*, 2018], en vulkaanerupties [Green *et al.*, 2012]).

De fundamentele uitdaging in dit proefschrift is om hoge-resolutie methodes te onderzoeken en te ontwikkelen, om hiermee individuele componenten van de globale infrasone omgeveningsruis te karakteriseren, in het bijzonder microbaromen. Dit wordt gerealiseerd door deze uitdaging op te splitsen in vier doelstellingen:

- Het ontwerpen, ontwikkelen, construeren en kalibreren van een mobiel multidisciplinair sensor platform voor het monitoren van infrageluid en andere geofysische variabelen. Het platform is ontwikkeld met de nieuwste sensortechnologie: bestaande uit kostenefficiënte MEMS (Micro-elektromechanische systemen) sensoren. Derhalve benodigen deze mobiele sensorplatformen geen vaste infrastructuur. Gebieden buiten het bereik van het vaste netwerk kunnen in kaart gebracht worden met deze sensorplatformen.

- Het ontwikkelen van hoge-resolutie dataverwerking-algoritmes. Het infrageluidsveld is complex: verscheidene infrageluidsignalen kunnen met elkaar interfereren. Hoge-resolutie dataverwerking-algoritmes zijn nodig om ruimtelijk gedistribueerde infrageluidsbronnen te kunnen onderscheiden die gelijktijdig actief zijn.

- De ontwikkeling van infrageluidlandschapskaarten. Het microbaromenlandschap wordt in kaart gebracht door de combinatie van een collectief van studies naar theoretische modellen van microbaromen en modellen van propagatie over lange afstanden. Hierdoor worden via een theoretische benadering verscheidene ruimtelijk gedistribueerde infrageluidsbronnen (microbaromen) inzichtelijk gemaakt.

- Het genereren van een stappenplan voor het reconstrueren van een klimatologiestudie van infrageluid. Deze klimatologiestudie zorgt voor een inzichtelijk beeld van de verschillende infrageluidssignalen die gemeten kunnen worden door een infrageluidssensor. Dit draagt bij aan de kennis over de globale infrasone omgevingsruis en wordt een vergelijking tussen geluidslandschappen en observaties mogelijk.

In hoofdstuk 2 wordt het ontwerp, ontwikkeling en kalibratie van twee multidisciplinaire sensorplatformen beschreven: de INFRA-EAR en Multi-EAR. De INFRA-EAR is in eerste instantie ontwikkeld als biologger voor de grote albatros (*Diomedea exulans*). Omdat de gebruikte sensoren een digitale output genereren, is het mogelijk om de platforms te integreren in bestaande vaste sensornetwerken. De gebruikte sensoren, en dus ook het platform, zijn klein en vereisen weinig vermogen. De kostprijs is laag waardoor de platforms uitgerust kunnen worden met meerdere sensoren. Het is hierdoor mogelijk om onconventionele sensorplatforms te maken die voor specifieke doeleinden gebruikt kunnen worden (ruimtelijke hoge-resolutie metingen of metingen op bewegende platforms). Daarnaast vereisen deze platforms geen uitgebreide infrastructuur, iets dat wel vereist is bij conventionele netwerken. Eveneens zijn mobiele meetcampagnes mogelijk.

Naast het construeren van hardware en de inzet hiervan om data te generen, om zo tot nieuwe modellen te komen, is er in dit proefschrift ook veel aandacht voor hoge-resolutie array dataverwerkings-algoritmes. De gebruikelijke algoritmes kunnen vaak enkel de meest dominante signaalbijdrage onderscheiden in een bepaalde tijd en frequentieband. Eerdere studies hebben aangetoond dat een overlap van signalen in tijd en frequentie mogelijk is. Dit is de reden dat in hoofdstuk 3 CLEAN-beamforming wordt geïntroduceerd. CLEAN is een nabewerkingsalgoritme voor de conventionele algoritmes. Middels deconvolutie wordt het iteratief mogelijk om meerdere bronnen in overlappende tijd en frequentie te kunnen onderscheiden. CLEAN zorgt voor een verbeterde monitoring van infrageluid, en daarmee tot een verbeterde monitoring van nucleaire testen en natuurverschijnselen, zoals vulkaanuitbarstingen, aardbevingen en stormen.

Van januari tot maart 2020 hebben 25 INFRA-EARs, bevestigd op albatrossen, rondgevlogen over de Zuidelijke Oceaan: een van de meest afgelegen plekken op aarde. In hoofdstuk 4 wordt de data die verkregen is tijdens deze meetcampagne gebruikt om geluidslandschappen te genereren voor microbaromen. In deze dissertatie zijn geluidslandschappen gedefineerd als een 4D landschap van geluid, gebaseerd op oceanische en atmosferische modellen. Geluidslandschappen brengen 2D ruimtelijk in kaart hoe over tijd en frequentie verschillende geluidsbronnen bijdragen aan het gemeten geluidsveld. In het bijzonder verschaffen de geluidslandschappen verschaffen informatie over de toedracht van microbaromen op het gemeten infrageluidsveld. Deze landschappen omschrijven de contributie van zowel de vergankelijke als de propagerende microbaromen in de infrageluidsmetingen van de infrageluidssensors. Voor zover bekend is, is de INFRA-EAR het eerste sensorplatform dat naast propagerende ook vergankelijke microbaromen heeft gemeten. Voorheen zijn vergankelijke signalen enkel theoretisch beschreven.

De aannames in de reconstructiemethode zijn te relateren aan (1) het initieel gebruikte microbaromen-bronmodel, en (2) de propagatiemodellering. Het is echter mogelijk om beide model variabelen te veranderen naar een andere gewenste input.

In de voorgestelde reconstructiemethode voor microbaromen-geluidslandschappen worden zowel vergankelijke als propagerende infrageluid bijdragen beschouwd. De geluidslandschappen worden gepresenteerd in absolute waardes, welke in overeenstemming zijn met de daadwerkelijke metingen van zowel de INFRA-EAR (direct boven het zeeoppervlak) als een op afstand gelegen (vaste) IMS-array.

Hoofdstuk 5 beschrijft een klimatologische studie van het infrasone geluidsveld rondom I23FR. De eerder beschreven hoge-resolutiemethodes van deze dissertatie zijn toegepast op meteorologische en infrageluid data. Hierbij is gebruik gemaakt van vijf jaar aan data. Daarnaast zijn er voor deze vijf jaar ook gesimuleerde microbaromen-geluidslandschappen gereconstrueerd en vergeleken met de microbaromen-observaties. Deze vergelijking toont aan dat er een overeenkomst is in richting en frequentie van de microbaromen tussen model en meting. De amplitude wordt echter onderschat. Mede door deze studie wordt de bijdrage van microbaromen rondom I23FR inzichtelijk, en zijn verbeteringen voor model en observatie duidelijk geworden.

De gepresenteerde hoge-resolutie methodes die in dit proefschrift zijn beschreven zijn modulair en generiek. Zij kunnen worden toegepast op alle infrageluid arrays. Zo kan de omgevingsruis van bestaande en nieuwe infrageluid-array locaties in kaart gebracht worden. In hoofdstuk 6 wordt beschreven hoe de methodes effectief gebruikt kunnen worden om relevant infrageluid te onderscheiden van ruis (filteren) om zo tot een betere analyse van het geregistreerde infrageluid te kunnen komen.

Contents

1

Introduction: from atmospheric motion to infrasonic wavefield

It doesn't matter how beautiful your theory is, it doesn't matter how smart you are. If it doesn't agree with experiment, it's wrong.

Richard P. Feynmann

Sound waves in air are elastic waves that temporarily bring air particles locally in motion while propagating at the speed of sound, i.e. approximately 334 m/s at mean sea level temperature ($\sim$ 15°C). As a sound wave passes, air particles oscillate from side to side around their resting positions and alternate between being compressed or rarefied (thinned out), Figure 1.1-a. Acoustic propagation consists of a continuous transfer of potential and kinetic energy, akin to the motion of a pendulum. Potential energy is stored during air compression (analogous to a lifted pendulum) and transferred to kinetic energy as the air particles move and the air rarefies (analogous to the pendulum movement), Figure 1.1-b [Pain and Beyer, 1993; Pierce, 2019]. The sound frequency quantifies the number of these oscillations per second, and a Power Spectral Density (PSD) shows how the signal power varies with frequency. The computation of the PSD involves a Fourier Transform. The wavelength is defined as the distance between two crests or zero crossings. The relationship between frequency (f), wavelength (λ) and speed of sound (c) is given as:

$$\lambda \cdot f = c \qquad (1.0.1)$$

Parts of this chapter have been published as part of: **Assink** & **den Ouden, et al. 2021**, *Infrasound as a cue for seabird navigation.* Frontiers in Ecology and Evolution, Volume 9, DOI: 10.3389/fevo.2021.740027
Note that minor changes have been introduced to make the text consistent with the other chapters.

The perturbations fully describe the acoustic field at any location in pressure p (sound pressure; pascal or Pa) and particle speed v (m/s) as a function of frequency (hertz or Hz). The sound level of an acoustic field in the air is commonly expressed in decibel (dB), relative to the reference value of 20μPa.

Particle velocity defines the propagation direction of a passing sound wave, although with 180-degree ambiguity, and is proportional to the spatial gradient of the acoustic pressure. The sound intensity $\vec{I}$ quantifies the acoustic power and directivity per unit area, and is calculated as the product of sound pressure and particle velocity [Pierce, 2019], i.e.,

$$\vec{I} = p \cdot \vec{v} \tag{1.0.2}$$

Sound intensity is a vector that points away from the sound source. Multiple pressure sensors must be positioned in an array to determine the direction to the sound source in the free field. Alternatively, particle motion sensors can be utilised to directly measure acoustic particle motion direction.

The intensity of the signal decreases with distance from the source and most rapidly in the near-field (Figure 1.1-b). The total sound energy density is computed as the sum of both acoustic kinetic and potential energy densities (note the logarithmic scale in Figure 1.1-b). Note that while the kinetic energy dominates in the near field, both are in equilibrium in the far-field.

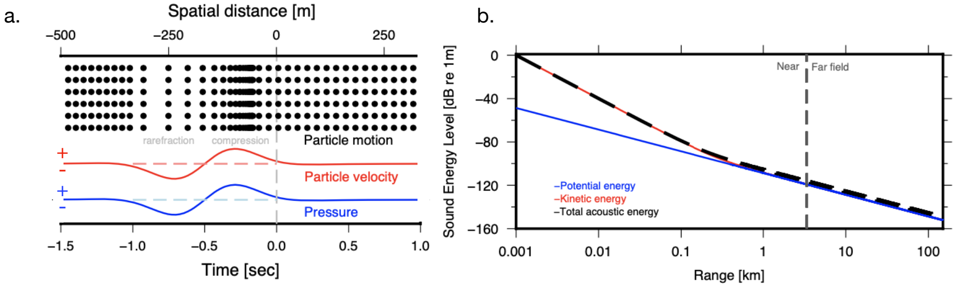

Figure 1.1: *Infrasonic wave-field parameters (a) Depiction of an acoustic wave (black dots) as alternating compressions and rarefactions, leading to perturbations in particle velocity (red) and pressure (blue). (b) The decrease and partitioning of acoustic energy with range and transition from near- to far-field for a spherical sound wave at 0.2 Hz with 1 Pa amplitude. The total acoustic energy (dashed black) is composed of potential (blue) and kinetic (red) energy, related to pressure and particle motion, respectively. While kinetic energy dominates in the near field, both forms are in equilibrium in the far-field.*

■ The perturbation method

Small atmospheric perturbations like sound waves occur on top of the existing moving media of the atmosphere. In order to describe small pressure perturbations, the perturbation method is applied [Gossard and Hooke, 1975; Wapenaar, 2014]. The perturbation method divides the atmospheric field variables into two parts. The first part is the basic state. It is assumed that the atmosphere is in a known basic state ($\overline{m}$). The second part is the perturbation part, which is a local deviation off the field from the basic state ($m^{'}$). This perturbation then is superposed on the basic state, hence:

$$m = \overline{m} + m^{'} \tag{1.0.3}$$

Within the perturbation method, two major assumptions are made. First, the basic state variables must satisfy the conservation equations when the perturbations are set to zero. Second, for linearisation of the perturbation, the quantities must be small enough so that all terms in the conservation equations that involve products of the perturbations can be neglected (Appendix A).

Given the simplified perturbation method concept (equation 1.0.3), the atmospheric motions can be described similarly.

$$\vec{v} = \overline{\vec{v}} + \vec{v}^{'}, \quad p = \overline{p} + p^{'}, \quad \rho = \overline{\rho} + \rho^{'} \tag{1.0.4}$$

where the over-line parameters represent the basic state variables, and the primed represents the perturbation variables.

1.1 Sound wave properties

Wave motions in the atmosphere are harmonic oscillations that propagate over space and time. One of the essential properties of linear harmonic oscillators is that the period (i.e., the time required to execute a single oscillation) is independent of the amplitude of the oscillation. The frequency of the wave generally depends on the wavenumber (k) and the physical properties of the atmosphere. Therefore the phase speed for a planar wave, the horizontal velocity, equals $c_p = 2\pi f/k$ (Figure 1.2-a). Waves for which the phase speeds change by varying wavenumbers are dispersive waves. Acoustic waves, which travel with the speed of sound, have phase speeds independent of the wavenumber and are non-dispersive waves.

In terms of sound waves it is assumed that:

- (1) In theory, sound perturbations are adiabatic within a homogeneous and lossless atmosphere, which means that internal friction between particles is neglected. Physically, however, the atmosphere is not lossless and causes absorption and scattering of sound waves.

- (2) The gravitational acceleration constant g becomes relevant at frequencies below 0.05 Hz. Above 0.05 Hz the effects can be neglected. The restoring force between the acoustic cutoff frequency of 3.3 mHz and 0.05 Hz is both pressure and gravity (acousto-gravity waves).

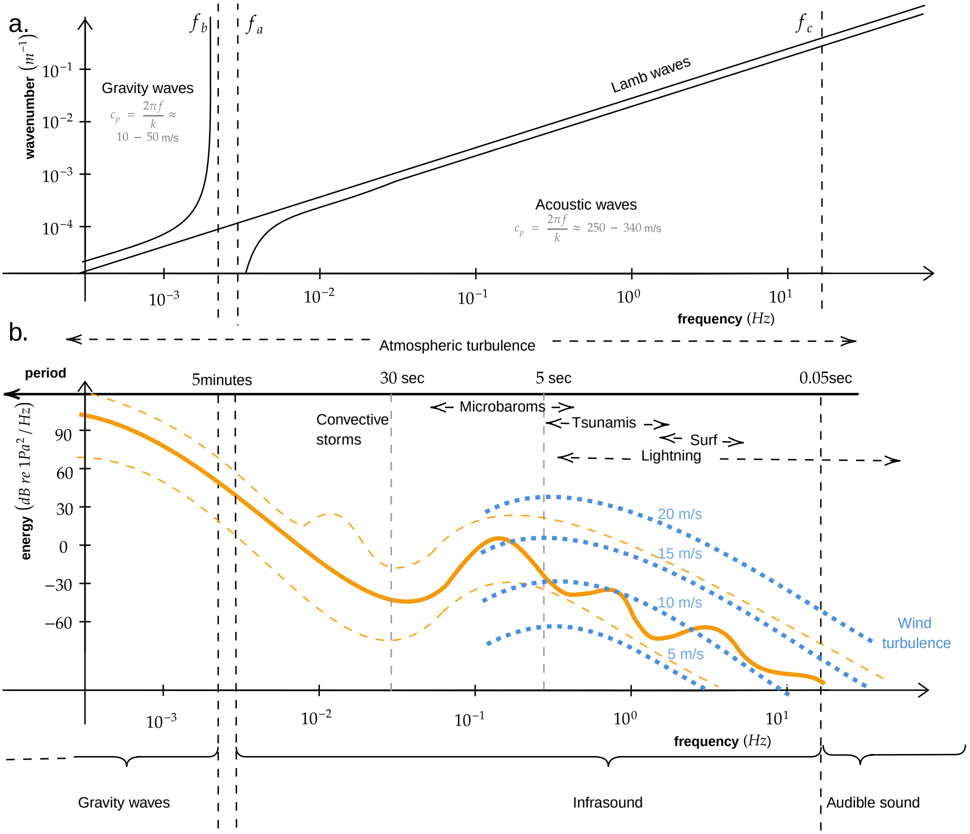

Figure 1.2: *Various wave types and their properties are visualised. (a) The frequency - wavenumber and phase velocity relation. Infrasound ranges between the acoustic cut-off frequency ($f_a \sim$ 3.3 mHz) and 20 Hz, above which sound becomes audible for humans. Gravity waves can propagate with periods between one day and the Brunt-Väisälä frequency (f_c). (b) The amplitude-frequency relation of infrasound sources (orange) and atmospheric turbulences (blue). The solid orange line indicates an expected amplitude range of various sources for short period. The dotted area shows the amplitude range over a longer period. Note that the turbulence area is broad. Whenever the turbulence amplitude is above the infrasonic amplitudes, the infrasound sources are masked by noise.*

1.2 Infrasound

The frequency range of atmospheric infrasound is typically defined between 3.3 mHz to 20 Hz (Figure 1.2). Infrasonic waves with frequencies below 3.3 mHz do not fit within the Earth's atmosphere. Above 20 Hz, sound becomes audible to humans.

Infrasound can be produced across various frequencies by displacements of large volumes of air (Figure 1.2-b), either from geophysical or anthropogenic sources. Two main signal type categories are defined: (1) transient signals are considered to have a finite, short-term duration, in contrast to (2) continuous signals. In practice, signals may also share characteristics from both signal type categories.

Within the atmosphere, several infrasonic sources have been identified. Standing ocean waves produce a near-continuous hum in a broad frequency range as microbaroms (0.1-1.0 Hz) in the open sea and interact with coastlines [Waxler *et al.*, 2007]. Microbarom source regions in the ocean can be quasi-stationary and transitory (e.g., when associated with marine storms). Surf can also be observed near coastlines at higher frequencies, typically above 1.0 Hz [Park *et al.*, 2008]. Transient sources of infrasound that are routinely detected within the atmosphere include severe weather, earthquakes, meteor explosions and volcanic eruptions. Notably, infrasound can radiate from sources underwater, under certain conditions, sound passes between water and air at low frequencies [Evers *et al.*, 2013].

The observations on the global infrasound array network [Marty, 2019] have advanced knowledge of infrasound sources, atmospheric infrasound propagation, and turbulence effects on detection. The global infrasound network is part of the International Monitoring System (IMS), which is being installed for the verification of the Comprehensive Nuclear-Test-Ban Treaty (CTBT). Since the certification of the first array in 2001, 54 out of the eventual 60 arrays have been installed. The IMS infrasound arrays are distributed relatively uniformly over the globe.

Earlier studies have shown that the infrasound detection statistics vary significantly between IMS arrays [Matoza *et al.*, 2013; Assink *et al.*, 2014; Ceranna *et al.*, 2019]. Each array has its characteristic background noise with specific infrasonic sources that are routinely detected. Microbarom signals tend to be present at most infrasound arrays. While some of the observed infrasound originates more locally to the array, other signals originate from much further away: propagation can occur over thousands of kilometres. It can even be global for exceptionally powerful signals, propagating various times around the world, such as the 1888 Krakatoa eruption [Strachey, 1888] and the 2013 Chelyabinsk meteor airburst [Brown, 2013].

1.3 Atmospheric propagation of infrasound waves

The infrasonic wavefield is complex and is composed of diverse source contributions [Campus and Christie, 2010]. The atmospheric environment plays an essential role in the detection of infrasound. The wind and temperature distribution throughout the atmosphere determines along which paths infrasonic waves can propagate [Waxler and Assink, 2019] the altitudes attained by these varying propagation paths controls the along-path absorption [Sutherland and Bass, 2004]. Wind conditions near infrasound sensors determine local turbulence levels that are detected as (non-acoustic) pressure variations, along with infrasound [Raspet *et al.*, 2019].

Up to distances of a few kilometres, it can be assumed that the atmospheric environment is homogeneous, implying that infrasound propagates along straight paths. More generally, the atmosphere is an inhomogeneous medium that is predominantly vertically layered. Within the atmosphere, infrasound is refracted by gradients in temperature and wind. It can efficiently propagate downwind in waveguides that form between the Earth surface and the atmosphere aloft. Global strong winds around the tropopause (the jetstream around 10-15 km), stratopause (the circumpolar vortex around 50 km), and thermosphere (around 100 km) form the upper limits of the tropospheric, stratospheric, and thermospheric waveguides, respectively. The characteristic waveguide propagation paths arise because vertical temperature and wind gradients within waveguides are such that upward refracted sound waves are bend back down to a reflective Earth surface. In the upwind direction, propagation efficiency is less, and therefore infrasound propagation is highly anisotropic [Waxler and Assink, 2019].

Detection statistics at infrasound arrays show seasonal patterns that correspond to the stratospheric circumpolar vortex's seasonal dynamics. Combined with enhanced propagation efficiency downwind, its time depend variation leads to seasonal variations in long-range infrasound propagation conditions that affect the observations. These winds show a strong variation with latitude and are intimately connected to the global atmospheric circulation [Smets, 2018].

The effective sound speed approximates the combined effect of wind and temperature on infrasound propagation in a horizontally layered atmosphere (c_{eff}), which is defined as the sum of the absolute adiabatic sound speed (c_T) and the wind in the direction of propagation [Drob, 2019].

$$c_T = \sqrt{\gamma R_d T} \quad c_{T,\text{air}} \sim 20.04\sqrt{T} \text{ m/s} \tag{1.3.1}$$

$$c_{\text{eff}} = c_T + w_{uv} \cdot \hat{n}_{xy} = c_T + w_a \tag{1.3.2}$$

where γ indicates the adiabatic index (γ_{adi}=1.4, γ_{iso}=1), R_d the specific gas constant for dry air, T the absolute temperature (Kelvin), and $w_{uv} \cdot \hat{n}_{xy}$ the horizontal wind in the direction of propagation. The horizontal wind can be divided into the along-track wind, w_a, and the cross-wind, w_{cross}, as:

$$\begin{pmatrix} w_a \\ w_{\text{cross}} \end{pmatrix} = \begin{pmatrix} \sin(\phi) & \cos(\phi) \\ \cos(\phi) & -\sin(\phi) \end{pmatrix} \begin{pmatrix} w_u \\ w_v \end{pmatrix}$$

While propagating, infrasound can be refracted by vertical variations in the effective sound speed. The Earth surface also acts as a reflector. The effective speed of sound ratio ($c_{\mathrm{eff,ratio}}$) is a practical measure to quantify favourable ground-to-ground ducting conditions. An effective sound speed ratio near to or greater than one is indicative of whether infrasound can refract back to the ground surface.

$$c_{\mathrm{eff,ratio}} = \frac{c_{\mathrm{eff}}(x, y, z)}{c_{\mathrm{eff}}(x, y, 0)} \tag{1.3.3}$$

Propagating wavefronts can be described by rays, while Snell's law describes refraction (e.g., Pierce [2019]). The index of refraction corresponds to the effective sound speed. The wave bends upward (downward) for negative (positive) gradients ineffective sound speed (Figure 1.3 -a and -b). Realistic temperature and wind profiles typically consist of these gradient types (Figure 1.4), leading to ground-to-ground propagation paths through the air instead of along the surface (Figure 1.5).

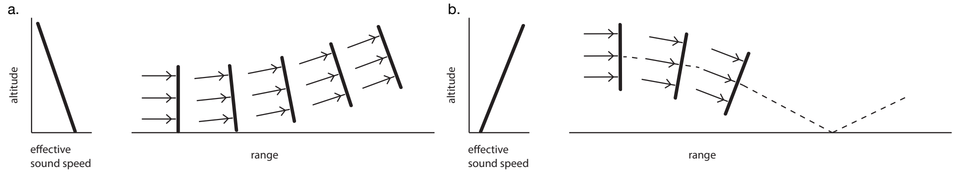

Figure 1.3: *Upward (a) and downward (b) refraction of acoustic waves due to gradients in the effective sound speed. Figure adopted from Assink [2012].*

Propagation losses are determined by geometrical spreading (the increase in area the sound wave covers, Figure 1.1-b) and intrinsic absorption during propagation. Close to the source, transmission loss is dominated by geometrical spreading (the increase in the area the sound wave covers), as absorption rates are small [Sutherland and Bass, 2004]. The absorption of energy while propagating is determined by the absorption coefficient, proportional to the frequency of sound squared. Signals with higher frequencies are only detectable over short ranges. Conversely, lower frequencies can be resolved over larger distances. For signals with a broad spectral content, the lower frequencies are less attenuated at more extensive propagation ranges. The absorption coefficients are dependent on the temperature and air composition, including humidity near the surface [Sutherland and Bass, 2004].

Various methods have been developed to simulate infrasound in realistic atmospheres accurately. This can either be done by raytracing [Waxler and Assink, 2019] or by applying empirical formulations of the atmosphere [Le Pichon *et al.*, 2012; Tailpied *et al.*, 2016].

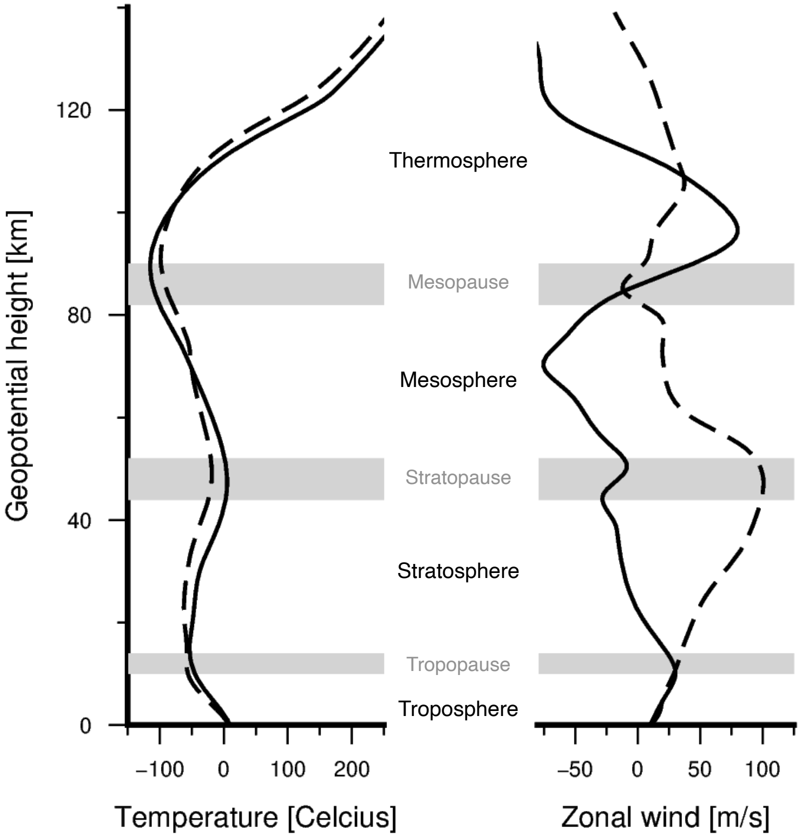

Figure 1.4: *Vertical profile based on the (solid) January and (dashed) July temperature and zonal wind at* $50^\circ S/70^\circ E$ *from the climatology analysis of HWM14 and MSIS-00.*

1.4 Statement of research

The fundamental challenge within this dissertation is to unravel the infrasonic ambient noise field and characterise individual source contributions. The wavefield is complex and often consists of interfering acoustic signals in overlapping frequency bands in the presence of incoherent noise (i.e., wind). The acoustic signals take the form of transients, (quasi-)continuous signals, or both. From the perspective of an infrasound sensor, coherent noise sources (i.e., microbaroms) appear as interfering signals that clutter the array detection bulletins and may obscure detections from signals of interest (e.g., seismo-acoustic signals of explosions [Assink *et al.*, 2018; Averbuch *et al.*, 2020], earthquakes [Shani-Kadmiel *et al.*, 2018], and volcanoes [Green *et al.*, 2012]). Low-yield atmospheric and underground explosions are likely to be masked by microbaroms [Bedard *et al.*, 2000; Haak and Evers, 2002; Golden *et al.*, 2012]. Sparse infrasound sensor arrays and most infrasound processing tools, which are often designed to detect the dominant acoustic signal in a given time segment and frequency band, limit the ability to distinguish interfering infrasound sources. Therefore, this dissertation aims to generate high-resolution monitoring systems, processing techniques, and knowledge of how source mechanisms and atmospheric propagation influence recorded signals.

To accomplish these challenges, the following objectives have been defined:

- The development of measurement techniques for atmospheric monitoring campaigns based on the latest technology (i.e., digital MEMS). This includes designing, developing, constructing, and calibrating a mobile multidisciplinary sensor platform for monitoring geophysical parameters.

- The development of high-resolution array processing techniques. High-resolution data-processing techniques are required to resolve spatially distributed infrasound signals that are concurrently active.

- The development of a reconstruction method for ambient infrasonic soundscapes. Combining collective studies on microbarom source region models together with long-range infrasound propagation will resolve multiple spatially distributed infrasound sources.

- To investigate the infrasound noise field at sea over multiple years using new monitoring devices, data processing techniques, and microbarom soundscapes as developed in this thesis. This will improve knowledge of the global infrasonic background noise, and allow beter comparisons of infrasound array observations and model outputs. This new knowledge contributes to a better verification of the CTBT and better applicability of infrasound as a remote sensing technique for the upper atmosphere.

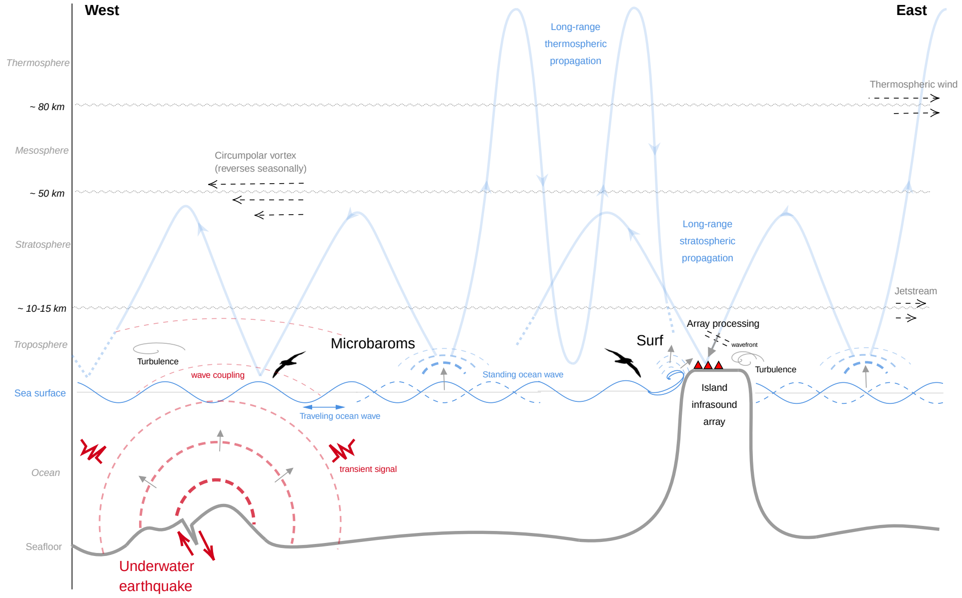

Figure 1.5: *A schematic representation of the infrasonic wavefield. The ocean produces continuous acoustic background noise (i.e., microbaroms and surf; depicted in blue). Microbaroms can propagate over long distances downwind (i.e., from east to west) in the stratospheric waveguide. In the upwind direction, microbaroms are not guided and propagate towards space. The wind direction changes seasonally. Surf infrasound is generated near coastlines and does not propagate over long distances. Transient acoustic signals (red) also occur in the marine environment, e.g., following an underwater earthquake. These vibrations can couple into the atmosphere. Besides the acoustic signals, the wavefield also consists of turbulence, which may mask signals of interest. Array processing techniques can be used to detect coherent acoustic waves in a turbulent atmosphere.*

1.5 Outline of this thesis

The dissertation is organised in the following way: chapter 2 describes two mobile multidisciplinary sensor platforms; the INFRA- and Multi-EAR. Both platforms measure concurrently various geophysical parameters, including; wind, barometric pressure, differential pressure, temperature, humidity, accelerations, audible sound, and GPS signals. The platforms are designed and developed with Dominique Filippi of Sextant Technology Inc. at Marton, New Zealand. The lab and field calibration/comparisons have been performed at the KNMI test facilities. Chapter 2 describes the electromechanical design of the platforms and the theoretical and measurement responses of the sensors on the platforms.

Chapter 3 reviews various array processing techniques for the detection of coherent infrasound signals. This involves conventional sensor processing techniques, conventional planar beamforming array processing techniques, and high-resolution beamforming techniques (i.e., CLEAN beamforming). In addition to the theoretical outline of these techniques, synthetic and IMS data are used to show the various outcomes and enable comparisons. Furthermore, a statistical threshold has been introduced to control the computational costs of the CLEAN algorithm.

Chapter 4 addresses a reconstruction method for the creation of infrasonic soundscapes. Within this dissertation, soundscapes are defined as 4D infrasonic landscapes based on oceanic and atmospheric reanalysis models. Soundscapes provide time and frequency depending 2D spatial insights into the various infrasonic source contributions. In particular, the method accounts for multiple microbarom source contributions in an infrasonic sensor's vicinity ($\sim$ 5000 km). Moreover, chapter 4 addresses the implementation and explanation of the different contributions of the microbarom field that are measured on the INFRA-EAR and IMS infrasound array I23FR.

In chapter 5, an infrasonic climatology study is presented in which the methodologies described in chapters 3 and 4 are used in concert. Infrasound station I23FR, located at the Kerguelen Islands, an island in the Southern Ocean, is often excluded from scientific studies because of the extreme weather conditions around the array. The reason for studying this array, however, are the challenging environment and location in the southern ocean. Local turbulences often mask the infrasound recordings. Within this chapter, meteorological and infrasonic climatology is presented, which includes the comparison between in-situ observations and modelled infra-soundscapes.

Chapter 6 concludes by summarising the major findings described in this thesis. Furthermore, potential future topics of research and new applications are reviewed.

2

Atmospheric monitoring techniques

Study hard what interests you the most in the most undisciplined, irreverent and original manner possible.

Richard P. Feynmann

Abstract Geophysical studies and real-time monitoring of natural hazards, such as volcanic eruptions or severe weather events, benefit from the joint analysis of multiple geophysical parameters. However, typical geophysical measurement platforms still provide logging solutions for a single parameter, due to different community standards and the higher cost rate per added sensor.

In this chapter, the 'Infrasound and Environmental Atmospheric data Recorder' (INFRA-EAR, section 2.1) and the 'Multi Earth and Atmospheric data Recorder' (Multi-EAR, section 2.2) are presented, which have been designed as low-cost mobile multidisciplinary measurement platforms for geophysical monitoring. Both platforms monitor in particular infrasound, but concurrently measures audible sounds, barometric pressure, accelerations, wind flow, temperature, humidity and uses the Global Positioning System (GPS) to position the platform. The INFRA-EAR is especially designed as bio-logger for the Wandering Albatross. During the 2020 incubation time, 25 of these devices have collected various geophysical parameters within the Southern Ocean near the Crozet Islands. The Multi-EAR is a research proposal based on the findings of the INFRA-EAR. The proposal has been granted by (1) the Netherland Ministry of Infrastructure and Water Management and (2) Delft University of Technology. The project aims to develop, based on earlier recommendations, a multidisciplinary mobile sensor platform to complement the existing high-fidelity monitoring network.

Due to the digital design of both platforms they can readily be integrated with existing geophysical data infrastructures and be embedded in geophysical data analysis. The small dimensions and low-cost price per unit allow for unconventional,

experimental designs, for example, high-density spatial sampling or deployment on moving measurement platforms. Moreover, such deployments can complement existing high-fidelity geophysical sensor networks. The platforms are designed by using digital Micro-electromechanical Systems (MEMS) sensors embedded on a Printed Circuit Board (PCB). The MEMS sensors on the PCB's are a GPS, a three-component accelerometer, a barometric pressure sensor, an anemometer, a microphone, a temperate/humidity sensor and a differential pressure sensor. A programmable microcontroller unit controls the sampling frequency of the sensors and data storage. Casings are used to protect the platforms against the weather. The casings are either created with a stereolithography (SLA) Formlabs 3D printer, using durable resin, or ordered polyethylene casings.

Thanks to low power consumption, both systems can be powered by a battery or solar panel. Besides the description of the platform design, the calibration and performance of the individual sensors is discussed.

2.1 The INFRA-EAR; a cost-efficient mobile multidisciplinary measurement platform for monitoring geophysical parameters

■ 2.1.1 Introduction

Real-time monitoring of natural hazards, such as volcanic eruptions or severe weather events benefit from the joint analysis of multiple geophysical parameters. However, geophysical measurement platforms are typically designed to measure a single parameter, due to different community standards and the higher cost rate per added sensor. The quality and robustness of geophysical measuring equipment generally scale with price, due to higher material costs and research and development (R&D) expenses. In addition, the deployment of such equipment comes with complex deployment and calibration procedures and requires the presence of a robust power and data infrastructure.

Geophysical institutes often place multiple sensor platforms co-located. Meteorological institutes, for example, measure various meteorological parameters for comparison, which improves the weather observations and weather forecast models. The Comprehensive Nuclear-Test-Ban Treaty Organization (CTBTO) performs various geophysical measurements at its measurement sites where possible. The International Monitoring System (IMS), which is in place for the verification of the CTBT, performs continuous seismic, hydroacoustic, infrasonic and radionuclide measurements [Marty, 2019]. In addition, the IMS infrasound arrays and radionuclide facilities host auxiliary meteorological equipment, as this data facilitates the review of the primary IMS data streams. Besides its use for verifying the CTBT, it has also been shown that a multi-instrumental observation observational network such as the IMS can provide useful information on the vertical dynamic structure

---

Published as: **den Ouden, et al. 2021**, *The INFRA-EAR; a low-cost mobile multidisciplinary measurement platform for monitoring geophysical parameters.* Atmospheric Measurement Techniques, Volume 14, DOI: 10.5194/amt-14-3301-2021.
Note that minor changes have been introduced to make the text consistent with the other chapters.

of the middle and upper atmosphere, in particular when paired with complementary upper atmospheric remote sensing techniques such as lidar [Blanc *et al.*, 2018]. Other studies that involve the analysis of multiple geophysical parameters include seismo-acoustic analyses of explosions [Assink *et al.*, 2018; Averbuch *et al.*, 2020], earthquakes [Shani-Kadmiel *et al.*, 2018], and volcanoes [Green *et al.*, 2012].

National Weather Services, such as the Royal Netherlands Meteorological Institute (KNMI), have expressed an interest in measuring weather on a local scale to inform citizens and warn in case of extreme weather. In addition, such measurements allow for higher-resolution measurements of sub-grid scale atmospheric dynamics, which will contribute to the improvement of short-term and now-casting weather forecasts [Manobianco and Short, 2001; Lammel, 2015]. Therefore it became part of a low-cost citizen weather station program, to increase the spatial resolution of conventional numerical weather prediction models. In the Netherlands, over 300 of those weather stations contribute to a global citizen science project, Weather Observations Website (WOW) [Garcia-Marti *et al.*, 2019; Cornes *et al.*, 2020]. Nonetheless, due to the required infrastructure of the equipment, many platforms are spatially static. Having a low-cost multidisciplinary mobile sensor platform allows for high-resolution spatial sampling and complement existing high-fidelity geophysical sensor networks (e.g., buoys in the open ocean [Grimmett *et al.*, 2019], and stratospheric balloons [Poler *et al.*, 2020]).

Various disciplines apply new sensor technology to obtain higher spatial and temporal resolution [D'Alessandro *et al.*, 2014] for geophysical hazard monitoring. Micro-electromechanical systems (MEMS) are small single-chip sensors that combine electrical and mechanical components and have low energy consumption. The seismic community has created low-cost reliable MEMS accelerometers [Homeijer *et al.*, 2011; Milligan *et al.*, 2011; Zou *et al.*, 2014] to detect strong accelerations that exceed values due to Earth's gravity field [Speller and Yu, 2004; Laine and Mougenot, 2007; Homeijer *et al.*, 2014]. Moreover, the infrasound [Marcillo *et al.*, 2012; Anderson *et al.*, 2018], as well as the meteorological community are integrating MEMS sensors into the existing sensor network [Huang *et al.*, 2003; Fang *et al.*, 2010; Ma *et al.*, 2011].

In this work, the INFRA-EAR is presented, which has been designed as a low-cost mobile multidisciplinary measurement platform for geophysical monitoring, in particular, infrasound. The platform uses various digital MEMS sensors embedded on a Printed Circuit Board (PCB). A programmable microcontroller unit, as well embedded on the PCB, controls the sensors' sampling frequency and establishes the energy supply for the sensors and the data-communication and storage. A waterproof casing protects the mobile platform against the weather. The casing is created with a stereo-lithography (SLA) Formlabs 3D printer, using durable resin. Because of its low power consumption, the system can be powered by a battery or solar panel.

Previous studies have presented similar mobile infrasound sensor designs [Anderson *et al.*, 2018; Marcillo *et al.*, 2012; RBOOM, 2017], which have shown how low-cost, miniature sensors can complement existing measurement networks (e.g., volcanic and earthquake monitoring). Those platforms differ from the INFRA-EAR by dimensions, multidisciplinary purpose, and digital design. All sensors of the INFRA-EAR have a built-in Analog-Digital-Converter (ADC), which directly generates digital outputs. Therefore, the INFRA-EAR can be easily integrated into the existing hardware and software sensor infrastructure. Furthermore, the casing design and development is based on the latest technology of 3D printing. Furthermore, the platform design and purpose are adaptive to various monitoring campaigns.

The ability to detect infrasonic signals of interest depends on the signal's strength relative to the noise levels at the receiver side, the signal to noise ratio (SNR). The signal strength depends on the transmission loss that a signal experiences propagating from source to receiver. Infrasound measurements benefit from insights into the atmospheric noise levels (e.g., wind conditions), the meteorological conditions (e.g., barometric pressure, temperature, and humidity), as well as the movement and positioning of the sensors (e.g., accelerations) [Evers, 2008].

While there are clear benefits associated with a MEMS-based mobile platform (e.g., cheap and rapid deployments to (temporarily) increase coverage), MEMS sensors are known to be less accurate than conventional high-fidelity equipment. Especially digital MEMS sensors, which have a built-in ADC, are known for their high self-noise level. Nonetheless, they could be used near geophysical sources which generate high SNR signals. Several geophysical measurements [Marcillo *et al.*, 2012; Grangeon and Lesage, 2019; Laine and Mougenot, 2007; D'Alessandro *et al.*, 2014] show the benefit of MEMS sensors, and how they complement the existing sensor network.

In this section , the design and calibration of the INFRA-EAR is discussed. The remainder of this chapter is organized as follows. Section 2.1.2 introduces the mobile platform, its design and features. Section 2.1.3 describes the various sensors embedded on the platform and the relative calibrations with high-fidelity reference equipment. Firstly, a novel miniature digital infrasound sensor is introduced, and its theoretical response is derived. Secondly, the barometric MEMS sensor is discussed. A wind sensor which relies on thermo-resistive elements is discussed next, followed by a discussion of the on-board MEMS accelerometer. In section 2.1.4, the platform's overall performance and design are discussed and summarized, from which the conclusions are drawn.

■ 2.1.2 Mobile platform design

Circuit design

The mobile platform contains a PCB created to embed the MEMS sensors and facilitate the electrical circuits. The PCB carries a Digital Low Voltage Range (DLVR) differential pressure sensor, an anemometer, as well as an accelerometer and barometric pressure sensor, in addition to a GPS for location and timing purposes (Figure 2.1-a). The sensors are controlled by a MSP430 microcontroller, which is integrated on the PCB, and are powered by an 1800 mAh lithium battery. Protecting the PCB is done with a weather- and waterproof casing, which has been designed (Figure 2.1-b) with the dimensions 110mm x 38mm x 15mm.

The communication between the microcontroller and MEMS sensor on the PCB is either done by Inter-Integrated Circuit (I2C) or Serial Peripheral Interface (SPI), and depends on the sensor and personal preference. Both communication methods are bus protocols and allow for serial data transfer. SPI is full-duplex communication, which is simultaneous communication between microcontroller and MEMS sensor. I2C is half-duplex and does not allow simultanious communication. Therefore, I2C has the option of clock stretching, and the communication is stopped whenever the MEMS sensor cannot send data. Besides, I2C has built-in features to verify the data communication (e.g., start/stop bit, acknowledgement of data). Although the I2C protocol is favorable, it requires more power.

The microcontroller runs on self-made software, complementing the required manufacturers electrical and communication protocols. The software allows determining the sample time, sample frequency, and data storage. The PCB includes a 64 MB flash memory, which is used to store the data. The raw output of the digital MEMS sensors are stored as bits, and the microcontroller performs no data processing to save power consumption. To extract data, the platform needs to be connected to a computer. There are no wireless communication possibilities.

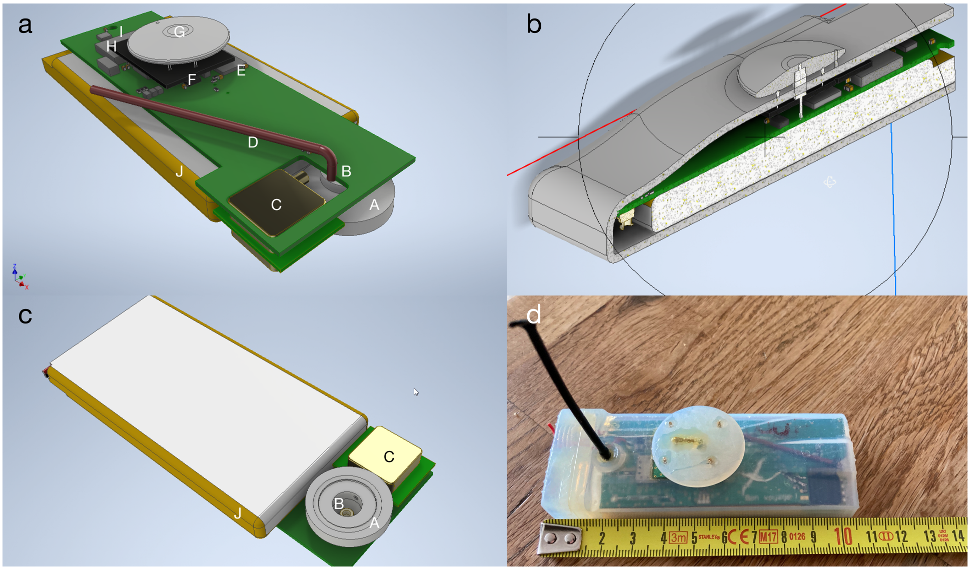

Figure 2.1: *3D CAD design of (a) the top of the PCB, (b) the casing, (c) the bottom of the PCB with pressure dome, and (d) a picture of the actual platform. The PCB hosts; a pressure dome (a-A/c-A), a barometric pressure sensor (a-B/c-B), a differential pressure sensor (a-C/c-C), a PEEKsil Red series capillary (a-D), an accelerometer (a-F), an anemometer (a-F) with the heating element (a-G), a microcontroller (a-H), a GPS (a-I), and a lithium battery (a-J/c-J).*

Casing design for pressure measurements

The mobile sensor platform is designed to measure atmospheric parameters. Hence, a waterproof casing has been created, by a Formlabs SLA 3D printer [Formlabs, n.d.], to protect the PCB. Because of the use of a durable resin, the casing is waterproof and air-tight. At the bottom of the casing, a dome structure is integrated (Figure 1-c), which acts as an inlet to both the absolute and differential pressure sensors. Note that the dome is not connected to the inside of the casing. The inlets of both sensors and a capillary are integrated within the dome designs and sealed with silicone glue, avoiding water and air leakage. Moreover, a Gore-TEX air-vent sticker [Gore-TEX, 2020] is used to cover the dome, which allows airflow but restrains water and salt in case of measurement near or above the ocean.

Air turbulence can generate dynamic pressure effects or stagnation pressure at the pressure dome [Raspet *et al.*, 2019], which results in higher wind speeds. Atmospheric measurements at altitude might therefore be influenced by stagnation pressure [Bowman and Lees, 2015; Smink *et al.*, 2019; Krishnamoorthy *et al.*, 2020]. The stagnation pressure increases with increasing wind speed (Bernoulli's Equation). So, as winds speeds increase exponentially with altitude, the stagnation pressure is expected to increase [Raspet *et al.*, 2008].

It has been suggested that the application of a so-called 'quad-disc' might remove the stagnation pressure. Quad-disks are developed to cancel dynamic pressure effects, and helps detect slower static pressure changes or acoustic perturbations. Theoretical analysis of the quad-disk indicates that it should remove sufficient dynamic pressure to be useful for turbulence studies [Wyngaard and Kosovic, 1994]. However, recent studies have shown a minimum effect of quad-disks on infrasound recordings [Krishnamoorthy *et al.*, 2020]. The casing of the INFRA-EAR is designed and developed for mobile and rapid deployments at remote places, adding a quad-disk to the design will expand the dimensions of the casing. Moreover, the pressure dome is positioned at the bottom of the casing, not orientated towards the dominant wind direction, in order to minimise the stagnation pressure on the pressure sensors.

Furthermore, within this design the casings volume acts as a backing volume for the differential pressure sensor. One inlet of the differential pressure sensor is attached to the outside (via the dome) while the casing encloses the other inlet. A PEEKsil Red series capillary is attached to the outside of the casing, ensuring pressure leakage between the backing volume and the atmosphere.

GPS

For measuring geophysical parameters on a high-resolution temporal scale, it is crucial to know the position and time of the measurement at high precision. To maintain knowledge regarding the position, a GNS2301 GPS is mounted on the PCB [Texim-Europe, 2020]. The GPS has a spatial accuracy of ± 2.5 m, up to 20 km altitude.

Besides providing an accurate position, the GPS also prevents drifting of the microcontroller's internal clock under the influence of, for example, weather. The time root mean square jitter, the deviation between GPS and actual time, is ± 30 nanoseconds.

2.1.3 Infrasound sensor

The human audible sound spectrum is approximately between 20 to 20,000 Hz. Frequencies below 20 Hz or above 20 kHz are referred to as infrasound and ultrasound, respectively. The movement of large air volumes generates infrasound signals with amplitudes in millipascals' range to tens of pascals. Examples of infrasound sources include earthquakes, lightning, meteors, nuclear explosions, interfering oceanic waves and surf [Campus and Christie, 2010]. Detection of infrasound depends on the signal's strength relative to the noise levels at a remote sensor (array), i.e., the signal-to-noise ratio. The signal strength depends, in turn, on the transmission loss that a signal experiences, while propagating from source to receiver [Waxler and Assink, 2019]. Local wind noise conditions predominantly determine the noise [Raspet *et al.*, 2019], in addition to the sensor self-noise. Due to the presence of atmospheric waveguides and low absorption at infrasonic frequency [Sutherland and Bass, 2004], infrasonic signals can be detected at long distances from an infrasonic source. Assumed that the source levels are sufficiently high so that the long-range signal is above the ambient noise conditions on the receiver side, and the sensor is sensitive enough to detect the signal.

The infrasonic wavefield is conventionally measured with pressure transducers since such scalar measurements are relatively easy to perform. Those measurements can either be performed by absolute or differential pressure sensors. An absolute pressure sensor consists of a sealed aneroid and a measuring cavity connected to the atmosphere. A pressure difference within the measuring cavity will deflect the aneroid capsule. The mechanical deflection is converted to a voltage [Haak and De Wilde, 1996]. The measurement principle of a differential infrasound sensor relies on the deflection of a compliant diaphragm, which is mounted on a cavity inside the sensor. The membrane deflects due to a pressure difference inside and outside the microphone, which occurs when a sound wave passes. A pressure equalization vent is part of the design to make the microphone insensitive to slowly varying pressure differences originating from long-period changes in weather conditions [Ponceau and Bosca, 2010].

Acoustic particle velocity sensors constitute a fundamentally different class of sensors that measure the airflow over sets of heated wires. This information quantifies the 3-D particle velocity at one location, since the measurement is carried out in three directions [De Bree *et al.*, 2003; Evers and Haak, 2000]. Although such sensors' design is more involved and the sensors are far more costly, these sensors do allow for the measurement of sound directivity at one position, besides just the loudness.

Various studies show sensor self-noise and sensitivity curves of infrasound sensors [Ponceau and Bosca, 2010; Merchant, 2015; Slad and Merchant, 2016; Marty, 2019; Nief *et al.*, 2019]. The IMS specifications state that the sensor self-noise should be at least 18 dB below the global low noise curves at 1 Hz [Brown *et al.*, 2014], generated from global infrasound measurements using the IMS. Typical infrasound sensor networks, such as the IMS, use analogue sensors connected to a separate data logger to convert the measured voltage differences to a digital signal. The sensor's characteristic sensitivity determines the sensor resolution, i.e., the smallest difference that the sensor can detect. The resolution of the built-in ADC and the digitizing voltage range determine the datalogger's resolution. Current state-of-the-art data loggers have a 24-bit resolution. New infrasound sensor techniques involve digital outputs since the ADC conversion is realized inside the sensor [Nief *et al.*, 2017, 2019].

Sensor design

In this section , the mobile digital infrasound sensor's design is discussed, the KNMI mini-microbarometer (mini-MB). The design of this instrument is based on the following requirements. The sensor should have a flat, linear, response over a wide infrasonic frequency band, e.g., 0.05 - 10 Hz. The sensor should be sensitive to the range of pressure perturbations in this frequency band, which are in the range of millipascals to tens of pascals. Moreover, the sensor and logging components' self-noise should be below the ambient noise levels of the IMS [Brown *et al.*, 2014]. In addition to the sensor capabilities, there are additional constraints regarding dimensions and energy consumption as well as cost.

In this study, infrasound is measured with a differential pressure sensor. The measurement principle relies on the deflection of a diaphragm, which is mounted between two inlets. One inlet is connected to the atmosphere while the other is connected to a cavity (Figure 2.2). The digital MEMS DLVR-F50D differential pressure sensor from All Sensors Inc. [All-Sensors, 2019] is used as a sensing element within the mini-MB. This sensor has a 16.5mm x 13.0mm x 7.3mm dimension and has a linear response between ± 125 Pa with a maximum error band of ±0.7 Pa. A Wheatstone bridge senses the diaphragm's deflection by measuring the changes in the piezo-resistive elements attached to the diaphragm. The sensor's output is an analogue voltage, which is subsequently digitized by the built-in 14-bit ADC, offering a maximum resolution of 0.02 Pa/count.

Theoretical response

To measure differential pressure, the atmosphere is sampled through inlet A, which has a low resistance (R_1), and is connected to a small fore-volume (V_1). Inlet B is connected to a backing volume (V_2), which is connected to the atmosphere by capillary that acts as a high acoustic resistance (R_2), which determines the low-frequency cut off. Due to an external pressure wave, an observed pressure difference between the two inlets occurs and causes a deflection of the membrane (C_d) (Figure 2.2-a).

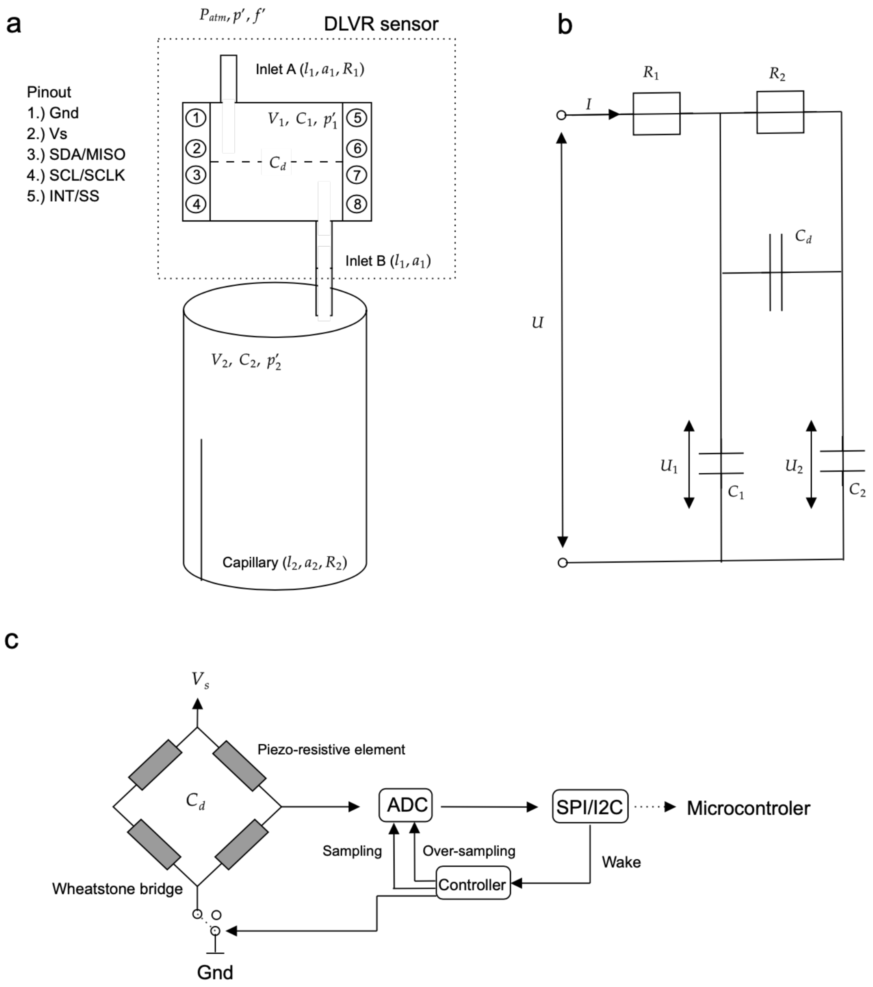

Figure 2.2: *The KNMI mini-MB design with the DLVR sensor and the parameters as listed in Table 2.1 (a) and the electrical circuit of the mini-MB (b). Panel (c) visualises the DLVR sensor.*

A theoretical response, $D(i\omega)$ for a differential pressure sensor, as function of the angular frequency $\omega(=2\pi f)$, has been derived by Mentink and Evers [2011] following Burridge [1971]:

$$D(i\omega) = \frac{i\omega\tau_2}{1 + i\omega\tau_2 A + (i\omega)^2\tau_1\tau_2 B} \tag{2.1.1}$$

where,

$$A = 1 + \frac{\tau_1}{\tau_2} + \frac{R_1}{R_2} + \frac{C_d}{C_2}, \quad B = 1 + C_d(\frac{1}{C_1} + \frac{1}{C_2}) \tag{2.1.2}$$

$$\tau_j = R_j C_j, \quad C_j = \frac{V_j}{P_{\text{atm}}\gamma} \tag{2.1.3}$$

and P_{atm} indicates the ambient barometric pressure, and γ is the thermal conduction of air. τ_j represent the time constants, and depend on R_1, and R_2, which are the resistances of the inlet and capillary, and C_1, and C_2, the capacities of the fore and backing volume.

KNMI mini-MB sensor specifications	
Components	
Inlet length	$l_1 = 3\text{x}10^{-2}\text{m}$
Capillary length	$l_2 = 5\text{x}10^{-2}\text{m}$
Inlet diameter	$a_1 = 2\text{x}10^{-2}\text{m}$
Capillary diameter	$a_2 = 1\text{x}10^{-4}\text{m}$
Diaphragm sensitivity	$C_d = 7.5\text{x}10^{-11}\text{m}^4\text{s}^2\text{kg}^{-1}$
Conditions	
Ambient pressure	$P_{\text{atm}} = 101\text{x}10^3\text{Pa}$
Isothermal gas constant	$\gamma_{iso} = 1$
Adiabatic gas constant	$\gamma_{adi} = 1.403$
Thermal conductivity	$\kappa_c = 2.5\text{x}10^{-2}$ W m^{-1} K^{-1}
Heat capacity	ρ c$_p$ = 1.1x10^3 J m^{-3} K^{-1}
Parameters	
Inlet resistance	$R_1 = 8.7\text{x}10^3$ kg m^{-4} s^{-1}
Capillary resistance	$R_2 = 2.3\text{x}10^{10}$ kg m^{-4} s^{-1}
Fore volume	$V_1 = 4.5\text{x}10^{-7}$ m ^{3}
Backing volume	$V_2 = 16.5\text{x}10^{-6}$ m ^{3}
Size fore volume	$L_1 = 2\text{x}10^{-4}\text{m}$
Size backing volume	$L_2 = 4\text{x}10^{-4}\text{m}$

Table 2.1: *KNMI mini-MB components, parameter values and standard conditions used in the computations.*

Figure 2.2-a represents the sensor setup from an acoustical perspective, where Figure 2.2-b represents the electrical analogues of the sensor. The acoustical pressure difference ($p' = p'_1 - p'_2$) and volume flux (f') are interpreted as an electrical voltage ($U = U_1 - U_2$) and current (I). The equivalent of the electrical resistance (R) corresponds to the ratio between acoustical pressure and the volume flux, whereas the capacitance (C) relates to the ratio of volume and ambient barometric pressure. The diaphragm's mechanical sensitivity (C_d) is the ratio of volume change and pressure change [Zirpel *et al.*, 1978].

From an analysis of Eq. 2.1.1, it follows that inlet A dominates in the high-frequency limit. Hence, $1/2\pi\tau_1$ indicates the high-frequency cut-off of the sensor:

$$\lim_{\omega\to+\infty} D(i\omega) \sim \frac{1}{i\omega\tau_1 B} = \frac{1}{\frac{i\omega R_1 V_1}{P_{\mathrm{atm}}}(1 + C_d(\frac{P_{\mathrm{atm}}}{V_1} + \frac{P_{\mathrm{atm}}}{V_2}))} \tag{2.1.4}$$

While at low frequencies it is obtained that frequencies much bigger than $1/\tau_2$ are averaged out. Therefore the low-frequency limit can be determined as:

$$\lim_{\omega\to 0} D(i\omega) \sim \frac{i\omega R_2 V_2}{P_{\mathrm{atm}}} \tag{2.1.5}$$

which is controlled by the characteristics of the capillary, R_2, and the size of the backing volume, V_2. The acoustical resistance of the inlet R_1 and the capillary R_2 is described by using Poiseuille's law [Washburn, 1921], which couples the resistance of airflow through a pipe (i.e., an inlet or capillary) to its length l_j and diameter a_j, by:

$$R_j = \frac{8 l_j \eta}{\pi a_j^4} \tag{2.1.6}$$

Where η stands for the viscosity of air, which equals 18.27 μPa·s at 18°C. Combining Equations 2.1.5 and 2.1.6 results in the theoretical low-frequency cut-off:

$$f_l \sim \frac{P_{\mathrm{atm}}}{2\pi R_2 V_2} \tag{2.1.7}$$

Besides the high and low ends of the response, it is of interest to determine the sensor response behavior within the passband ($\tau_2^{-1} < \omega < \tau_1^{-1}$).

$$D(i\omega) \sim (\tau_2^{-1} < \omega < \tau_1^{-1}) = \frac{1}{1 + \underbrace{\tau_1/\tau_2}_{1} + \underbrace{R_1/R_2}_{2} + \underbrace{C_d/C_2}_{3}} \tag{2.1.8}$$

The three contributions in the denominator influence the passband behaviour of the sensor:

[1] A broadband frequency response depends on a constant pressure within the reference volume over the frequencies of interest (i.e., $\tau_1 \ll \tau_2$)

[2] The pressure difference at the diaphragm is determined by the relative acoustical resistances connected to the sensor. The stability of the sensor response is assured by the capillary's large resistance, because of which $R_1 \ll R_2$.

- **[3]** The sensor response depends on the ratio between the volumetric displacement of the diaphragm (C_d) versus the reference volume (C_2). For the mini-MB, this term can be neglected.

Figure 2.3 shows the theoretical sensor frequency response for amplitude (Fig. 2.3-a) and phase (Fig. 2.3-b) for isothermal (red) and adiabatic (blue) behavior. The transitional behaviour of the sensor response between isothermal and adiabatic behaviour will be discussed in the next section.

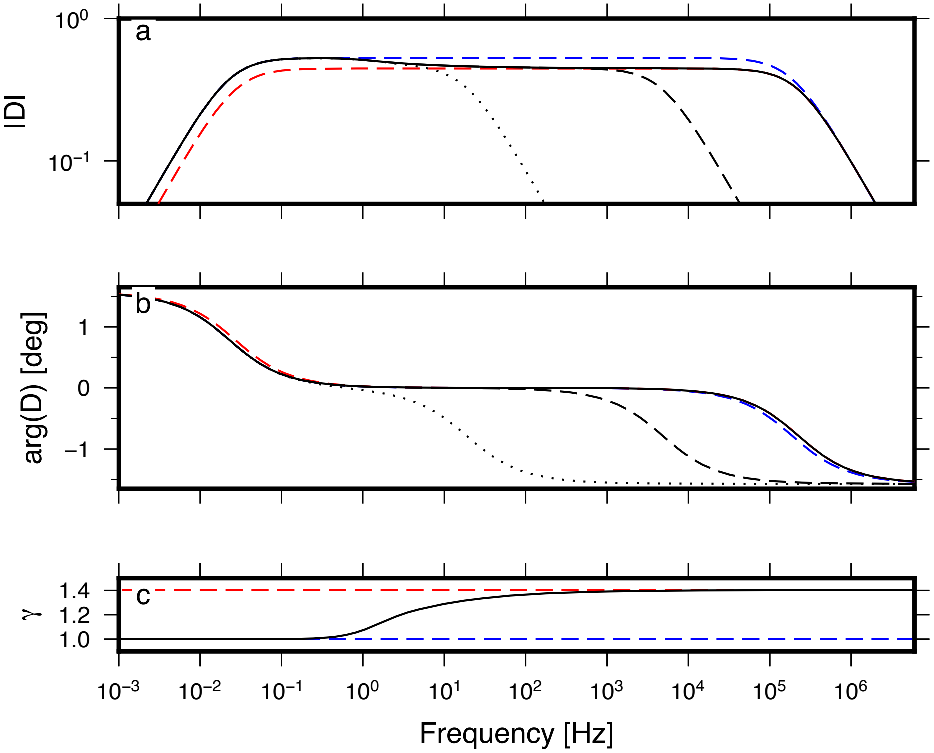

Figure 2.3: *The theoretical sensor frequency response function for (a) amplitude and (b) phase in the case of isothermal and adiabatic gas behaviour in blue and red, respectively. The solid black line indicates the corrected sensor response by* $\overline{\gamma}$ *(c). The dotted and dashed line indicate the high-frequency shifting cut-off due to* R_{gore}*.*

Adiabatic-Isothermal transition

Due to the presence of heat conduction within the sensor, air's compressive behaviour is neither isothermal nor adiabatic. Instead, a transition from isothermal to adiabatic behaviour is expected in the infrasonic frequency band [Richiardone, 1993; Mentink and Evers, 2011]. In the transition zone, the heat capacity ratio can be effectively described by:

$$\overline{\gamma} = \Lambda\gamma \tag{2.1.9}$$

where Λ indicates the correction factor, to heat capacity ratio γ. A difference in Λ will influence the capacitance values of the fore and backing volumes (Eq. 2.1.3).

Whether a sound wave in an enclosure behaves isothermally or adiabatically depends on the size of the thermal penetration depth δ_t relative to characteristic length L of the enclosure. L is defined as the ratio between the enclosure's volume and surface, i.e. $L = \frac{V}{S}$. The thermal penetration depth is specified as the gas layer thickness in which heat can diffuse through, during the time of one wave period and is derived as $\delta_t = \sqrt{\frac{2\alpha}{\omega}}$. Where $\alpha = \frac{\kappa_c}{\rho c_p}$ indicates the thermal diffusivity, defined as ratio of thermal conductivity (κ_c) and heat capacity per unit volume (ρc_p). Adiabatic gas behaviour is obtained when $\frac{\delta_t}{L} \ll 1$, isothermal gas behaviour when $\frac{\delta_t}{L} \gg 1$. The correction factor Λ is a function of δ_t/L, and is thus frequency-dependent, which can be derived as:

$$|\Lambda| = \sqrt{X^2 + Y^2}, \quad \arg(\Lambda) = \frac{\pi}{2} + \arctan(\frac{X}{Y}) \tag{2.1.10}$$

where

$$X = x(\gamma_{adi} - 1) - \gamma_{adi}, \quad Y = y(\gamma_{adi} - 1) \tag{2.1.11}$$

x and y represent the real and imaginary components of a complex-valued function $Z(\frac{\delta_t}{L})$, which is dependent on the geometrical shape of the enclosure and the thermal pentration depth. In between the adiabatic and isothermal limits, the correction factor Λ describes the transition from an adiabatic heat ratio (i.e., $\gamma = 1.4$) to an isothermal heat ratio (i.e., $\gamma = 1$). The transition frequency $\overline{f}$ defines the point where the maximum correction of Λ occurs, i.e., for which $L\delta_t \approx 1$, from which follows that $\overline{f} = \frac{\alpha}{\pi L^2}$.

In the case of the mini-MB, the fore and backing volume have different shapes and sizes. The backing volume can be described as a long cylinder, L_2, whereas the fore volume has a rectangular shape, L_1. According to those geometries, the transition frequency $\overline{f}$ of the fore and backing volume are 0.5 and 2.2 Hz, respectively. Since $\overline{f}_1 \cdot \tau_1 \ll 1$ and $\overline{f}_2 \cdot \tau_2 \gg 1$ the sensor response above τ_1^{-1} is adiabatic, while the response below τ_2^{-1} is isothermal. Therefore, the thermal conduction correction's main effect is found to be in the passband region (Eq. 2.1.8).

The mini-MB has been designed to have a broadband response, therefore only the third term of the denominator is influenced by the correction factor. The effect of thermal conduction to the response is due to ratio $\frac{C_d}{C_2}$, which means that the correction factor is characterized by the geometric component of the backing volume.

$$Z(\frac{\delta_t}{L}) = x_z + iy_z = 1 - \frac{2J_1(\zeta)}{\zeta J_0(\zeta)} \tag{2.1.12}$$

here Z indicates the characteristic correction assuming a long cylinder [Mentink and Evers, 2011]. $\zeta = \sqrt{-2i}\frac{L}{\delta_t}$ indicates the ratio of L to δ_t, while J_0 and J_1 are zeroth and first order Bessel functions of the first kind.

The corrected theoretical sensor response is obtained by substituting $\overline{C_j} = \frac{C_j}{\Lambda}$. Figure 2.3-c shows the value of $\overline{\gamma}$ in the transaction zone between isothermal and adiabatic gas behaviour. The black line in Figure 2.3-a and b indicates the corrected theoretical sensor response.

In the case of the mini-MB the isothermal-to-adiabatic transition results in an effect on the amplitude of $\Delta|D| = (\gamma - 1)\frac{C_d}{C_2} = 2.8\%$ and on the phase of less than a degree. Note that $\frac{C_d}{C_2} \ll 1$ implies that the backing volume is relatively large such that the change in gas behaviour does not influence the sensitivity of the diaphragm.

Gore-Tex air-vent

As discussed in section 2.1.2., the high and low-frequency cut-off are controlled by the resistivity of the inlet and backing volume, respectively. A Gore-Tex V9 sticker is added to the opening of the casing's pressure dome, which changes the resistivity of the inlets. The Gore-Tex V9 vent allows an airflow of 2x10^{-8} m^3 s^{-1} m^{-2}. Poiseuille's second law, Equation 2.1.6, describes the airflow resistivity caused by an open pipe, and can be re-written as;

$$R_j = \frac{\Delta p}{q_v} \tag{2.1.13}$$

where Δp indicates the pressure difference between both sides of the pipe, and q_v the volumetric airflow.

For the differential pressures that the mini-MB sensor is able to sense, ranging from 0.02 to 125 Pa, the equivalent resistivity R_{gore} ranges from 5x10^5 to 3.125x10^8 kg m^{-4} s^{-1}, with a Gore-Tex air-vent area of 5x10^{-2} m^2. Comparing the resistivity of the air-vent with the resistivity values of the capillary and the inlet of the sensor, it follows that the air-vent will only influence the inlet's resistivity (Table 2.1). Assuming the vent behaves linearly, the high-frequency cut-off of the sensor decreases to a value of around 15 Hz. Figure 2.3 shows the theoretical transfer function for the mini-MB with a Gore-Tex air-vent attached to the inlet. The high-frequency cut-off varies between the dotted line and the dashed line, due to varying values of R_{gore}.

Experimental response

The theoretical sensor response describes the high and low-frequency cut-off. From Equation 2.1.7 and the parameters listed in Table 2.1, a theoretical low-frequency cut-off value of 0.042 Hz can be calculated. This value can be estimated experimentally by application of a sudden over or under pressure (i.e., impulse response) to the sensor [Evers and Haak, 2000]. The impulse forces the diaphragm out of equilibrium. The capillary and the size of the backing volume control the time to return into equilibrium again. The time it takes for the diaphragm to reach equilibrium again corresponds to a characteristic relaxation time proportional to the low-frequency cut-off.

The outcome of the experimental low-frequency cut-off was determined to be 0.044 ± 0.0025Hz. The theoretical low-frequency cut-off falls within the error margins of the experimental cut-off frequency. The small difference between both is assumed to be due to experimental errors in timing the relaxation time as well as small imperfections in the used capillary [Evers, 2008]. It follows from Eq. 2.1.6 that the low-frequency cut-off is inversely proportional to the radius to the fourth power. Hence, a one per cent deviation in the capillary radius will lead to a four per cent deviation in low-frequency cut-off.

Sensor self-noise

The resolution, the smallest change detectable by a sensor, depends on the sensor measurement range and the number of ADC bits. Having a linear response over a pressure range of ± 125 Pa and a 14-bit built-in ADC results in a 0.02 Pa/count resolution. The accuracy of the measurement depends, besides the ADC resolution, on the sensor self-noise. The self-noise corresponds to the diaphragm's deformation caused by the mass of the diaphragm plus the electrical noise from the digitiser. As it is a digital sensor, it is impossible to follow the conventional methods to determine self-noise [Sleeman *et al.*, 2006]. Therefore the self-noise is determined by opening both inlets to a closed pressure chamber, ensuring no pressure difference between them. From this experiment, it follows that the self-noise falls within the sensor's maximum error band, ±0.7 Pa [All-Sensors, 2019]. Since no backing volume is used, and the cavities at both sides of the diaphragm are small, the relation $\frac{C_d}{C_2}$ changes (Eq. 2.1.8). Due to this, it is necessary to correct the sensor response for the adiabatic to isothermal transition.

The self-noise consistency is determined by calculating the Power Spectral Density (PSD) curves for each hour over a test period of 24 hours [Merchant and Hart, 2011]. Figure 2.4-a shows in black the average 90 percentile confidence interval of the self-noise. Note that the instrumental self-noise exceeds the global low noise model [Brown *et al.*, 2014] at frequencies above 0.4 Hz. Compared to high-fidelity equipment that typically falls entirely below the global low noise models, such self-noise levels are relatively high, yet comparable to levels attained by similar sensor designs [Marcillo *et al.*, 2012]. Furthermore, note that the self-noise follows the dynamic range of a 12-bit ADC, as indicated by the gray dotted line [Sleeman *et al.*, 2006]. The sensor has a maximum 'no missing code' of 12-bits, the effective number of bits [All-Sensors, 2019].

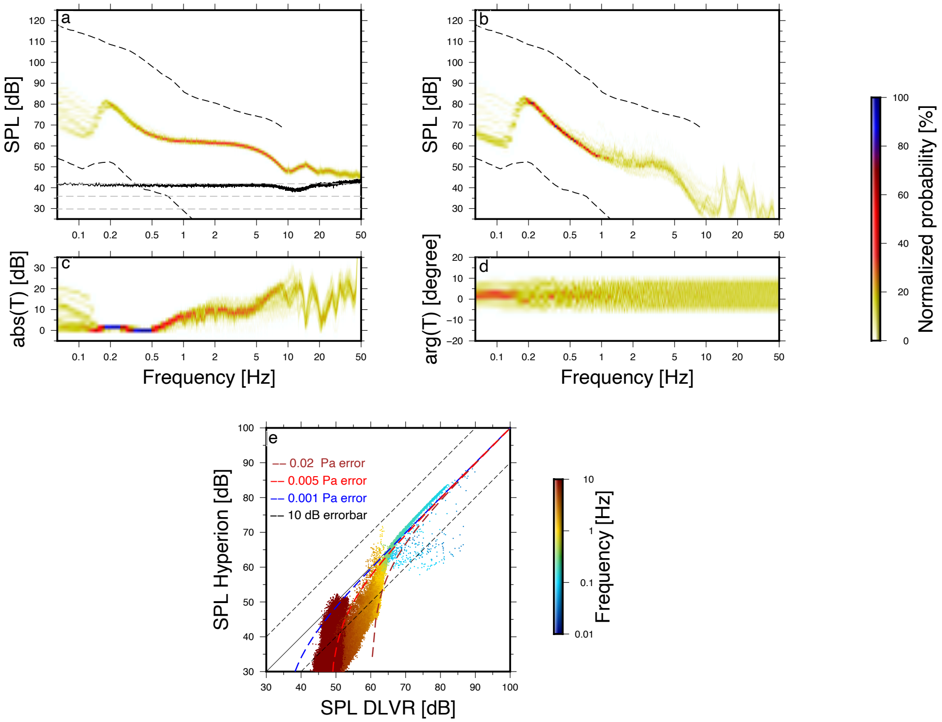

Figure 2.4: *PPSD of pressure spectra recorded with the mini-MB (a) and the Hyperion sensor (b) for a week of continuous recording in dB re.* 20^{-6} *Pa*^{2}*/Hz. The dashed lines indicate the infrasonic high and low ambient noise levels [Brown* et al.*, 2014]. Panel (a) shows the PSD of the 24hr self-noise recording of the mini-MB in black, and the theoretical self-noise for a 12-, 13-, and 14-bit ADC as the gray dashed lines. Panels (c) and (d) visualise the absolute difference T in amplitude and phase between the mini-MB and the Hyperion as a function of frequency. Panel (e) displays the differences in sound pressure level measured by the mini-MB and the Hyperion sensor for the various frequencies.*

Sensor comparison

A comparison between the mini-MB and a Hyperion IFS-5111 sensor [Merchant, 2015] is made to assess the mini-MB performance relative to the reference Hyperion sensor. Both sensors have been placed inside a cabin next to the outside sensor test facility at the leading author's institute. There is a connection to the outside pressure field through air holes in the wall of the cabin. The Hyperion sensor has been configured with a high-frequency shroud. Figure 2.4-a and b show the PPSD [Merchant and Hart, 2011] of the data recorded by the mini-MB and the Hyperion sensor, respectively. Both sensors resolve the characteristic microbarom peak around 0.2Hz [Christie and Campus, 2010]. The spectral peaks above 10 Hz correspond to resonances that exist inside the measurement shelter.

A direct comparison of the pressure recordings are shown in Figures 2.4-c, -d, and -e. Figure 2.2-c shows the absolute difference in amplitude over frequency, where panel d indicates the phase difference between both sensors. Panel e shows the relative difference between the mini-MB and the Hyperion sensor. The sensors are in good agreement over the passband frequencies. A larger deviation is shown for the low end ($f < 0.07$ Hz) and high end frequencies($f > 8$ Hz). At frequencies between 0.1 and 0.5 Hz, the pressure values are positively biased by 5 ± 1 dB, which equals a measurement error by the KNMI mini-MB of ± 0.005 Pa (Figure 2.4-e). Above 1 Hz, the pressure values are biased by 10 ± 5 dB, which equals a measurement error of ± 0.02 Pa.

The high-frequency deviation is due to the relatively high noise level of the mini-MB. For the higher frequencies, the mini-MB PPSD follows the 12-bit dynamic range. Only in case of significant events or loud ambient noise, the sensor can sense pressure perturbations in the high-frequency range. Nonetheless, the mini-MB falls within a 30 dB error range over the entire frequency band compared to the Hyperion IFS-5111 sensor.

■ 2.1.4 Barometric pressure sensor

The detectability of infrasound is directly linked to wind noise conditions and the atmosphere's stability in the infrasound sensor's surrounding since noise levels are increased when turbulence levels are high. Therefore, it is beneficial to have simultaneous measurements of the basic meteorological parameters, i.e., pressure, wind and temperature.

The barometric pressure is sensed by the LPS33HW sensor [STMicroelectronics, 2020*a*], which is part of the pressure dome. Similarly to the differential pressure sensor, piezo-resistive crystals measure the barometric pressure.

Calibration tests are performed within a pressure chamber, in which a cycle of static pressures between 960 and 1070 hPa can be produced. Besides the MEMS sensor, the chamber is equipped with a reference sensor. This procedure results in a calibration curve, which describes the pressure-dependent systematic bias. After correcting for the bias, the LPS sensor has an accuracy of ± 0.1 hPa, i.e., the LPS sensors measure values within ± 0.1 hPa of the value measured by the KNMI reference sensor. Furthermore, the LPS sensor has been field-tested (Figure 2.5-a), along with a Paroscientific Digiquartz 1015A barometer, which has an accuracy of 0.05 hPa. From the distribution of observations, it can be estimated that the LPS sensor has a precision of ±0.1 hPa for 93% of the time (Figure 2.5-b). For the remainder, the maximum deviation was ±0.15 hPa.

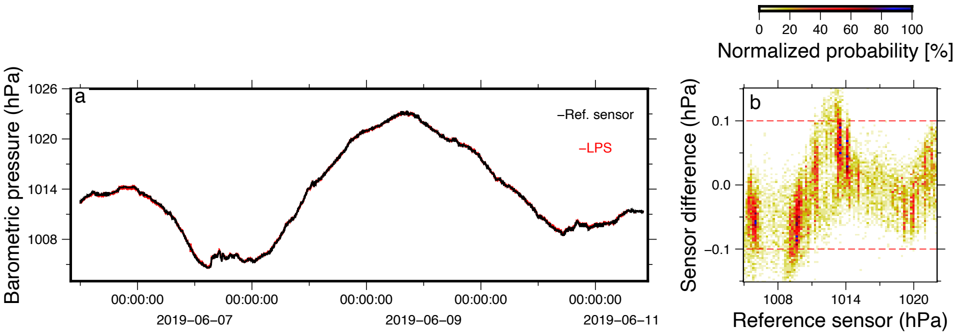

Figure 2.5: *A comparison between the Barometric MEMS sensor (red) and a KNMI reference barometer (black). Panel (a) shows five days of barometric pressure recordings using both sensors, while panel (b) displays the difference in measured barometric pressure by the MEMS and the reference sensor.*

2.1.5 Wind sensor

The pressure field at infrasonic frequencies consists, in addition to coherent acoustic signals, to a large degree of pressure perturbations due to wind and turbulence [Walker and Hedlin, 2010]. This turbulent energy is present over the complete infrasonic frequency range with a typical noise amplitude level decrease with increasing frequencies, following a $f^{-5/3}$ slope [Raspet *et al.*, 2019].

To reduce wind turbulence interference with the acoustic perturbations, a Wind-Noise-Reduction-System (WNRS) can be put in place [Walker and Hedlin, 2010; Raspet *et al.*, 2019]. Most WNRS filters consist of a non-porous pipe rosette, with low impedance inlets at each pipe's end. All pipes are connected to four main pipes, which connect to the microbarometer. Doing so, the atmosphere is sampled over a larger area. The non-acoustic pressure perturbations are not coherent over this area in contrast to acoustic waves. Hence, the non-acoustic perturbations are filtered out.

The sensor presented in this chapter is designed for mobile sampling campaigns. In such cases, the application of similar WNRS filters cannot be attained. The SNR may decrease due to wind turbulences. Nonetheless, implementing the wind measurements of the anemometer provides insight into the wind conditions. Therefore, a simultaneous measurement of wind and infrasound provides better insight into the infrasonic SNR conditions.

Sensor design

A 2D omnidirectional heat mass flow sensor has been designed to measure the wind conditions, which is a robust and passive anemometer (Figure 2.6-a). The sensor is built with a central heating element, which heats to approximately 80°C, and is circularly surrounded by six TDK thermistors [TDK, 2018]. Depending on the wind direction and speed, the temperature field around the center element is modified. The wind speed and direction can be estimated from the 2D temperature gradient, i.e., from its absolute value and direction.

Theoretical response

The six sensing elements are placed within a distance of one centimeter from the heating element, while two thermistors and the heating element are at a spatial angle of 60°. The thermistors measure the temperature gradient caused by the wind flow since the resistance is strongly sensitive to temperature. The thermistors are made of semiconductor material and have a negative temperature coefficient. The resistance decreases non-linearly with increasing temperature. The Steinhart-Hart equation approximately describes the temperature T as a function of resistance value R_Ω [Steinhart and Hart, 1968]:

$$\frac{1}{T} = C_{\Omega_1} + C_{\Omega_2}\ln(R_\Omega) + C_{\Omega_3}\ln(R_\Omega)^3 \tag{2.1.14}$$

where $C_{\Omega_1}, C_{\Omega_2}$, and C_{Ω_3} are the thermistor constants according to the manufacturer [TDK, 2018]. However, they can as well be determined by taking three calibration measurements, for which the temperature and resistance are known, after which a linear system of equations can be solved simultaneously. Figure 2.6-b shows the sensitivity curve for the TDK thermistor. The thermistor has a relative value of 1Ω at 25°C, and a precision of ±4%/°C, which leads to a 0.05°C error. This error value is placed in context by modeling the expected temperature difference under representative meteorological conditions in the next section .

Numerical sensor response

The heating element needs to transfer a minimum temperature difference around the sensing elements (i.e., the sensing elements error). A numerical model has been built in ANSYS [ANSYS, n.d.] to define the amount of temperature difference around the sensing elements under different meteorological circumstances. The model is a first approximation of the sensitivity and is based on homogeneous laminar airflow passing by the sensor. Turbulent flow, along the anemometer, caused by the sensor design or casing, generates uncertainties within the measurements.

This first approximation of sensitivity follows a numerical forward modeling technique to approximate the heat probe's shape and intensity at a sensing element. The model was run at stable meteorological parameters (i.e., 8°C air temperature, 50% humidity, and 10 m/s wind speed). The outcome shows that under those circumstances, the sensing element experiences a temperature difference of around 4°C. Together with the outcome of the thermistors' sensitivity curve, it is concluded that the designed sensor can resolve this airflow and is used to estimate wind speed and direction.

Conversion of sensor output into atmospheric parameters

To convert the measured resistivity into atmospheric parameters, a 2D planar temperature gradient has been estimated numerically from the discrete set of measurements. The measurement resistivities have been transformed into temperature measurements following Eq. 2.1.14. Based on those temperatures, a 2D numerical temperature gradient has been reconstructed. The problem is analogous to the estimation of the wave-front directivity from travel time differences [Szuberla and Olson, 2004].

In the present case, there are $N = 6$ discrete sample points, each with an $r_j = (x_j, y_j)$ coordinate and a temperature value T_j. The total differential of the temperature describes the variation of temperature $T(x, y)$ as a function of x and y:

$$dT = \frac{\partial T}{\partial x}dx + \frac{\partial T}{\partial y}dy. \tag{2.1.15}$$

From equation 2.1.15, it follows that we can determine the two dimensional gradient $\nabla T = (\frac{\partial T}{\partial x}, \frac{\partial T}{\partial y})$ by setting up a system of N equations. In this case, the number of unknowns is two, and thus the gradient could be estimated by two measurements. However, in practice, errors are introduced due to measurement errors. Therefore the set of equations becomes inconsistent, which leads to nonsensical solutions. The unknown set of parameters is solved by over-determining the system in a least-squares sense to overcome this problem. Equation 2.1.15 can be rewritten in terms of a matrix-vector system:

$$\mathbf{y} = \mathbb{X}\mathbf{p} + \epsilon \tag{2.1.16}$$

where $\mathbf{y}$ represents the temperature difference between two measurement points, matrix $\mathbb{X}$ represents the $M = \frac{N(N-1)}{2}$ pair-wise separations and $\mathbf{p}$ represents the temperature gradient ∇T. It is assumed that the measurement errors ϵ can be described by a normal distribution, i.e. a random variable with mean $E(\epsilon) = 0$ and variance $Var(\epsilon) = \sigma^2$. It can be been shown that the least-squares estimate of $\mathbf{p}$, here labeled $\hat{\mathbf{p}}$, can be obtained by solving the following equation:

$$\hat{\mathbf{p}} = (\mathbb{X}^\dagger\mathbb{X})^{-1}\mathbb{X}^\dagger\mathbf{y} \tag{2.1.17}$$

$$\mathbf{p_x} = \frac{\hat{\mathbf{p}}_x}{\hat{\mathbf{p}}_x^2 + \hat{\mathbf{p}}_\mathbf{y}^2}, \mathbf{p_y} = \frac{\hat{\mathbf{p}}_y}{\hat{\mathbf{p}}_x^2 + \hat{\mathbf{p}}_y^2} \tag{2.1.18}$$

where † represents the transpose operator, the solution satisfies equation 2.1.16 with the constraint that the sum of squared errors is minimized. The matrix $\mathbb{X}$ and the error term ϵ determine the solution's accuracy. If a Gaussian distribution can represent the measurement errors, it can be shown that the least-squares solution is unbiased.

Based on the 2D reconstruction of the temperature gradient (Equation 2.1.18), the wind direction and speed is resolved, with an estimated accuracy. Furthermore, this method allows determining the uncertainty based on geometric sensor set-up [Szuberla and Olson, 2004]. Figure 2.6-c shows the least-squares error analyses of the sensor design (Figure 2.6-a). It stands out that the uncertainty increases when one element is positioned close to the wind flow (i.e., at 60°).

Reference calibration

Experimental calibration of the anemometer has been performed at KNMI's calibration lab. The calibration lab features a wind tunnel, which generates a laminar airflow ranging between 0 - 20 m/s. Within the wind-tunnel, two mechanical anemometers are installed, which serve as reference sensors. With its MEMS anemometer, the mobile platform is installed right below one of the reference sensors to ensure that the mobile platform does not obstruct the laminar flow in the tunnel.

The calibration procedure consists of multiple independent calibration tests that will be described next. First, the sensor is placed inside the wind tunnel while there is no airflow. This way, the relative difference between the sensing elements is determined, the so-called zero-measurement. The sensor is corrected for the internal bias by correcting for the relative difference, which varies around ± 25 ohm. After correcting the sensor bias, the sensor is placed within the horizontal plane (i.e., with a pitch angle of 0°) at different angles concerning the airflow. For every angle, the flow speed is varied between 0 to 20 m/s.

The calibration shows that the measured resistance of the thermistors increases with increasing wind speeds. High wind speeds increasingly cool down the thermistors, resulting in higher resistances. Figure 2.6-d shows the six thermistors' measured resistance over the actual wind speed.

The wind direction and the accuracy of the anemometers have been determined according to Eq. 2.1.17. Three different sensor set-ups show the accuracy and precision over increasing wind speeds as a function of directivity. The outcome of calibration set-ups 1 (270°), 2 (90°), and 3 (60°) are shown respectively in Figure 2.6-c. The mean direction over all wind speeds, for the three set-ups, is 272°, 89°, and 57°. The standard deviation shows that the sensor's accuracy is ±5°. Furthermore, it is shown that the precision of the wind direction increases with increasing wind speeds. The resolved wind speeds by the anemometer and the difference with the correct wind speed are shown in Figure 2.6-e. The colors indicate the difference between resolved wind speed and correct wind speed within the wind tunnel. The mean deviation between resolved and correct wind speed is ±2 m/s. Again, it is shown that the accuracy increases with increasing wind speeds.

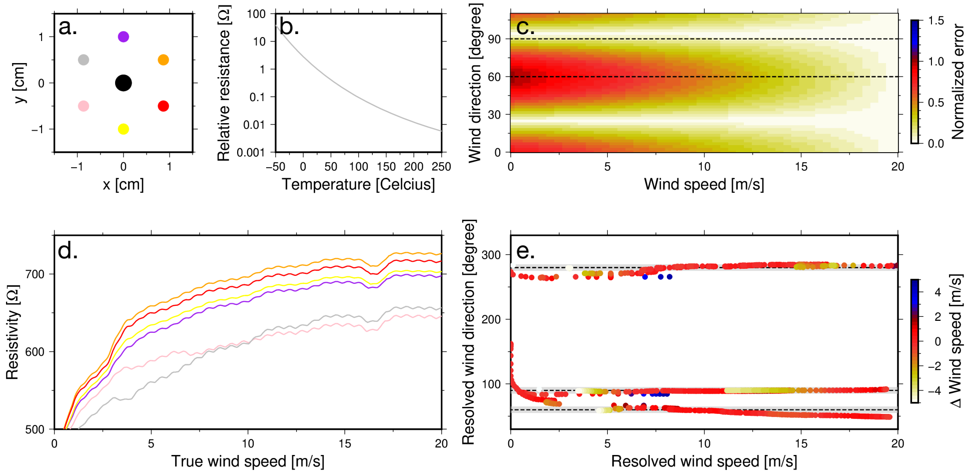

Figure 2.6: *Analyses of the anemometer. Panel a shows the top view of the sensor design, with the central heating element. Panel b indicates the resistivity of the thermistors over temperature. The geometric sensitivity for the anemometer is shown in panel c. The thermistors' measured resistance for calibration set-up 2 (90°), the colors are in agreement with the sensor design (a), are shown in panel d. Panel e indicates the resolved wind direction and wind speed compared with the actual direction (dotted lines) and correct wind speed of set-ups 1 (270°), 2 (90°), and 3 (60°). The gray shaded area indicates the ±5° accuracy interval.*

2.1.6 Accelerometer

The sensing element of the infrasound sensor on this platform is a sensitive diaphragm. Strong accelerations of the platform will cause a deflection of the diaphragm and may obscure infrasonic signal levels. In addition, such accelerations may be misinterpreted as infrasound if no independent accelerometer information is available. To be able to separate the mechanical response of the sensor from actual signals of interest, the platform measures accelerations for which the LSM303, a 6-axis inertial measurement unit (IMU), is deployed [STMicroelectronics, 2020*b*]. The LSM303 consists of a 3-axis accelerometer and 3-axis magnetometer. The measurement range of the accelerometer varies between approximately 2-16 g. The magnetometer is out of the scope of this study and therefore neglected for the remainder.

Accelerometers measure differential movement between the gravitational field vector and its reference frame. In the absence of linear acceleration, the sensor measures the rotated gravitational field vector, which can be used to calibrate the sensor. A rotational movement of the sensor will result in acceleration. The IMU is a digital sensor with a built-in 16-bits ADC and has a resolution of 0.06 mg when choosing the lowest measurement range.

A comparison test has been carried out in the seismic pavilion of the author's institute. Inside this pavilion, the LSM is compared to a Streckeisen STS-2 seismometer connected to a Quanterra Q330, as a reference sensor [KNMI, 1993]. Both sensors are installed on pillars, to ensure a good coupling between the subsurface and the sensor. The comparison test, which consist of 24 hours of recording, shows that the accuracy of the LSM303 3-axis accelerometer is ±1.5 mg (1.5 cm/s^2). Figure 2.7 shows the PPSDs of the comparison test between the MEMS and STS-2 sensors. While the sensors are deployed on the same seismic pillar and are thus subject to similar seismic noise conditions, the MEMS sensor could not measure ambient seismic noise [Peterson, 1993; McNamara and Buland, 2004] due to its high self-noise level. The LSM accelerometer exceeds both the U.S. Geological Survey New High Noise Model (NHNM) [Peterson, 1993] and the STS-2 reference sensor by at least 35 dB.

It is therefore unlikely to use this IMU for monitoring purposes of ambient seismic noise or teleseismic events. Previous studies drew similar conclusions concerning the performance of MEMS accelerometers. Various calibration set-ups are considered while comparing MEMS accelerometers with conventional accelerometers of geophones [Hons *et al.*, 2008; Albarbar *et al.*, 2009; Anthony *et al.*, 2019], each concluding that the accuracy of the MEMS is not sufficient for recording ambient seismic noise. However, the MEMS sensor will resolve seismic signals of strong local events or boisterous environments.

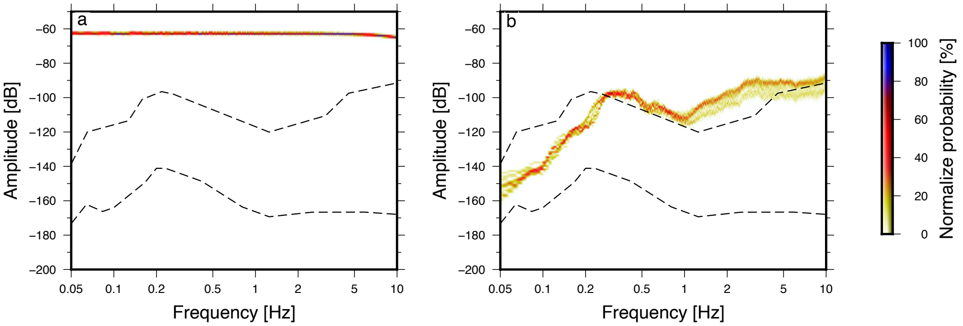

Figure 2.7: *PPSD's of the LSM IMU accelerometer (a) and the Streckeisen STS-2 connected to a Quanterra Q330 (b) for 24 hours of continuous recording in dB re.* $m^2s^{-4}Hz^{-1}$*. The dotted lines indicate the seismic high and low ambient noise levels [Peterson, 1993].*

2.1.7 Discussion and Conclusion

In this study, the constructional efforts and calibration protocols of the INFRA-EAR are presented. The INFRA-EAR is a low-cost mobile multidisciplinary sensor platform for the monitoring of geophysical quantities. It includes sensors for the measurement of infrasound, acceleration, as well as barometric pressure and wind.

The platform uses the newest sensor technology, i.e., digital MEMS, which have a built-in ADC. The MSP430 programmable microcontroller unit controls the sampling of the ADCs and the storage of the data samples. A MEMS GPS is embedded as well, to determine the positioning and to prevent clock-drift. Due to the small dimension of MEMS, and their low energy consumption, the "infrasound-logger" is a pocket-size measurement platform, powered by an 1800 mAh lithium battery. The platform does not require any infrastructure (e.g., data connection, power supply and specific mounting) like commonly used for the deployment of high-fidelity systems, which makes it mobile and allows rapid deployments and measurements at remote places.

The INFRA-EAR is specifically designed to measure infrasound. The platform hosts the KNMI mini-MB, a novel design with a pressure dome as inlet, the casing as backing-volume with a PEEKsil capillary, and the DLVR-F50D as sensing element. The low-frequency cut-off of mini-MB depends on the size of the backing volume, and the capillary characteristics. The high-frequency cut-off depends on the mini-MB inlet parameters, which is partly controlled by a Gore-Tex air-vent (section 2.1.4). The INFRA-EAR has a low-frequency cut-off frequency of 0.044 ± 0.0025 Hz, while the high-frequency cut-off varies between 15 and 90 Hz.

A comparison between the mini-MB and a Hyperion infrasound sensor [Merchant, 2015] have shown the differences in amplitude and phase (Figure 2.4). The mini-MB has an amplitude difference of 30 dB for the passband frequencies band compared to the Hyperion sensor. The sensors are in good agreement for the lower frequencies, and both sensors resolved the characteristic microbarom peak around 0.2 Hz [Christie and Campus, 2010]. However, the higher frequencies show small deviations, which is due to the relatively high noise band of the mini-MB. From 8 Hz onward, the mini-MB PPSD follows the 12-bit dynamic range of the ADC. Nonetheless, the mini-MB can resolve the infrasonic ambient noise field up to ± 8 Hz. Only in case of significant events or boisterous conditions, the sensor can sense pressure perturbations in the higher frequency range.

When the wind-noise levels are high, infrasound signals can be masked and remain undetected. Therefore, the sensor platform presents a passive anemometer to give insights into the wind conditions during infrasonic measurements. The MEMS anemometer is built up as an omnidirectional sensor. Numerical tests indicate that the temperature difference caused by a wind flow around the thermistors should be significant to be sensed. For validation, the anemometer has been calibrated inside a wind tunnel. Figure 2.6 shows the outcome of the calibration tests. Based on this outcome, one can conclude that the anemometer can determine wind direction and wind speed, given that the sensor is calibrated. The sensor measures a difference in resistance, which is converted into a temperature measurement. The temperature measurements are used to reconstruct a 2D planar temperature gradient, which is used to determine the wind speed and direction. Based on the calibration tests within the windtunnel, it is shown that the anemometer has a directional accuracy of ±5°, and a wind speed accuracy of ±2 m/s. Nonetheless, it is shown in Figure 2.6-c that the anemometer has geometrical uncertainties, due to it design. Future 2D hot-wire anemometers, should consider a minimum of 8 thermistors to exclude geometric uncertainties [Szuberla and Olson, 2004].

Besides an anemometer and infrasound sensor, the platform also hosts a barometric pressure sensor, an accelerometer, and GPS. Each sensor has been calibrated and compared with a reference sensor. It was shown that the accelerometer has a relatively high self-noise, which restricts the sensors ability to determine the ambient seismic noise [Peterson, 1993; McNamara and Buland, 2004]. Nonetheless, the sensor will most likely resolve local transient events, which could possibly influence the mini-MB's sensitivity and its ability to resolve infrasonic sources. The barometric sensor shows good agreement with a reference sensor (Figure 2.5). Absolute pressure perturbations due to the weather are resolved. After calibration, the sensor has a precision of ±0.1 hPa for 93% of the time. For the remainder maximum deviation, compared to the reference sensor, was ±0.15 hPa.

Calibration tests, performed in this study, show that the MEMS sensors perform less well than the commonly used high-fidelity sensors. These results are in line with results from earlier studies (REF). The self-noise of the sensors is a critical problem. Furthermore, the MEMS sensors manufacturers highlight a significant change of measurement drift [All-Sensors, 2019; TDK, 2018; STMicroelectronics, 2020*a*,*b*]. Hence, regular calibration is needed. Nonetheless, the MEMS sensor techniques are continuously developing [Jacob *et al.*, 2014; Johari, 2003]. The INFRA-EAR design is such that the platform can be adjusted and improved by adding or swapping sensors. Mobile sensor platforms, built up using PCB's and digital MEMS sensors, are therefore scalable, flexible, and ready for various geophysical measurements.

In addition, a low-cost mobile multidisciplinary sensor platform can complement existing high-fidelity geophysical sensor networks. This study shows that, as long as the MEMS are well-calibrated, they complement existing sensor networks. Therefore, mobile platforms such as the INFRA-EAR could contribute significantly to providing observations during remote or rapid deployments (e.g., meteorological towers, weather balloons, and scientific balloons). Although the sensor data does not fully satisfy the measurement requirements, the application of low-cost MEMS sensor enables measurements at much higher spatial resolution. Such deployments allow for increasing the SNR. This can be realized by stacking the output of various sensor platforms or adding more sensors to the same sensor platform and averaging the output [Nishimura *et al.*, 2019]. Stacking improves the signal-to-noise ratio by $1/\sqrt{N}$, where N is the number of observations.

Initially, the INFRA-EAR has been designed as a biologger for the monitoring of atmospheric parameters. In total 25 INFRA-EAR's are produced and used during the 2020 field campaign at Crozet Island in the Southern Ocean. The loggers have been fitted to the Southern Ocean's largest seabirds, the Wandering Albatross (*Diomedea exulans*). The Southern Hemisphere has very little in situ measurements, due to limited shore areas. The use of INFRA-EAR in such areas is ideal for monitoring geophysical parameters, comparing in situ measurements, and comparing INFRA-EAR data with model data (chapter 4).

2.2 The Multi-EAR; to complement the existing high-fidelity monitoring network

2.2.1 Introduction

Within this section , the Multi Earth and Atmospheric data Recorder (Multi-EAR) is introduced. The Multi-EAR is a mobile, low-cost multidisciplinary sensor platform for scientific monitoring of the earth and atmosphere. The platform can complement existing high-quality, sensor networks. This platform is designed using digital MEMS sensors embedded on a PCB. Due to the low power consumption of MEMS, the system can be powered by a battery or solar panel.

The Multi-EAR is a further development of the INFRA-EAR (section 2.1), which was designed as biologger designed to fit a Wandering Albatross. Such requirements, and thus dimensional restrictions, were not applicable in the design and development of the Multi-EAR. This project aims to develop, based on earlier recommendations, a multidisciplinary mobile sensor platform to complement the existing high-fidelity monitoring network. Due to its digital design, the sensor platform can readily be integrated with existing geophysical data infrastructures and be embedded in geophysical data analysis. To include the Multi-EAR within existing monitoring networks, a Technology Readiness Level (TRL) of 8 is needed (Figure 2.8, [NASA, 2021]).

This section is the technical report of the Multi-EAR. The subsections will describe the sensor platform. Section 2.2.2 discusses the sensors on the board, their response functions and the accuracy/tolerance. Section 2.2.3 describes the design of the casings. Two different casings are designed. The smaller casings are for rapid deployment, whereas the larger casings are entirely autonomous and serve remote places. The calibration and comparison study of the Multi-EAR is highlighted within section 2.2.4. The conclusion and discussion are discussed in section 2.2.5. The outlook and next steps of this project are summarised in section 2.2.6.

The project description, goals, applications, and news can be found on the Multi-EAR website (www.multi-ear.org). The complete description, codes, firmware, software, and STEP files of the Multi-EAR are available on the GitHub page (https://github.com/Multi-EAR). The GitHub repository will be an up-to-date database for information regarding the Multi-EAR.

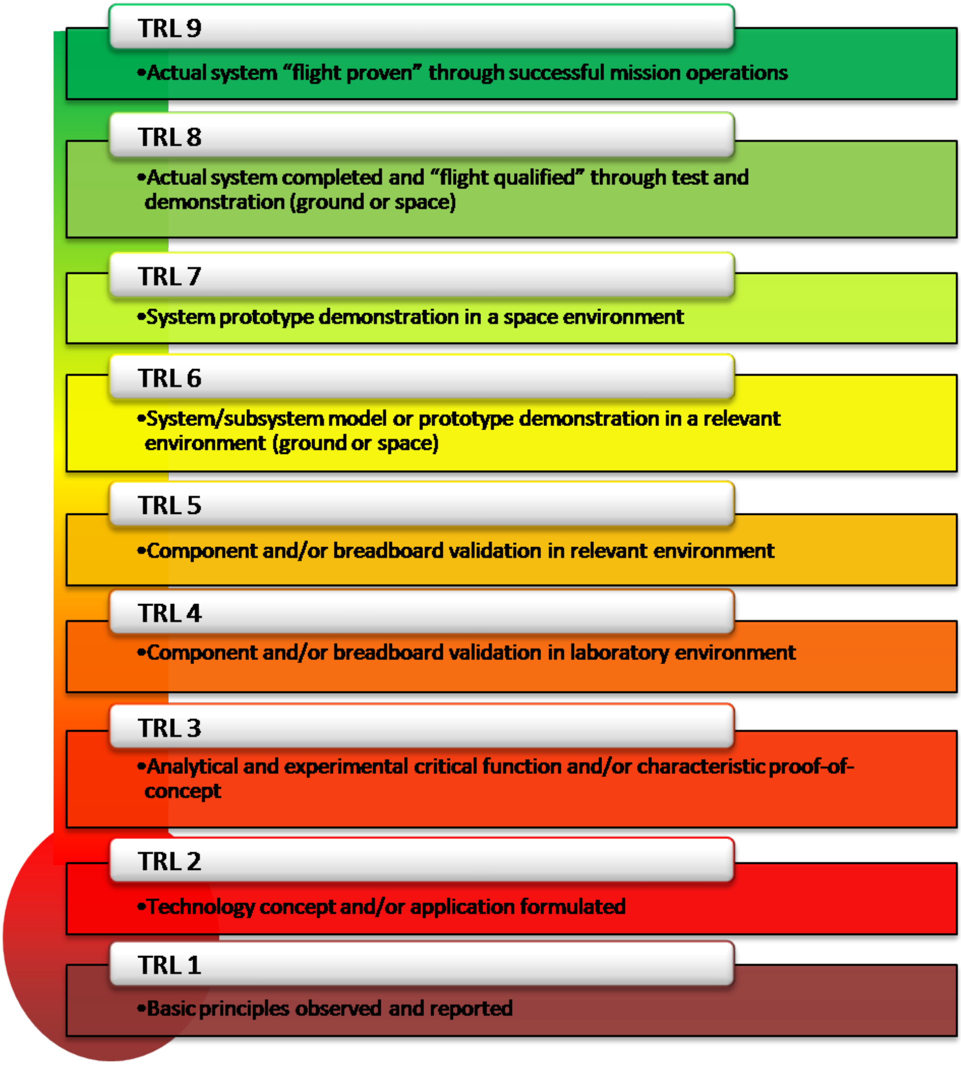

Figure 2.8: *Technology Readiness Levels (TRL) are a measure to assess the maturity level of a particular technology. There are nine technology readiness levels, TRL 1 is the lowest and TRL 9 is the highest. The figure and definitions are adopted from NASA [NASA, 2021].*

■ 2.2.2 Mobile platform design

Circuit design

The platform of the Multi-EAR uses various digital MEMS embedded on a PCB. A programmable microcontroller unit, embedded on the PCB, controls the sensor's sampling frequency, establishes the energy supply for the sensors, the data communication, and data storage.

The MEMS on the PCB are; two differential pressure sensors (to monitor infrasound), a 6-axis accelerometer/gyroscope, a 6-axis accelerometer/magnetometer, a barometric pressure sensor, a temperature/humidity sensor, microphones (to monitor audible sound), a GPS for location and timing purposes, and LoRa telecommunication for data exchange.

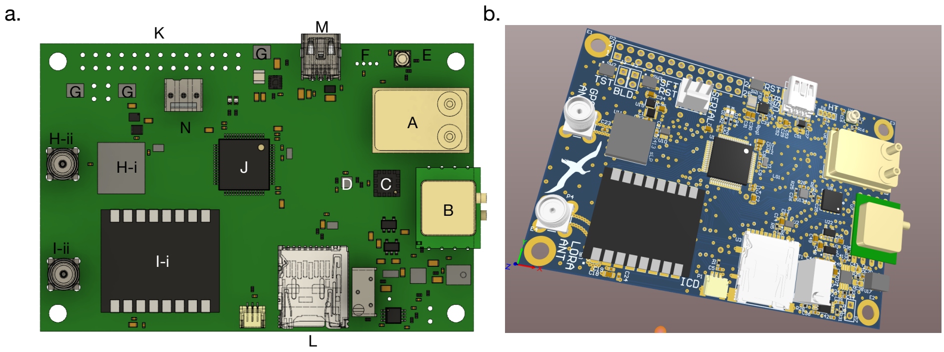

Figure 2.9: *3D CAD design of the Multi-EAR. (a) The top view of the PCB, and (b) the 3D STEP file. The PCB hosts: a Superior Sensor SP210 differential pressure sensor (A), an All-Sensor DLVR-F50D differential pressure sensor (B), a ST Electronics LSM303 6-axis accelerometer/magnetometer (C), a LIS3DH 6-axis accelerometer/gyroscope (D), a ST Electronics LPS33HW barometric pressure sensor (E), a Sensirion SHT8x temperature and humidity sensor (F), three ICS microphones (G), a Texim GNS2301 (H-i) and LoRa telecommunication (I-i) connected to LINX passive antennas (H-ii/I-ii), and a MSP430 Texas instruments microcontroller (J). The platform can either be powered over the GPIO pins (K) or via mini-USB (M). The data can be stored on the microcontroller's flash memory, locally on a micro-SD card (L), or using an external device connected using the GPIO interface.*

Firmware

The communication between the microcontroller and MEMS on the PCB is similar to the INFRA-EAR (section 2.1.2). It is either done by I2C or SPi and depends on the sensor, the available ports on the microcontroller, and personal preference. The microcontroller runs, also similar to the INFRA-EAR, on self-made software, complementing the required manufacturers electrical and communication protocols. The software allows determining the sample time, sample frequency, and data storage of selected MEMS. The raw output of the digital MEMS sensors are stored as bits, and the microcontroller performs no data processing to save power consumption. The firmware, and thus the data acquisition, can be changed by updating the microcontroller.

Raspberry Pi - an external data logger

The microcontroller communicates in two ways with the MEMS. After sampling, the MEMS send their data back to the microcontroller. The data can be stored locally on the PCB, using a micro-SD card, or can be recorded by a Raspberry Pi (RPi) [Raspberry-Pi, 2018] through the Universal Asynchronous Receiver Transmitter (UART). The UART communication is facilitated by the General-Purpose Input/Output (GPIO) pins that are embedded on the PCB. The RPi can therefore act as a small datalogger. The RPi receives on a pre-specified baud-rate the data in bytes.

The metadata of the Multi-EAR can be found within the XML files. Within these files, the response functions of the sensors are stored, as well as the transformation constants to convert the bytes/floats into actual geophysical units.

The RPi is a useful datalogger for this type of sensor platform, because it is a small single-board computer and has all the usual connections (i.e., HDMI, USB, Micro-USB, Ethernet). The operating system on the RPi's of the Multi-EAR is 'raspbian-lite' and can connect with WiFi. The data can be accessed directly on the RPi or be transferred towards an external device. Data can be retrieved over the (wireless) network interface, using standard protocols such as SSH.

LoRa Telecommunication

Besides transferring data via the RPi and WiFi, the data can also be transferred by LoRa Telecommunication [RF-LoRa, 2021]. LoRa is a type of wireless telecommunication protocol designed to allow long-range communications at a low bit rate between nodes. The low power consumption, low bit rate and intended use distinguishes this type of network protocol from a wireless wide area network (WAN), which is designed to connect more users and carry more data, using more power. The LoRa data rate ranges from 0.3 kbit/s to 50 kbit/s per channel. LoRa may be used to create a private wireless sensor network but may also be a service or infrastructure offered by a third party, allowing the owners of sensors to deploy them in the field without investing in gateway technology.

2.2.3 Sound sensors

Audible sound

For the monitoring of the audible sound spectrum, three omnidirectional ICS-40300 microphones are embedded on the PCB [TDK, 2021]. These microphones can record between 6 Hz - 20kHz, while having a flat instrument response between $50 - 2500$ Hz (Figure 2.10). The A-weighted noise floor of the frequency band between 20 Hz - 20kHz is -108 dB. The maximum Sound-Pressure-Level (SPL) before the overload is reached is 130 dB for these microphones. The intention of combining audible and infrasound sensors is to broaden the acoustic frequency range that can be measured.

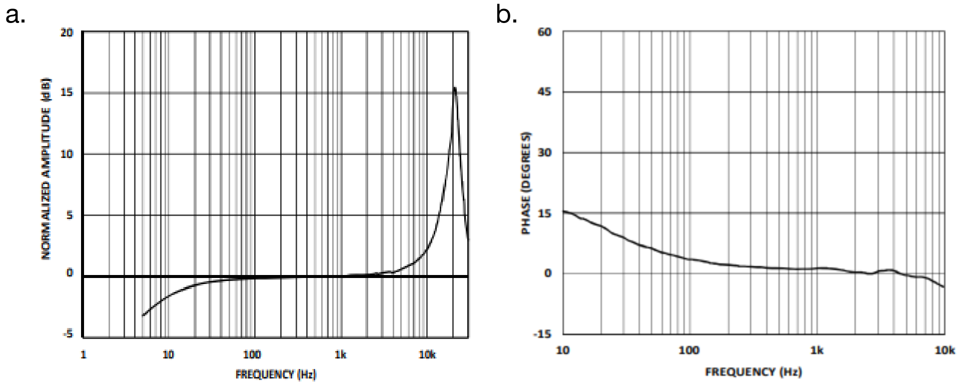

Figure 2.10: *The response curves of the embedded ICS-40300 microphones. Panel (a) shows the amplitude response over the frequency range. Panel (b) the phase response.*

Infrasound

The infrasound sensors aboard the Multi-EAR are the KNMI mini-MB (section 2.1.3) and the Superior Sensor Technology SP210 differential pressure sensor [SuperiorSensor-Technology, 2021]. The KNMI mini-MB is also embedded on the INFRA-EAR, its details and theoretical response are discussed in section 2.1.3.

The SP210 has similarly to the mini-MB two pressure inlets of which one is connected to the atmosphere and the other to a backing volume. The difference between both sensors is the sensing mechanism. The infrasound measurements of the mini-MB are based on the deflection of a diaphragm, which cause a pressure difference in the piezo-resistive crystals attached to the diaphragm's corners. The SP210 does not have a diaphragm. The inlets are separated by a piezo-resistive chip, which measures the difference in applied pressure between both sides. The sensor is temperature compensated, has a dynamic pressure range from ±250 Pa to ±40 kPa, and has selectable bandwidth filters from 25 to 250 Hz. The sensor has a digital output by its 16 bit built-in ADC. The accuracy, resolution, and total error of the measurement linearly increases with the selected measurement range. However, the theoretical response of this sensor is unknown and can not be determined by following section 2.1.3. In addition, before the sensor can be used, an empirical response function needs to be determined, for example by following the method of Marcillo *et al.* [2012]. The further study of this sensor is deferred to future studies.

■ 2.2.4 Meteorological sensors

Infrasound detectability is directly linked to local noise conditions and the atmosphere's stability in the infrasound sensor's surroundings since noise levels are increased when turbulence levels are high. Therefore, it is beneficial to have simultaneous measurements of the basic meteorological parameters, i.e., pressure, humidity and temperature. The sub-sections below describe the different meteorological measurements contained on the sensor platform.

Barometer

The barometric pressure is sensed by the LPS33HW sensor (section 2.1.4, [STMicroelectronics, 2020*a*]). Section 2.1 stated that after calibration, the sensor has an accuracy of ±0.1 hPa.

Temperature/Humidity

The SHT8x sensor measures the temperature and humidity at the PCB [Sensirion, 2021]. The SHT8x is a temperature and humidity sensor with a pin-type connector. This connector allows easy integration and replacement of the sensor. Furthermore, it allows for the best possible thermal coupling to the environment and decoupling from potential heat sources on the PCB. The sensing is done by the SHT3x sensor, which is part of the SHT8x set-up. The SHT8x has a built-in 16-bit ADC.

The humidity is sensed over the range of $0 - 100\%$. The SHT3x has a resolution of 0.01%, with a relative error of 1.5%. The absolute error needs to be determined by lab calibration. This calibration is based on a controlled environment (e.g., climate chamber), which enables either to generate constant humidity level or sweep over a range. Besides the Multi-EAR, a certified reference sensor is included within the climate chamber, which allows to determine the absolute error of the SHT3x.

The operating range of the temperature sensor is between -40 and $105°$ C. The resolution is $0.01°$ C, with a relative error of $0.3°$ C.

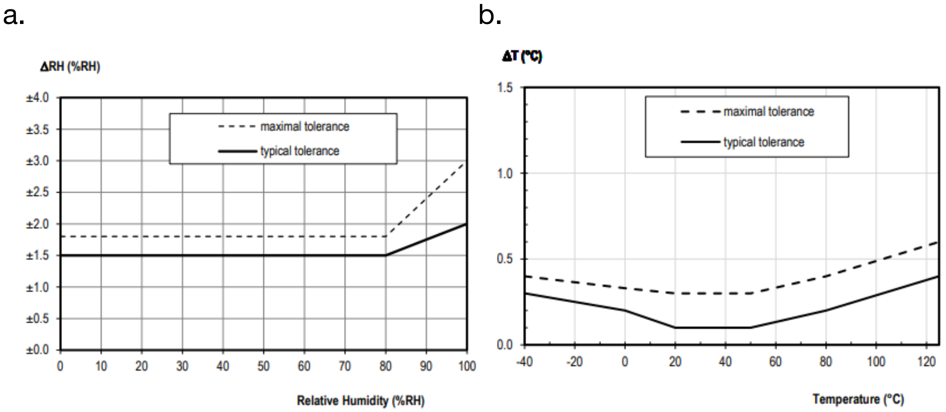

Figure 2.11: *Sensitivity curves of the SHT3x MEMS sensor. Panel (a) shows the expected tolerance of the humidity sensor over the measurement range. Panel (b) shows the tolerance of the temperature sensor.*

■ 2.2.5 Inertial measurement units

The Multi-EAR measures accelerations by using a MEMS Inertial Measurement Unit (IMU). On the platform the LSM303 [STMicroelectronics, 2020*b*], a 6-axis IMU, and LIS3DH [STElectronics, 2021], as well a 6-axis IMU, are embedded. The LSM303 (section 2.1.6) consists of a 3-axis accelerometer and a 3-axis magnetometer. The LIS3DH is the successor of the LSM, and consists of a 3-axis accelerometer and 3-axis gyroscope. The measurement range of both accelerometers varies between 2-16 g, while having a built-in 16-bit ADC, which results in a resolution of 0.06 mg when choosing the lowest measurement range.

■ 2.2.6 Casings

The protection of the PCB is done with a weather- and waterproof casing. The RPi and Multi-EAR PCB are connected by the GPIO pins, and by four screws on the corners for extra stability. The casing exists of a pre-ordered polythene case with a self-designed 3D-printed inlet dome on top. The RPi is mounted to the casing, by a 3D-printed ground-plate, for direct coupling.

Inlet dome

An inlet dome is placed on top of the casing, fastened with screws and glue. The dome allows air to flow in and out of the casing, which is essential for the atmospheric measurements, but avoids water entering. Figure 2.12 shows the 3D CAD design of the dome. Air can flow into the dome via the inlets on the side and top of the dome. This way, the dome enables airflow inside the casing but obstructs water. Whenever moisture becomes a problem, GoreTex air vents may be considered. These air-vents should be placed on the inlet of the dome. Furthermore, the design of the dome reduce the effects of stagnation pressure, which can easily mask the differential pressure perturbations off interest [Raspet *et al.*, 2019].

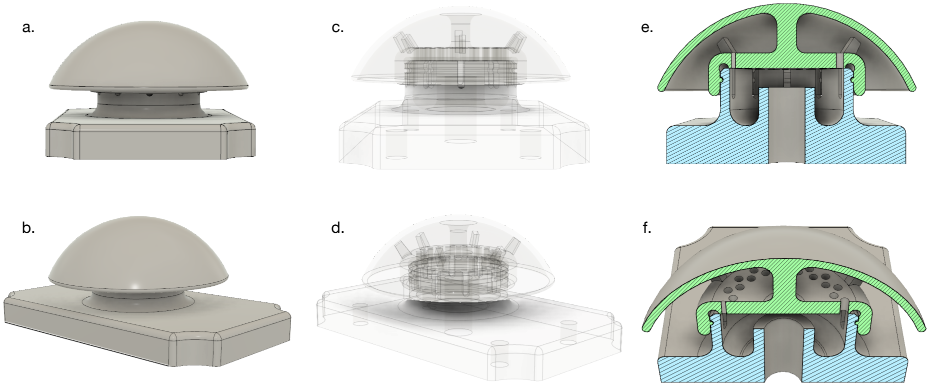

Figure 2.12: *3D CAD design of the dome. (a) and (b) show the solid outline of the dome, (c) and (d) the transparant outline, (e) and (f) the cross sections.*

Casing designs

Two different casings are designed and developed for the Multi-EAR. The smaller casing [Schneider, 2021] has a dimension of 130 x 85 x 115 mm (Figure 2.13). The dome is placed on top of the transparent lid of the casing, while two antennas are mounted to the side, as well as the external power supply plug. The smaller casings are not autonomous, it does not function without connection to an external power supply. Whenever powered, the Multi-EAR starts recording and collecting data, as pre-defined in the firmware.

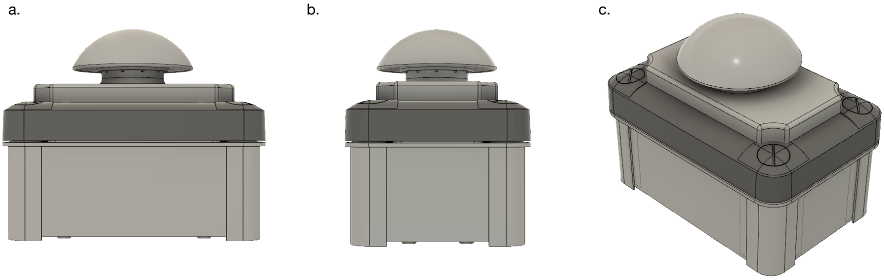

Figure 2.13: *CAD-drawings of the small casing design for the Multi-EAR. The dimensions of this casing are; 130 x 85 x 115 mm.*

The larger casings have a dimension of 240 x 191 x 130 mm [FIBOX, 2021] and includes an external solar panel. These casings are designed to create a completely autonomous sensor platform. Again a polyethylene case with the atmospheric dome on top is used. The GPS and LoRa antenna are connected to the outside of the casing, as well as the external power plug.

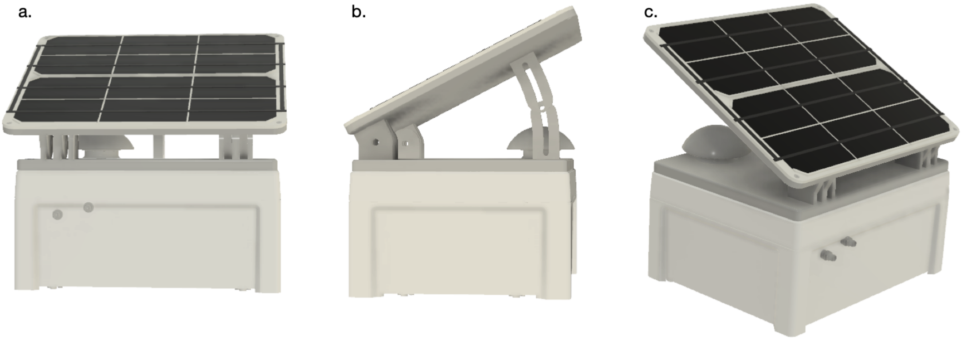

Figure 2.14: *CAD-drawings of the large casing design for the Multi-EAR. The dimensions of this casing are; 240 x 191 x 130 mm.*

Antennae

The LoRa and GPS on the PCB are both connected to external antennas. The antennae are passive LinX antennae [Linx-Technologies, 2021]. The frequency range of the antenna is between 617MHz - 5 GHz. For optimal signal coverage, a high-blade positioning is suggested (i.e., with the antenna pointing up-wards).

The polarization of the antennae is linear, and the radiation of signals omnidirectional. The receiver that is used for timing and location is a GNSS receiver that is compatible with GPS (global system), GLONASS (Russian navigational system), Beidou (Chinese navigational system), Galileo (European navigational system).

The antennae are mounted to the outside of the casings and connected to the MEMS of the GPS and LoRa by SubMiniature version A (SMA) extension cables [Emerson, 2021], which is a coaxial RF connector cable.

External power supply

The sensor platform and RPi require a minimal power supply of 5 Volt (V). This is attained by a standard micro-USB connector. However, to ensure complete protection and enclosure of the casing the cable has been modified. The power supply cable has been divided into two parts. One part of the modified cable consist of a 220 V to 5 V adapter, and the male part of the 3-pin Amphenol connector. The other part is fixed and remains untouched inside the casing. This part consist of the micro-USB, which is connected to the RPi, and a female Amphenol 3-pin connector, which is attached to the casing. The use of a 3-pin Amphenol connector ensures complete enclosure of the casing, while using an external power supply. Moreover, it allows to break the electrical circuit apart, which is ideal for transport.

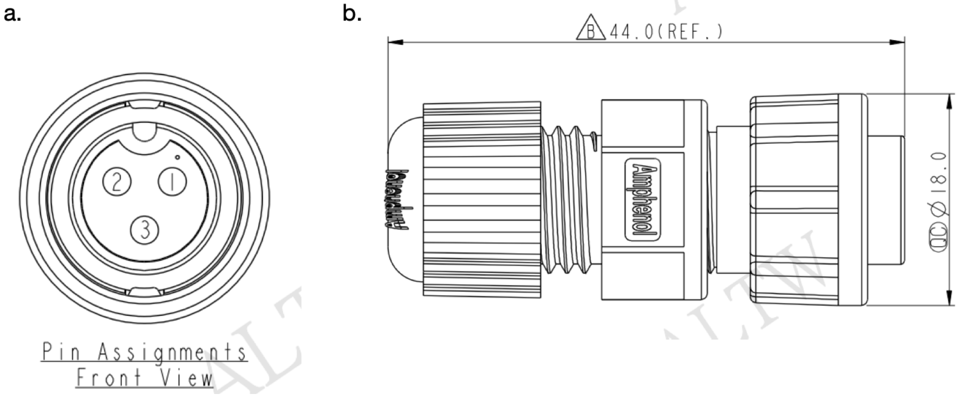

Figure 2.15: *Amphenol connector. Panel (a) shows the front view of the pin assignment. Pin 1 is the power supply, Pin 2 the ground, while Pin 3 remains available. Panel (b) shows the side view of the connected male and female connector.*

2.2.7 Autonomous system

The large casings are equipped with a solar panel [Voltaic, 2020*a*] and battery pack [Voltaic, 2020*b*]. These platforms can either be powered by an external power supply or by a battery pack. The battery pack is a V75 battery and is placed within the casing. It has an 'always-on mode'; it can power, charge, and pass-through while charging. The capacity is 19.200 mAh (71 Watt-Hours), and has a 5V output.

The external solar panel charges the V75 battery pack, and is positioned on the lid of the casing. The angle of solar panel may be modified to optimize for the (variable) angle of the sun with the horizon. The panel is waterproof and has a 9 Watt, 6 V output.

To determine whether the autonomous system can monitor continuously, an energy analysis is performed. The energy analysis is divided into (1) the energy consumption by the PCB and RPi during concurrently continuous monitoring and the (2) power supply by the solar panel and battery capacity to survive the evenings as a function of month for mid-latitudes (52 degrees N).

Power consumption Multi-EAR

The energy consumption of the sensor platform can be divided into the consumption by the RPi and the PCB/MEMS. Assuming continuous measurements, the RPi will approximately use 1 Watt hour (Wh), which adds to a maximum of 24 Wh per day.

The consumption by the PCB depends on the low-energy MEMS sensors, which is marginal compared to other monitoring devices. The power consumption is estimated at around 5 Wh per day.

The total power consumption of the entire monitoring system is estimated to be approximately 29 Wh per day.

Power supply

The V75 battery pack has a maximum capacity of 71 Wh. Without charging the battery pack, the monitoring system can therefore be active for approximately 70 hours. During summer, the time between sunset and sunlight is approximately 6 hours. Therefore it can be expected that the system will 'survive' the summer evenings. In winter, the nights are longer and it is not always sunny, and therefore the re-charging time of the battery is shorter. The monitoring system is expected to run out of power during the winter periods.

With day-light, the battery pack will be charged and if it holds sufficient charge, power up the Multi-EAR. An analysis on solar power has been performed to determine the expected charging energy of the solar panel. For the analysis, the solar panel has positioned at the Campus of the TU Delft (51.6° N, 4.22° E). Based on the technical specifications of the 9 Watt solar panel, and the expected sunlight at the Campus, the energy analysis is calculated [EUSCIENCE-HUB, 2021].

Figure 2.16 shows the average energy output of the solar panel in Wh per day. Note that from March until September, the Solar panel provides more power than needed by the Multi-EAR. During these periods, the battery will be charged during the day. During the winter months, however, the solar panel does not provide enough power to charge the battery. Therefore, it can be expected that after a while the battery will run out of power. The battery and solar panel will not provide sufficient power for continuous and concurrent monitoring during the winter period.

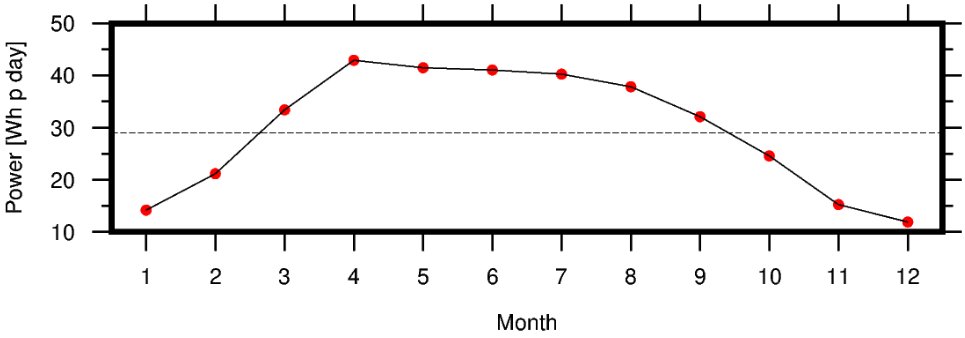

Figure 2.16: *Performance of the 9Watt, 6Volt, solar panel. The red dots indicate the average daily power provided by the solar panel per day. The dotted line shows the required power per day by the monitoring system. When the provided power is larger than the required power the battery will be charged.*

■ 2.2.8 Laboratory sensor calibration and comparison

The sensor calibration and comparison have been performed according to the KNMI-calibration standards within the KNMI calibration lab.

Barometric pressure

The INFRA- and Multi-EAR are using the same barometric pressure sensor. Within section 2.1.4, the controlled laboratory calibration of the LPS sensor is described. Although the inlet domes of both platforms differ, the calibration outcome is similar. After correcting for the sensor bias, the LPS sensor has an accuracy of ± 0.1 hPa, i.e., the LPS sensors measures values within ± 0.1 hPa of the value measured by the KNMI reference sensor.

Temperature/Humidity

The calibration tests on the temperature and humidity sensor are performed within the climate chamber. The climate chamber is a certified calibration tool, which can generate temperatures between -30 till 50°C and a relative humidity level (depending on the temperature) between $10 - 90\%$. Within the chamber, various reference sensors are placed. Again, the calibration results in a calibration curve, which describes the temperature/humidity dependent bias. After the bias correction, the temperature sensor has an accuracy of $\pm 0.3°$, whereas the humidity sensor has an accuracy of $\pm 1\%$.

■ 2.2.9 Field sensor calibration and comparison

Besides lab calibrations, the sensor platform has also been placed on the KNMI test field, enabling a comparison of the platform with high-fidelity equipment. The field test has been performed within building K of the KNMI. This building is placed at the border of the KNMI test field, and provides power supply for the Multi-EAR. The building is located at a distance of approximately 50 to 100 meter from the reference meteorological equipment that is compared to. Ideally, comparisons would be carried out by co-locating the sensors.

Meteorological observations

The LPS sensor has been field-tested along with a Paroscientific Digiquartz 1015A barometer, which has an accuracy of 0.05 hPa. Figure 2.17 shows the comparison between the Multi-EAR (red line) and the barometric reference sensor (black line). It can be concluded that both sensors resolve the changing barometric pressure. From the distribution of observations, it has been estimated that the LPS sensor has a precision of ± 0.1 hPa for 87% of the time. For the remainder, the maximum deviation was ± 0.2 hPa.

Figure 2.18-a presents the comparison between the Multi-EAR's temperature sensor (red) with the reference sensor (black). The maximum temperature is often correctly resolved by the Multi-EAR. The minimum temperatures that typically

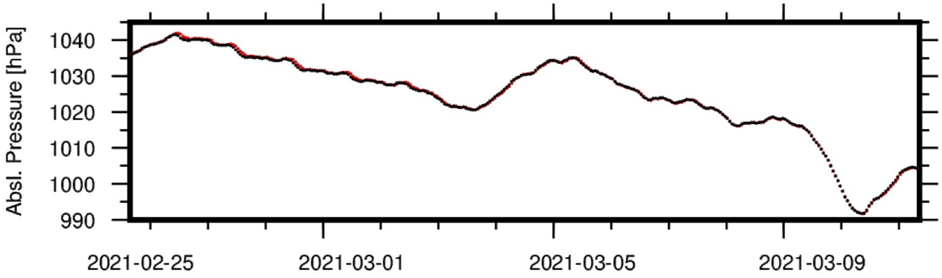

Figure 2.17: *Barometric pressure comparison between the Multi-EAR (red line) and the KNMI sensor (black line) at the KNMI test field.*

occur during the night, are not correctly measured. This is due to the monitoring circumstances, building K conserves the heat that has built up throughout the day.

The same issue occurs with the humidity sensor (Figure 2.18-b). The humidity within building K is continuously below the actual meteorological humidity. Therefore an actual comparison between the Multi-EAR's humidity sensor and the KNMI reference sensor can not be performed. Future comparison studies should be carried out outside, as close as possible to the reference sensors.

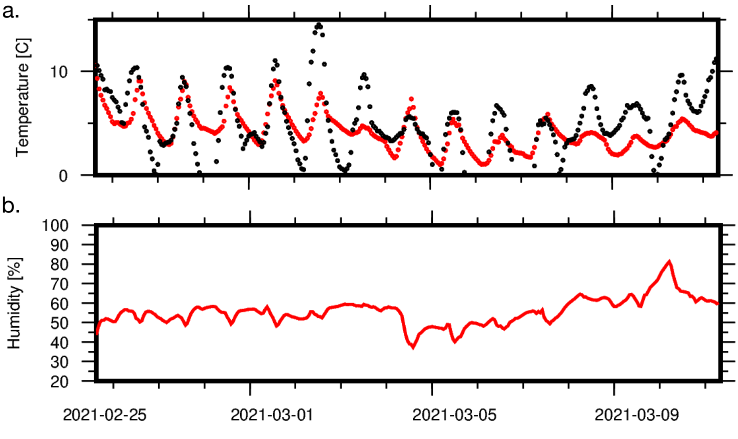

Figure 2.18: *Temperature and humidity measurements by the Multi-EAR (red) compared to the KNMI reference sensor (black). The measurements are obtained within building K, therefore a correct comparison between the Multi-EAR and KNMI sensors is not possible.*

Infrasound observations

The infrasonic wavefield is monitored by the KNMI mini-MB (section 2.1.3). Figure 2.19 -a shows the PSDs calculated from the KNMI mini-MB recordings. Panel b shows the PSDs calculated from the infrasonic reference sensor at the KNMI test field, a Hyperion IFS-5100. The grey dotted lines indicate the global high and low noise curves [Brown *et al.*, 2014]. Based on a visual comparison between both sensors, it can be noted that the KNMI mini-MB is able to resolve the characteristic microbarom peak around 0.2 Hz. Microbaroms are known to be one of the most omnipresent ambient noise sources within the infrasonic wavefield. Moreover, it can be noted that the KNMI mini-MB is suffering from self-noise within the higher frequencies.

Although the KNMI mini-MB does not resolve the complete ambient noise field, the sensor is able to resolve most of it. Transient infrasonic events (e.g., explosions, earthquakes, volcanic eruptions) have a higher amplitude level compared to the ambient noise. Therefore, any infrasonic explosion will most likely be detected by the KNMI mini-MB.

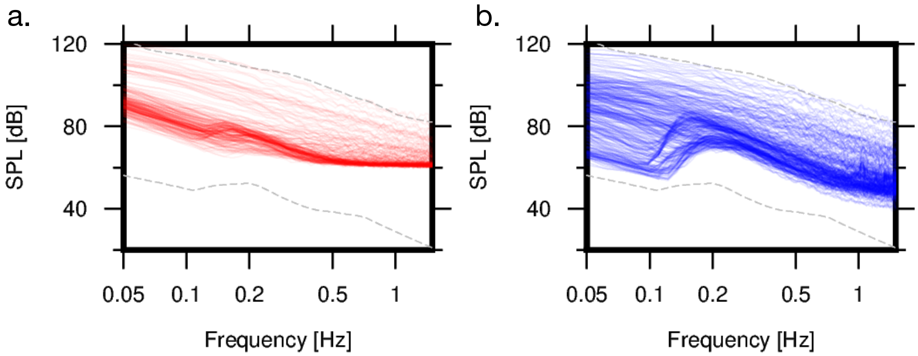

Figure 2.19: *Infrasonic wavefield measurement by the KNMI mini-MB (panel a) and a Hyperion IFS-5100 (panel b). The gray dotted lines indicate the global high and low noise curves [Brown* et al.*, 2014]. Note that both sensors resolve the characteristic microbarom peak around 0.2 Hz. At the higher frequencies, the self noise levels of the KNMI mini-MB dominate the measurements.*

Movement observations

Within section 2.1.6, the comparison test between MEMS and a Streckeisen STS-2 seismometer is discussed. Although the sensors are deployed on the same seismic pillar and are thus subject to similar seismic noise conditions, the MEMS sensor could not measure ambient seismic noise [Peterson, 1993; McNamara and Buland, 2004] due to its high self-noise level. For the comparison between the two accelerometers on the Multi-EAR a similar test set-up has been established. The full recordings of the z-component are divided into hourly recordings, which are used to calculate PSD's. The reference sensor in the seismic pavilion confirms no major seismic activity has been recorded (blue PSD's in Figure 2.20). Therefore, only ambient seismic noise is expected within the recordings.

Figure 2.20 shows the stacked PSD's for the LSM (panel a) and LIS (panel b) MEMS sensors. The solid grey lines indicate the high and low ambient seismic noise curves [Peterson, 1993; McNamara and Buland, 2004]. The MEMS don't resolve ambient noise signals, due to their high self-noise. However, note that the self-noise levels of the different MEMS sensors is not similar. The LIS has a lower self-noise compared to the LSM (i.e., 15 dB difference), while the ADC has the same amount of bits [Sleeman *et al.*, 2006]. Sometimes ADC's are suffering a 'loss of bits' due to power supply. The LIS sensor includes an accelerometer and gyroscope, whereas the LSM includes an accelerometer and magnetometer. The combination of various sensors within one MEMS may influence the efficiency of power towards the ADC, explaining the difference in self-noise.

Based on Figure 2.20 it can be concluded that the MEMS will not resolve ambient seismic noise signal. However, the MEMS will resolve signals with an amplitude above the self-noise levels. The dotted black lines within both panels of the figure indicate the expected amplitude levels of earthquakes with an approximate distance of 10 km (nearby transient sources) [RaspberryShake, 2021]. Those theoretical amplitude curves lie above the self-noise levels of both MEMS.

The MEMS accelerometers of the Multi-EAR are not for monitoring purposes of ambient seismic noise or teleseismic events. Previous studies drew similar conclusions concerning the performance of MEMS accelerometers. Various calibration set-ups are considered while comparing MEMS accelerometers with conventional accelerometers of geophones [Hons *et al.*, 2008; Albarbar *et al.*, 2009; Anthony *et al.*, 2019], each concluding that the accuracy of the MEMS is not sufficient for recording ambient seismic noise. However, for strong local events or boisterous environments the MEMS sensor will resolve those seismic signals. Alternatively for seismic ambient noise monitoring, an ADC can be placed on the sensor platform to connect external geophones. The relative performance of external geophone / MEMS accelerometer is shown in Anthony *et al.* [2019].

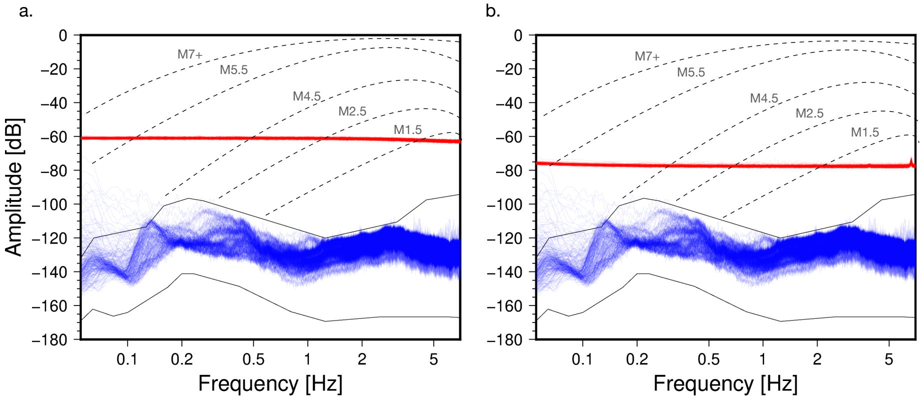

Figure 2.20: *Power Spectral Density curves, hourly calculated for the LSM (red lines, panel a), the LIS (red lines, panel b), and the reference sensor (blue lines in both panels). The solid gray lines indicate the global high and low ambient seismic noise curves [Peterson, 1993; McNamara and Buland, 2004]. The dotted lines indicate the theoretical amplitude levels of a nearby transient event.*

■ 2.2.10 Discussion and conclusion

Within this section, the Multi-EAR has been introduced, which is the successor of the INFRA-EAR (section 2.1). It has been shown that the coinciding sensors of the INFRA- and Multi-EAR perform similarly although the platforms have different casings. Besides the identical sensors of the INFRA-EAR, the Multi-EAR also has additional sensor types aboard. The Multi-EAR can measure concurrently the barometric pressure, infrasound, audible sound, accelerations, temperature and humidity, and GPS time and positioning. The sensors are controlled by a microcontroller, and a RPi is used as datalogger. Furthermore, the Multi-EAR has LoRa telecommunication, which has the potential to enable low-range data communication between various platforms.

The innovative character and scientific quality of the Multi-EAR:

- Research-grade mobile geophysical platform that allows for the selection of specific sensors and sample rates.
- Ability to sample multidisciplinary data on one platform.
- Ability to install sensors at strategic locations to better assess specific events, like aftershocks of an earthquake or severe weather.
- Low energy consumption, which facilitates deployment at a wide variety of locations as well as on drones and high-altitude balloons.
- The design of the mobile platform uses the latest trends in miniature sensor technology, and 3D print technology.
- The calibration of the sensor follows high quality standards that have been developed at the KNMI.

The Multi-EAR reaches for some sensors a TRL of 7/8. However, the application of the audible sensor requires attention. More sensor knowledge is needed before it can be used within scientific studies or for monitoring purposes. Proper laboratory and field tests need to be performed. Moreover, for future deployments of the Multi-EAR it is recommended to investigate the SP210 differential pressure sensor. This sensor shows great potential thanks to the ability to shift measurement range and bandwidth filters. However, this sensor technology is novel and for correct interpretation more knowledge is required (e.g., an empirical instrument response).

■ 2.2.11 Outlook

It is proposed to integrate the Multi-EAR within the KNMI/TU-Delft sensor network. A low-cost mobile platform will complement the existing network, and allows higher spatial resolution data.

Having a low-cost mobile platform enables:

- High spatial-temporal sampling of multiple geophysical parameters, which can be used for validation of high-resolution weather models such as the high-resolution HARMONIE model that is used operationally within KNMI.

- Quality measurements on unique and/or remote locations where the network is relatively sparse (on sea or at land/sea transitions, on volcanoes on the Dutch Caribbean islands, drones, balloons, the Cabauw tower).
- Allows measurement of meteorological circumstances that can be very local (fog, thunderstorms, sleet). This could contribute to the further refinement of weather alarms from the province to the zip code level.
- Rapid deployments in predicted code orange/red scenarios for which there is interest to collect more field data.
- The observations provide information of natural hazards on much higher time- and spatial-scales; allowing for meso-scale and local scale observations in natural hazards research (convective storms, volcano monitoring)

Examples of possible future projects

The Multi-EAR is interesting to use as monitoring platform for various studies. One study could focus on deployment near the Cabauw Tower, which is a 213 meter high meteorological tower that is part of the Ruisdael observatory. The tower consists of various geophysical sensors, including an infrasound array [Smink *et al.*, 2019] and an internationally renowned meteorological reference site.

Furthermore, the sensor platform can be used on hot-air - and weather/scientific balloon observations in collaboration with KNMI [De Bruijn *et al.*, 2020]. Such balloons fly at a constant altitude. Besides balloons, the sensor platform can be attached to a radiosonde, which samples at many different altitudes and rise up fairly monotonously. Those observations give insights in changing of various geophysical parameters with altitude and can be used to determine lightning, severe weather development (outflow), as well as sea breeze fronts.

Moreover, the Multi-EAR can be used as TU-Delft campus array. Currently, the Delft tech-campus is not equipped with a seismo-acoustic array. However, there are plans for a geothermal well on campus. Therefore it is important to perform seismo-acoustic measurements to characterise the vibrations, caused by the drill activity.

Finally, the Multi-EAR has the ability to become an educational platform. It can be used for education at primary and secondary schools, introducing children with technology and physics. Furthermore, the platform can be used by university under-grad students during fieldwork courses. Using the MULTI-EAR, students could design a measurement campaign, including the acquisition, processing and interpretation of data.

3

High-resolution infrasound array processing

Our imagination is struck only by what is great;
but the lover of natural philosophy should reflect equally on little things.

Alexander von Humboldt

Abstract The detection and characterization of signals of interest in the presence of (in)coherent ambient noise is central to the analysis of infrasound array data. Microbaroms have an extended source region and a dynamical character. From the perspective of an infrasound array, these coherent noise sources appear as interfering signals which conventional beamform methods may not correctly resolve. This limits the ability of an infrasound array to dissect the incoming wavefield into individual components. In this chapter, this problem will be addressed by proposing a high-resolution beamform technique in combination with the CLEAN algorithm. CLEAN iteratively selects the maximum of the f/k spectrum (i.e., following the Bartlett or Capon method) and removes a percentage of the corresponding signal from the cross-spectral density matrix. In this procedure, the array response is deconvolved from the f/k spectral density function. The spectral peaks are retained in a 'clean' spectrum. A data-driven stopping criterion for CLEAN is proposed that relies on the framework of Fisher statistics. This allows the construction of an automated algorithm that continuously extracts coherent energy until the point is reached that only incoherent noise is left in the data. CLEAN is tested on a synthetic data-set and is applied to data from multiple IMS infrasound arrays. The results show that the proposed method allows for the identification of multiple microbarom source regions in the Northern Atlantic, that would have remained unidentified if conventional methods had been applied.

Published as: **den Ouden, et al. 2020**, *CLEAN beamforming for the enhanced detection of multiple infrasonic sources*, Geophysical Journal International, Volume 221, DOI: 10.1093/gji/ggaa010
Note that minor changes have been introduced to make the text consistent with the other chapters, and that the Sections 3.2 and 3.4 are extended with non peer-reviewed content.

3.1 Introduction

Sensor arrays are used in various geophysical disciplines for a detailed study of signals that are part of a complex wavefield. The use of arrays allows for an enhanced detection of signals in the presence of incoherent noise, as the SNR is improved by summation across the array elements. In addition, arrays can be used to estimate the directivity of incoming wavefronts, and therefore can be used as spatial filters by steering the array towards the direction of interest. This has led to applications in the fields of seismology [Harjes and Henger, 1973; Husebye and Ruud, 1989; Schweitzer *et al.*, 2002], acoustics [Billingsley and Kinns, 1976; Michel *et al.*, 2006] and astronomy [Jansky, 1932; Garrett, 2013].

In this chapter, array detection of inaudible low-frequency sound, or infrasound, is discussed. The detection of infrasonic sources over long distances depends on the spectral content of the source, the atmospheric propagation conditions along the source-receiver path, as well as the local noise conditions near the array. The vertical temperature and wind structures determine the propagation paths while absorption affects the amplitude and frequency contents of the received signal [Waxler and Assink, 2019]. Because attenuation is strongly dependent on the acoustic frequency, lower frequency signals can propagate over significantly longer distances when compared to higher frequencies [Sutherland and Bass, 2004]. The local noise conditions are determined by the turbulent motions in the atmospheric boundary layer, near the array [Smink *et al.*, 2019].

The IMS is in place for the verification of the CTBT and monitors the atmosphere globally for infrasonic signals from nuclear tests, using microbarometer arrays. Currently, 51 out of 60 microbarometer arrays provide real-time infrasound recordings from around the world. The IMS has played a central role in the characterization of the global infrasonic wavefield and the localization of infrasound sources, which include earthquakes, lightning, meteors, (nuclear) explosions, colliding ocean wave-wave and surf [Campus and Christie, 2010]. The infrasonic wavefield is complex and often consists of interfering acoustic signals in overlapping frequency bands, in the presence of incoherent noise. The acoustic signals take the form of transients, (quasi-)continuous signals or a combination of both. From the perspective of an array, coherent noise sources appear as interfering signals that clutter the array detection bulletins and may obscure detections from signals of interest.

Most infrasound processing routines, including those that are used for real-time processing of the IMS infrasound arrays, are designed to only detect the dominant acoustic signal in a given time segment and frequency band. However, various beamform techniques exist in the literature that allow for the detection of signals from multiple spatially distributed sources [Viberg and Krim, 1997; Rost and Thomas, 2002]. The capability of detecting and classifying interfering sources relies on the beamform resolution as quantified by the array response, which is determined by the beamform technique and the array layout. A low beamform resolution could lead to the dominant source masking sub-dominant sources.

In this chapter, the CLEAN algorithm [Högbom, 1974] is applied for high-resolution array processing of infrasound data. CLEAN is a post-processing method that iteratively selects the main contribution in the f/k spectrum and removes a percentage of the corresponding signal from the cross-spectral density matrix. In this procedure, the array response is deconvolved from the resolved f/k spectral density function. The spectral peaks are retained in a 'clean' spectrum. This iterative process continues until a stopping criterion is reached. The beamform techniques proposed by Bartlett [1948] and Capon [1969] can be used to compute the f/k spectrum. Previous studies [Clark, 1980; Sijtsma, 2007; Gal *et al.*, 2016], have shown that the application of CLEAN provides a superior beamform resolution. Moreover, it has been shown that the performance critically depends on the setting of two parameters: the percentage of removal and the stopping criterion. In this work, the use of Fisher statistics is proposed and applied as stopping criterion for the iterative CLEAN procedure. This statistical framework has been established for significance testing of multivariate data [Fisher, 1948], and has applications in geophysical signal processing [Melton and Bailey, 1957; Shumway, 1971; Smart and Flinn, 1971].

The remainder of this chapter is organized as follows. Section 3.2 introduces various beamform techniques, CLEAN as post-processing method and the proposed CLEAN parameterization. This parameterization and the evaluation of the performance of CLEAN, as tested using synthetic data, is presented in section 3.3, and is an addition to the beamforming review of the earlier section. In section 3.4, CLEAN is applied to IMS infrasound array data and it demonstrates that multiple microbarom source regions can be resolved in the Northern Atlantic. Finally, the results are discussed and summarized in section 3.5.

3.2 Description of beamforming

Consider an array of N omnidirectional receivers, with $N \geq 3$ (Figure 3.1 and 3.3). Each array element has position $r_{m,\ldots,N} = (x_m, y_m, z_m)$, of which the absolute value is the distance between the element and a reference distance, e.g., the geometrical center of the array. Often an array consists of elements close to the geometrical center to resolve the high frequencies of the wavefront, and elements which lie further away to resolve the low frequencies [Christie and Campus, 2010]. In the case of interest, it is assumed that the array is situated in the far-field. Therefore, the wavefield can be represented as a superposition of three-dimensional planar wavefronts, propagating with phase speed c. Figure 3.1 illustrates an inclined planar wavefront that impinged a ground-based infrasonic microbarometer array. The array elements record the wavefront at times τ_1, τ_2, and τ_3 (Figure 3.2). The goal is to estimate the three-dimensional wavefront parameters as a function of time t and frequency f. For this purpose, it is useful to consider a plane-wave decomposition of the incoming wavefield, in terms of a frequency-wavenumber (f/k) spectral density $G(f, \vec{k})$:

$$G(f,\vec{k}) = \int_{-\infty}^{\infty}\int_{-\infty}^{\infty}\int_{-\infty}^{\infty} G(f,\vec{r})e^{i(\vec{k}\cdot\vec{r})}\text{dx dy dz} \tag{3.2.1}$$

here, $\vec{k} = (k_x, k_y, k_z)$ and $G(f, \vec{r})$ represents the three-dimensional wavenumber vector and the Fourier transformed array recordings, respectively. Beamforming can be used to separate the coherent and incoherent parts of $G(f, \vec{k})$.

Most infrasound arrays are ground-based planar arrays [Edwards and Green, 2012], in which case the integral in Equation 3.2.1 can be reduced to a two-dimensional integral over x and y. This also implies that only the horizontal component of $\vec{k}$ can be directly estimated in the beamforming process. The vertical component, k_z, is typically inferred through the dispersion relation, $|\vec{k}| = \frac{2\pi f}{c}$ and an estimate of the phase speed c, i.e., the speed of sound near the array. The wavenumber vector $\vec{k}$ can be expressed in terms of a slowness vector $\vec{p}$ by scaling with the angular frequency, $\omega = 2\pi f$. The horizontal component of $\vec{p}$ can be related to the apparent velocity c_{app} and back azimuth θ as follows:

$$c_{\text{app}} = \frac{1}{|\vec{p}_{x,y}|} \qquad \theta_b = \arctan\frac{p_x}{p_y}$$

.

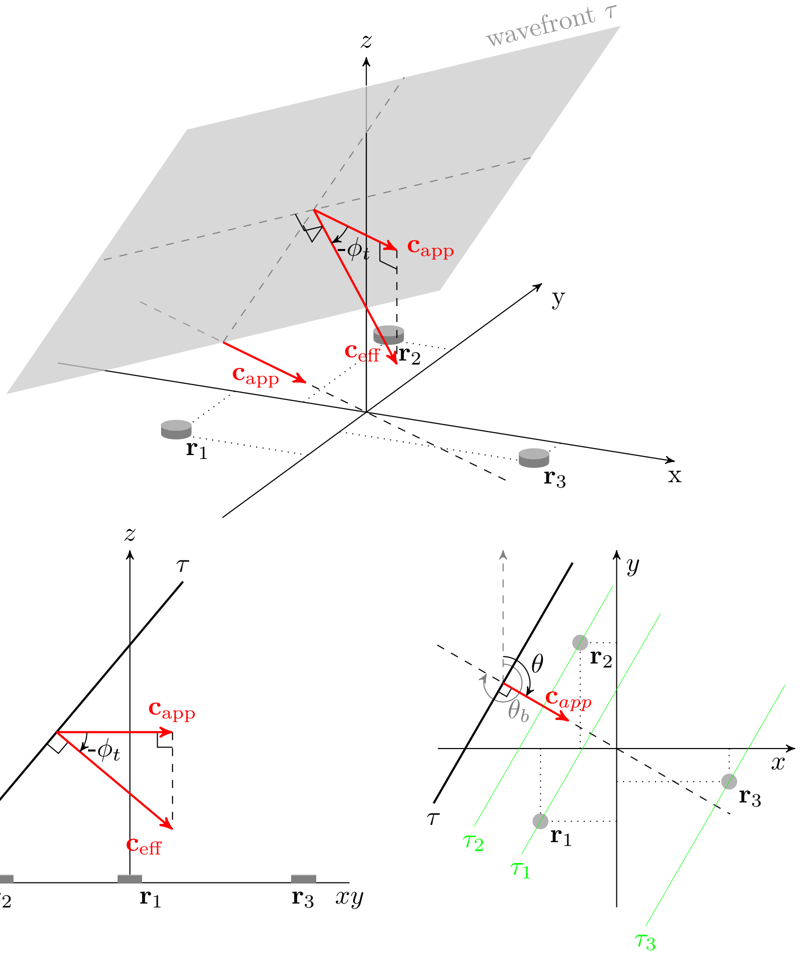

Figure 3.1: *An inclined three-dimensional planar wavefront τ traveling over an array of three microbarometers located in the xy-plane, i.e., the earth's surface. The wavefront propagates with an effective sound speed c_{eff} normal to the wavefront. The inclination angle with the Earth surface is ϕ_t, and the propagating direction relative to the array is indicated by θ_b. The apparent velocity of the wavefront (c_{app}) is the velocity with which the wavefront is measured by the array, where $c_{app} \geq c_{eff}$. Figure is adapted from Smets [2018].*

The apparent velocity corresponds to the horizontal propagation speed of a wavefront, i.e. as would be measured by the ground-based array. The back azimuth relates to the horizontal incidence angle, with respect to the north.

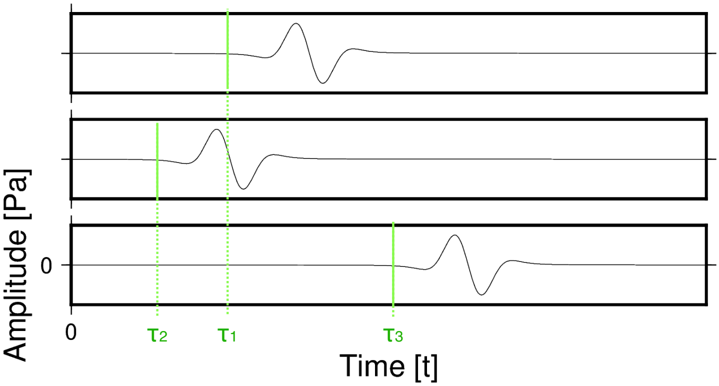

Figure 3.2: *Theoretical recording of the three-dimensional wavefront (Figure 3.1) by a three element microbarometer array.* τ_i *indicates the time of recording by receiver* r_i*.*

To beamform the array data, a cross-spectral density matrix $C(f)$ is to be estimated:

$$C(f) = \frac{1}{L} \sum_{l=1}^{L} G_l(f, \vec{r}) G_l^*(f, \vec{r}) \tag{3.2.2}$$

here, $*$ denotes the conjugate transpose. The off-diagonal elements of matrix $C(f)$ contain the phase delays between each sensor pair, while the diagonal elements contain the power spectral density of each element. It is common to estimate the cross-spectral density matrix $C(f)$ by averaging over L snapshots within one single time window of waveform data, $G_l(f, \vec{r})$. The averaging using snapshots is crucial for the application of Capon's method [Capon, 1969], as the beamform weights rely on the matrix inverse of $C(f)$. To ensure that the inverse exists, $C(f)$ must be full-rank and therefore L needs to be sufficiently large, i.e., $L \geq N$ [Viberg and Krim, 1997]. Assuming that the mathematical representation of the signal of interest and noise are statistically independent, the cross-spectral density matrix can be factored into a signal and noise co-variance matrix:

$$C(f) = E\{GG^*\} = E\{G_s G_s^*\} + E\{G_n G_n^*\} \tag{3.2.3}$$

where $E\{\}$ indicates the statistical expectation, $E\{G_s G_s^*\}$ indicates the signal co-variance matrix and $E\{G_n G_n^*\}$ the noise co-variance matrix. Noise has a common variance σ^2 and is assumed to be uncorrelated between all sensors. This decomposition is useful in the development of the CLEAN stopping criterion as will be discussed in section 3.3.

With the definition of $C(f)$, the f/k spectrum $P(f, \vec{k})$ can be computed by multiplying with beamform weight factor $w(\vec{k})$:

$$P(f, \vec{k}) = w^*(f, \vec{k}) C(f) w(f, \vec{k}) \tag{3.2.4}$$

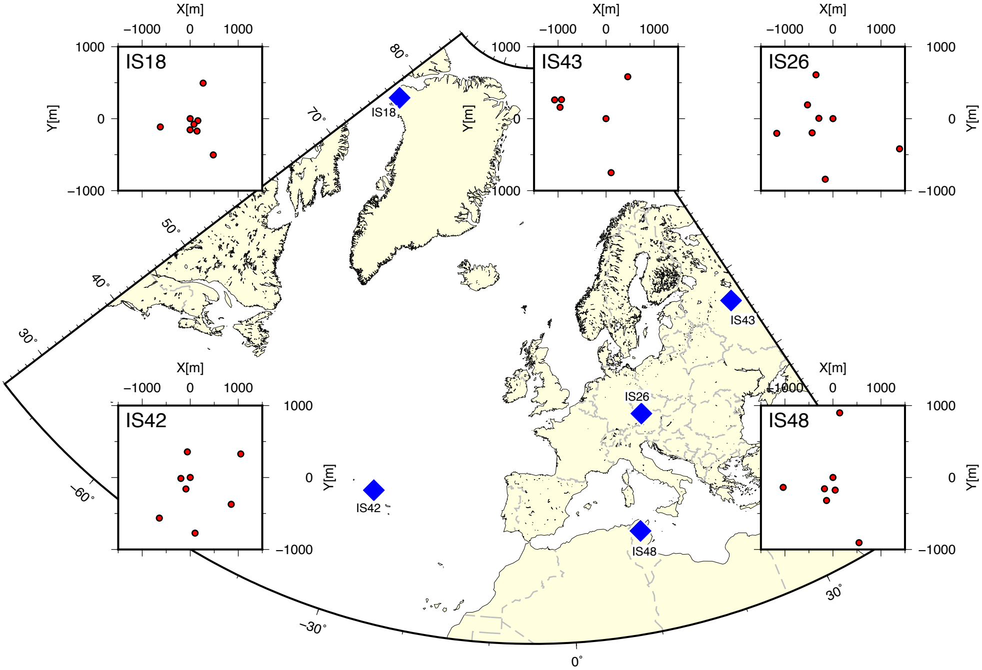

Figure 3.3: *Array locations and layouts of I18DE, I26GE, I42PT, I43RU and I48TN.*

This formulation allows for the comparison of various beamform weights. In this chapter, the Bartlett and Capon weights and corresponding f/k spectra are compared.

3.2.1 Bartlett beamforming

The 'classical' frequency beamforming analysis is based on the f/k spectrum obtained from the Bartlett method [Bartlett, 1948]. The signal power in $P(f, \vec{k})$ is maximized by summing the phase-aligned spectral values. The Bartlett weight $w_B(\vec{k})$ has been derived as:

$$w_B(\vec{k}) = \frac{a(\vec{k})}{\sqrt{a^*(\vec{k})a(\vec{k})}} \tag{3.2.5}$$

where $a(\vec{k}) = e^{-i(\vec{k}\cdot\vec{r})}$ represents the steering vector. The calculation of the f/k spectra occurs over a vector space spanned by those steering vectors, which is dependent on the used slowness grid. Figure 3.4 shows the design of the slowness grid, which consists of a 360° ring grid plus a rectangular grid. The ring grid is a linear grid in back azimuth and apparent velocity, ranging from 0° to 360° and 285 to 500 m/s with steps of 1° and 1 m/s, respectively. This ring grid is, however, non-linear in the slowness domain.The rectangular grid consists of linearly spaced values between -0.005 s/m and 0.005 s/m. This grid is added to ensure that energy from outside the ring grid does not clutter on its boundaries, which would result in biased outcomes.

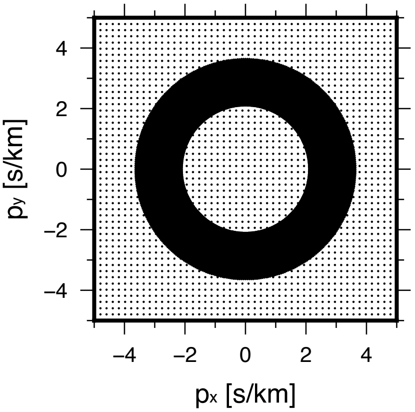

Figure 3.4: *The applied slowness grid, consisting of a 360° ring grid (between 275 and 475 m/s with steps of 1 m/s every 1°), and a 2500 points equidistant squared grid (between 200 and 10000 m/s).*

■ 3.2.2 Capon beamforming

Capon's method is derived as a maximum likelihood filter [Capon, 1969]. The filter design is determined by the inverse of cross spectral density matrix $C(f)$ and steering vector $a(\vec{k})$. With this design, the noise in the power spectrum is optimally suppressed while keeping a constant gain in the direction of interest. For Capon's method, $w_C(\vec{k})$ has been derived as:

$$w_C(\vec{k}) = \frac{C^{-1}(f)a(\vec{k})}{a^*(\vec{k})C^{-1}(f)a(\vec{k})} \tag{3.2.6}$$

■ 3.2.3 MUSIC beamforming

The MUltiple SIgnal Classification technique, MUSIC [Schmidt, 1986], exploits the eigen structure of the cross-spectral density matrix to estimate a f/k power spectral density. It is assumed that the NxN cross-spectral density matrix is separable in a signal and noise subspaces. The signal subspace is positive semidefinite. The smallest eigenvalues of C correspond to the noise subspace.

The MUSIC beam relies on the orthogonality between the steering vectors $a(\vec{k})$ and the eigenvectors of the noise subspace (V). The orthogonality minimizes the denominator which leads to to peaks in the $P(f, \vec{k})$ function;

$$P_{\text{MUSIC}}(f, \vec{k}) = \frac{1}{a^*(f, \vec{k})V(f)V(f)^*a(f, \vec{k})} \tag{3.2.7}$$

where P_{MUSIC} is not a true measure of the f/k power, it exhibits peaks in the vicinity of the true direction of arrivals. To compute P_{MUSIC}, an estimation of the number of sources D_{MUSIC} is needed in order to split the cross spectral density matrix C into a noise and a signal subspaces. In addition, MUSIC is known to fail when resolving closely spaced signals in small samples and at low SNR [Viberg and Krim, 1997].

Estimating the number of sources is not an easy process since one does not simply have this information. A threshold is needed to separate the noise from signal subspaces. This threshold can be estimated using the SORTE method, an eigenvalue-based approach [Han *et al.*, 2015]. The SORTE method is a statistical-based anomaly detection method, which determines a gap (or jump) within the eigenvalues of the cross-spectral density matrix. Based on the difference between consecutive eigenvalues of the matrix, the gap variance is determined:

$$D_{\text{MUSIC}}(d) = \begin{cases} \frac{var(\nabla\lambda_i)_{i=d+1}^{N-1}}{var(\nabla\lambda_i)_{i=d}^{N-1}}, & var(\nabla\lambda_i)_{i=d}^{N-1} \neq 0. \\ +\infty, & var(\nabla\lambda_i)_{i=d}^{N-1} = 0. \end{cases} \tag{3.2.8}$$

Where $d = 1, \dots N-1$, $\nabla\lambda_i = \lambda_i - \lambda_{i+1}$

$$var(\nabla\lambda_i)_{i=d}^{N-1} = \frac{1}{N-d}\sum_{i=d}^{d-1}\left(\nabla\lambda_i - \frac{1}{N-d}\sum_{j=d}^{N-1}\nabla\lambda_j\right)^2 \tag{3.2.9}$$

The estimated number of sources is given by;

$$\tilde{D}_{\text{MUSIC}} = \arg\min{}_d(D_{\text{MUSIC}}(d)) \tag{3.2.10}$$

This source number will be used to split the cross-spectral density matrix into a noise and signal subspaces. Note that the MUSIC algorithm can only resolve $N-1$ sources.

Since the cross-spectral density matrix is formed by N array elements, this implies that the number of sources that MUSIC can resolve is limited by the number of array elements. For example, in the case of a four-element array, only three sources can simultaneously be resolved in theory.

3.2.4 Array responses of various beamforming methods

To study the spectral properties of these beamform techniques, it is instructive to evaluate the array response [Evers, 2008]. Ideally the array response characterised by a delta pulse. However, due to summation of multiple array elements the delta pulse becomes a main lobe with various side lobes. The sample rate of the array elements determines the temporal resolution of the measurements (i.e., Nyquist frequency), and the array response indicates the spatial resolution.

Figure 3.5 shows the Bartlett and Capon array responses for IMS Infrasound array I48TN, for a monochromatic wave with $f_0 = 0.3$ Hz and $k_0 = 0$ m^{-1}. The array layout of I48TN is shown in Figure 3.3. Capon's array response has a much sharper main lobe when compared to Bartlett's response, which reflects its well-known high spatial resolution property. Moreover, it can be noted that the side lobes in Capon's spectrum are significantly reduced, when compared to Bartlett's response. This gain in resolution comes at a computational cost, because of the matrix inversion of $C(f)$. In addition, some temporal resolution (e.g., transient signals) is lost because of the necessary averaging process. When using Bartlett it is harder to distinguish between two closely located sources in the f/k spectrum, due to resolution. This favours the use of Bartlett's method for the analysis of transient signals, as it merits higher temporal resolution analyses. Whereas Capon's method is more suited for the analysis of (quasi-)continuous signals with longer time windows, such as microbaroms.

3.2.5 Neele and Snieder beamforming

Figure 3.5 shows how different beamforming techniques influence the array response resolution. Ideally the array response approaches a delta function. Besides the beamforming technique, the array response resolution is critically influenced by the array layout. [Evers, 2008] describes how array lay-out and aperture influence the array response. Although theory provides guidelines for the installation of arrays, it is in practice often difficult to obtain an ideal response for the frequency range of interest. This can for example be related to availability of land, or the presence of topography [Edwards and Green, 2012]. Nonetheless, [Neele and Snieder, 1991] describes a weighting technique, which implies the optimization of the array response towards a delta function.

The array elements are weighted such that the array response is closest to a delta function $(\delta(f, \vec{k}_0))$. Those weighting factors are found by minimizing

$$J_{\text{Neele}} = \iint_{|p| \leq p_{max}} \left[P(f, \vec{k}_0) - \delta(f, \vec{k}_0) \right]^2 d^2p + \epsilon |\vec{q}_N|^2 \tag{3.2.11}$$

where ϵ is a trade-off between resolution (deltaness of the array response) versus variance (error in the result). The optimum value of ϵ can be estimated by calculating the variance and resolution of J_{Neele} as a function of ϵ and frequency [Backus *et al.*, 1964; Aki and Richards, 2002].

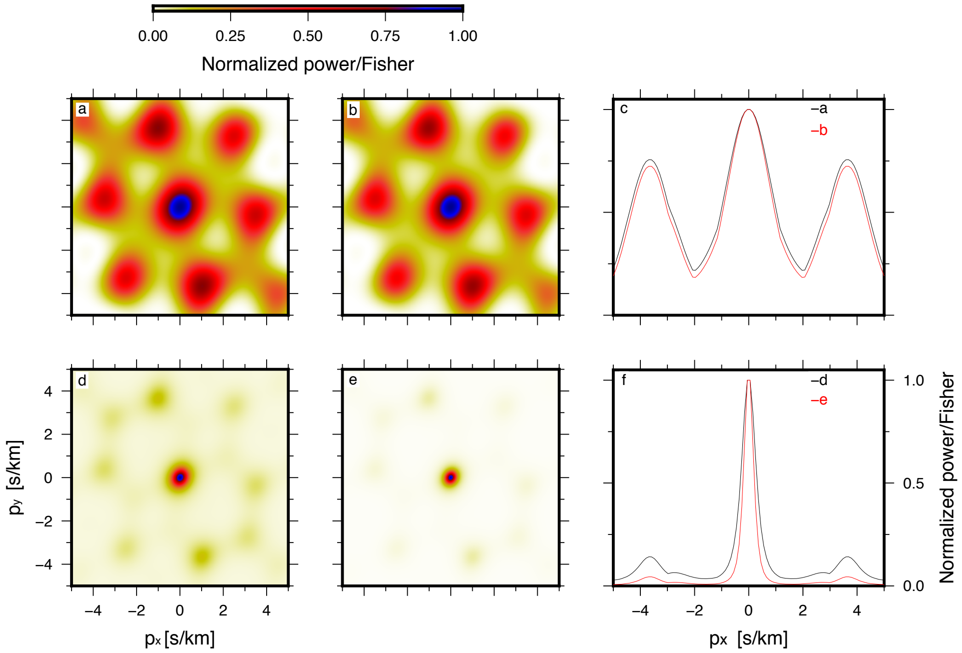

Figure 3.5: *Array response of infrasound array I48TN at 0.3 Hz, following the Bartlett (a) and Capon (d) beams. The array response improves after applying the Fisher statistics for Bartlett (b) as well Capon (e). The side spectra (c, f) show the improvement of the Fisher ratio (red curve) with respect to the array response in terms of normalized power (black curve) at* $p_y = 0$.

Minimising Equation 3.2.11 results in the optimum array element weights:

$$q_{N_i}(\vec{k}\ ) = \sum_j (aa^\dagger + \epsilon I)^{-1}_{ij} a_j(\vec{k_0}\ ) \tag{3.2.12}$$

where $aa^\dagger$ is defined as;

$$aa^\dagger_{ij} = \iint_{|\vec{p}\ | \leq p_{max}} e^{i\omega\vec{p}\ (r_i - r_j)} d^2p \tag{3.2.13}$$

Resulting in the optimum weights $q_N(\vec{k}\ )$ for all the array elements per frequency

$$G_l(f, \vec{k}) = q_N(\vec{k}\ )^\dagger G_l(f, \vec{k}) \tag{3.2.14}$$

Figure 3.6 shows the improvement in array response of IMS array I48TN in Tunisia after applying the optimum weight to the outcome of the Bartlett and Capon beamforming array response. For both Bartlett and Capon (Figure 3.5), the main lobe is modified towards a delta function. Nonetheless, due to applying those weights, the amount of side lobes as well as the power increases significantly, which may be deducted by applying CLEAN (section 3.3).

■ 3.2.6 Fisher detection

The Fisher detection is commonly used in analyzing the variance within measurements [Fisher, 1948]. Melton and Bailey [1957] introduced the F-ratio in combination with array processing, when after multiple studies implemented it. The detector aims to detect coherent signals impinging the microbarometer array. The algorithm uses the analysis of variance within a recording, which included both noise and signal [Fisher, 1948]. The F-ratio, the outcome of the algorithm, is a measure of SNR, and expresses the coherency between the recordings of the array elements for a specific slowness value. The maximum F-ratio can than be linked to the specific parameters concerning the dominant arriving wavefront impinging the array [Evers, 2008]. In the frequency-domain the Fisher detection is based on the outcome of the f/k spectra of the used beamform technique [Smart and Flinn, 1971]. $P_t(f)$ represents the total f/k spectral power as a normalised sum of the diagonal elements of the cross-spectral density matrix:

$$P_t(f) = \frac{1}{N} \sum_{n=1}^{N} C_{nn}(f) \tag{3.2.15}$$

Assuming that the signal is identical over all array elements while the noise can be modeled as uncorrelated Gaussian white noise, [Smart and Flinn, 1971] have shown that the F-ratio in the frequency domain can be defined using the following estimates of signal power on the beam $P_{\max}$, and total power P_t:

$$F(f, \vec{k}) = \frac{P_{\max}(f, \vec{k})}{P_t(f) - P_{\max}(f, \vec{k})}(N-1) \tag{3.2.16}$$

The relation between the F-ratio and the SNR has been derived by Melton and Bailey [1957].

$$F = N \cdot \mathrm{SNR}^2 + 1 \tag{3.2.17}$$

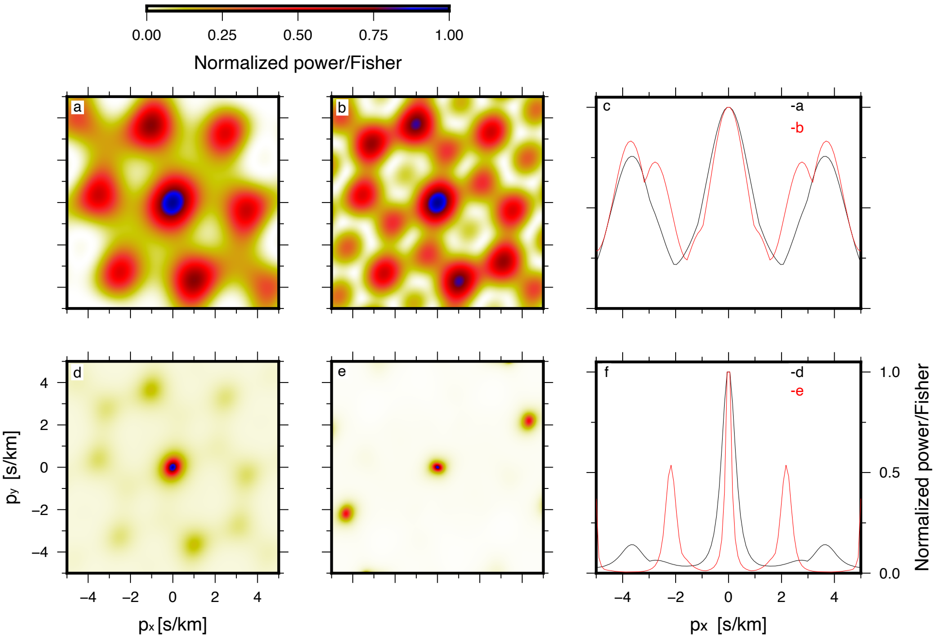

Figure 3.6: *Array response of infrasound array I48TN at 0.3 Hz, following the Bartlett (a) and Capon (d) beams. The array response improves after applying the frequency dependent weighting values following [Neele and Snieder, 1990] for Bartlett (b) as well Capon (e). The side spectra (c, f) show the improvement (red curve) with respect to the array response in terms of normalized power (black curve) at* $p_y = 0$.

3.3 CLEAN beamforming

In the processing of real data, the f/k spectrum often consists of multiple maxima with varying amplitude. In such a convoluted spectrum, it can be difficult to distinguish interfering sources and identify concurrent, sub-dominant sources from the side lobe of a dominant source. It is the objective here, to design a method that can unravel the f/k spectrum in terms of individual contributions to the f/k spectrum, while being able to distinguish between main lobe and side lobes. For this purpose, the CLEAN method can be applied.

CLEAN [Högbom, 1974] is a post-processing method that can be applied to conventional beamform methods, e.g., Bartlett and Capon as introduced in the previous subsection. CLEAN iteratively removes phase and amplitude information associated with the strongest contribution in the f/k spectrum, P_{max}, from the cross-spectral density matrix [Sijtsma, 2007; Gal *et al.*, 2016]. A partly cleaned cross-spectral density matrix, C_{clean}, is obtained:

$$C^{j+1}_{\mathrm{clean}}(f) = C^{j}_{\mathrm{clean}}(f) - \phi P^{j}_{\mathrm{max}} w_{\mathrm{max}} w^{*}_{\mathrm{max}} \tag{3.3.1}$$

with $w_{\mathrm{max}} = w(k_{\mathrm{max}})$ the beamform weight for which P_{max}, with wavenumber k_{max}, was resolved, C^{j}_{clean} the cross-spectral density matrix at j^{th} iteration and ϕ the parameter that determines the fraction of removed power. Note that the subtraction in Equation 3.3.1 involves a convolution of the array response function with P_{max}. This ensures that the array response pattern is suppressed in the $(j+1)^{\mathrm{th}}$ beamform iteration. It is precisely this deconvolution operation that allows for the identification of sub-dominant f/k spectral density peaks. Such peaks could otherwise have been masked due to spatial aliasing of the dominant source in the beamforming process.

The CLEAN algorithm has a relatively high computational cost because of the potentially large number of beamform iterations in lieu of one single beamforming run. The number of iterations is controlled by the ϕ value. A small value will result in resolving more sub-dominant sources at the cost of a larger number of iterations and therefore a higher computational load, while a larger value leads to a faster algorithm but may be less accurate in resolving sub-dominant sources. Gal *et al.* [2016] stated that the optimal value for ϕ depends on the combination of array layout, frequency range of beamforming and the SNR. In general, a small ϕ value is recommended when processing data from arrays with a small number of elements and/or data with low SNR values.

In this study, the number of iterations is not predefined but depends on a stopping criteria. CLEAN beamforming with ϕ values between 5 and 15% provided similar results. Since this study deals with a low number of array elements and a low SNR, a ϕ value of 10% has been chosen (following Gal *et al.* [2016]).

For each processed frequency f, the maximum of the f/k spectral density as well as the corresponding wavenumber vector $\vec{k}_j$ is stored in a CLEAN power spectrum:

$$P_{\mathrm{clean}}(f, \vec{k}) = \sum_{j}^{Q} \phi P^{j}_{\mathrm{max}}(f, \vec{k}_j) \tag{3.3.2}$$

Q is the total number of CLEAN iterations. The CLEAN process continues until reaching a stopping criterion. Because the array response function is deconvolved, the smearing of energy in the original f/k power spectrum $P(f, \vec{k})$ has been reduced. As a result, $P_{\mathrm{clean}}(f, \vec{k})$ has a sharper and cleaner appearance, which is useful in obtaining an enhanced insight in the diversity of acoustic sources around the array.

The individual contributions $P^j_{\max}(f, \vec{k}_j)$ in $P_{\text{clean}}(f, \vec{k})$ are characterized by a new and clean, Gaussian point spread function (PSF) [Sijtsma, 2007]. Every PSF has a standard deviation of three times the spatial f/k spectral resolution. Hence, sources are distinct if the the distance between the maxima of two PSF's is greater than two standard deviations.

■ 3.3.1 Fisher Statistics as CLEAN stopping criterion

As CLEAN is an iterative beamforming procedure, a maximum number of iterations is to be defined after which the procedure stops. Hitherto, setting of this parameter has been user-defined [Clark, 1980; Sijtsma, 2007; Gal *et al.*, 2016], which is impractical for application to large datasets, for which the number of iterations may be strongly dependent on the analysis window. Here, the use of Fisher statistics and the F-ratio as a test statistic [Fisher, 1948] is proposed for the definition of a data-driven stopping criterion.

The processing of data from a ground-based infrasound array corresponds to a bivariate analysis problem where the pressure fluctuations are modeled as a random process. Within each analysis window, the variance of the (phase-shifted) pressure signals between the array elements is compared with the variance of the pressure values at each individual element [Melton and Bailey, 1957]. The F-ratio compares both measures of variance. In the associated statistical test, the null hypothesis is tested that these variances are not significantly different. In other words: the null hypothesis corresponds to the case that no coherent signal is present. The F-ratio deviates from unity if the variances are not equal, which corresponds to a probability that a coherent signal is present in the data. Fisher's test statistic is evaluated for every steering vector that is considered in the beamforming procedure. This procedure allows an evaluation of the significance of detection on each steering vector of interest.

The probability density of the F-ratio is described by a F-distribution. The particular shape of the distribution is dependent on the statistics of the data samples as well as the degrees of freedom of the dataset. In the beamform application, the degrees of freedom are a function of the number of samples points T_s and array elements N. If the samples points follow the statistical distribution of Gaussian white noise, the resulting F-ratio statistic follows a central F-distribution $F_{\text{Fisher}}(\nu_1, \nu_2)$. The degrees of freedom in the time-domain Fisher analysis, ν_1 and ν_2, are given by: $\nu_1 = T_{s_t} - 1$ and $\nu_2 = T_{s_t}(N-1)$ [Evers, 2008]. In the frequency-domain, the degrees of freedom are given by: $\nu_1 = 2T_{s_f}$ and $\nu_2 = 2T_{s_f}(N-1)$ [Shumway, 1971]. The mean of the central distribution is $F_{\text{Fisher}} = 1$. The F-ratio statistic follows a non-central F-distribution $F_{\text{Fisher}}(\nu_1, \nu_2, \lambda_{nc})$ in the case where a signal with a certain SNR is present. The non-centrality parameter λ_{nc} is determined by the SNR of the signal as: $\lambda_{nc} = \nu_1 \cdot \text{SNR}^2$ [Shumway, 1971].

The statistical properties of the F-ratio allow for the estimation of the missed event and false alarm probabilities, given a specified confidence level. Likewise, a probability of detection can also be quantified. Therefore, the Fisher's test statistic is a robust and efficient method for the detection of coherent signals in the presence of incoherent noise. Besides, representing the spectra in terms of the F-ratio sharpens the main lobes, as can also be seen in Figure 3.5.

By evaluating the Fisher ratio at every CLEAN iteration, the probability of detection and the SNR of the detected signal can be estimated. Moreover, this framework allows to determine a CLEAN stopping criterion from a statistical perspective. Indeed, as the Fisher ratio approaches unity, the likelihood of a false alarm increases and the iterative procedure can be stopped, as no coherent signal is likely to be left in the cross-spectral density matrix. The effectiveness of this method will be demonstrated using synthetic data in the following section.

3.4 Synthetic data

Three different synthetic waveform tests are discussed in this section. The tests have been designed to (1) evaluate the use of Fisher statistics as a CLEAN stopping criterion, (2) compare the Bartlett and Capon beamform techniques, and (3) evaluate the performance of the proposed CLEAN algorithm in the processing of infrasound array data. The synthetic waveforms are generated given the array element locations of infrasound array I48TN (Figure 3.3). The temporal sample rate of the waveforms is 20 Hz, which corresponds to the actual sample rate of this IMS array.

■ 3.4.1 Fisher threshold testing using uncorrelated Gaussian white noise

To demonstrate the use of Fisher statistics in the determination of a CLEAN stopping criterion, a Monte Carlo simulation is performed. The Monte Carlo simulation consists of 500 Capon beamform runs on synthetic waveform data that consists of uniform Gaussian white noise. The beam forming analysis is carried out in the frequency band ranging from 0.1 to 0.3 Hz. Smoothing is applied by averaging power estimates for Z adjacent frequencies around a frequency of interest, which is defined by the amount of steps within the frequency band. To satisfy the degrees of freedom in the time domain and the frequency domain, smoothing should avoid overlapping frequencies. For each run, each with a duration of 1000s, data is beamformed. The Fisher ratio is computed for every beam. Figure 3.7a shows an example f/k spectrum.

The resulting distribution of calculated Fisher ratios is plotted in Figure 3.7b as a histogram. The histogram distribution follows a central F-distribution, which would be expected as the data samples follow the statistical distribution of Gaussian white noise. The F-distribution is characterised by the degrees of freedom which are specified by $N = 7$ and $T_{s_f} = Z + L = 10 + 40 = 50$, which indicates the number of sample points that are used, depending on the smoothing and the number of snapshots, L, within one window. The distribution is plotted with a solid black line in Figure 3.7b. The 95 percentile is found at $F_{\text{Fisher}} = 1.28$ and is indicated by the dotted line. For this particular choice of processing parameters, the Fisher threshold should be set to 1.28 in order to have a 95% confidence for avoiding false-alarms. More generally, this test demonstrates the use of Fisher statistics in the estimation of a CLEAN stopping criterion.

■ 3.4.2 Slowness estimates for multiple, interfering sources

CLEAN beamforming as postprocessing algorithm

Two additional synthetic datasets are constructed in order to test the ability to accurately discriminate between interfering sources within one analysis window. The synthetic waveforms are generated for each of the array elements, by adding Gaussian white noise with a specified amplitude as described in Table 3.1. The synthetic waveforms for each element are coherent, but shifted in time with respect to one another, according to the array layout and the imposed directivity of signal m. Each source is continuous, to represent ambient noise. Table 3.1 shows the characteristics of dataset A. The applied band-pass filter has corner frequencies of 0.1 and 0.3 Hz. Note that the three sources are continuously interfering throughout the record.

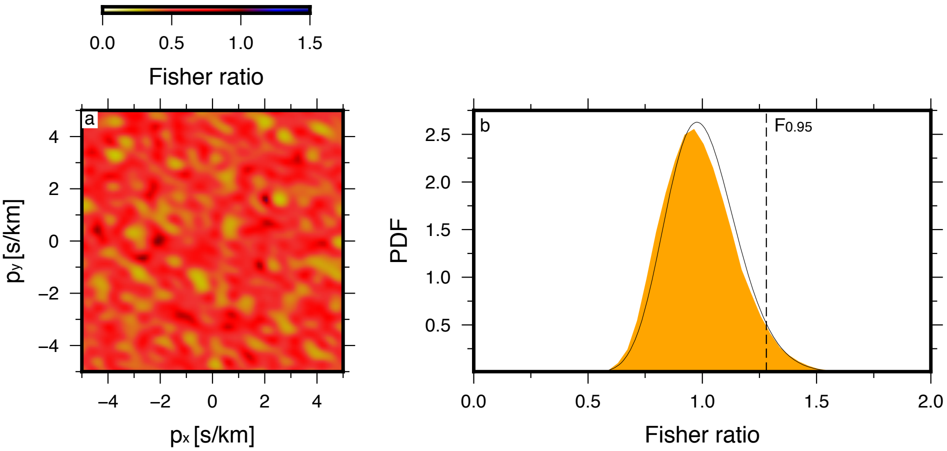

Figure 3.7: *Outcome of the Monte Carlo runs on randomly generated data. (a) F/k beamforming result of a random generated dataset. (b) Histogram F-ratio outcome of 500 Monte Carlo runs. The grey line indicates the central F-distribution. The dotted line is the 95 percentile,*$F_{0.95} = 1.28$.

The time shift for each array element is computed using the steering vector $a(\vec{k}_m)$ and wavenumber vector parameters:

$$k_{x,m} = \frac{2\pi f}{c_{\mathrm{app},m}} \sin(\theta_m) \qquad k_{y,m} = \frac{2\pi f}{c_{\mathrm{app},m}} \cos(\theta_m)$$

The individual signal contributions are added up per element, thereby generating a complex signal that is composed of several individual signals. Finally, uncorrelated Gaussian white noise with amplitude 0.5 Pa is added to each of the array element waveforms, individually. As this signal is incoherent between the array elements, it represents the noise level. Hence, a theoretical SNR and Fisher ratio can be estimated from Equation (3.2.17).

Input				Output Bartlett			Output Capon		
θ_m	$c_{\mathrm{app},m}$	s_m	Exp. $\mathrm{F}_{\mathrm{Fisher}}$	θ_m	c_{app}	$\mathrm{F}_{\mathrm{Fisher}}$	θ_m	c_{app}	$\mathrm{F}_{\mathrm{Fisher}}$
300	340	1.0	29	294	335	28	300	339	27
90	340	0.8	19	93	330	14	90	340	20
280	340	0.6	11	277	324	7	280	338	7

Table 3.1: *Input source parameters for dataset A and its estimated parameters using the CLEAN algorithm, following Bartlett's and Capon's method. The amplitude of the added incoherent white noise is 0.5 Pa. The expected F-ratio is computed using Equation* (3.2.17).

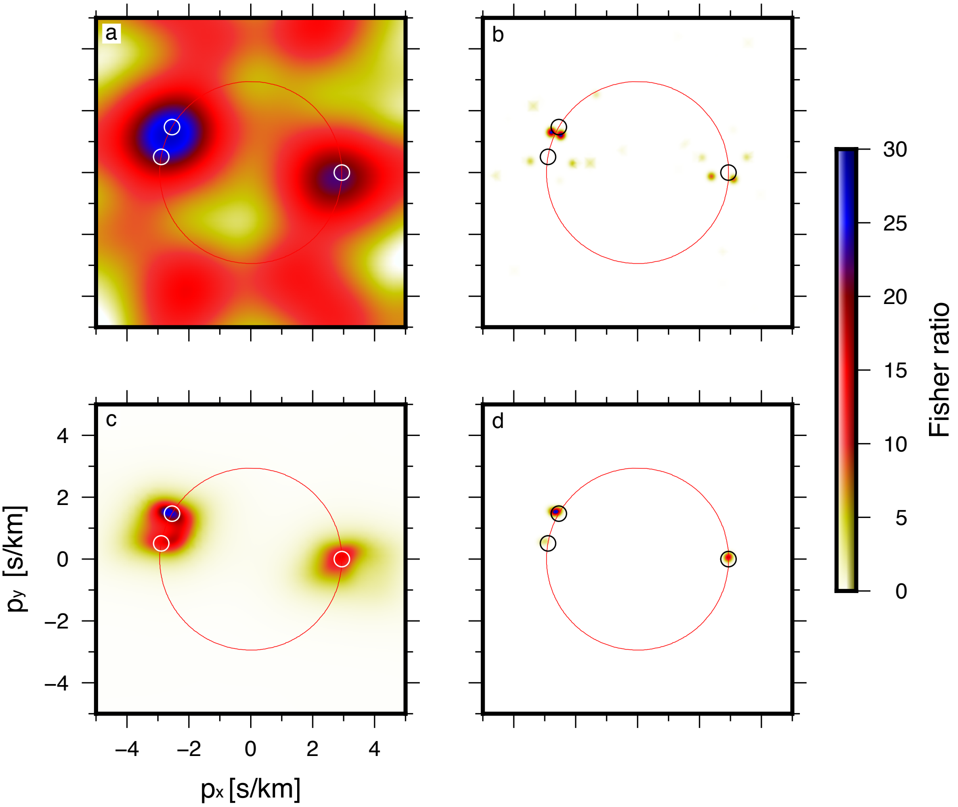

Figure 3.8: *Beamform results of I48TN between 0.1-0.3 Hz on synthetic dataset A (Table 3.1). Figures (a) and (b) show the results of the Bartlett beamformer before and after CLEAN has been applied. (c) and (d) are the results when Capon has been applied. The circles indicate where sources are expected in the f/k spectrum. The red ring indicates the apparent velocity,* $c_{app} = 340 m/s$*. Note that the apparent sources in frame (b) correspond to side-lobes due to Bartlett's method.*

Figure 3.8 shows the initial f/k spectra before and after application of CLEAN. Three features should be noted. First, CLEAN improves the resolution of both spectra, as can be seen in the sharpening of the main lobes. This enables to resolve two closely located sources within the f/k spectrum. The highest resolution is obtained by combining Capon and CLEAN. Gal *et al.* [2016] earlier stated that a high-resolution initial f/k spectrum with a sharp main lobe is beneficial to the performance of CLEAN. Second, with Capon the sources are better identified than with Bartlett, as can be seen from the coincidence of the lobes with the circles, which have their center-points at the expected source locations and a radius of $\pm 1.5°$. This is a consequence of the lower resolution of Bartlett. Last, the low spatial resolution of Bartlett leads to various spurious peaks in the f/k spectrum, after application of CLEAN.

The θ_m and c_{app} parameters that correspond to the maxima of the resolved f/k spectral densities after CLEAN has been applied are tabulated in Table 3.1. In case of Capon in combination with CLEAN, a close agreement between the source parameters and the resolved values is noted. This is not the case when applying Bartlett's method, due to the low resolution of the initial f/k spectra.

While a particularly good agreement is noted for the back azimuth and the resolved apparent velocity in case of Capon and CLEAN, the resolved Fisher ratio is biased low compared to the theoretical Fisher ratio, which will be further explained in the discussion.

Based on the comparative performance of the beamform techniques, the future synthetic tests are performed with Capon's method only.

Comparison between CLEAN and MUSIC beamforming

Besides CLEAN beamforming, MUSIC beamforming can also be applied to resolve multiple spatially distributed sources within overlapping frequencies and time windows. The algorithm is based on splitting the cross-spectral density matrix into a signal and noise subspace. The splitting, however, brings two significant limitations. First, the number of sources that the algorithm can resolve depends on the number of array elements. Second, in practice, the exact number of interfering sources is unknown. An incorrect number of expected sources results in a biased f/k spectrum with various sidelobes. Moreover, MUSIC does not represents a true spectrum, it exhibits peaks in the vicinity of the true direction of arrival. In addition, there are known issues for signals with low SNR and short integration times (Figure 3.9, Viberg and Krim [1997]).

The SORTE algorithm has been introduced as a threshold measure for the unknown number of sources within this chapter. SORTE is a gap measure between values and is therefore used as a threshold for separating the noise and signal subspaces.

Figure 3.9 shows the f/k spectra obtained from the MUSIC algorithm while analysing the synthetic waveforms from dataset A, which contains three sources. The panels represent the algorithm's outcome for 1, 2, 3 and 4 pre-defined sources. Note how the beamform resolution increases when the MUSIC algorithm approaches the number of sources and how an incorrect number of expected sources biases the resolution. The figure shows that an exact expected number of sources is critical for a correct f/k analysis. For this example, the SORTE threshold correctly indicated three expected sources (panel c).

Although the threshold function agrees with the dataset, the f/k resolution of MUSIC is low compared to the CLEAN spectra of Figure 3.8. Furthermore, the presence of sidelobes in the MUSIC spectrum further complicates interpretation of the results. Therefore the CLEAN algorithm is favorable compared to the MUSIC algorithm. CLEAN iteratively filters the coherent signals from the f/k spectra while applying a deconvolution of the array response.

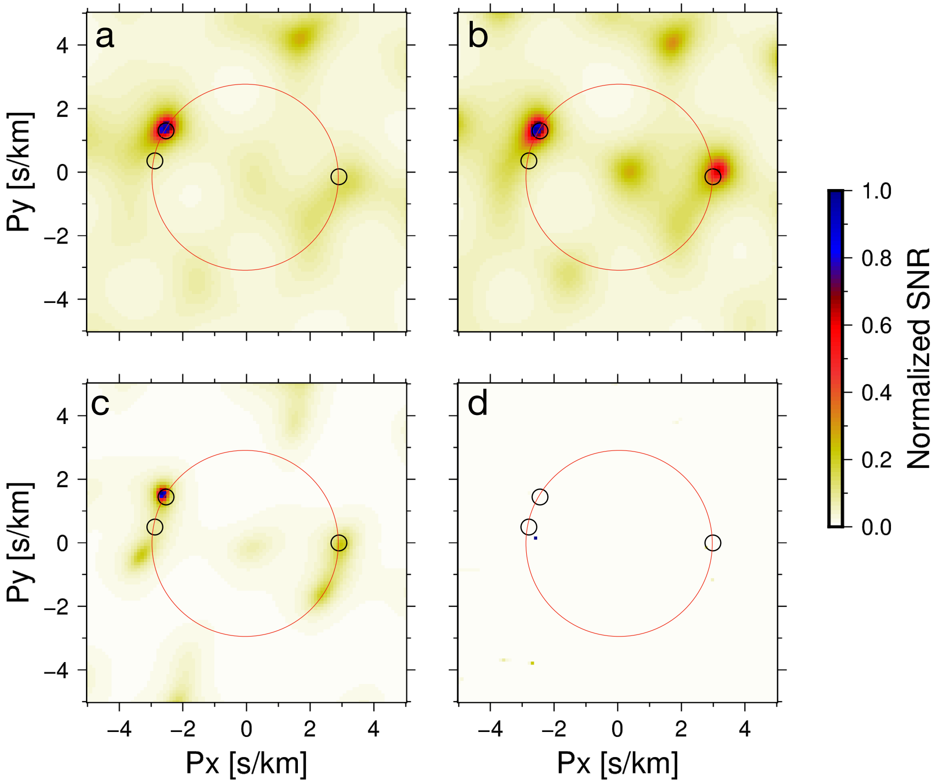

Figure 3.9: *Outcome of the MUSIC beamforming algorithm on the synthetic waveforms of dataset A. (a) The f/k spectrum for the MUSIC algorithm with one expect source. Panels (b), (c), and (d) show the spectra for 2, 3, and 4 expected number of sources, respectively.*

3.4.3 Performance of the CLEAN algorithm in the processing of infrasound array data.

The parameters used in the construction of dataset B are summarized in Table 3.2. Dataset B represents the case of an increasing number of interfering, continuous sources with time. The synthesis of the signals is otherwise equal to the method described earlier in this section. Figure 3.10 shows the f/k spectra and the resulting θ_m and c_{app} as function of time. The circles indicate the expected source positions and the color rings indicates the expected apparent velocity of the signals. Again, a close agreement between the source parameters and the resolved values is noted. The numerical values are summarized in Table 3.2.

Input					Output		
θ_m	c_{app}[m/s]	s_m[Pa]	Exp. F_{Fisher}	Time [s]	θ_m	c_{app}[m/s]	F_{Fisher}
300	360	1.0	29	100-4000	300	359	28
90	320	0.8	19	1100-4000	89.8	319	17
280	280	0.6	11	2100-4000	279.6	278	9

Table 3.2: *Similar as Table 3.1, but now for dataset B, which features three different sources that are active during different time intervals. In this case, the CLEAN method is used with Capon's method, only.*

Since the input and output of both datasets are in good agreement, we conclude that the proposed Fisher ratio as a stopping criterion and the PSF in combination with the two standard deviation distribution are robust parameters. Both enable CLEAN to be data-driven and reliable.

3.4.4 Monte-Carlo run on synthetic infrasound data.

To determine the consistency of the results for the Capon method in combination with CLEAN (Table 3.2), a second Monte Carlo run was performed. This Monte Carlo run consists of 500 runs for which each run a new dataset is created with the input of Table 3.2. The results are again in line with earlier results. A good agreement is noted for the back azimuth and apparent velocity.

In the estimation of SNR levels, it has been found that the resolved Fisher ratio is not always in agreement with the theoretical value that would be expected from the SNR conditions and the degrees of freedom in the dataset. This is further outlined in Figure 3.11, which shows the theoretical central and non-central Fisher distributions for datasets A. The solid gray lines indicate the theoretical non-central Fisher distributions for each source, the dotted lines are the resolved mean Fisher ratios. One of the three resolved sources is in agreement with the theoretical distribution, the other sources show a slight deviation. The bias is attributed to the fact that the noise cannot longer be considered as uncorrelated Gaussian white noise when multiple coherent signals are present in the array recordings. Further research is needed to understand the noted bias between theoretical and resolved Fisher ratio, in the case of multiple sources.

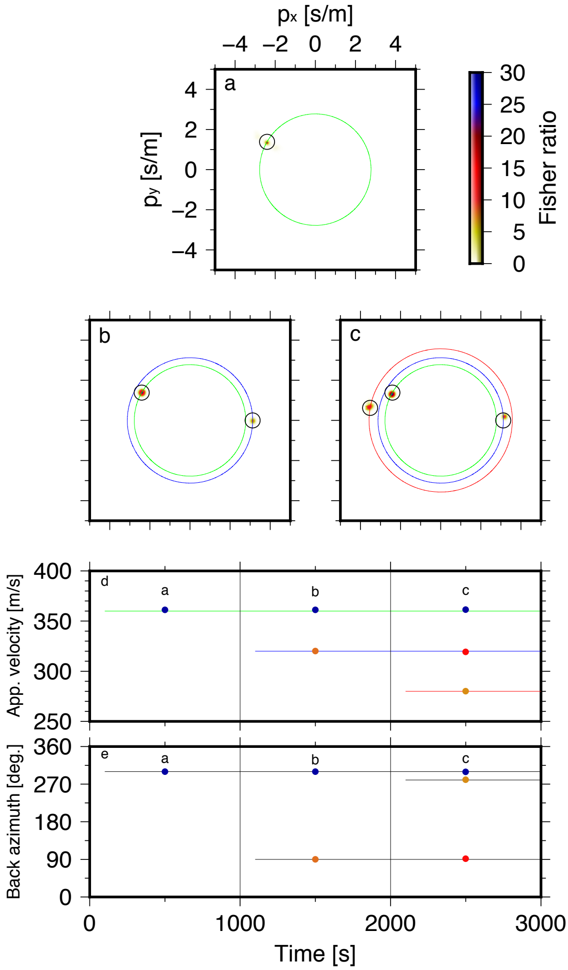

Figure 3.10: *Result of Capon beamforming with CLEAN on waveforms of dataset B, Table 3.2. F/k spectra of window 1 (a), window 2 (b) and window 3 (c) after CLEAN has been applied. The circles indicate where sources are expected, and the colored rings indicates the apparent velocity* c_{app} *(green;* $c_{app} = 360m/s$*, blue;* $c_{app} = 320m/s$*, and red;* $c_{app} = 280m/s$*. (d-e) are the CLEAN results plotted as a function of time, for the three windows considered. The lines indicate expected results regarding back azimuth and apparent velocity, color of the dots indicate the Fisher ratio.*

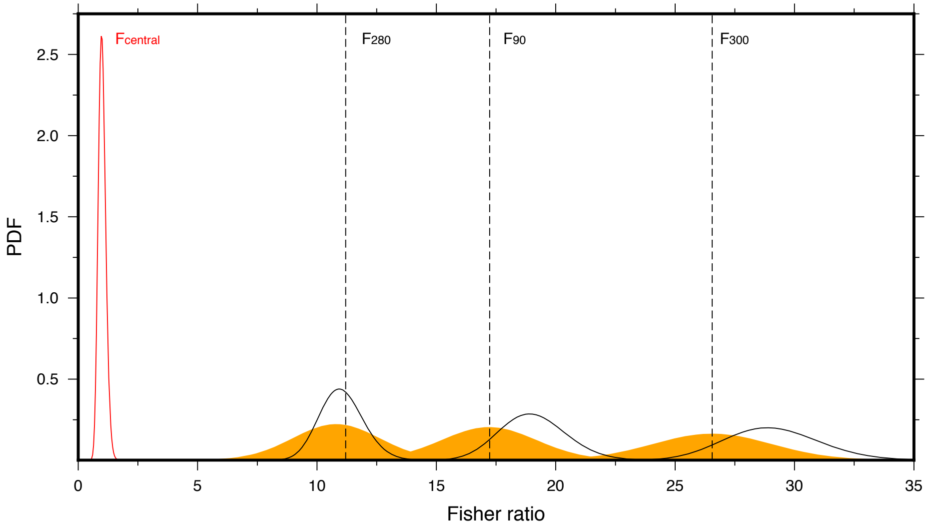

Figure 3.11: *The theoretical central and non-central F-distribution based on synthetic dataset A (Table 3.1). The red curve indicates the central distribution, the gray curves the theoretical non-central distribution for each source. The dotted lines are the resolved mean Fisher ratio's, while the orange histograms determine the outcome of the Monte Carlo runs. The observed differences between histograms and theoretical distributions can be explained by the coherence of the background noise.*

3.5 Real data example

The proposed CLEAN method is applied to infrasound measurements recorded on 17 January 2011 on the IMS infrasound arrays I48TN (Tunisia), I42PT (Açores), I26GE (Germany), I43RU (Russia) and I18DE (Greenland).

This analysis builds on an earlier study by Assink *et al.* [2014] in which two simultaneous infrasound sources were identified in the microbarom frequency band using a beamform technique using Bartlett's method and Fisher statistics. It was hypothesised that the detections corresponded to microbarom activity in the Northern Atlantic and Mediterranean Sea.

The two sources had an overlapping frequency content around 0.2 Hz, but the Mediterranean microbaroms were found to be coherent up to 0.6 Hz while the North Atlantic microbaroms are coherent up to 0.3 Hz.

Figure 3.12 shows the f/k spectra of the IMS arrays for the first 2000 seconds of data on 17 January 2011, before and after CLEAN has been applied and by using the 95 percentile Fisher threshold. In these spectra, multiple sources are resolved in the 0.1-0.3 Hz frequency band. It should be noted that sub-dominant sources can be identified, which would have been obscured in traditional infrasound processing schemes that only report on the dominant source. Figures 3.13 shows the processing results of I48TN for the entire day. Figures 3.13a and 3.13b show the dominant source per time-window, using Bartlett's and Capon's method, respectively. Figure 3.13c list all the resolved sources by using Capon in combination with CLEAN. The conventional beamforming methods detect two sources intermittently, while CLEAN continuously resolves three sources.

Furthermore, the frequency band of processing can highlight different sources, which is illustrated in Figure 3.14. Figure 3.14 shows that the microbaroms from the Atlantic Ocean have a lower center frequency than those of the Mediterranean Sea. The Atlantic Ocean microbaroms are most coherent to the north-west in the frequency range of 0.1-0.3 Hz, those from the Mediterranean Sea appear from the east between 0.3-0.6 Hz. This is consistent with the earlier analysis by Assink *et al.* [2014].

Microbarom source regions are identified by cross-bearing localization, in which the detections at multiple IMS arrays are combined. In this procedure, it is assumed that there is an atmospheric duct in all directions, and that the propagation of microbarom signals is not strongly influenced by cross-winds or other along-path meteorological conditions [Smets and Evers, 2014*b*]. The source locations are compared with microbarom source regions that have been predicted using the microbarom source model described by Waxler *et al.* [2007], following the implementation described in Smets [2018]. As an input for this model, the two-dimensional wave spectra (2DFD) obtained from the European Centre for Medium-Range Weather Forecast (ECMWF) deterministic high-resolution ocean wave model Cycle 36r1 (HRES-WAM) analysis [ECMWF, 2008, 2016] have been used.

Figure 3.15a and b show the results of this approach for the frequency ranges of 0.1-0.3 Hz and 0.3-0.6 Hz. For both frequency bands CLEAN resolved several sub-dominant sources, which could have been missed when applying conventional beamforming methods. Because of this, the same microbarom sources are resolved at different IMS stations, resulting in better microbarom source localization based on IMS observations. In case of the lower frequency band more microbarom sources are resolved in the region of the Atlantic ocean, the higher frequency band highlights two sources towards the Mediterranean sea. For both ranges of frequency, the resolved microbarom source regions are in a particularly good agreement with the microbarom prediction model.

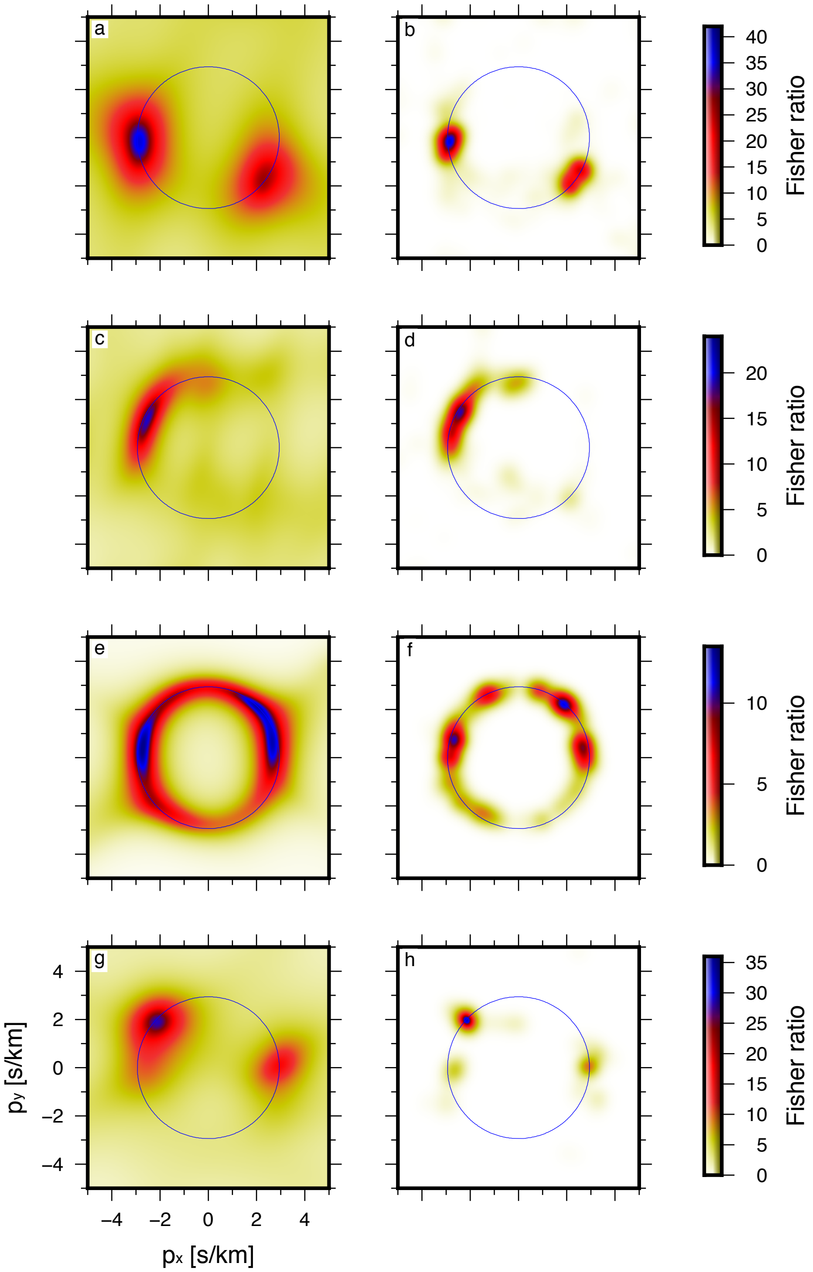

Figure 3.12: *F/k spectra of I18DE (a-b), I26GE (c-d), I42PT (e-f) and I48TN (g-h) before and after CLEAN, between 0.1-0.3 Hz for the first 2000 sec of data on 17 January 2011. The blue ring indicates the speed of sound at standard sea level (15° C and 1.225 kg/m*^{3}*),* $c_{app} = 340 m/s$.

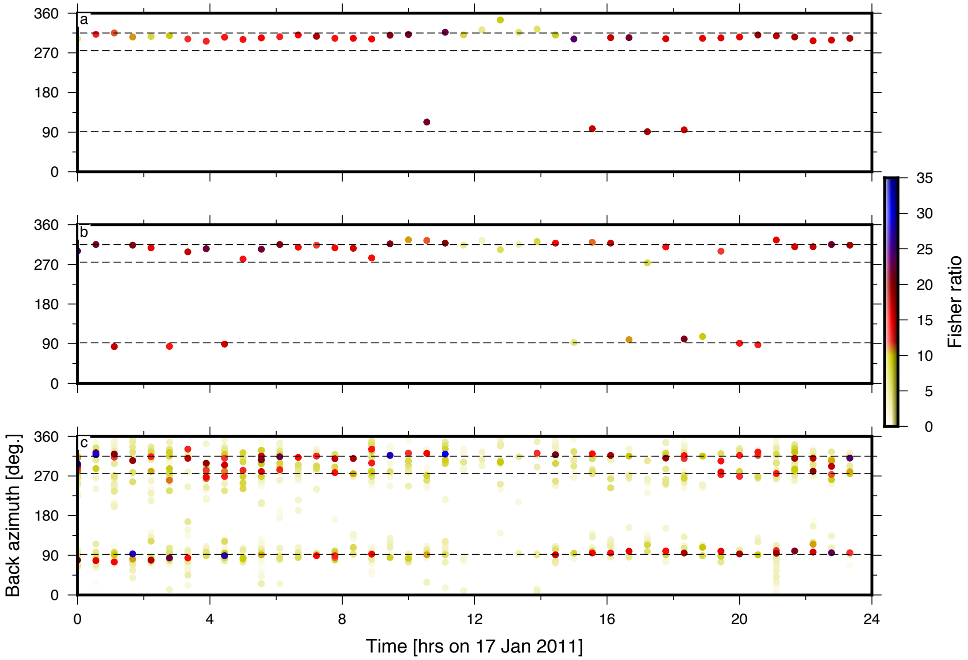

Figure 3.13: *Infrasound detections on 17 January 2011 in the 0.1-0.3 Hz frequency band. (a) shows the maximum contribution of the Bartlett f/k spectrum without CLEAN. (b) the maximum contribution of the Capon f/k spectrum without CLEAN and (c) reveals the outcome after application of the proposed CLEAN algorithm on the Capon f/k spectra. The dotted lines indicate the mean back azimuths that are associated with the observed microbaroms throughout the day. The dots are coloured coded by the Fisher ratio.*

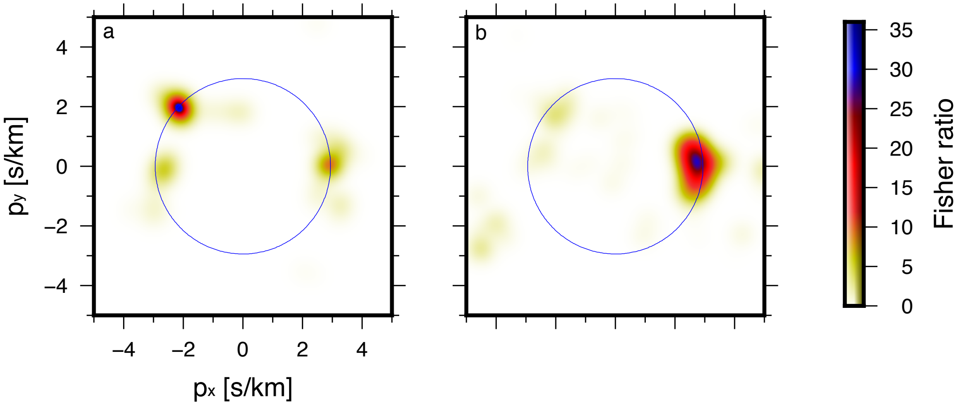

Figure 3.14: *CLEAN f/k spectra of I48TN between (a) 0.1-0.3 Hz and (b) 0.3-0.6 Hz for the first 2000 sec of data on 17 January 2011.*

3.6 Discussion and conclusion

In this study, a CLEAN array processing algorithm is presented that has been inspired by earlier work [Sijtsma, 2007; Gal *et al.*, 2016]. CLEAN is a post-processing method that can be applied to conventional beamform techniques, such as Bartlett and Capon. Because contributions to the total f/k spectrum are iteratively removed in this procedure, sub-dominant sources can be identified. Moreover, a more peaked f/k spectrum is obtained because the array response is deconvolved in the process. The performance of CLEAN is found to be dependent on the beamform resolution, which is in line with earlier work by Gal *et al.* [2016].

Moreover, the use of Fisher statistics for signal detection and the determination of a CLEAN stopping criterion is proposed. This stopping criterion has been identified in earlier work as a critical parameter for the performance of CLEAN [Clark, 1980; Sijtsma, 2007; Gal *et al.*, 2016]. The efficiency of the method is demonstrated using a Monte Carlo simulation with uniform Gaussian white noise. From this test, it can be concluded that the central F-distribution can be used as guidance to estimate a CLEAN stopping criterion. The probability of false alarms can be estimated when it is assumed that the remainder of the cross-spectral density matrix consists of (incoherent) white noise after beamform iterations.

Furthermore, synthetic tests have been performed to simulate the detectability of multiple continuous infrasound sources surrounding an array. The tests show that the back azimuth and the apparent velocity are accurately resolved. Based on this, it is concluded that that the PSF in combination with the two standard deviations distribution is adequate for distinguishing multiple sources. The Capon method has been found to provide more accurate results when compared to the Bartlett method, which is related to the higher spectral resolution of the former method.

It has been shown that the properties of Fisher statistics can be used to discriminate between coherent and incoherent signals. As a result, the Fisher ratio shall be used as the CLEAN stopping criterion. Nonetheless, in the estimation of SNR levels, it has been found that the resolved Fisher ratio is not always in agreement with the theoretical value that would be expected from the SNR conditions and the degrees of freedom in the dataset. The bias is attributed to the fact that the noise cannot longer be considered as uncorrelated Gaussian white noise when multiple coherent signals are present in the array recordings. Further research is needed to understand the noted bias between the theoretical and the resolved Fisher ratio, in the case of multiple sources.

CLEAN has been applied to infrasound data recorded on multiple IMS arrays that are located around the Northern Atlantic. The results show that multiple microbarom sources can be resolved, including regions that would would have been obscured if conventional processing methods would have been used. Microbarom source locations are obtained by cross-bearing localization and are in agreement with simulated microbarom source regions. It should be noted that the effect of propagation conditions are neglected in the current approach which, in combination with the dynamic nature of the microbaroms, explain some variation in back azimuth with time. Such effects could be accounted for by back projecting using a ray theoretical approach [Smets and Evers, 2014*b*].

Although the use of CLEAN beamforming allows for the detection of concurrent sources around an infrasound array, the method is computationally expensive compared to methods in which only the dominant source is to be detected. Moreover, the performance of CLEAN depends on the setting of various parameters that require careful tuning. This includes the choice of the beamforming weights and the setting of the ϕ value, the percentage of source removal per iteration. The setting of ϕ depends on the combination of array layout, processing frequency and the SNR. Therefore, it is important to analyse the sensitivity of the beamforming results to the choice of processing parameters.

Conventional beamforming algorithms can only confidently detect the most dominant source in each processing window and cannot confidently distinguish other concurrent sources from side lobes. The CLEAN implementation by Gal *et al.* [2016] iteratively resolves more sources. However, without a statistical framework, the number of iterations, which is predefined, is arbitrary and there is no certainty in the process with regard to true or false sources. In the presented implementation, a Fisher statistics framework is used to define a stopping criterion so that there is statistical certainty that the resolved sources are real. In the case of I42PT the initial f/k spectrum is 'smeared' over almost 360°. This is because I42PT is located on an island with sources all around it, including perhaps local and weaker sources that are not resolved in the microbarom model. The model averages microbarom source activity over a period of six hours. Therefore sources that are active for only a small fraction of that period are suppressed. However, a processing window of 2000 seconds with CLEAN can resolve such local, short duration sources. Additionally, I42PT is located relatively close to North-Atlantic microbarom source regions highlighted in the model (Figure 3.15). Thus, it can separate the source region into more sub-sources that are two standard deviations apart in the f/k spectrum.

Previous studies have discussed other beamforming algorithms to identify multiple sources within the same frequency band (e.g., MUSIC [Schmidt, 1986]). Within section 3.4.2 the CLEAN and MUSIC algorithms are compared and discusses the benefits of CLEAN over MUSIC. CLEAN does not require source knowledge while the MUSIC algorithm needs the user to define the number of sources. If this number is incorrect, the outcome of the algorithm is incorrect. Furthermore, MUSIC can only resolve as many sources as array elements.

The enhanced beamforming resolution of CLEAN improves the capabilities of infrasound as a monitoring technique. This comes to the benefit of infrasonic monitoring of nuclear tests as well as natural hazards, such as volcanoes, earthquakes and hurricanes. In addition, high resolution microbarom observations can be useful in the assessment of microbarom source models [Waxler *et al.*, 2007] as well as in the remote sensing of the middle and upper atmosphere, for which microbarom signals have been used in previous research [Donn and Rind, 1972; Smets, 2018]. Besides the application to infrasound arrays, the algorithm can be applied to improve on the limited f/k spectral resolution of arrays with a low number of elements, such as the IMS hydro-acoustic triplet arrays that are deployed in the world's oceans.

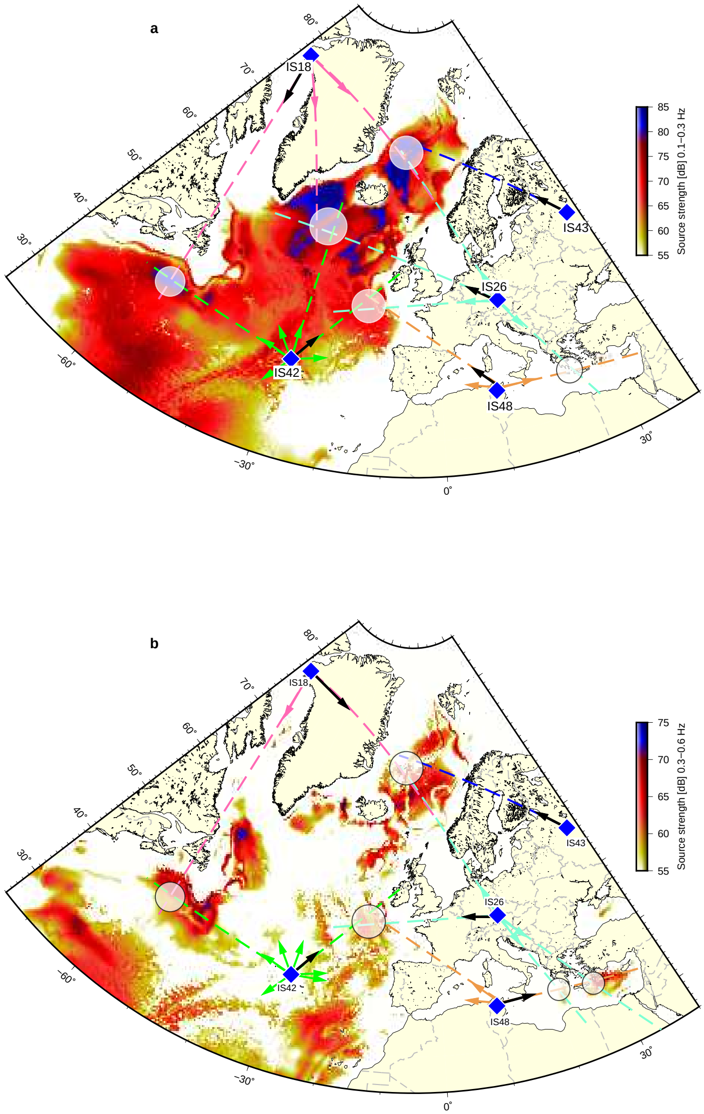

Figure 3.15: *Microbarom source region predictions for frequencies between 0.1- 0.3 Hz (a) and between 0.3-0.6 Hz (b) from 17 January 2011 00:00 UTC till 00:30 UTC [Waxler and Gilbert, 2006; Smets, 2018]. I48TN, I42PT, I26GE, I43RU and I18DE are indicated by blue diamonds. Back azimuth projection of all resolved sources are indicated by solid arrows(Figure 3.12), the black solid arrow indicates the dominant source. Transparent circles indicate possible source location found by cross bearing.*

4

Modelling of microbarom soundscapes

Statistical projections which speak to the senses without fatiguing the mind, possess the advantage of fixing the attention on a great number of important facts.

Alexander von Humboldt

Abstract Within this chapter a method is introduced to reconstruct microbarom soundscapes in absolute values. The soundscapes are compared to remote infrasound recordings from infrasound array I23FR (Kerguelen Island) and in-situ recordings by the INFRA-EAR, a biologger deployed near the Crozet Islands. The reconstruction method accounts for all-acoustic contributions, divided into evanescent microbaroms (detectable directly above the source) and propagating microbaroms (detectable over long ranges). It is computed by integrating acoustic intensities over the ocean surface, convolved with the transfer function quantifying the propagation losses and propagation time. The reconstructed soundscapes are found within 2.7 dB for 85% of the measurements in the microbarom band of 0.1-0.3 Hz. Infrasonic soundscapes are essential for understanding the ambient infrasonic noise field and are a basic need for applications such as atmospheric remote sensing, natural hazard monitoring, and verification of the Comprehensive Nuclear-Test-Ban Treaty.

Published as: **den Ouden, et al. 2021**, *A bird's-eye view on ambient infrasonic soundscapes*, Geophysical Research Letter Volume 48, DOI: 10.1029/2021GL094555
Note that minor changes have been introduced to make the text consistent with the other chapters, and that Section 4.4 is extended with non peer-reviewed content.

4.1 Introduction

The Southern hemisphere is characterized by its sparsity of in-situ atmospheric observations due to large ocean volumes and consequently limited landmass. Meteo-France maintains and operates meteorological measurement facilities at some of the French Sub Antarctic and Antarctic lands. The Southern Oceans weather forecasts benefits from those in-situ facilities in combination with remote satellite data [Levy and Brown, 1991; ECMWF, 2017]. This study discusses the measurement of atmospheric pressure perturbations and their variations. Those observations have shown to be valuable for studying both infrasound and gravity waves [Blanc *et al.*, 2018; Marlton *et al.*, 2019; Hupe, 2019]. Such observations can be retrieved from microbarometer arrays that are part of the global IMS. The IMS is in place to verify the CTBT [Marty, 2019], and globally monitors the infrasonic wavefield.

Deep oceanic ambient noise is globally the most omnipresent seismic and infrasound source. The sea state describes the energy of the ocean surface and is the driving force for four different seismo-acoustic wave contributions (Figure 4.1-a). (1) Evanescent microbaroms at the ocean-air interface are a direct product of travelling ocean surface waves, unregarded the water depth nor bathymetry, and decays vertically [Waxler and Gilbert, 2006; Hetzer *et al.*, 2010]. (2) The primary microseisms are related to a travelling ocean waves as well; however, these are only generated at the seafloor whenever the surface wave is in phase with the ocean bathymetry [Ardhuin *et al.*, 2015]. Non-linear interaction of counter travelling ocean surface waves results in standing ocean waves, causing the radiation of acoustic energy and resonance within the water column [Longuet-Higgins, 1950; Hasselmann, 1963]. At the interfaces of the water column, acoustic energy is radiated into the atmosphere as (3) propagating microbaroms [Brekovskikh, 1973] and down into solid seafloor as (4) secondary microseisms [Longuet-Higgins, 1950].

Propagating microbaroms are often received at distant infrasound arrays and typically peak around 0.2 Hz [Campus and Christie, 2010]. Various studies have focused on comparing microbarom simulations and distant IMS array observations [Landes *et al.*, 2012; De Carlo *et al.*, 2020*b*; Vorobeva *et al.*, 2020]. Such studies are hampered by the relatively large distance of the arrays to the microbarom source regions, which is often largely spread out (~ 10.000 km^2). Typically, array processing techniques are applied to detect the dominant acoustic signal and direction-of-arrival in a given time segment and frequency band. Therefore, only the resolved direction and amplitude of this most dominant microbarom observation is compared with microbarom models. However, Assink *et al.* [2014] and Smets and Evers [2014*a*] showed that multiple spatially distributed sources within the same time segment and frequency could occur (see also chapter 3 of this thesis).

In this chapter, atmospheric in-situ and remote measurements of microbaroms within the Southern Ocean are obtained by, respectively, the INFRA-EAR (chapter 2) and IMS array I23FR (Kerguelen Island). The INFRA-EAR is a multidisciplinary sensor platform for the monitoring of geophysical parameters. It has been fitted to the Southern Ocean's largest seabirds, the Wandering Albatross (*Diomedea exulans*). During foraging trips, an albatross can fly thousands of kilometres away from its nest. Throughout the 2020 foraging trips, 25 INFRA-EARs have flown over the Southern Ocean to collect geophysical data. Furthermore, the INFRA-EARs are used to investigate the extent of infrasound and weather patterns in the navigation decisions by Wandering Albatrosses [Clay *et al.*, 2020; Zeyl *et al.*, 2020]. The INFRA-EARs have collected a total of 115 hours of absolute and differential pressure data while travelling over 42,184 km.

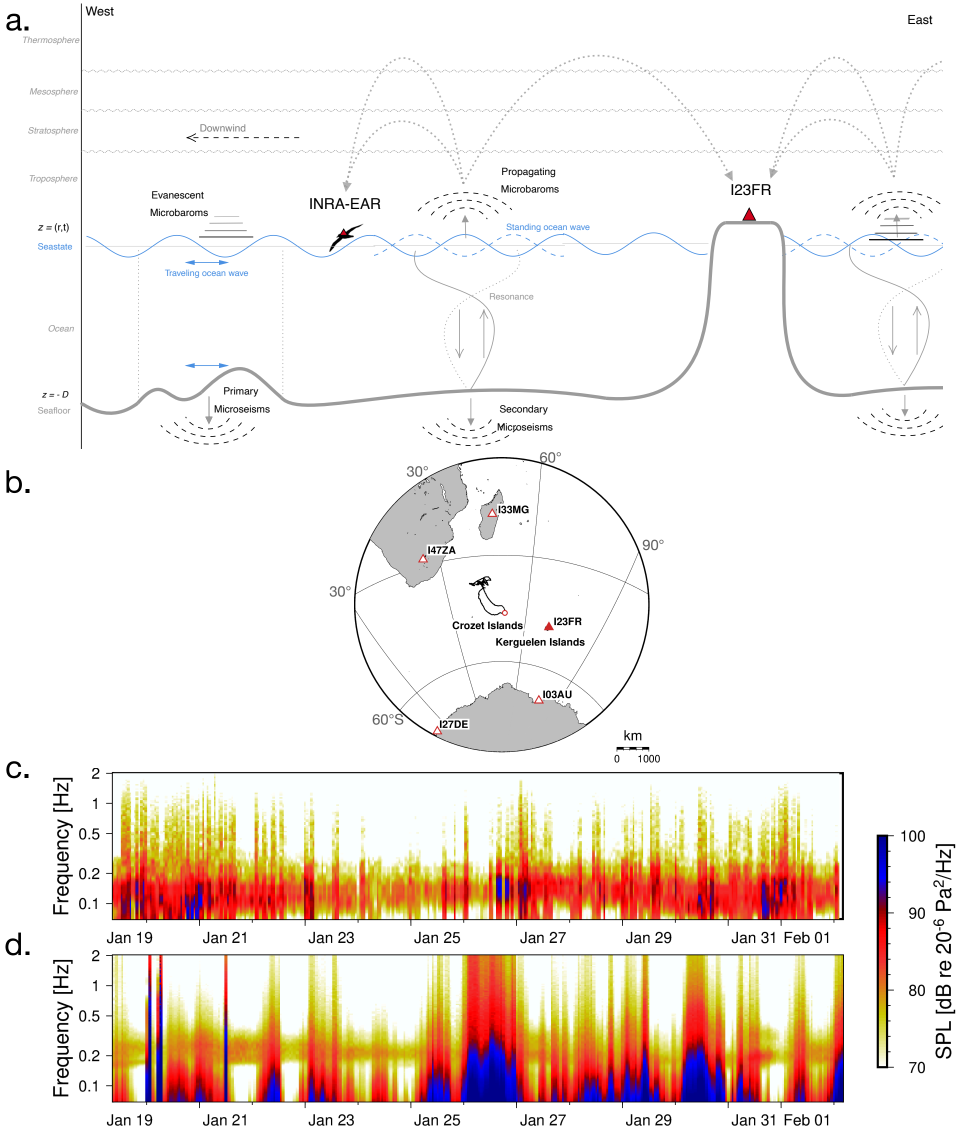

Figure 4.1: *(a) A schematic overview of deep oceanic ambient noise. The blue signatures highlight the sea state and its products (travelling and standing ocean waves). The gray arrows indicate the generation of the acoustic components and the coupling to the interfaces. The black half-spheres show the radiation within the atmosphere and solid earth, from where a simplistic atmospheric propagation path is described. (b) The trip of the INFRA-EAR over the Southern Ocean. The triangles show IMS infrasound array locations. The circles indicate the start and end position of the trip. (c) and (d) show the spectrogram of the recording by the INFRA-EAR and IMS array I23FR, respectively.*

High-resolution array processing techniques to resolve spatially distributed infrasound sources, e.g., CLEAN beamforming (chapter 3), cannot be applied to the INFRA-EAR observations. This is because the individual INFRA-EAR's exist beyond the required aperture for beamforming [Evers, 2008]. Instead, a method is developed to derive the different contributions of the microbarom field that are measured by the INFRA-EAR and I23FR array.

4.2 Microbarom observations near Crozet Islands

■ 4.2.1 The INFRA-EAR: in-situ infrasound measurements

The INFRA-EAR is a multidisciplinary sensor platform for monitoring geophysical parameters (chapter 2). The platform uses digital MEMS and monitors concurrently various geophysical parameters, such as differential and absolute pressure. The battery lifetime depends on the sensors power consumption. Therefore, the sensors are not continuously recording during a trip, as the battery lifetime is limited. The differential pressure sensor (KNMI mini-MB) is activated in bursts of five minutes, each hour, with a sampling frequency of 10 Hz to measure the small pressure perturbations. Section 2.1 stated that the KNMI mini-MB measures on the order of 10^{-2} Pa and is biased by 2 ± 1 dB at frequencies below 1 Hz. The logger provides a GPS timestamp per sample point and a position every 15 minutes.

The INFRA-EAR is fitted to wandering albatrosses at the Crozet Islands. The average trip takes approximately 15 days while travelling thousands of kilometres. The recordings of the INFRA-EAR occur directly above the sea surface, ~ 5 m [Richardson *et al.*, 2018].

■ 4.2.2 IMS array I23FR: remote infrasound observations

Infrasound array I23FR is located at Kerguelen Island, ±1500 km from the INFRA-EAR recordings. Due to the INFRA-EAR's proximity to I23FR, it is reasonable to assume that the differential pressure recordings show similar characteristics. The I23FR array has an aperture of ±1700 m and is divided into five triplets of MB 2005 microbarometers [Ponceau and Bosca, 2010] with an inter spacing of ±100 m. This array, however, is often excluded from scientific studies due to adverse weather conditions and strong westerly winds [Brown *et al.*, 2014]. The array continuously measures small pressure perturbations with a sampling frequency of 20 Hz.

■ 4.2.3 Comparison between the microbarom measurements

The in-situ recordings of the INFRA-EAR are compared with remote observations at I23FR. Both are analysed in the frequency domain by means of spectra and interpreted as coherent infrasound and incoherent pressure fluctuations due to the wind and turbulence [Raspet *et al.*, 2019]. The INFRA-EARs recordings are transferred into a PSD [Welch, 1967], which are combined in a spectrogram. The I23FR recordings are zero-delayed processed, and as well transferred into a PSD and combined in a spectrogram.

Within this study, recordings of one INFRA-EAR's trip have been compared with I23FR observations (Figure 4.1-c and -d, respectively). While significant overlap is noted, the INFRA-EAR spectra include low frequencies that do not appear to be measured by I23FR. This discrepancy can be understood when reconstructing the microbarom infrasoundscape, as will be done in the next section.

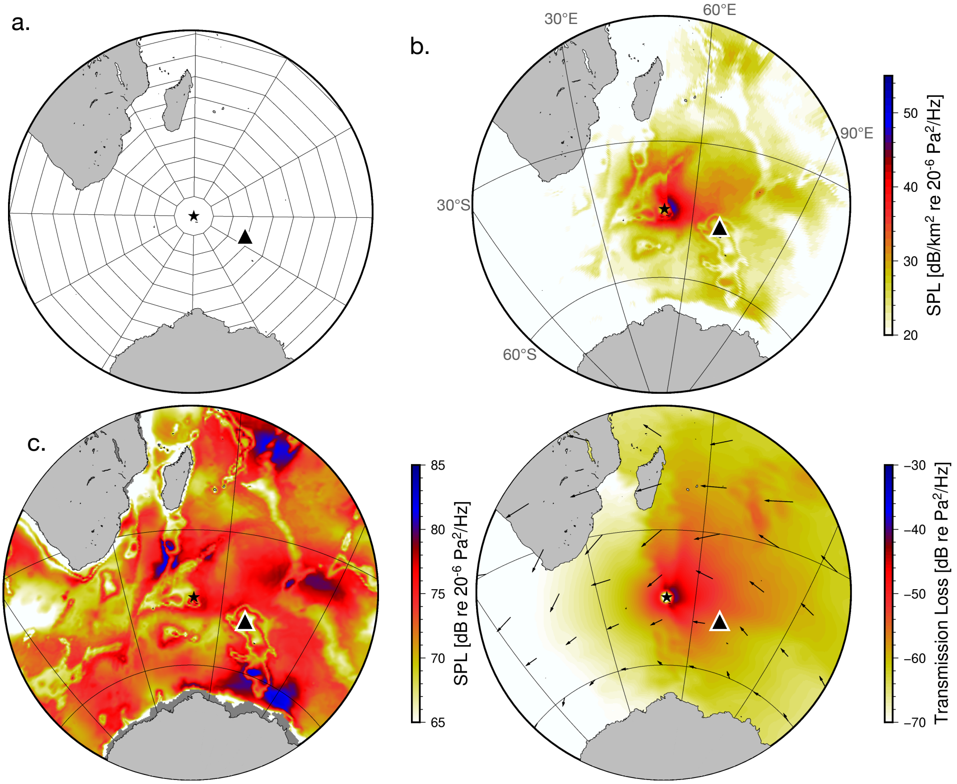

Figure 4.2: *The reconstruction of the synthetic microbarom source model integrated between 0.1-0.3 Hz for illustration. (a) The stereographic polar grid, where the star indicates the origin and so the GPS position of the INFRA-EAR on 2020-01-19T14:00 UTC. (b) The reconstructed acoustic power per area in the surrounding of the INFRA-EAR. (c) The microbarom source model according Waxler* et al. *[2007], implemented by Smets and Evers [2014*a*] using the ERA5 HRES 2DFD reanalysis. (d) The transmission loss, following Le Pichon* et al. *[2012] and Tailpied* et al. *[2016], from every grid cell towards the sensors GPS position, using the ERA5 HRES reanalysis. The vectors indicate the wind direction and speed. The triangle indicates the location of I23FR at Kerguelen Islands. Similar analysis has been performed for I23FR, by positioning the infrasound array as origin of the sterographic polar grid.*

4.3 Microbarom infra-soundscape reconstruction

The most omnipresent infrasound sources are deep oceanic microbaroms, for which several source models have been published in literature [Brekovskikh, 1973; Waxler *et al.*, 2007; De Carlo *et al.*, 2020*a*]. From the order expansion of the equations of fluid mechanics [Waxler and Gilbert, 2006], it follows that the acoustic response of microbaroms can be described with an evanescent and propagating component.

These components are derived from the sea state ($\xi(x,t)$ at position x at time t), describing the excitement and energy within the ocean due to surface winds. The sea state is expressed as a slowly varying two-dimensional stochastic wave variance spectrum F_w:

$$\xi(r,t) = F_w(f_w, \phi_w) \tag{4.3.1}$$

where f_w indicates the ocean wave frequency, and ϕ_w the direction, F_w describes the distribution of the wave variance for a steady-state by superposition of linear waves over different frequencies and directions. The Hasselman integral [Hasselmann, 1963] is related to this spectrum and is defined by the superposition of linear waves to the statistical density spectrum of ideal counter-propagating ocean surface waves by:

$$\mathcal{H}(f_w) = \int_0^{2\pi} F(f_w, \phi_w) F(f_w, \phi_w - \pi) d\phi_w \tag{4.3.2}$$

This vibrating interface acts as a membrane, causing a velocity potential inducing a pressure oscillation near this interface. Acoustic energy is radiated into the ocean, propagating through the water column and outwards into the atmosphere. Interference between the downward and upward propagation of signals within the water column may lead to resonance. The resonance terms within the water column for the finite ocean depths are described by the coefficients A, B, and C:

$$\begin{aligned} A &= \mathcal{R}^2 \cos^2(\phi_w) + \sin^2(\phi_w) \\ B &= \cos^2(\phi_w) + \mathcal{R}^2 \sin^2(\phi_w) \\ C &= (1-\mathcal{R}^2)\sin(\phi_w)\cos(\phi_w) \end{aligned} \quad .$$

with $\mathcal{R} = (\rho_w c_w)/(\rho_b c_b)$, which is reflection coefficient obtained from the continuity of pressure between water (w) and the solid sea floor (b). ρ and c are the density and speed of sound within the ocean (w) and bedrock (b). Whenever $\mathcal{R} = 1$, such that the resonance terms become $A/B = 1$ and $C = 0$, the microbarom source model assumes an infinitely deep ocean. The water column's resonance depends on the acoustic wavelength λ_w and the ocean depth D_{bath} (bathymetry), assuming microbaroms radiate on a direct path between the surface and solid seafloor without spreading. The amount of interference patterns depends on the phase difference $\phi_w = 2\pi D_{\text{bath}}/\lambda_w$ between the signals. Vertical resonance occurs when $D_{\text{bath}}/\lambda_w = 1/4 + n/2$ for any integer n [Smets, 2018].

The evanescent microbaroms directly correspond to a travelling ocean surface wave. Indifferent of the ocean depth nor bathymetry. This evanescent component does not radiate and decays vertically [Waxler and Gilbert, 2006; Hetzer *et al.*, 2010], and can only be resolved directly above the source area. The propagating microbaroms are a result of the standing surface wave [Longuet-Higgins, 1950; Hasselmann, 1963] and depends on the ocean depth and bathymetry [Brekovskikh, 1973; Waxler *et al.*, 2007]. This propagating component does radiate, propagates over large distances, and is measured at distant ground-based infrasound arrays. The monitored microbarom spectrum by the IMS typically peak around 0.2 Hz [Campus and Christie, 2010], which are the propagating microbaroms. The sea state producing these signals peaks at 0.1 Hz [Waxler and Gilbert, 2006], as the evanescent component.

For the construction of both microbarom signals, the ECMWF ERA5 HRES ocean wave model has been used (2DFD), consisting of 30 steps for frequency and 24 for direction, respectively. This 2DFD reanalysis is coupled to the atmosphere model, which allows interaction between the ocean waves and the surface winds [Haiden *et al.*, 2018]. This 2DFD reanalysis has an hourly output, with a spatial resolution of 0.36°.

■ 4.3.1 Integrating microbarom source power

Evanescent microbaroms are detectable directly above the source, whereas the propagating microbaroms are detectable over long ranges. The total acoustic power is a summation of all-acoustic contributions. It is computed by integrating the computed acoustic intensities over the ocean surface [Pierce, 2019], convolved with the transfer function quantifying the propagation losses and propagation time.

$$\begin{aligned}\mathcal{P}_{av}(f,t_{\text{obs}},x_r) &= \sum_i \mathcal{P}_{av,i}(f,t_{\text{obs}},x_r)\\ &= \underbrace{\iint_{S_r} \mathcal{P}_1(f,t_{\text{obs}},x_r)dS_r}_{\text{Evanescent microbaroms}}\\ &\quad+\underbrace{\sum_i \iint_{S_i} \mathcal{P}_2(f,t_0(\tau),x_s)\times G_p(f,t_{\text{obs}}-\tau,x_s,x_r)dS_i}_{\text{Propagating microbaroms}}\end{aligned} \tag{4.3.3}$$

In Equation 4.3.3, $\mathcal{P}_{av}$ is the average acoustic power over frequency f received at t_{obs} and receiver position x_r, which has radiated from the area S_i, which encloses the ith sound source. $\mathcal{P}_{av}$ can be subdivided into an evanescent ($\mathcal{P}_1$) and propagating component ($\mathcal{P}_2$). The source area of the evanescent component (S_r) is derived within section 4.1. The propagation factor of the second-order component is presented by G_p, which describes the attenuation function and the propagation time (τ) between source (t_0, x_s) and receiver (t_{obs}, x_r). This integration holds when the total surface S encloses the entire collection of individual surfaces from sources S_i. Note that the value of $\mathcal{P}_{av,i}$ is construed to be dependent on the strength of other nearby sources. These assumptions apply if the source is multiple wavelengths apart from the other sources within S_i [Pierce, 2019].

■ 4.3.2 Evanescent microbaroms

It has been theorized that the evanescent microbaroms are detectable by measurements just above the source region. Such measurements are limited [Bowman and Lees, 2018], and do not mention nor adjudge evanescent microbaroms. The amplitude of the received evanescent microbaroms depends on the initial amplitude and the vertical decay between source and receiver.

Source model

The acoustic power of the evanescent microbaroms has been derived by Waxler and Gilbert [2006] as:

$$\mathcal{P}_1(f_a) \sim \rho_a c_a^2 \frac{2\pi f_{p0}^2}{k_{p0} c_a} \frac{2\pi f_0 \overline{F}_w(f_w)}{c_a} \tag{4.3.4}$$

where a and w represents the media of propagation (i.e., the atmosphere (a) and water(w)). $\overline{F}_w$ is the integral of F_w over all direction, resulting in the sea mean energy spectrum. k_{p0} represents the wavenumber at the peak frequency f_{p0} of the spectrum.

Vertical decay

The energy of evanescent microbaroms decays vertically [Waxler and Gilbert, 2006]. Therefore this acoustic component is negligible outside its source region. The attenuation is rather simple and can be expressed as:

$$A(x_r, z) = e^{-k_z \cdot z} \tag{4.3.5}$$

where z indicates the receiver's altitude, and k_z the corresponding vertical wave number.

■ 4.3.3 Propagating microbaroms

As outlined in Equation 4.3.3, the integration of the propagating microbaroms is more complex since the attenuation due to long-range propagation of distant source has to be taken into account. This is numerically implemented by spanning a local polar stereographic grid, with the sensor as the polar position (Figure 4.2-a). The computation of acoustic power, with accounted propagation effects, has been interpolated over this stereographic grid. It has been weighted for the variable surface area dS, as this grows with increasing distance as a function of azimuth. Figure 4.2-b shows the corrected and interpolated microbarom source regions around the INFRA-EAR (50°E, 45°S) at 2020-01-19T14:00 UTC. This figure defines the acoustic power per area, which potentially has been recorded by the INFRA-EAR.

Source model

The propagated microbarom source model is described by Waxler *et al.* [2007] and implemented and verified by Smets and Evers [2014*a*]. This source strength model is based on the work by Longuet-Higgins [1950], Brekovskikh [1973] and Waxler and Gilbert [2006]. Waxler *et al.* [2007] describes the source regions as an isotropic source above an ocean with finite depth:

$$\mathcal{P}_2(f_a) = 4g^2\pi^4 f_a^3 \mathcal{H}(f_w) \frac{\rho_a^2}{c_a^2} \left(\frac{9g^2}{4\pi^2 c_a^2 f_a^2} + \frac{c_a^2}{c_w^2}\frac{A}{B} + \frac{3g}{2\pi c_w f_a}\frac{C}{B} \right) \tag{4.3.6}$$

where $f_a (= 2f_w)$ is the acoustic frequency. $\mathcal{H}$ indicates the Hasselman integral [Hasselmann, 1963], which describes the standing wave density spectrum. A, B, and C are the describing resonance terms within the water column for the finite ocean depths. Figure 4.2-c shows the microbarom source regions for 2020-01-19T14:00 UTC.

Long-range propagation

Infrasound can propagate over large distances facilitated by acoustic waveguides, formed between the Earth surface and atmospheric layers (Figure 4.1-a). These waveguides change with time and location. The effective sound speed approximates the combined effect of wind and temperature on infrasound propagation in a horizontally layered atmosphere (c_{eff}), which is defined as the sum of the adiabatic sound speed (c_T) and the wind in the direction of propagation [Drob, 2019]. The effective speed of sound ratio ($c_{\mathrm{eff,ratio}}$) is a practical measure to quantify favourable ground-to-ground ducting conditions. An effective sound speed ratio near to or greater than one is indicative of whether infrasound can refract back to the Earth surface.

Various methods have been developed to accurately simulate infrasound in realistic atmospheres [Waxler and Assink, 2019], such as Parabolic Equation (PE) methods. Within this study, the empirical formation by Tailpied *et al.* [2016] is used, which extends the original methodology by Le Pichon *et al.* [2012] for a range-dependent atmosphere. The empirical relation according Le Pichon *et al.* [2012] represents the average of a large number of representative PE runs and is formulated as:

$$A(x_{\mathrm{r}}, x_{\mathrm{s}}) = \frac{1}{r} 10^{\frac{\alpha(f)r}{20}} + \frac{r^{\beta(f, c_{\mathrm{eff,ratio}})}}{1 + 10^{\frac{\delta - r}{\sigma(f)}}} \tag{4.3.7}$$

where α, β, δ, and σ are the dissipation of the direct wave, the geometrical spreading and dissipation of both the stratospheric and thermospheric paths, the width of the shadow zone, and is a scaling distance controlling the strength of the attenuation in the shadow zone. Equation 4.3.7 includes both the classical and relaxation losses, which are frequency-dependent and modelled using vertical profiles of temperature, density, and the concentration of atmospheric gasses [Sutherland and Bass, 2004]. The empirical relation, which account for lateral heterogeneity [Tailpied *et al.*, 2016] between receiver position x_{r} and source x_{s} at a reference distance of 1 km, is formulated as:

$$A(x_{\mathrm{r}}, x_{\mathrm{s}}) = \prod_{i} \frac{A^{i+1}_{x_{\mathrm{r},i+1}, x_{\mathrm{s}}}}{A^{i+1}_{x_{\mathrm{r},i}, x_{\mathrm{s}}}} \tag{4.3.8}$$

Figure 4.2-d shows the transmission loss for propagation from each grid cell towards the INFRA-EAR's GPS position at 2020-01-19T14:00 UTC, integrated between 0.1-0.3 Hz for illustration. This highlights the potential source regions that can be recorded and the associated attenuation along the source-reciever path. In addition, it is shown that the propagation is effective downwind, as is illustrated by the stratospheric wind direction (vectors).

The source contributions of the microbarom model have been compensated for the attenuation along its propagation path towards the INFRA-EAR at the time of recording. However, this only describes the attenuation along the propagation path. In order to account for significant propagation times between source region and receiver, each grid cell is evaluated at the model time t_m that is nearest to the observation time t_{obs} minus the propagation time τ, i.e. $t_m = q_m(t_{\mathrm{obs}} - \tau)$, where q_m represents the rounding to the nearest model time. The simulated soundscape consists of microbarom source regions that exist throughout different hours of the day. The stratospheric propagation has been characterised by a celerity range of 0.25 to 0.31 km/s, which is directly correlated to the $C_{\mathrm{eff,\ ratio}}$. Whenever the stratospheric propagation is not feasible, thermospheric propagation is assumed with a range of 0.21 to 0.25 km/s [Evers and Haak, 2007; Assink *et al.*, 2012; Vergoz *et al.*, 2019].

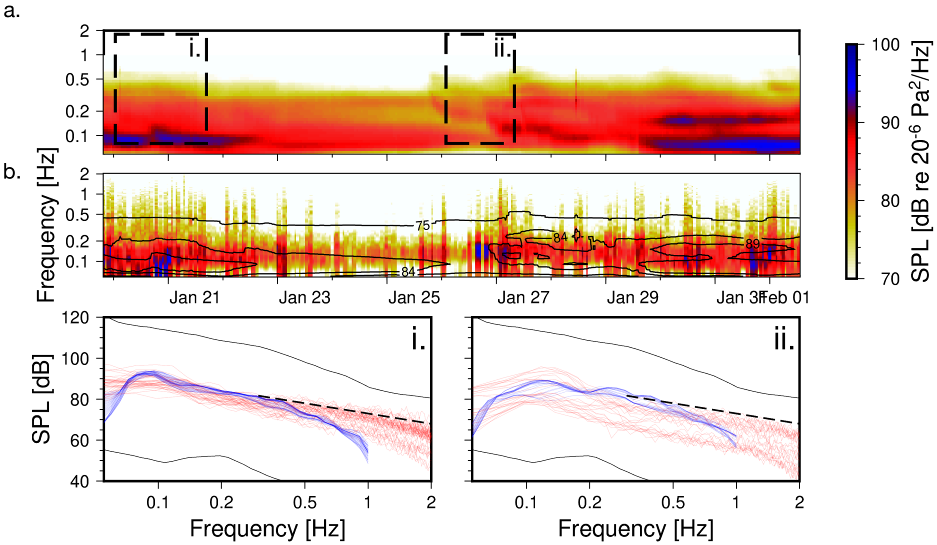

Figure 4.3: *The comparison between the synthetic microbarom spectra (a) and the recorded infrasound by the INFRA-EAR (b). Overlaying the recorded spectrograms by contour lines of the synthetics in (b) allows a visual comparison. (i) and (ii) show the PSD of the synthetic (blue) and observations (red) for a specific time. The gray lines indicate the high and low global IMS noise levels [Brown* et al.*, 2014], whereas the dotted line highlights the* $f^{-5/3}$ *slope expected for turbulence [Chunchuzov and Kulichkov, 2019].*

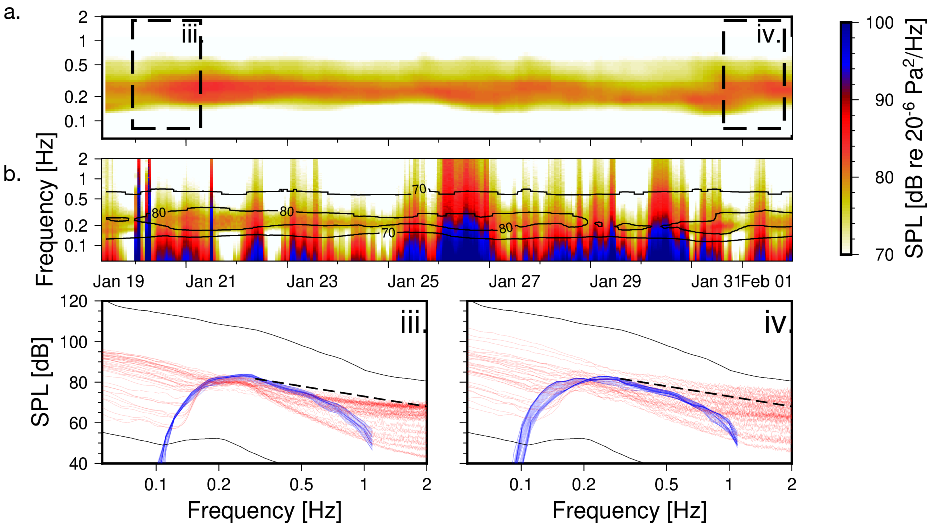

Figure 4.4: *The comparison between the synthetic microbarom spectra (a) and the recorded infrasound by I23FR (b). Overlaying the recorded spectrograms by contour lines of the synthetics in (b) allows a visual comparison. (iii), and (iv) show the PSD of the synthetic (blue) and observations (red) for a specific time. The gray lines indicate the high and low global IMS noise levels [Brown* et al.*, 2014], whereas the dotted line highlights the* $f^{-5/3}$ *slope expected for turbulence [Chunchuzov and Kulichkov, 2019].*

4.4 Comparison of in-situ observations and soundscapes

The route of the INFRA-EAR, as mounted on an albatross, has been simulated using the method outlined in section 4.3 to compare model and observations. The measurement of the INFRA-EAR occurs directly above the sea surface ($\sim$ 5 m [Richardson *et al.*, 2018]). Therefore, a synthetic sound spectrum has been created to obtain a spectrogram for each frequency within the evanescent and propagating microbarom model. Figure 4.3-a shows the synthetic spectrogram for the INFRA-EAR, while 4.3-b shows the recorded spectrogram by the INFRA-EAR. For the same period, the analysis has been performed on I23FR, a distant ($\sim$ 1500 km) ground-based infrasound array (e.g.,Green *et al.* [2012], Figure 4.4-a and -b). The synthetic spectrograms' contour lines are plotted over the recorded spectrograms for comparison. The panels below the spectrograms highlight specific recording periods and directly compare the observed (red) and synthetic spectra (blue). The microbarom spectral information of recordings and observations are found to be in close agreement. The structure of the overlayed contour lines in panel 4.3-b and 4.4-b are in agreement with the recorded data. It should be reminded that I23FR is a ground-based array and thus only records propagating microbaroms. The INFRA-EAR, however, can observe both the evanescent and the propagating microbaroms, explaining the low-frequency contents down to 0.1 Hz.

Figure 4.5-a and 4.6-a show the integrated acoustic power summation (eq. 4.3.3) between 0.1-0.3 Hz for the INFRA-EAR's and I23FR's synthetic and recorded spectra. The integrated amplitudes of the observations (red) align with the integrated total acoustic power summation of the synthetic microbarom model (black). Based on the mean absolute error (MAE) and bias between the model and observations, the relative frequency (RF) for which the bias is below the MAE, is 2.7 dB for 85% of the INFRA-EAR recording. The computation shows that the near- evanescent component needs to be taken into account for the INFRA-EAR and not for I23FR.

Figure 4.5-b and 4.6-b shows the statistical reconstruction of the total acoustic power summation over the stereographic polar grid. The percentile of total power has been determined as a function of distance away from the INFRA-EAR and I23FR, respectively. Furthermore, it suggests that 95% of the microbarom source field contributes up to 2000 km from the INFRA-EAR's recording. Source contributions from outside this region are minimal. Since the reconstruction around an infrasound sensor depends critically on the characteristics of the microbarom source model and propagation conditions, it is expected that the size of the contributing source region will vary as a function of geographical location and time. For example, array-specific cumulative probability distributions could be constructed for global IMS infrasound arrays to quantify the array's microbarom exposure and hence the noise levels.

4.4.1 The influence of flight-height on the evanescent contribution

The contribution of the evanescent microbaroms is computed by following section 4.3.2. This study assumes that the INFRA-EAR's observations occur at a constant altitude (z) of 1 meter above the sea surface. The scaling of the evanescent source region is done by assuming a cone structure beneath the INFRA-EAR, a three-dimensional geometric shape. Thanks to a pre-determined flight height and a constant receiving angle (15°), the cone presents a two-dimensional circle at the air-ocean interface. This projected circle is used to scale the evanescent source region. Moreover, the flight height influences the decay of the evanescent wave field. As a result, the vertical decay of the evanescent microbaroms is exponential.

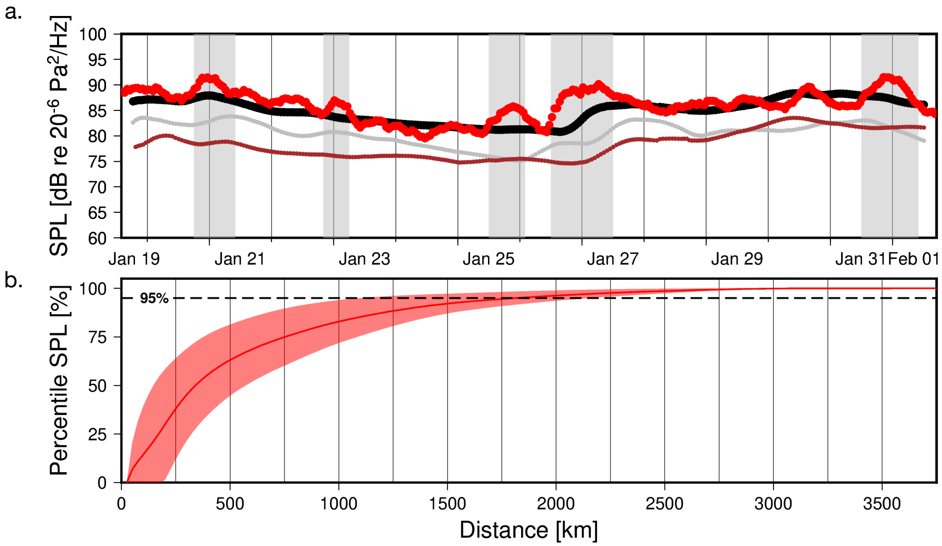

Figure 4.5: *(a) The total acoustic power summation of the reconstructed microbarom source model (black) integrated between 0.1-0.3 Hz and the measured infrasound by the INFRA-EAR (a, red). The total power can be divided into an evanescent (grey line) and propagating (brown line) microbarom contribution. The grey areas indicate periods when the recorded power spectra follow the* $f^{-5/3}$ *slope. (b) The cumulative probability of the percentile SPL per distance from the receiver.*

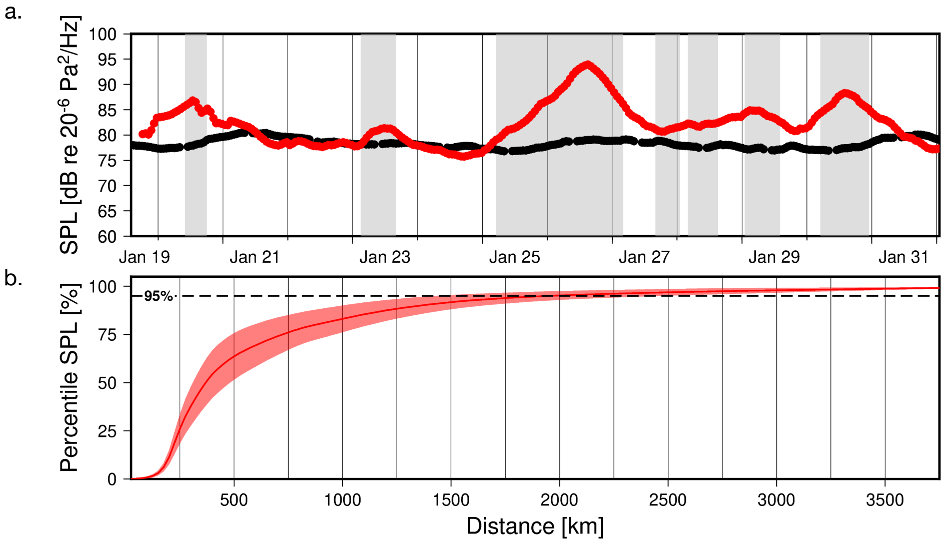

Figure 4.6: *(a) The total acoustic power summation of the reconstructed microbarom source model (black) integrated between 0.1-0.3 Hz and the measured infrasound by I23FR (a, red). The grey areas indicate periods when the recorded power spectra follow the* $f^{-5/3}$ *slope. (b) The cumulative probability of the percentile SPL per distance from the receiver.*

■ 4.4.2 The INFRA-EAR measuring the evanescent and propagating microbaroms

Without prior knowledge, one would expect that a double-peaked spectrum, indicating evanescent and propagating microbaroms, would be visible in the INFRA-EAR PSD. The evanescent and propagating microbaroms occur concurrently and have overlapping frequency ranges. Naming and handling both within the analysis and paper are essential for the understanding of the infrasonic wavefield. The albatrosses fly one meter above the sea surface. Therefore the evanescent component is most dominant and partially masks the propagating microbaroms, particularly near the low-frequency end (0.2 Hz and below). Whenever the bird increases its altitude relative to the sea surface, the dominance of the evanescent microbaroms decreases and the propagating microbaroms become more dominant/visible.

An analysis has been performed by comparing the modeled evanescent and propagating spectra with the recordings. Figure 4.7 shows this PSD analysis. From this figure, it becomes clear that both microbarom contributions have overlap within the range of 0.1-0.3 Hz. Below 0.2 Hz, the evanescent microbarom component is dominant when after the propagating microbarom component takes over.

A statistical comparison has been made between both modeled components of the microbarom wavefield and the observed SPL. This detailed comparison further supports our claim that the INFRA-EAR detects both fields in partly overlapping frequency bands. In line with Figure 4.5, the INFRA-EAR recordings have been integrated between 0.05-0.15 Hz, 0.1-0.2 Hz, and 0.2-0.3 Hz compared to the same frequency range of the modeled SPL. Figure 4.8-a shows in grey the outcome of the evanescent SPL between 0.05-0.15 Hz. The red line shows the integrated INFRA-EAR SPL over the same frequency range. Panel (b) shows the comparison between integrated SPL of 0.1-0.2 Hz, which is a combination of evanescent (grey line) and propagating (brown line) microbaroms. At the same time, panel (c) shows the comparison between INFRA-EAR (red) and propagating microbaroms (brown), integrated between 0.2-0.3 Hz.

Note within Figure 4.8 the close agreement between the modeled and actual SPL from the INFRA-EAR recordings. The SPL difference between modelled microbaroms and the INFRA-EAR recordings is 3 dB for 80%, 85%, and 79% of the time, for the frequency bands considered in panels (a), (b) and (c). In addition, note that the SPL levels of the INFRA-EAR, as well the modelled SPL, decreases with increasing frequency range.

Although one would expect a double-peaked spectrum, the PSDs from the INFRA-EAR recordings show overlapping energy. The evanescent microbaroms are the most dominant contribution. However, the modelled PSDs (of the combined total acoustic power) also show a broad PSD instead of a double-peaked spectrum (Figure 4.7-e). Thanks to this analysis, and the statistical comparison between modelled microbarom contributions and the INFRA-EAR, it can be concluded that the INFRA-EAR indeed records both microbarom contributions.

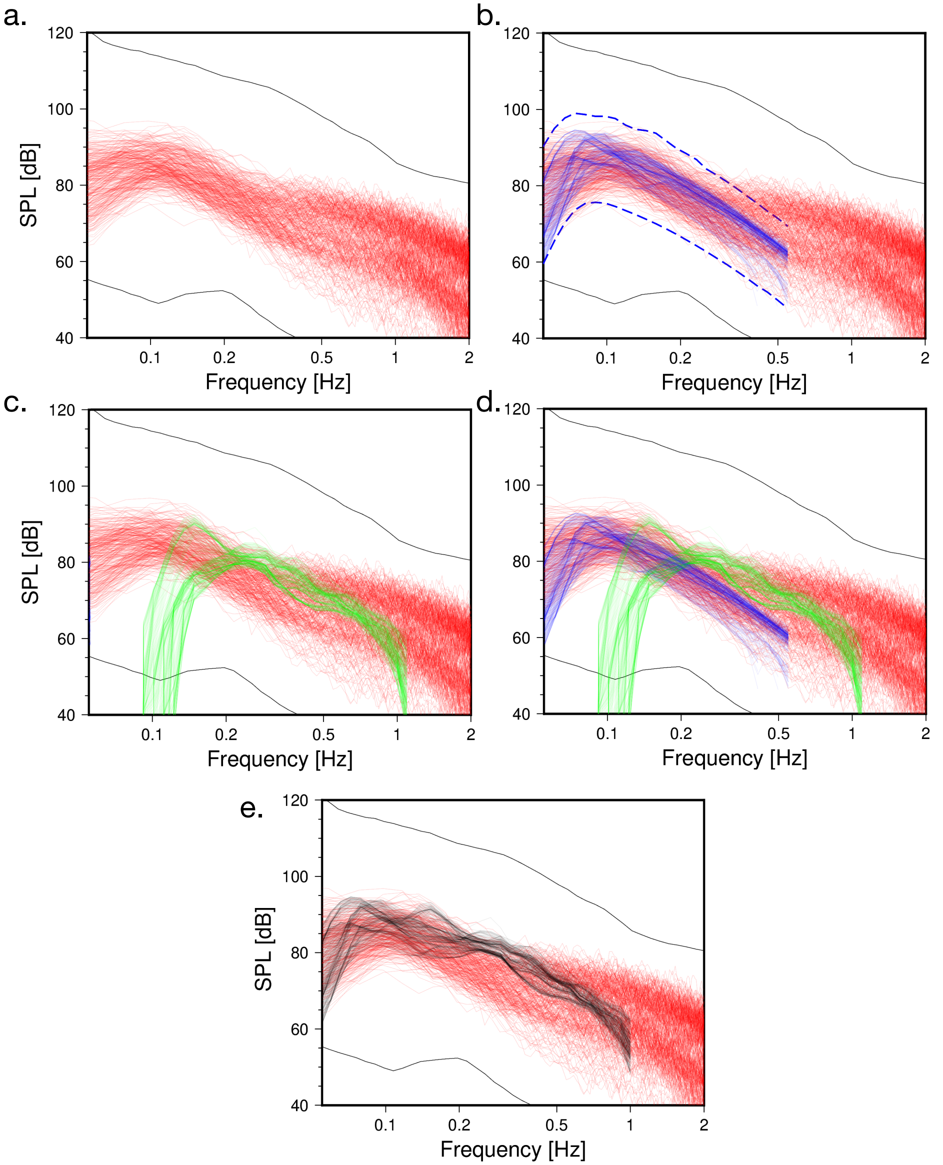

Figure 4.7: *The PSD's of the INFRA-EAR recordings (a) in red, and the global ambient high and low noise curves in gray [Brown* et al.*, 2014]. (b) shows in blue the evanescent microbaroms' contribution on a constant fly height of 1m above the sea surface (section 4.3.2). The blue dotted lines indicate the expected SPL for flight heights off 0.01m and 5m Richardson* et al. *[2018]. (c) shows the contributions of the propagating microbaroms (section 4.3.3). (d) shows both components compared to the INFRA-EAR recordings. (e) shows the total acoustic synthetic power summation of both the evanescent and propagating microbaroms in black.*

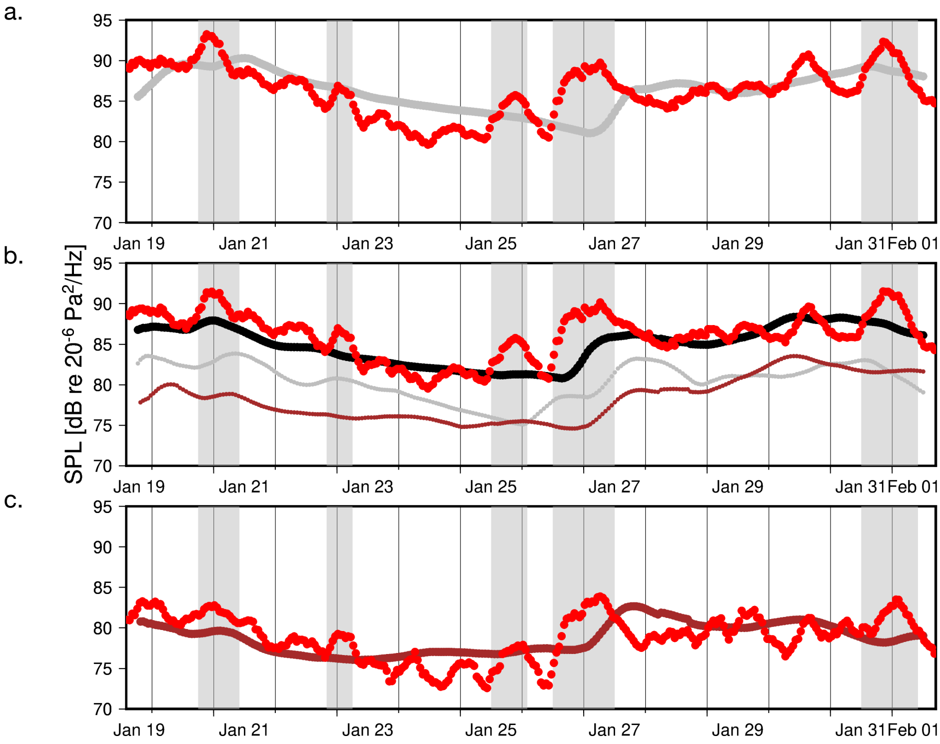

Figure 4.8: *Statistical comparison between modelled and recorded infrasonic wavefield. (a) shows in grey the outcome of the evanescent SPL between 0.05-0.15 Hz. The red line shows the integrated INFRA-EAR SPL over the same frequency range. Panel (b) shows the comparison between integrated SPL of 0.1-0.2 Hz, which is a combination of evanescent (grey line) and propagating (brown line) microbaroms. At the same time, panel (c) shows the comparison between INFRA-EAR (red) and propagating microbaroms (brown), integrated between 0.2-0.3 Hz.*

■ 4.4.3 Comparison of initial microbarom source model

The reconstruction of soundscapes (section 4.3) is modular. Equation 4.3.3 shows that any microbarom source region model, or propagation model, can be implemented within the proposed methodology. The results that have been presented so far have been based on the microbarom source region model as derived by Waxler *et al.* [2007]. This source strength model is based on the work by Longuet-Higgins [1950], Brekovskikh [1973] and Waxler and Gilbert [2006]. Waxler *et al.* [2007] describes the source regions as an isotropic source above an ocean with finite depth (Equation 4.3.6), whereas other source models assume an infinite ocean depth [Waxler and Gilbert, 2006; De Carlo *et al.*, 2020*a*].

Previous studies have addressed the usage of bathymetry features within the derivation of the initial propagating microbarom source region model [Waxler *et al.*, 2007; Smets and Evers, 2014*a*; De Carlo *et al.*, 2020*a*]. A recent study by De Carlo has demonstrated that the influence of bathymetry on microbarom source strength depends on the acoustic radiation angle. In particular, it was shown that the influence strongly increases with increasing angle. For near-horizontal radiation angles that are relevant for long-range waveguide propagation, the effects of bathymetry can be neglected [De Carlo *et al.*, 2020*a*].

Figure 4.9 shows the spectral and integrated comparison of the reconstructed propagating microbaroms by implementing Waxler and Gilbert [2006] and Waxler *et al.* [2007] during the period of recording by the INFRA-EAR (Figure 4.1). Also, the effects of bathymetry do not play any role in the theoretical model of evanescent microbaroms. From a visual comparison, it stands out that the spectrograms are similar. However, the spectrogram by Waxler *et al.* [2007] shows that the spectral content is broader and the SPL levels are slightly higher. In particular, a peak around 0.15 Hz around 30 January 2020 can be noted. Panel (c) shows the SPL of the integrated spectrograms between 0.2-0.35 Hz. The integrated SPLs make it clear that the difference between both microbarom source region models is ±2dB.

A similar comparison has been performed for I23FR. Figure 4.10 shows the comparison between both source models for I23FR. Contrary to Figure 4.9, both source models do not show a change in spectral content. The statistical difference of the integrated spectra between 0.2-0.35 Hz is ±0.22dB.

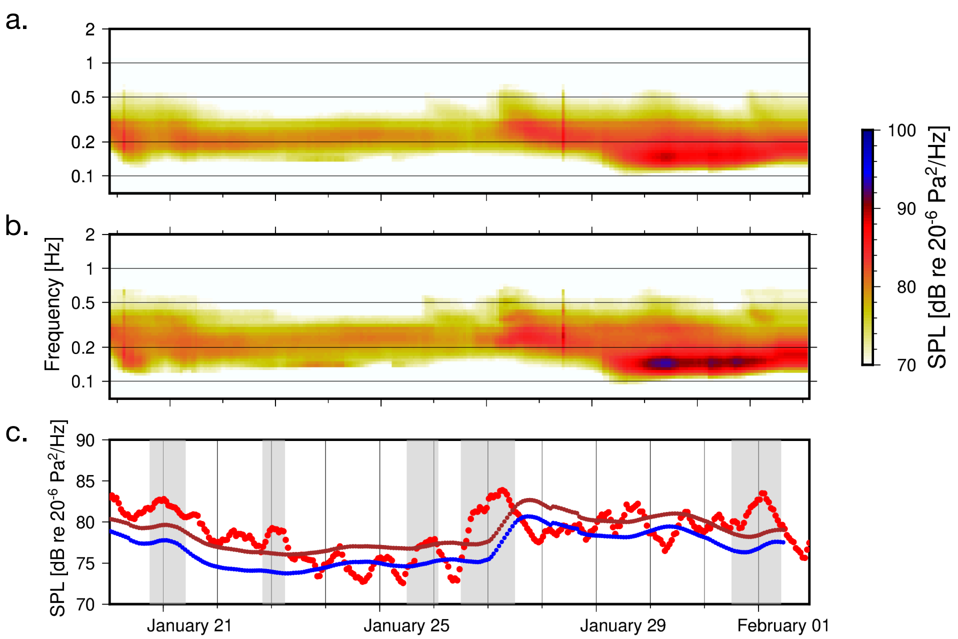

Figure 4.9: *Spectral comparison between the microbarom soundscape spectra with the initial source model as derived by Waxler and Gilbert [2006] (a) and Waxler* et al. *[2007] (b). (c) The total acoustic power summation of the reconstructed microbarom source model integrated between 0.2-0.35 Hz. The blue line indicates the integration of panel (a), the brown line the integration of panel (b), the recorded propagated microbarom component by the INFRA-EAR (red line) is added for visual comparison.*

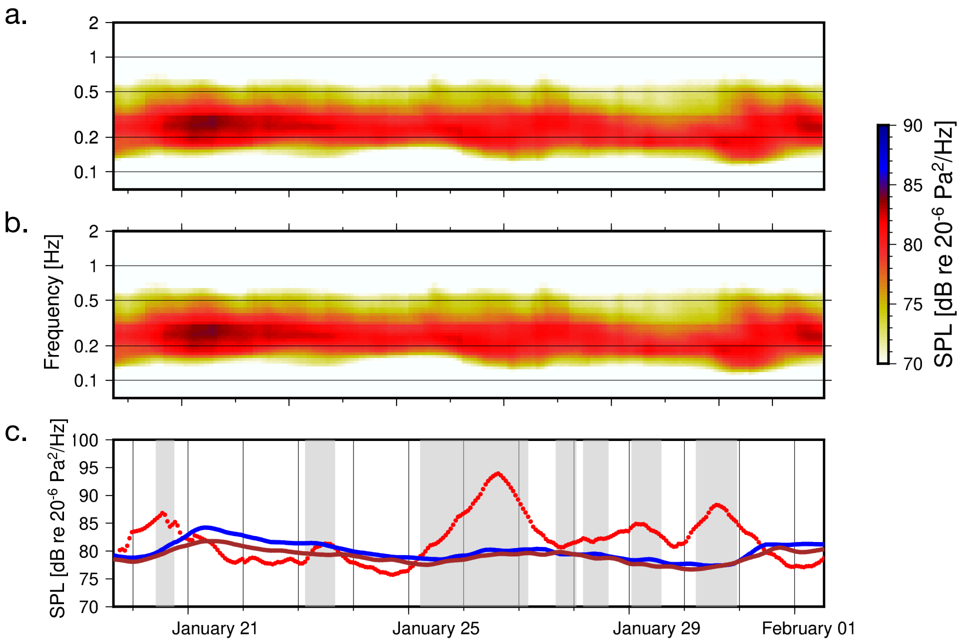

Figure 4.10: *Spectral comparison between the microbarom soundscape spectra with the initial source model as derived by Waxler and Gilbert [2006] (a) and Waxler* et al. *[2007] (b). (c) The total acoustic power summation of the reconstructed microbarom source model integrated between 0.2-0.35 Hz. The blue line indicates the integration of panel (a), the brown line the integration of panel (b), the recorded propagated microbarom component by the I23FR (red line) is added for visual comparison.*

4.4.4 Spatial frequency analysis

The reconstructed soundscapes are generated from an initial 2DFD file that contains 30 frequency steps. The soundscapes can therefore be used for spectral analysis of the source regions. From Figures 4.9 it was shown that there is a frequency and amplitude difference when implementing Waxler and Gilbert [2006] (infinite ocean depth) or Waxler *et al.* [2007] (finite ocean depth, including bathymetric features).

Figure 4.11 shows the spatial frequency and SPL analysis of the reconstructed soundscapes from the perspective of the INFRA-EAR on 30-01-2020. Both soundscapes are reconstructed by applying Waxler and Gilbert [2006] and Waxler *et al.* [2007]. Panels (a) and (b) show the spatial frequency analysis. Within both panels, the bathymetry features [GEBCO, 2020] are highlighted by the gray contour lines. Note in panel (b) that the center frequencies of the microbarom source are clustered around those bathymetric features. Panels (c) and (d) highlight the corresponding sound pressure levels, respectively, to the panels (a) and (b). It stands out that the microbarom source regions cluster around bathymetry. Furthermore, there is an amplitude increase around these features.

A similar analysis has been performed from the perspective of I23FR (Figure 4.12). The center frequencies of the soundscapes are again clustered around bathymetric features. In addition, it is shown that the SPL is as well clustering around bathymetry. Nevertheless, I23FR is a distant infrasound array, which causes a negligible difference in SPL around the bathymetry source regions, which explains the spectrograms of Figure 4.10.

Although the spectral and integrated comparison for I23FR (Figure 4.10) show minor differences between both microbarom source region models, the variance between both reconstruction models for the INFRA-EAR is notable (Figure 4.9). Such observations are expected and in agreement with the conclusions by De Carlo *et al.* [2020*a*]. The spatial comparison of the reconstructed soundscapes with different source models, however, shows remarkable differences (Figure 4.11 and 4.12). The source intensities appear to cluster around bathymetry features. Soundscapes enable to analyse the omnidirectional source intensities in the vicinity of an infrasound sensor. Such an analysis includes a spatial interpretation of the potential microbarom source regions.

The input for the initial microbarom source region model [Waxler and Gilbert, 2006; Waxler *et al.*, 2007; De Carlo *et al.*, 2020*a*] is the 2D wave-direction spectrum (2DFD) that is forecasted by ECMWF's Wave Action Model. The 2DFD describes the sea-state as a function of direction and frequency. Although it has been mentioned explicitly that Waxler *et al.* [2007] assumes a finite ocean depth in the calculation of the microbarom source regions, other models assume this as well unintentionally. The ocean wave model (WAM) describes the sea-state of the ocean. The bathymetry directly influences the ocean in the generating of swell and travelling surface waves. The WAM output therefore depends on bathymetry, which clarifies the overlap between microbarom source regions between both models. Assuming a finite ocean in calculating resonances within the water column (Equation 4.3.6) highlights and intensifies the SPLs around bathymetry features.

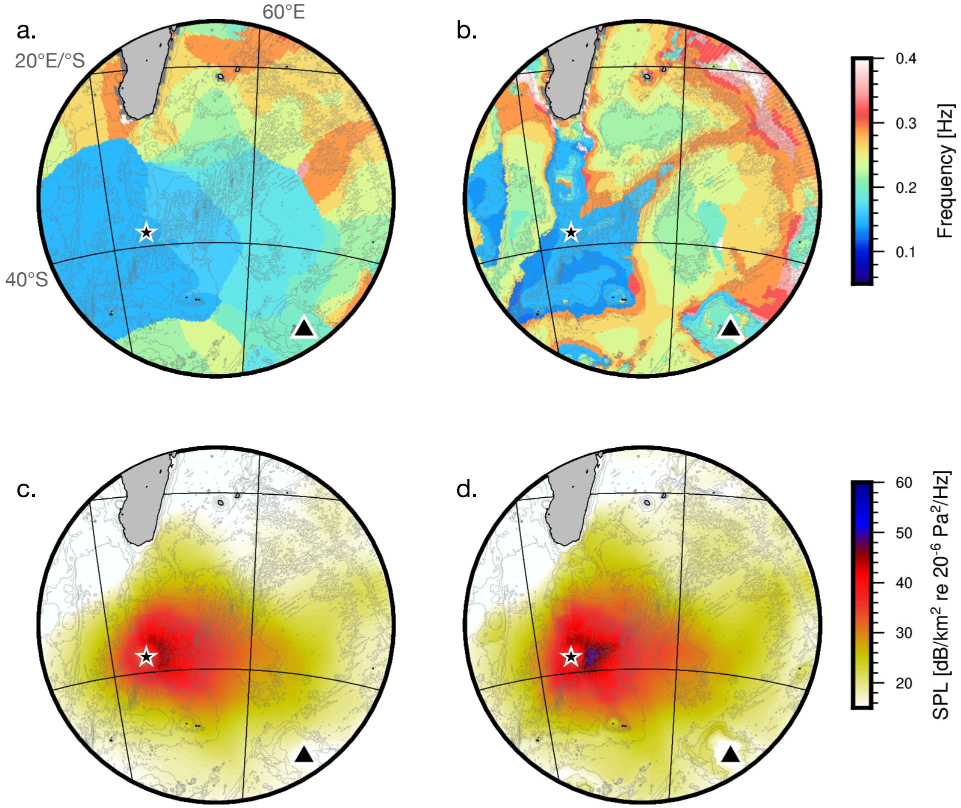

Figure 4.11: *The spatial frequency analysis based on the initial source models of Waxler and Gilbert [2006] (a) and Waxler* et al. *[2007] (b) from the perspective of the INFRA-EAR (star). (c) and (d) indicate the corresponding SPL analysis of both models, respectively.*

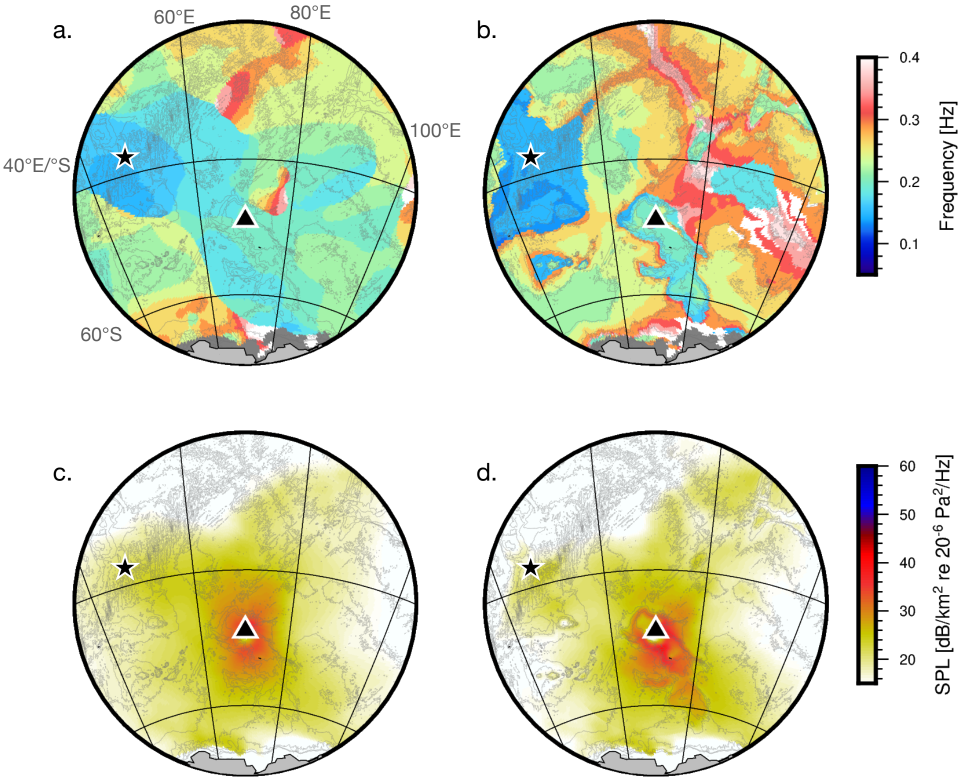

Figure 4.12: *The spatial frequency analysis based on the initial source models of Waxler and Gilbert [2006] (a) and Waxler* et al. *[2007] (b) from the perspective of I23FR (triangle). (c) and (d) indicate the corresponding SPL analysis of both models, respectively.*

4.5 Discussion and conclusion

In this chapter, a method has been introduced for the reconstruction of microbarom soundscapes. This method accounts for evanescent and propagating microbaroms of multiple source contributions in an infrasound sensor's vicinity. The method generates synthetic spectra in absolute numbers, which agree with infrasound recordings by a mobile logger deployed in the middle of the Southern Ocean and a distant IMS infrasound array. The presented soundscapes rely on several approximations related to (1) the source model and (2) the assumptions made in the propagation modelling. However, the methodology is modular and allows plugging in different microbarom models, ocean wave models, and propagation models.

The microbaroms source region model, evanescent and propagating microbaroms, as described by Waxler and Gilbert [2006]; Waxler *et al.* [2007] has been used within this study as source intensity input for the reconstructed soundscapes and has been computed using the ERA5 WAM model of the ECMWF. Recently, De Carlo *et al.* [2020*a*] have studied the propagating microbarom source radiation pattern. This work concluded that including finite-depth ocean effects in the model is especially relevant for near-vertical propagation [Brekovskikh, 1973]. Here, synthetic soundscapes are compared with in-situ measurements of the INFRA-EAR, which record both the evanescent and propagating microbaroms. It is therefore relevant to account for the near-vertical propagation of the propagating microbaroms (Figure 4.9). The source model by Waxler *et al.* [2007] includes these effects and is therefore used within this study. The effect of near-vertical propagation does not apply to distant ground-based IMS arrays (Figure 4.10). Nevertheless, the spatial interpretation of the potential microbarom source regions (Figure 4.11 and 4.12) show that both the center frequencies and SPL are clustering around bathymetry features.

Furthermore, the assumptions made in the propagation model influence the soundscapes. The empirical formulation of sound propagation by Tailpied *et al.* [2016], and Le Pichon *et al.* [2012], is modelled along the great circle path from source to the receiver only, neglecting out-of-plane propagation effects. This model can be used to approximate propagation losses in atmospheres with a dual (stratospheric-thermospheric) duct and neglects tropospheric ducting. A different approach could involve using a 3-D ray-theory model cast in spherical coordinates [Smets, 2018; Blom, 2019], to quantify propagation losses. The use of formal propagation models requires atmospheric specifications from the ground to the upper atmosphere. As upper atmospheric specifications are typically limited to climatologies, this has implications for the accuracy of thermospheric returns [Assink *et al.*, 2012; Drob, 2019].

Although various assumptions have been made, the close agreement between the model and observations shown in Figures 4.3, 4.4, 4.5 and 4.6 show that the proposed methodology can be used to reconstruct the microbarom soundscape around an infrasound sensor. Both comparisons, integrated and spectral, between soundscapes and recordings show a near-perfect agreement for frequency and amplitude. For example, the agreement between the integrated soundscapes and recordings is 2.7 dB for 85% off the time (Figure 4.5). Despite the agreement, some significant differences between model and observations stand out. The measured power is sometimes higher than predicted by the soundscape. It should be recalled that the synthetic soundscapes describe the radiated microbarom power that is predicted from the modelled ocean wave spectra. It is conceivable that local noise from wind and turbulence could have affected the measurements at intervals, which cause a discrepancy between model and observation, due to higher noise levels at the receiver [Marty, 2019; Raspet *et al.*, 2019]. When comparing Figure 4.5-a with the barometric pressure measurements (Figure 4.13), it is shown there is a strong barometric pressure gradient whenever a difference occurs between the microbarom model and observation. Barometric pressure gradients are often associated to higher winds and local turbulence, i.e., higher noise conditions. Figure 4.3-i shows the INFRA-EAR's acoustic power spectra compared to the synthetic power spectra around 2020-01-21. The dotted line in the figure indicates the $f^{-5/3}$ slope, which is typical for turbulence in the atmospheric boundary layer [Gossard and Hooke, 1975; Bacmeister *et al.*, 1996; Chunchuzov and Kulichkov, 2019]. Note that the power spectra of the INFRA-EAR follow this slope from 0.2 - 1 Hz. The grey areas in Figure 4.5-a and -b indicate the periods when the recorded power spectra follow the $f^{-5/3}$ slope. When the incoherent noise levels are high due to wind, acoustic signals can be masked and remain undetected.

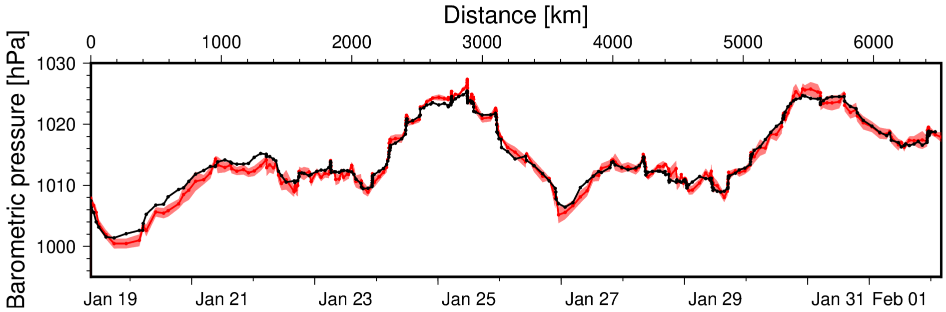

Figure 4.13: *The comparison between measured barometric pressure by the INRA-EAR (red) and the ERA5 HRES model (black) during the INFRA-EAR's trip (Figure 4.1-b).*

The presented soundscapes give insight into how much various source regions contribute to the total acoustic power measured in the microbarom band. Earlier studies have been limited to analysing normalised microbarom amplitudes, i.e. no absolute microbarom power values. Furthermore, earlier work focused on the maximum contribution of a specific region rather than considering the field to distribute multiple source contributions based on directional data processing. Nonetheless, Assink *et al.* [2014] showed that multiple spatially distributed sources within the same time segment and frequency could occur. Those can be resolved by applying high-resolution data-processing techniques (chapter 3). However, the entire microbarom source field contributes and influences the total acoustic power. The application of this reconstruction is essential in understanding the infrasonic wavefield, the ambient noise field, and for remote sensing of the atmosphere. The analysis shown in Figure 4.3 and 4.4 leads to a better understanding of microbaroms' contributions to array recordings. In conclusion, the reconstruction of microbarom spectra with absolute numbers, instead of normalised values, improves the knowledge in the global infrasonic background noise and compares infrasound array observations with model outputs. This new knowledge contributes to a better verification of the CTBT and a better applicability of infrasound as a remote sensing technique for the upper atmosphere. Moreover, only a few studies have considered evanescent microbaroms. The recordings, analysis, and comparison of the evanescent microbarom component within this study is a direct product of the sea-state and can be used by oceanographers for monitoring purposes.

5

A climatology of microbarom detections at the Kerguelen Islands

> *Nobody ever figures out what life is all about, and it doesn't matter. Explore the world. Nearly everything is really interesting if you go into it deeply enough.*
>
> Richard P. Feynman

Abstract The ambient infrasonic noise field is complex due to the interference of spatially distributed infrasound sources. Microbaroms are one of the most dominant omnipresent infrasonic sources within this wavefield. These microbaroms are generated by non-linear ocean surface wave interactions, and have a characteristic and continuous signature within the infrasound spectrum. Under noisy conditions, microbaroms can mask infrasonic signals of interest, such as infrasound from volcanoes or explosions, which limits detection and identification of such sources. This study performs an infrasonic climatology for infrasound array I23FR, using five years of data between 2015-2020. The array is located on the Kerguelen Islands, within the Southern Ocean, and is part of the International Monitoring System (IMS) for the verification of the Comprehensive Nuclear-Test-Ban Treaty (CTBT). The climatology analysis addresses the expected ambient noise levels, propagation paths, and potential sources within the vicinity of an infrasound sensor. Time and frequency domain beamforming methods have been applied to analyse the infrasonic wavefield from the I23FR observations. A recently introduced method is applied to compute so-called soundscapes, to be compared with beamform results. Although the comparison indicates a disagreement in amplitude, there is a good agreement in directionality and frequency between both.

Published as: **den Ouden, et al. 2022**, *A climatology of microbarom detections at the Kerguelen Islands: unravelling the ambient noise wavefield.* Geophysical Journal International, Volume 229, DOI: 10.1093/gji/ggab535
Note that minor changes have been introduced to make the text consistent with the other chapters.

5.1 Introduction

The atmosphere, earth and ocean are globally monitored by the International Monitoring System (IMS) for the verification of the Comprehensive Nuclear-Test-Ban Treaty (CTBT). The infrasound component of the IMS monitors the infrasonic wavefield. IMS microbarometer arrays provide real-time infrasound recordings from around the world. Therefore, the IMS has played a central role in the characterization of the global low-frequency wavefield (i.e. frequencies lower than 20 Hz) and the localization of sound sources [Campus and Christie, 2010; Marty, 2019].

Infrasound station I23FR is one of the IMS microbarometer arrays and provides real-time monitoring. The array is located at the Kerguelen Islands, which is part of the French Sub-antarctic and Antarctic lands (Figure 5.1). The microbarometer array is located on the east side of the main island and consists of 15 microbarometers, which is the largest number of elements within the IMS infrasound network [Marty, 2019]. Although I23FR continuously monitors the infrasonic wavefield on the boundary of the Indian and Southern Ocean, the array is often excluded from scientific studies due to the environmental conditions [Brown *et al.*, 2014]. The islands experience strong surface winds and severe weather conditions. Local noise conditions (e.g. wind turbulence) may mask infrasonic signals off interest [Raspet *et al.*, 2019]. Nonetheless, the IMS infrasound station density at mid-latitudes is lower for the Southern Hemisphere compared to the Northern Hemisphere. Hence, understanding the infrasonic wavefield surrounding I23FR will be important if there was ever a suspected test within the Southern Hemisphere.

I23FR is located on the Kerguelen Plateau near the Indian and Southern Ocean intersection, where various ocean currents meet. Deep oceanic ambient noise is globally the most omnipresent infrasound source. The driving force of the ambient atmospheric noise (i.e. microbaroms) is the sea state, which describes the energy of the ocean travelling surface waves. Nonlinear interaction of counter travelling ocean surface waves results in standing ocean waves, causing the radiation of acoustic energy and resonance within the water column [Longuet-Higgins, 1950; Hasselmann, 1963]. At the interfaces of the water column, acoustic energy is radiated into the atmosphere resulting in microbaroms [Brekovskikh, 1973]. Microbaroms typically peak around 0.2 Hz, with a characteristic amplitude range of 55-110 dB with respect to 20 micro-pascals [Campus and Christie, 2010]. Earlier studies have shown that the microbarom signal can be a dominant background noise signal [Donn and Rind, 1972] that can obscure signals of interest, for example volcanic eruptions [McKee *et al.*, 2021]. Microbarom signals can, therefore, potentially mask other infrasonic signals of interest. Characterizing microbaroms is essential for the understanding of the infrasonic wavefield. Knowledge regarding frequency, amplitude and propagation of the microbaroms could help assess the microbarom source contributions to the infrasonic wavefield, which adds to a better understanding of the IMS's verification capability and infrasound as a remote sensing technique for the upper atmosphere [Donn and Rind, 1972; Smets, 2018].

This study performs an infrasonic climatology for infrasound array I23FR, using five years of data between 2015-2020. Within this climatology study, various tools are combined. The analysis addresses the expected noise levels, propagation paths, and potential sources within the vicinity of the infrasound array. The analysis gives insights into the performance of an infrasound array and the ability to resolve infrasonic sources. Previous studies have introduced and applied various methods to unravel and characterize the wavefield into individual components [Landes *et al.*, 2012; Matoza *et al.*, 2013; De Carlo *et al.*, 2020*a*].

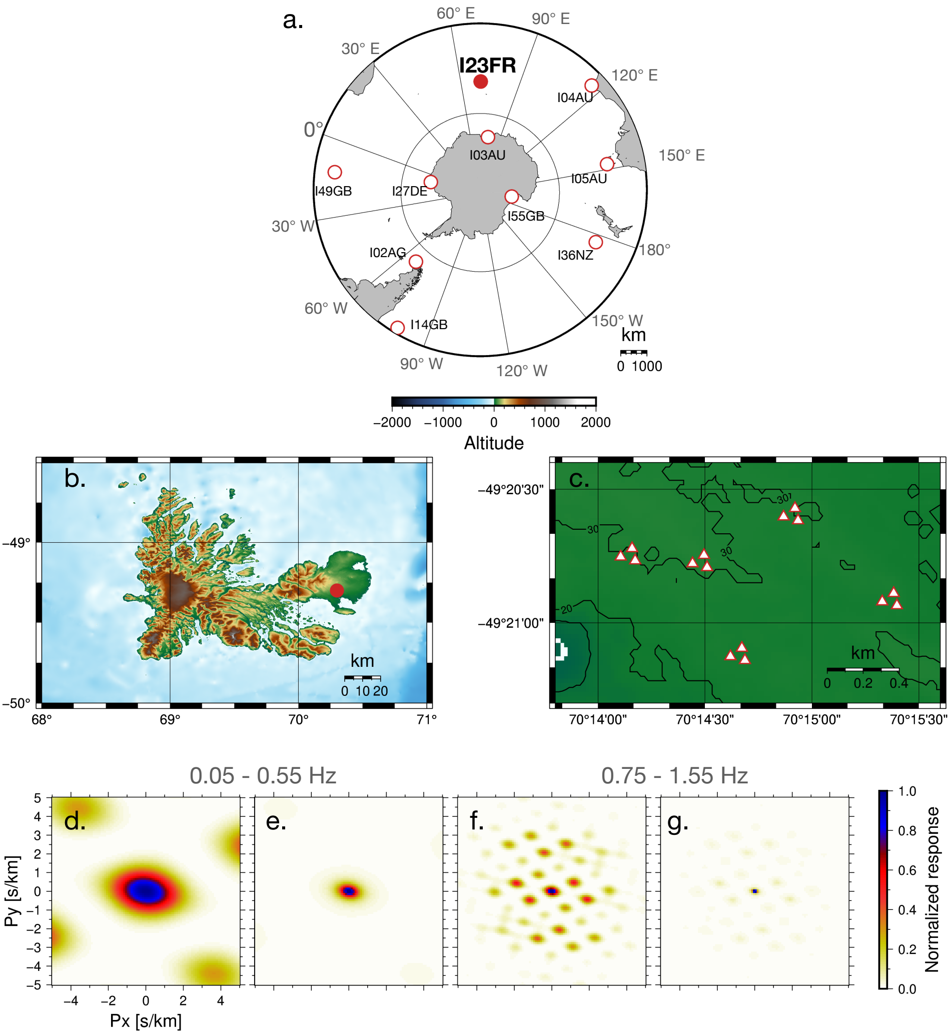

Figure 5.1: *(a) An overview of Infrasound IMS arrays in the Southern Hemisphere. The solid red dot highlight the location of I23FR at the Kerguelen Islands. (b) The main island of the Kerguelen Islands and location of the infrasound array. (c) Positions of the 15 microbarometer elements (triangles) of the I23FR array, divided into five triplets. (d) and (e) show the array response of I23FR, based on Bartlett [1948] and Capon [1969], respectively, for the frequency ranges 0.05-0.55 Hz. (f) and (g) represent the responses for the frequency range 0.75-1.55 Hz.*

The climatology study outlined within this paper is based on in-situ observations of I23FR and model data. Therefore the analysis allows for a comparison and validation of the model, which determines the reliability as a measure for the infrasonic wavefield. The in-situ observations depend on the array layout and system response of the array elements. Moreover, meteorological phenomena may influence the detection capability of an infrasound array. Meteorological data are used to determine the local noise conditions at the ground and the propagation conditions of infrasound with altitude. These observations highlight expected noise conditions and seasonality of the infrasound conditions at an array.

The in-situ infrasound observations include microbarometer array recordings to evaluate the noise levels and apply data processing techniques for separating the wavefield into a coherent and incoherent part. The model analysis covers omnidirectional infrasoundscapes, reconstructed from the perspective of the array (chapter 4). Such soundscapes provide the infrasonic sound levels in the vicinity of the array from a theoretical and model perspective. A comparison is performed to indicate the agreement between in-situ observations and model data.

The chapter is organized as follows. Section 5.2 discusses the array layout, array responses and the system response. The meteorological conditions influencing the local noise conditions and propagation conditions are reviewed in section 5.3. Within section 5.4, the infrasound observations are analysed by applying data processing techniques. Section 5.5 addresses the reconstruction of infrasonic soundscapes and the interpretation of these. The comparison between the soundscapes and the observations is described in section 5.6. The outcome of this climatology study is summarized and discussed in the final section.

5.2 Microbarometer array I23FR, Kerguelen Islands

Microbarometer arrays are used to study the infrasonic wavefield. The use of arrays allows for enhanced detection of signals in the presence of incoherent noise, as the signal-to-noise ratio (SNR) is improved by summation across the array elements. In addition, array processing enables to resolve the direction, apparent velocity and frequency content of the impinging wave front. Localization and characterization of the source depend on the source-receiver distance. Nearby sources can be distinguished as spherical wave fronts and localized by single arrays [Szuberla *et al.*, 2009; Stettner, 2018]. Distant sources, however, can be characterized by planar waves. Localization of distant sources is possible by combining various array detections through the process of cross-bearing the resolved backazimuths [Evers [2008], chapter 3].

The I23FR microbarometer array is divided into five identical triplets of $\sim$ 100 m aperture (Figure 5.1-c). The inter distance between the triplets is $\sim$ 500m, while the total aperture is $\sim$ 1750 m. The closely spaced triplet elements enhance the detection and parameter estimation at higher frequencies which may be less coherent over the entire array [Campus and Christie, 2010]. The lower frequencies of the wavefield are resolved by combining elements of the various triplets.

Atmospheric noise limits the ability to detect signals of interest due to the influence of near-surface wind close to the microbarometer. Therefore, each microbarometer array has a different detection threshold for monitoring, which varies significantly due to those local wind conditions. A vital consequence of this is that the background noise between arrays and array elements is different. This has implications for infrasound array processing [Walker and Hedlin, 2010].

The array elements at I23FR consist of (1) MB2005 microbarometers and a (2) wind noise reduction system (Figure 5.2-a) to establish theoretically similar noise conditions.

The absolute microbarometers provide a flat-to-pressure response across (and beyond) the 0.02-4 Hz passband required by the IMS specifications (Figure 5.2-b and -c). The WNRS is a 108-inlet, 36 m diameter, hexagonal pipe rosette (see Table 1 for specifications). Moreover, all inlets are covered with gravel to reduce the wind noise. The amplitude and phase responses of the I23FR WNRS were calculated, following the methodology of Gabrielson [2011] (brown lines within Figure 5.2-b and -c). The resonance peak of the WNRS is expected to be around 6.6 Hz according to citealcoverro2005design.

One of the main assumptions for data processing of the infrasonic wavefield is similar conditions at each array element [Shumway, 1971; Brachet *et al.*, 2010]. This includes a coherent sound wave front impinging the array, while each element encounters similar Gaussian-white-noise conditions. The installation of identical measurement systems theoretically secures this assumption. In reality, however, the array elements are not always similar nor experience similar noise conditions. Defects in the WNRS or different locations of array elements cause a difference in local noise conditions, which leads to variances in the outcome of the data processing techniques.

5.2.1 Microbarometer response

The infrasonic wavefield is conventionally measured with pressure transducers. Those measurements can either be performed by absolute or differential pressure sensors [Mentink and Evers [2011]; Nief *et al.* [2019]; chapter 2]. An absolute pressure sensor consists of a sealed aneroid and a measuring cavity connected to the atmosphere. A pressure difference within the measuring cavity will deflect the aneroid capsule. The mechanical deflection is converted to a voltage [Haak and De Wilde, 1996].

The IMS specifications for microbarometers state that the sensor self-noise should be at least 18 dB below the global low-noise curves at 1 Hz [Brown *et al.*, 2014], generated from global micropressure measurements using the IMS [Marty, 2019]. Typical infrasound sensor networks use analogue sensors connected to a separate data logger to convert the measured voltage differences to a digital signal. The sensor's characteristic sensitivity determines the sensor resolution, i.e., the smallest difference that the sensor can detect. The resolution of the built-in ADC converters and the digitizing voltage range determine the data logger's resolution. Current state-of-the-art data loggers have a 24-bit resolution. Advances in sensor techniques now also allow for digital outputs since the ADC conversion is realized inside the sensor [Nief *et al.* [2019]; chapter 2].

Furthermore, the IMS requires a flat-to-pressure response in the IMS passband spanning from 0.02 - 4 Hz [Marty, 2019]. The use of sensors with the flat-to-pressure-derivative response could, for example, allow better matching of typical infrasound background noise levels in the IMS frequency band. It is commonly interpreted as flat in amplitude within 3 dB with no specific requirement for the phase.

The microbarometer array elements at I23FR are MB2005 microbarometers, which are IMS certified microbarometers. The MB2005 is an absolute pressure sensor that complies with the specified IMS infrasound sensor requirements. The solid grey lines in Figure 5.2-b and -c show the amplitude and phase response of the MB2005 [Slad and Merchant, 2016].

5.2.2 Wind Noise Reduction System response

A wind noise reduction system (WNRS) is applied to each element to reduce the wind noise and to establish similar conditions at each array element. The applied WNRS is a pipe construction and exists of multiple low-impedance air inlets, which are distributed over a spatial area, and linked to the microbarometer by a network of pipes and manifolds [Marty, 2019]. Besides pipe arrays, there are various other types of windscreens, which include porous hoses and domes [Raspet *et al.*, 2019]. All WNRS filters have a characteristic response that must be considered in the design of the infrasound array. The filter response can be theoretically evaluated and is ideally flat and stable over the passband of the sensor.

The array elements of I23FR are attached to a 108-inlet, 36-meter diameter, hexagonal pipe WNRS. Moreover, all inlets are covered with gravel to reduce the wind noise. Various theoretical acoustic response models exist for the calculation of the WNRS response [Marty *et al.*, 2017]. The theoretical models derived by Alcoverro and Le Pichon [2005] and Gabrielson [2011] have a similar outcome, with a different approach. It was shown that both models could confidently be used to estimate the acoustic response of pipe arrays in the infrasound frequency band.

The specifications of the I23FR WNRS are listed in Table 5.1. The total amplitude and phase response of the applied WNRS on I23FR is calculated following Gabrielson [2011] and indicated by the solid brown lines in Figure 5.2-b and -c. The WNRS diameter and the volume of the summation cavities influence the frequency position of the first resonance peak. In contrast, the number of inlets and pipe diameter influences the amplitude of the resonance peak. The frequency position f_{WNRS} of the first resonance peak is inversely proportional to the average diameter, D_m, of the WNRS and depends on the speed of sound (c) [Alcoverro and Le Pichon, 2005]:

$$f_{\text{WNRS}} = 0.7 * \frac{c}{D_m} \tag{5.2.1}$$

Given the WNRS parameters listed in Table 5.1, the first resonance peak of the WNRS is expected to be around 6.6 Hz.

WNRS I23FR			
Length pipe$_1$	$l_1 = 10.27$ m	Diameter pipe$_1$	$a_1 = 15$ mm
Length pipe$_2$	$l_2 = 5.13$ m	Diameter pipe$_{2,3}$	$a_{2,3} = 8$ mm
Length pipe$_3$	$l_3 = 2.56$ m	Summation cavity volume	$a_2 = 1e^{-3}$ m
Length pipe to sensor	$l_s = 3$ m	Length pipe to sensor	$a_s = 8$ mm

Table 5.1: *Specifications of the WNRS system applied to I23FR.*

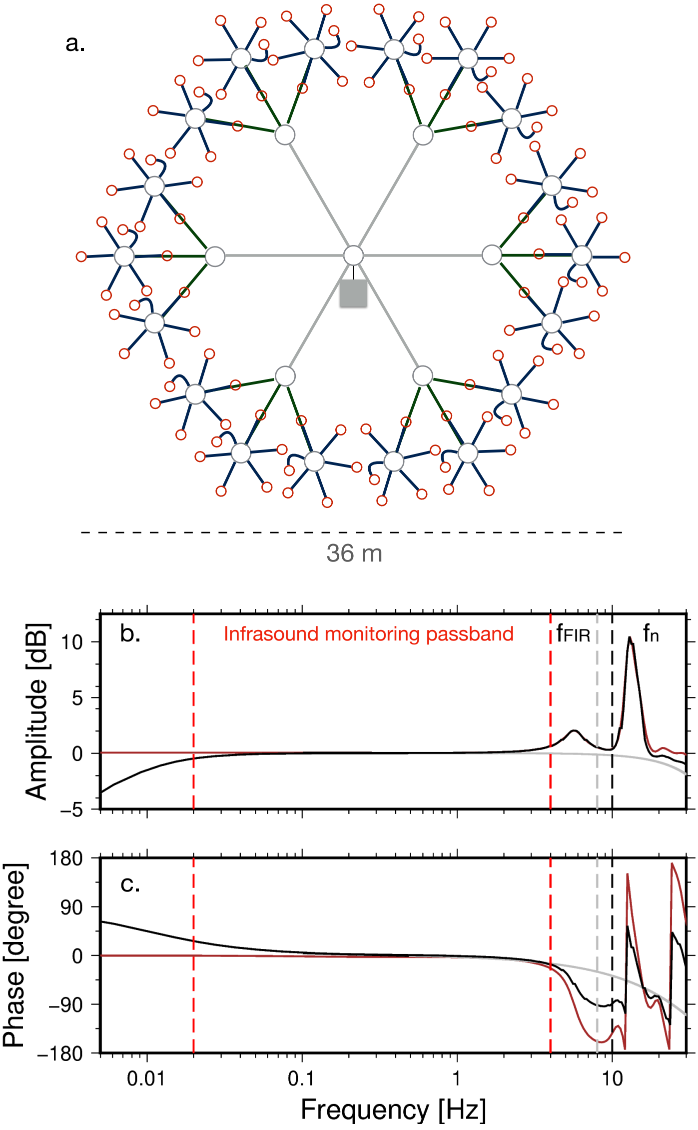

Figure 5.2: *(a) A model of the WNRS featuring 18 pipe rosettes, which is applied to all microbarometers (centre) of the I23FR array. (b) and (c) the amplitude and phase response of one array element (solid black line), which is based on the response of the microbarometer equipment (solid grey line) and the response of the WNRS (solid brown line). The red dotted lines indicate the monitoring passband for the CTBT [Marty, 2019]. The black dotted lines indicate the Nyquist frequency (fn) of I23FR, and the grey dotted lines indicate the limit above which the data should not be utilised due to the effects of the analogue-to-digital converter filters ([Sleeman et al. 2006,* f_{FIR}*).*

5.3 Meteorological conditions

The pressure spectrum of turbulence has been described statistically to decay with a slope of $f^{-5/3}$ [Gossard and Hooke, 1975]. This implies that the effect of wind noise increases towards lower frequencies [Raspet *et al.*, 2019]. Wind typically masks the background acoustic noise when turbulent processes in the lower atmosphere prevail at infrasonic frequencies. Various methods can be applied to reduce this wind-noise at infrasound arrays [Walker and Hedlin, 2010; Raspet *et al.*, 2019].

The meteorological conditions around an array give a first impression of the expected noise levels. The first element of the I23FR array includes a meteorological instrumentation to measure the horizontal wind, barometric pressure and temperature. The meteorological instruments are installed 2 m above the ground and sample at 1 Hz.

Meteo France operates and maintains a weather observation facility at a $\sim$ 1000 m distance from I2301. This facility measures the same meteorological parameters, as hourly synoptic observations (SYNOPS). The meteorological station of Meteo France is part of the Global Telecommunication System (GTS) of the World Meteorological Organization (WMO) [Panel, 2005] and provides near real-time weather information. The meteorological observations are therefore WMO certified, meaning the measurements are performed at an elevation of 10 m above the ground.

Since the Meteo France and IMS facilities are not located at the exact same geological position, and measure at different heights, a a direct comparison is not correct. However, since the IMS and Meteo France measure similar weather parameters, a comparison to conclude on the use of the IMS observations is useful. Especially since the IMS's sample rate (1 Hz) is favorable compared to hourly SYNOPS observations by Meteo France.

Besides in-situ meteorological measurements, ECMWF ERA5 atmospheric reanalysis data are used in this study. ERA5 offers a high-resolution realization (HRES) and a reduced resolution ten-member ensemble (EDA). The ERA5-HRES is available per hour and has a spatial resolution of 0.36°. The ERA5-EDA has a spatial resolution of 0.5° and a temporal resolution of 3 hr. The Southern and Indian Oceans surround Kerguelen Island. Therefore, rapid changes in atmospheric variables are expected. The ERA5 EDA is applied within this study to exclude outliers from individual ECMWF members [ECMWF, 2017].

■ 5.3.1 Analysis of Meteorological ground observations

In this section, a comparison between the three different meteorological data sets for Kerguelen Island is made over five years of data (2015-2020).

The left-hand column of Figure 5.3 shows the comparison between ERA5 and in-situ observations at I23FR. For this comparison, daily means of the meteorological data have been determined for both data sets. The middle column compares the in-situ observations measured at the Meteo France and I23FR meteorological stations. Here, hourly means have been used for comparison. The right-hand column indicates the monthly averages of the I23FR meteorological observations. The differences and standard deviations are shown in Figure 5.3 and listed in absolute values within Table 2. It stands out that there is a good agreement between the in-situ data measured by Meteo France and I23FR.

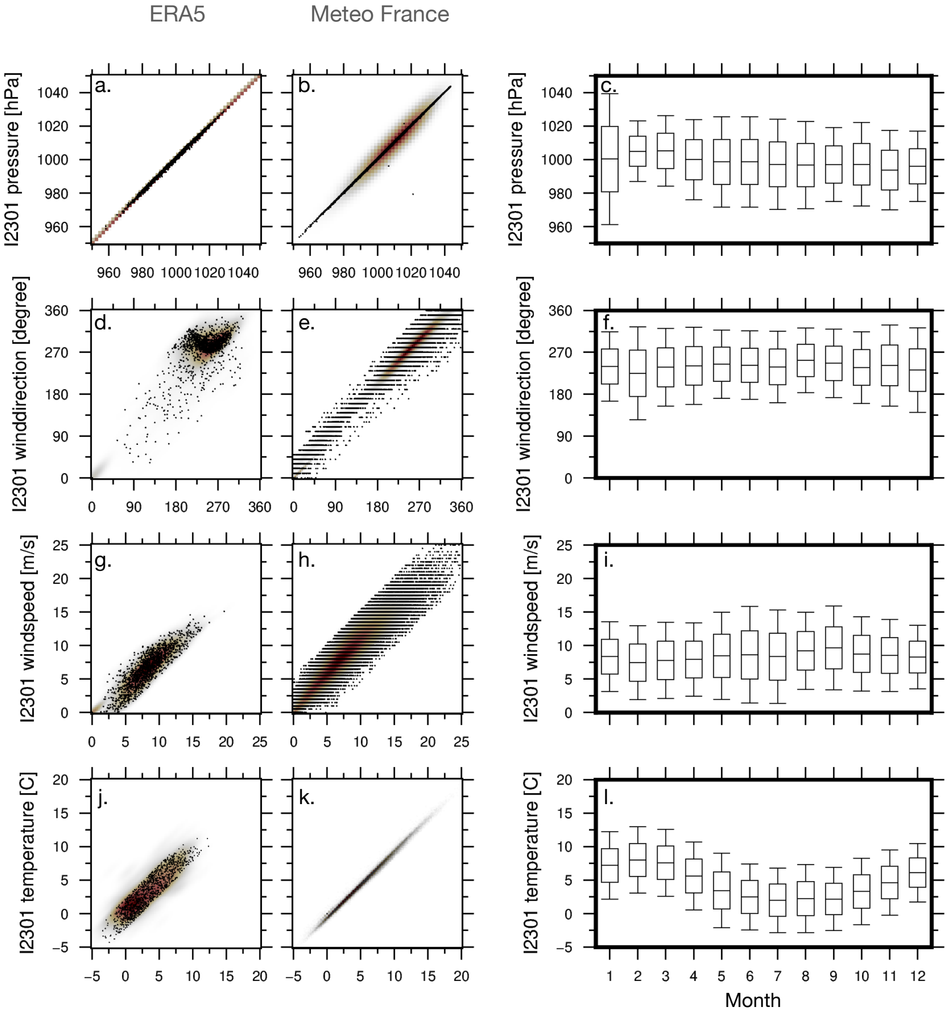

Figure 5.3: *Meteorological observation and comparison at Kerguelen Island. The left-hand panels (a), (d), (g) and (j) compare 3-hr meteorological observations at I23FR with ERA5 EDA data. The middle panels (b), (e), (h) and (k) show hourly comparisons between between I23FR data and MeteoFrance. Overlayed on the data points the normalized distribution is shown. The right-hand panels show the monthly average with a 95 percentile error bar from 2015 until 2020.*

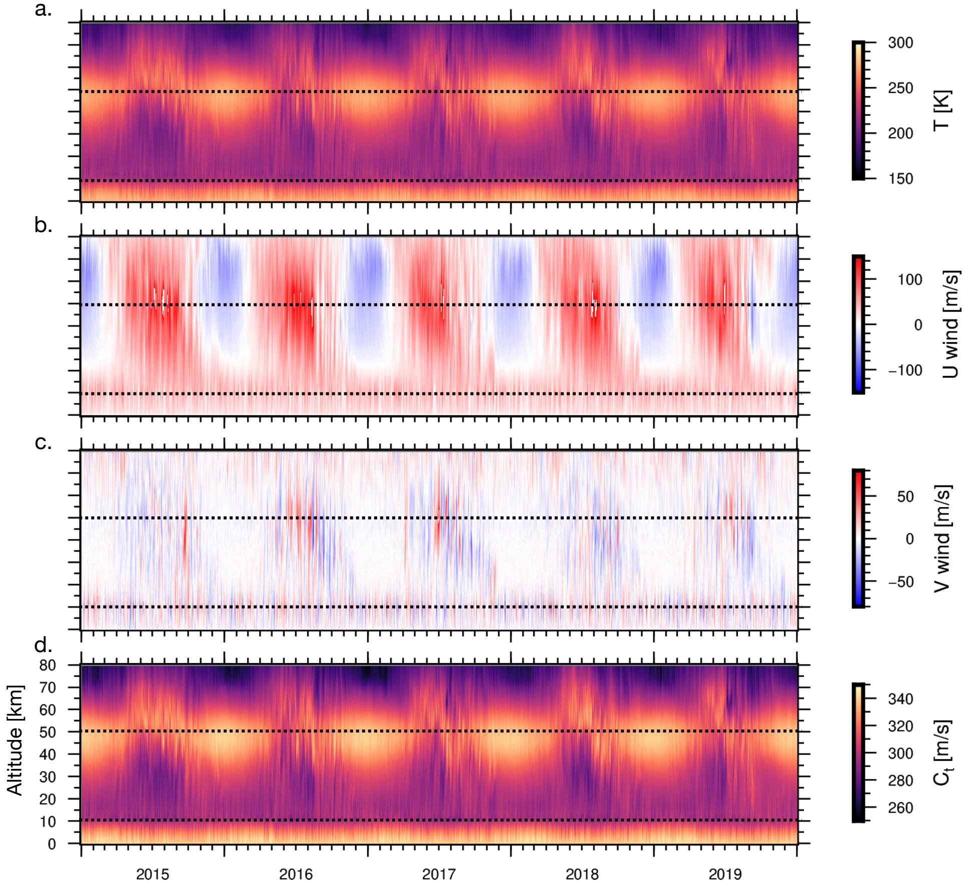

Figure 5.4: *Vertical atmospheric profiles above I23FR derived from ERA5 data. As a function of time and geopotential height are shown: (a) temperature (K), (b) zonal wind (m s-1), (c) meridional wind (m s-1) and (d) adiabatic sound speed (m s-1). The black dotted lines indicate the tropopause* $\sim$ *10 km, and stratopause* $\sim$ *50 km.*

ERA5, 2m	MeteoFrance, 10m
Barometric pressure: -0.75 ± 0.68 hPa	Barometric pressure: 0.38 ± 0.69 hPa
Wind direction: $-7.21 \pm 4.01°$	Wind direction: $-3.87 \pm 1.57°$
Wind speed: 1.65 ± 1.38 m/s	Wind speed: -0.85 ± 0.07 m/s
Temperature: -0.01 ± 0.19°C	Temperature: 0.72 ± 0.01°C

Table 5.2: *Comparison of meteorological in-situ data of I23FR (2 m instrument height) and ECMWF ERA5 atmospheric reanalysis data (2 m height, left column), and in-situ observations from MeteoFrance (10 m height, right panel). Note that negative values indicate an underestimation by I23FR compared to ERA5/MeteoFrance, and positive values indicate an overestimation.*

5.3.2 Analysis of vertical ECMWF profiles above Kerguelen Island

Besides local noise conditions, vertical profiles give insight into the atmospheric propagation conditions of infrasonic signals. Infrasound can propagate over large distances facilitated by acoustic waveguides, that can form between the Earth surface and various altitudes throughout the atmosphere, depending on the temperature and horizontal wind conditions. These waveguides change with time and location. The effective speed of sound ratio is a practical measure to quantify favourable ducting conditions. As the interest in this study is with ground-based sources, ground-to-ground ducting conditions are considered. For this, the effective sound speed ratio is normalized to the sound speed at the ground surface. An effective sound speed ratio near or greater than one indicates that infrasound can propagate efficiently in a waveguide.

The effective sound speed approximates the combined effect of wind, temperature (T), and the specific gas constant ($R_{\mathrm{air}} = 287\mathrm{J\ kg^{-1}\ K^{-1}}$) on infrasound propagation. The effective sound speed (C_{eff}) is defined as the sum of the adiabatic sound speed ($C_t = \sqrt{\gamma R_{\mathrm{air}} T}$) and the wind in the direction of propagation [Drob, 2019; Assink *et al.*, 2019] for a fixed horizontal position and time:

$$c_{\mathrm{eff}}(z, \theta) = c_T(z) + \mathbf{W}_{xy}(z) \cdot \hat{n}_{xy}(\theta) \tag{5.3.1}$$

where $\mathbf{W}_{xy}(z) \cdot \hat{n}_{xy}(\theta)$ indicates the horizontal winds at altitude z in sound propagation direction θ. The vertical variation in $C_{\mathrm{eff,\ ratio}}$ indicates the refractivity of the atmosphere and is defined as the ratio of the effective speed of sound at an altitude z and at the ground, equal time and location:

$$c_{\mathrm{eff,\ ratio}}(z, \theta) = \frac{c_{\mathrm{eff}}(z, \theta)}{c_{\mathrm{eff}}(0, \theta)} \tag{5.3.2}$$

Figure 5.4 shows the climatology of the meteorological parameters that are relevant for infrasound propagation, derived from the ERA5-EDA. From this figure, the various waveguides within the atmosphere become clear. ERA5 resolves atmospheric model data up to 80 km altitude. The tropopause ($\sim$ 10 km), stratopause ($\sim$ 50 km) are visible within this figure. The mesosphere and lower thermosphere is not resolved by the ECMWF model. However, these regions make up the upper layers of the thermospheric waveguide. This duct always exists due to the strong temperature gradient around the mesopause region

[Drob *et al.*, 2003; Waxler and Assink, 2019], but is less efficient for long-range propagation because of the increase in acoustic attenuation at these altitudes [Sutherland and Bass, 2004]. Nonetheless, from the figure, it stands out that the stratospheric duct is dominant.

Figure 5.5 shows the effective sound speed profiles at I23FR for four different periods and back azimuths. The summer, autumn, winter and spring profiles are represented by ECMWF ERA models for the first day of January, May, July and October 2015 respectively. The blue lines indicate the effective sound speed profiles, whereas the grey areas indicate whenever a specific angle has a $C_{\mathrm{eff,\ ratio}}$ greater than one. From this figure, it stands out that during the austral summer (January), an easterly stratospheric duct occurs within the atmosphere. Infrasonic signals will most likely be propagated from the east to the west. In contrast, during the austral winter (July), a westerly stratospheric duct occurs in the atmosphere, signals will most likely propagate from the west to the east.

The thermospheric propagation conditions are causing a continuously effective speed of sound ratio greater than one (Figure 5.4 and 5.5), and thus a favourable ground-to-ground ducting condition. However, compared to stratospheric propagation the thermospheric propagation is less effective due to the high thermo-viscous absorption [Sutherland and Bass, 2004].

5.4 Infrasound observations

5.4.1 Ambient local noise

The meteorological conditions near the array provide insight into the infrasonic noise conditions Figure 5.3). From those observations, it can be stated that I23FR experiences winds stronger than 5 m s-1 all year round. Such harsh conditions may reduce the array's ability to detect coherent infrasound and estimate the parameters of interest as the infrasonic signals are masked by incoherent pressure perturbations from wind noise [Walker and Hedlin, 2010].

Within this study, hourly power spectral densities (PSDs) are computed for each array element. The PSDs are aggregated into probabilistic power spectral density (PPSD) distributions that give insight into noise distribution as a function of frequency. Figure 5.6-a shows the PPSD of I23FR for 2015 until 2020 (excluding elements 12 and 14, which were unavailable during that period). The PPSD distribution shows that the noise conditions around I23FR are relatively high over the entire infrasonic frequency band, compared to the global high and low noise curves [Brown *et al.*, 2014]. These observations are in line with earlier observations by Brown *et al.* [2014] and chapter 4.

Besides the high noise levels, the resonance peak around 6.6 Hz stands out due to the system response function (Figure 5.2). This feature can be suppressed from the spectra by deconvolving the system response from the spectra [Bracewell and Bracewell, 1986], as shown in Figure 5.6-b.

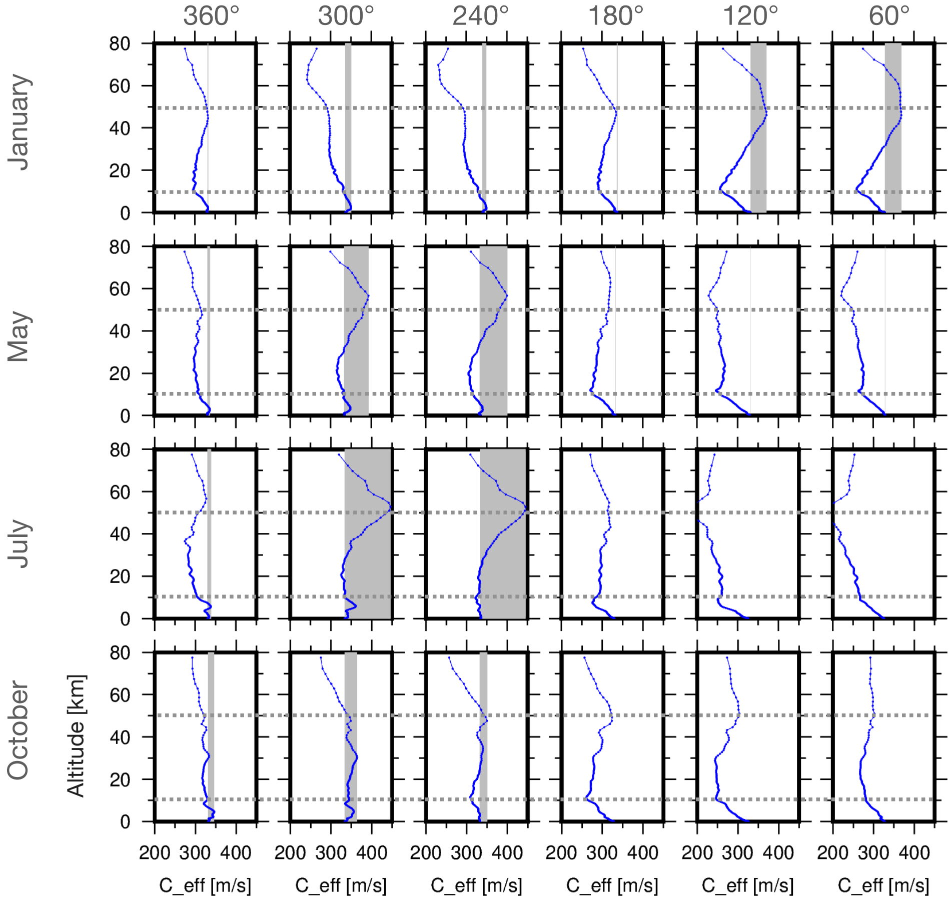

Figure 5.5: *Effective sound speed profiles at Kerguelen Island for different periods and back azimuth directions. The gray areas indicate when the effective sound speed is above one. The gray dotted lines indicate the tropopause* $\sim 10km$*, and stratopause* ~ 50 *km.*

5.4.2 Triplet noise

Algorithms used to process infrasonic array data typically rely on the assumption that the background noise can be modelled as Gaussian stationary white noise with equal noise levels at all array elements. Moreover, the signal of interest is typically considered to be perfectly correlated over the array's aperture. To assess the detection capability of an infrasonic array, it can therefore be helpful to analyse the PSDs at each array element [Brachet *et al.*, 2010; Green, 2015]. PSDs of individual elements are compared to determine the difference in noise conditions per array element. For each hour, the residual PSD is determined and plotted against the average wind direction and speed over that particular hour from the CTBT data (section 5.3).

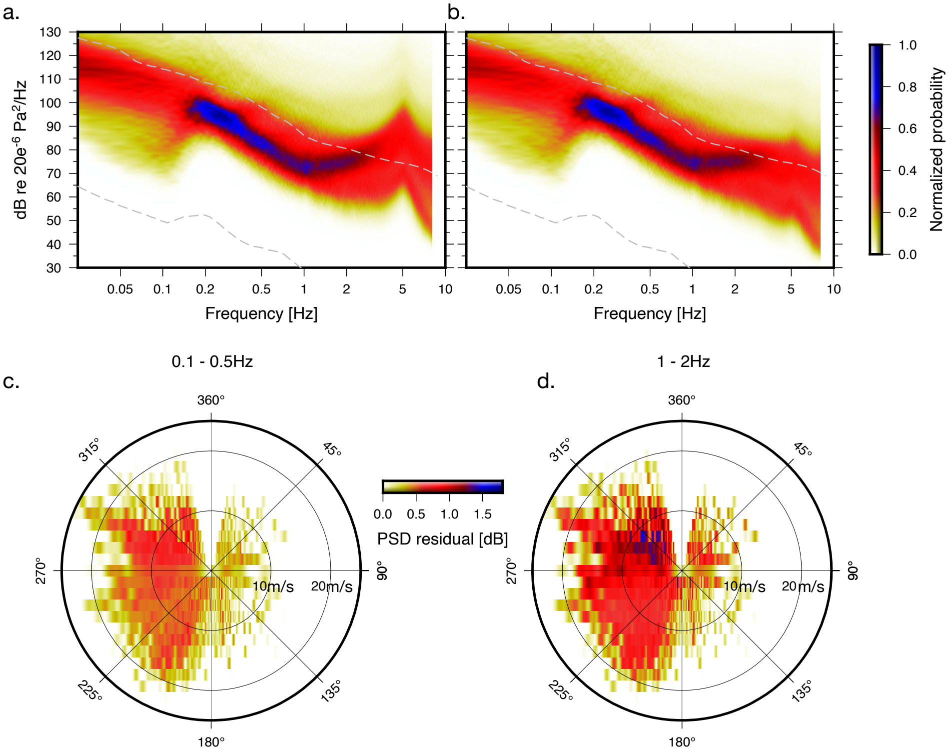

Figure 5.6: *PPSDs computed for five years of I23FR data. PPSDs are computed for I23FR sensor data (except elements 12 and 14, which were unavailable during that period) (a) without and (b) with correcting for the WNRS response (Figure 5.2). Panels (c) and (d) show the power difference between individual array elements of I23FR under varying meteorological conditions (wind speed and direction) for 0.1-0.5 and 1-2 Hz, respectively.*

The residual PSD is determined as:

$$\sigma_{\mathrm{PSD}}(f,t) = \sqrt{\frac{1}{N}\sum_{i}^{N}(\mathrm{PSD}_i(f,t) - \mu_{\mathrm{PSD}}(f,t))^2} \tag{5.4.1}$$

where PSD_i is the PSD of element i, N the number of elements, and μ_{PSD} indicates the average PSD over the entire array.

The average residual has been calculated over the array recordings between 2015 and 2020 with a 99.9 percentile Gaussian distribution (Figs 6c and d). Note that the dominant wind direction is westerly (Figure 5.3), which results in more data within that quadrant. It stands out that the omnidirectional residual between the elements PSDs is $\sim$ 1 dB. Although the array experiences harsh weather conditions and the PSD noise levels are relatively high (Figure 5.6-b), the difference in PSD between array elements is constant over various wind directions and speeds. The local noise conditions over the array elements are determined to be similar.

This remark, however, does not express anything about the ability to resolve infrasonic signals. However, it does state the differences in local noise conditions over the array. It is a measure for local noise over an array, which is an important observation before applying data processing techniques.

■ 5.4.3 Beamforming methods

Array processing techniques (e.g. beamforming) can separate the coherent parts of the infrasonic array recordings. The ability to detect and estimate the incident direction of the microbarom wavefield relies on the beamform resolution as quantified by the array response. The array response is determined by the beamform technique, frequency of interest and the array layout. Ideally, the array response function approximates a delta function that is unity for the slowness $\vec{p}_0$ of interest (typically chosen $\vec{p}_0 = 0$ s/m. However, because a limited number of array elements are used in practice, the array response function is described by a main lobe of a finite width and multiple side lobes [Evers, 2008].

Often the Bartlett [Bartlett, 1948] and Capon [Capon, 1969] beamforming algorithms are applied. For the Bartlett, known as the 'classical analysis', the signal power is maximized by summing the phase-aligned spectral values. Capon's method is derived as a maximum-likelihood filter. Due to the filter design, the noise in the power spectrum is optimally suppressed while keeping a constant gain in the direction of interest. The array responses for I23FR while applying Bartlett and Capon are shown in the bottom panels of Figure 5.1, for a vertically incident wave with $f_0 = 0.05$-0.55 Hz and 0.75-1.55 Hz. Capon's responses (panels d and f) have a sharper main lobe compared to the Bartlett responses (panels e and g). Moreover, the amount and amplitude of the side lobes when applying Capon's method are significantly reduced (chapter 3).

Within this study, time- and frequency-domain array processing techniques (i.e. beamforming) are applied and compared. The microbarometer elements at I23FR continuously acquire infrasound measurements at a rate of 20 samples per second. To detect possible events of interest, beamforming can be performed in the time or the frequency domain, searching for correlated signals. The time-domain beamforming is performed by using the time-domain Fisher detector [Melton and Bailey, 1957; Evers, 2008], which enables to determine the dominant source contribution. The frequency-domain beamforming within this study is performed by Capon [1969] beamforming, which is used to calculate a f/k spectrum. A comparison between Capon and Bartlett array responses illustrates that the Capon method is a higher-resolution method than the Bartlett beamformer [Viberg and Krim, 1997]. As a post-processing method on the initial Capon spectrum, CLEAN beamforming has been applied (Capon-CLEAN, Högbom [1974]). CLEAN allows for the identification of multiple infrasound signals within the same time and frequency window (chapter 3).

Both beamforming methods are applied in the passband of 0.05-0.55 Hz. The window size of both methods is 2000 seconds, with 90 percent overlap. The calculation of the f/k spectra occurs over a vector space spanned by steering vectors, which is formed by the slowness grid. The design of the slowness grid consists of a 360° ring grid plus a rectangular grid. The ring grid is a linear grid in backazimuth and apparent velocity, ranging from 0° to 360° and 285 to 500 ms^{-1} with steps of 2° and 1 ms^{-1}, respectively. This ring grid is nonlinear in the slowness domain. The rectangular grid consists of linearly spaced values between -0.005 and 0.005 sm^{-1}. This grid is added to ensure that energy from outside the ring grid does not clutter on its boundaries, which would result in biased outcomes. Within this study a Fisher detection threshold is used as a confidence interval for avoiding false alarms [Shumway, 1971]. The threshold depends on the array layout, frequency range and beamforming window size. The Fisher threshold is set to 1.19 in order to have a 95% confidence on the resolved sources to be an actual signal instead of a false alarm.

5.4.4 Microbarom observations

Microbaroms are the most dominant infrasound sources detected worldwide and are the atmospheric counterpart of microseisms. The spectral peak of these signals is typically found around 0.2 Hz, but more generally, microbarom energy is detected in the 0.1-1.0 Hz band [Campus and Christie, 2010; Landes *et al.*, 2012; Hupe, 2019]. Both beamforming methods have been applied on the frequency band 0.05-0.55 Hz. The resolved infrasound signals within this frequency band are classified as propagating microbaroms, in contrast to evanescent microbaroms that are only present above the source (chapter 4).

Figure 5.7 shows the outcome of the time-domain Fisher detector (a and b) and the frequency-domain Capon-CLEAN algorithm (c-e). The results show the expected seasonality in direction and apparent velocity. Note that both detectors have similar results. However, the CLEAN outcome contains more spatial information of the infrasonic sources since the CLEAN algorithm detects multiple spatially distributed sources within overlapping frequencies and time windows. Moreover, CLEAN gives insight into the frequency content of the resolved infrasound signals (panel e).

The beamforming outcomes show that the dominant infrasound signals in the austral summer are resolved from the east and in the austral winter from the west. Besides the seasonal change in the directivity of infrasound signals, the apparent velocity also changes with the seasons. The apparent velocities are higher in the austral winter than in the austral summer periods (Figure 5.5). Furthermore, a frequency shift of the infrasonic wave front is revealed within the results. During the austral winter, microbaroms are observed over a wider frequency band, that also include lower frequencies (0.1-0.5 Hz) when compared to the summer (0.15-0.3 Hz). In addition, the amplitudes of the resolved microbarom signals change seasonally. During the austral winter the sound pressure level (SPL) of the microbarom is higher compared to the austral summer. This is due to the initial source power of the microbaroms, during winter the initial source power is higher, but also due to the propagation conditions during winter, which are favourable and therefore the microbarom signals will attenuate less during propagation towards the array.

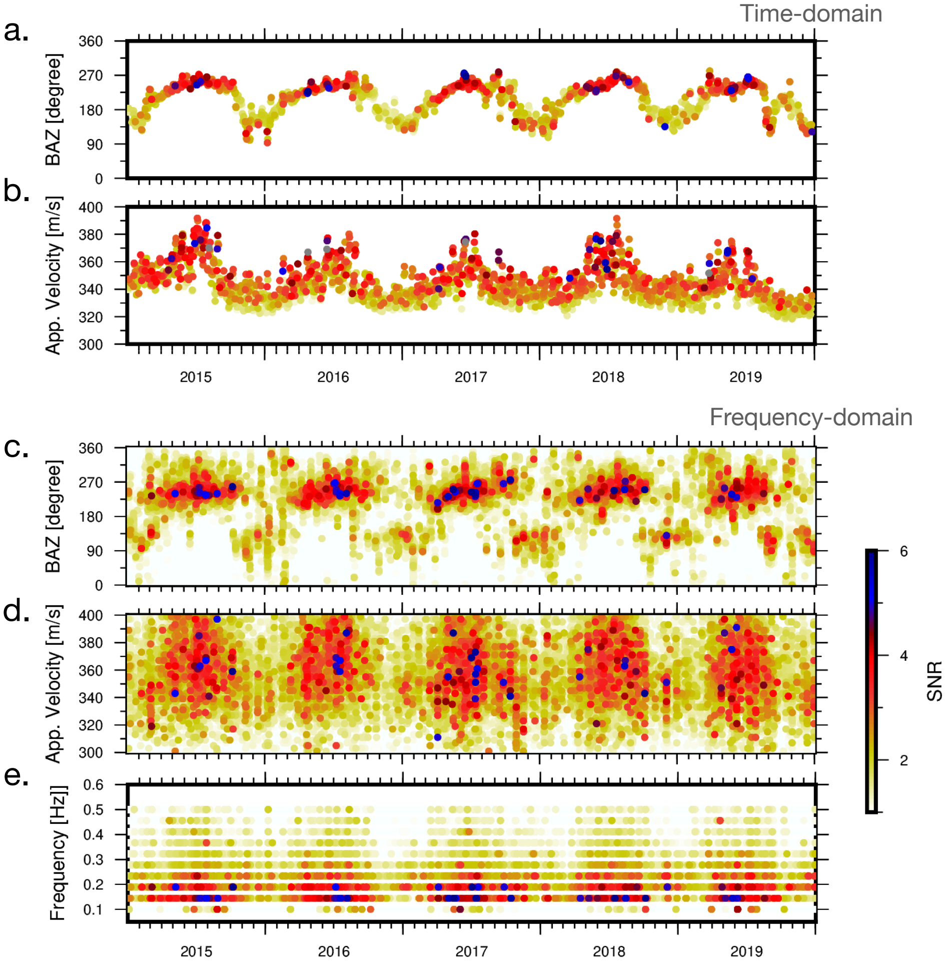

Figure 5.7: *The outcome of the time-domain Fisher (panels a and b) and the frequency-domain CLEAN beamforming analysis (panels c-e).*

5.5 Simulating microbarom soundscapes

Chapter 4 presented a method for the reconstruction of microbarom soundscapes. Such soundscapes account for all omnidirectional propagating microbarom source contributions and present microbarom spectra in absolute values. The computed acoustic intensities are integrated over the ocean surface, based on a microbarom source model [Waxler *et al.*, 2007], and accounts for long-range propagation [Tailpied *et al.*, 2016].

In the literature, there are various studies that compare infrasonic microbarom observations and microbarom source region models [Landes *et al.*, 2012; De Carlo *et al.*, 2020*a*; Vorobeva *et al.*, 2020; Šindelářová *et al.*, 2021]. Typically, array processing techniques are applied to detect the dominant microbarom signal and direction in a given time segment and frequency band. Therefore, only the resolved direction and amplitude of this dominant microbarom observation is compared with microbarom models. However, Assink *et al.* [2014], Smets and Evers [2014*a*], and chapter 3 have shown that multiple spatially distributed sources within the same time segment and frequency often occur.

For the computation of soundscapes, the microbarom source model is calculated with the use of the 2-D wave spectra (2DFD) that are computed by the ECMWF ERA5 Wave Action Model (WAM). The 2DFD field is available at 30 oceanic wave frequencies spaced exponentially between 0.035 and 0.5476 Hz and 24 wave directions, linearly spaced over 360°. This 2DFD reanalysis is coupled to the atmosphere model, which allows interaction between the ocean waves and the surface winds [Haiden *et al.*, 2018]. The reanalysis has an hourly output, with a spatial resolution of 0.36°. The transmission loss from each position in the grid to the infrasound array location at Kerguelen island is computed using the empirical relation proposed by Tailpied *et al.* [2016]. This relation extends the original methodology by Le Pichon *et al.* [2012] for range-dependent atmospheres. This class of empirical propagation loss functions is derived as a functional fit to transmission loss curves computed using the Parabolic Equation (PE) method [Le Pichon *et al.*, 2012].

An example of a soundscape analysis for the four different seasons considered in this study is shown in Figure 5.8. The panels on the top row show the initial microbarom source region model as derived by Waxler *et al.* [2007] and implemented by Smets [2018] for summer (left-hand column), autumn (middle-left column), winter (middle-right column) and spring (right-hand column). The middle row panels indicate the long-range propagation conditions within the atmosphere, where the vectors describe the strength and direction of the stratospheric winds (Figure 5.4). The panels on the bottom row show the interpolated microbarom soundscapes from the perspective of I23FR, integrated between 0.05-0.55 Hz. The microbarom soundscapes illustrate the source regions that potentially have been detected at the array. Note that the microbarom soundscapes change significantly with the seasons. While the sources are centred around the island for the May and October cases, there is a strong directional difference of microbarom source regions between January and July due to the propagation conditions (Figure 5.5). During the austral summer and winter a strong easterly and westerly stratospheric propagation duct is expected. These propagation ducts weaken during the autumn and spring, when the middle atmospheric winds reduce as the circumpolar vortex reverses direction. This results in an omnidirectional spread of microbarom source regions that can be sensed by I23FR.

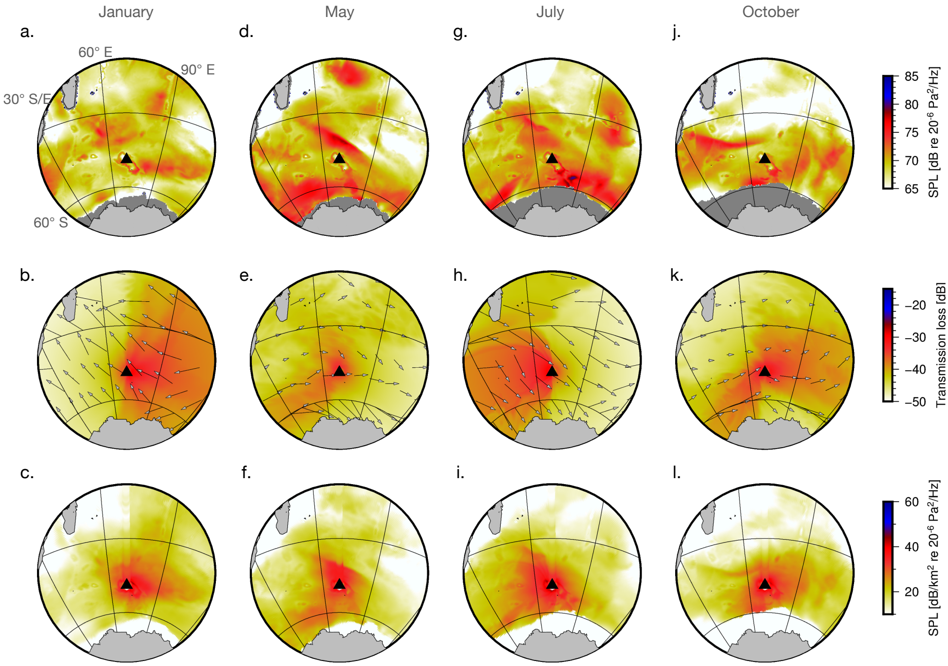

Figure 5.8: *Synthetic soundscape reconstruction of the infrasonic wavefield around I23FR, integrated between 0.05-0.55 Hz. The top panels (a), (d), (g) and (j) show the initial microbarom source region model for summer (left-hand column), autumn (middle-left column), winter (middle-right column) and spring (right-hand column) conditions. The middle panels (b), (e), (h) and (k) indicate the long-range propagation conditions within the atmosphere, where the vectors describe the magnitude and direction of the stratospheric winds (∼ 30 km altitude). The bottom panels show the interpolated microbarom soundscapes.*

■ 5.5.1 Spectral analysis

The soundscapes can be used to create omnidirectional PSDs of the spatial distribution of microbarom source regions around I23FR:

$$\mathrm{PSD}_{\mathrm{synth}}(f,t) = \sum_{\theta_i}^{\theta} \sum_{S_i}^{S} \mathrm{SPL}_{\mathrm{Synth}}(f,t,\theta_i,S_i) \tag{5.5.1}$$

where f represents the frequency, t the time period, θ_i the directional angle and S_i the distance within the stereo-graphic polar grid .

Synthetic PPSDs indicate the expected SPL contributions of microbaroms from a model perspective. The PSDs are calculated with a time resolution of one hour, over the entire frequency range (0.069-1.095 Hz) of the soundscapes, aggregated and displayed as PPSDs.

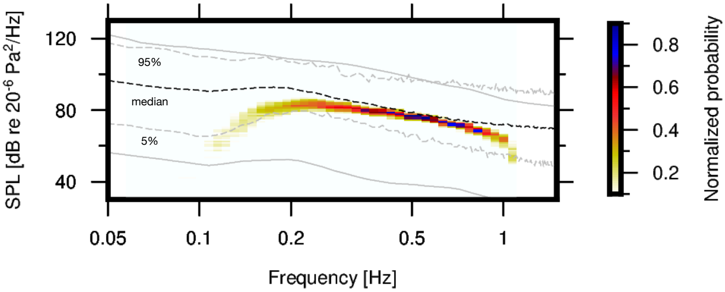

Figure 5.9: *Synthetic PPSD of the soundscapes for I23FR. The grey solid lines indicate the global high and low noise curves [Brown* et al.*, 2014]. The grey and black dotted lines present the* 5 *and* 95 *percentile and the median curve of the observed PPSD levels at I23FR (Figure 5.6).*

Figure 5.9 shows the synthetic PPSD for I23FR, using five years of data between 2015-2020. The grey solid lines indicate the global high and low noise curves [Brown *et al.*, 2014]. By comparing this synthetic PPSD with the PPSD obtained from the in-situ measurements, Figure 5.6-b, it becomes clear that there is a difference in spectral power. Note that I23FR experiences extreme meteorological conditions (section 5.3). Therefore, in the comparison of these spectra the synthetic soundscapes only account for remote microbarom contributions. Local coherent and incoherent noise around the array are neglected. In particular the 95% PPSD is likely determined to a great extent by local turbulence in the vicinity of the array and not by microbarom noise levels. Therefore, the 95 percentile PPSD of the recordings can not be directly compared with the synthetic PPSD. The median level PPSD of the I23FR observations (Figure 5.6-b) shows a better agreement, especially for the higher frequencies ($\sim 0.3 - 0.8$ Hz). Nevertheless, the typical 0.2 Hz microbarom peak is moderately visible due to the lower SNR values compared to microbarom spectra that are typically observed at (IMS) infrasound stations [Marty, 2019]. This is most likely due to the high noise conditions experienced within the recordings of I23FR compared to the other IMS arrays (section 5.3). In the synthetic PPSD, this wind noise contribution is not taken into account. The 5th percentile PPSD level corresponds to periods of low noise conditions. Therefore, this curve can be used to compare against the synthetic PPSD. Both show similar SPL's while resolving the characteristic microbarom amplitude signature around 0.2 Hz [Campus and Christie, 2010]. The wind-noise effects on microbarom recordings decrease at increasing frequencies [Gossard and Hooke, 1975].

5.5.2 Seasonal effects

The seasonal effects on microbarom signal propagation depend on the atmospheric conditions (Figure 5.4 and 5.5). The detectability of the most dominant microbarom source is highly influenced by these conditions (Figure 5.8). A similar analysis as time-domain Fisher beamforming can be performed using microbarom soundscapes. Figure 5.10-a shows the characteristics of the most dominant sources within the microbarom soundscapes. Those soundscapes are calculated for each hour of model output and created between 2015-2020 from the perspective of I23FR. From this outcome, it becomes clear that the most dominant source contribution from the soundscapes changes with the seasons. During the austral summer (January), the east is the dominant source direction, while during the austral winter (July), the sources propagate from the west.

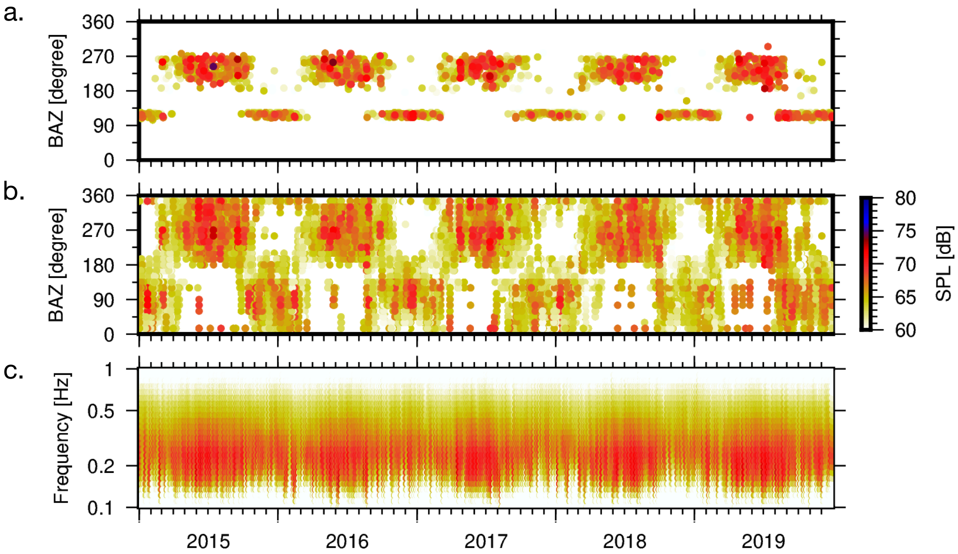

Figure 5.10: *Seasonal SPL analysis of the synthetic soundscapes. Panels (a) shows the characteristics of the most dominant sources within the microbarom soundscapes. Panel (a) indicates the resolved backazimuth. Panels (b) and (c) show the outcome of the omni-directional analysis of the soundscapes. The soundscapes have been divided into* 10° *cones, for which the SPL has been determined. Whenever the SPL is above* 5% *of total SPL, it has been included within the figure. Panel (b) indicates the directionality, and panel (c) the frequency content.*

Besides resolving the most dominant source contribution, an analysis similar to CLEAN beamforming can be performed. For each soundscape, the total SPL has been determined. Based on the total SPL, a directivity and frequency study has been performed. From the perspective of I23FR, the total soundscape field is divided up by direction. The cones that describe the directions are described by a Gaussian distribution, centered around a mean direction and a standard deviation of 10°. Each cone has an overlap of 5%. For each cone, the SPL is determined. A threshold of 5% of total SPL has been used. Figure 5.10-b and -c show the outcome of this analysis. The outcome presented in panel (b) shows a similar season pattern as in panel (a). However, accumulating multiple source contributions results in a more insight into the spatial microbarom contributions. Microbarom source regions are often dynamic and largely spread out ($\sim$ 10000 km^2). The most dominant microbarom contribution, therefore does not always correctly represent the actual infrasonic wavefield. Besides the directional analysis of microbarom source regions from the soundscapes, frequency analysis can be performed. Panel (c) shows a spectrogram of the accumulative microbarom source region contribution from panel (b). This analysis shows that the microbarom source contributions during the austral winter (July) have a lower frequency content than the austral summer (January). Moreover, the distribution of frequencies is wider during the austral winter.

■ 5.5.3 I23FR microbarom exposure

Besides directional and frequency information of microbarom source regions, the soundscapes also enable the construction of cumulative probability distributions to quantify the exposure of the array to microbarom source energy. The smallest area that encloses 95 percent of SPL generation has been determined for each soundscape, and is parametrized by the largest distance to the boundary of this area (Figure 5.11-a, black dots). The most dominant source contribution is always located considerably closer to the array (aat $\sim$ 250 km distance, Figure 5.11-a, red line). From this analysis, it is concluded that the SPL contributions by microbaroms at I23FR are from source regions within an area that has an approximate radius of 2000 km.

Nevertheless, the SPL percentile analysis is relative. During the austral winter the propagation conditions and the microbarom source areas are favourable for higher SPL levels (Figure 5.7 and 5.10). Figure 5.11-b shows the omnidirectional SPL contribution of the microbaroms over distance in absolute numbers. From this panel it becomes clear that the exposure of microbaroms around the array is changing with the seasons. While the 95 percentile distance is of the same order of magnitude, I23FR is exposed to higher microbarom levels during the austral winter.

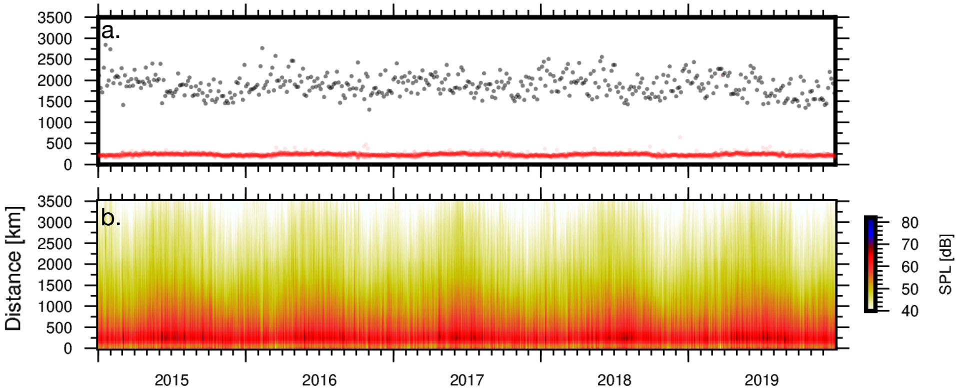

Figure 5.11: *(a) The cumulative probability distribution of I23FR, which quantifies the exposure of microbaroms around the array. The black dots indicate the radius of the area which encloses the 95 percentile of the resolved SPL. The red dots correspond with the radius of the area of the most dominant source contribution within the soundscapes. (b) The microbarom SPL distribution at I23FR over radius.*

■ 5.5.4 Comparing f/k analysis to soundscapes

In this study, a climatology of the infrasonic wavefield around Kerguelen has been studied by using (1) in-situ infrasound data from array I23FR and (2) synthetic infra-soundscapes. Two beamforming methods, that is, time-domain Fisher and frequency-domain Capon-CLEAN, have been used to estimate the directivity, frequency content and amplitude spectra of coherent infrasound between 0.05-0.5 Hz.

Figure 5.12 shows a comparison between beamforming results and the synthetic soundscape for 2015 October 01 at 00 UTC. Panels (a) and (b) show the f/k spectra of the initial Capon beamforming result and after applying CLEAN, respectively. Panels (c) and (d) show a similar analysis based on Bartlett beamforming. Below the f/k spectra, the corresponding soundscape for the same period is plotted. Within the soundscapes, the direction of the dominant source contribution from the beamforming observations is plotted (black arrow) and the CLEAN results (grey cones). The resolved dominant source direction by Capon-CLEAN points towards the dominant source contribution of the soundscape. Moreover, note that the initial f/k spectrum of Capon beamforming is of a higher resolution than the Bartlett spectrum, which results in a more accurate outcome of the CLEAN algorithm (chapter 3). The Capon-CLEAN beamforming results are in general agreement with the derived soundscapes outcome.

5.6 Climatology comparison

In section 5.5, it was shown that the beamforming results are in general agreement with the soundscape simulations. The comparison over time between observations and model has been divided into two analyses. The first comparison is between soundscapes and the time-domain Fisher results, based on the most dominant source signal. The second comparison is between the soundscapes and frequency-domain CLEAN beamforming results and accounts for surrounding microbarom sources.

The outcome of the first comparison (Figure

Nevertheless, this first comparison is not complete. Various studies have made the comparison between the dominant infrasonic observations and model outputs [Landes *et al.*, 2012; Vorobeva *et al.*, 2020]. However, microbaroms source regions are dynamic, fast-changing, and often extended areas from the perspective of a distant array. Therefore all sound contributions should be taken into account, instead of only the most dominant contribution. The second comparison, therefore, is based on the CLEAN beamforming results and the omnidirectional soundscapes. Both methods account for the omnidirectionality of infrasonic sources, which can be divided into directional Gaussian cones. The cones span a range of 10° while having a 50% overlap. The resolved power within each cone can be assigned to the coherent part of the infrasonic wavefield.

Figures 5.14 and 5.15 show the 'cone' comparison between the soundscapes and CLEAN observations. The direction of the sources in the modelled soundscapes and array processing (CLEAN) results are in good agreement, and both approaches resolve seasonal variations (Figure 5.14-a and -b). However, the SPL differs ~ 5 dB. Panel (c) indicates the difference in SPL between soundscapes and CLEAN related to backazimuth. Note that incoherent noise has not been taken into account while reconstructing the soundscapes. The CLEAN beamforming results do contain effects of incoherent noise and are therefore slightly biased. However, these incoherent noise effects are minimal for higher amplitude signals. The synthetic soundscapes are derived from model data, which are a smooth and unvarying representation of the reality. Rapid changes and local differences are not resolved within these models. Comparisons between model and observations will enable improvements to be made to the models.

Figure 5.15 shows a similar analysis based on the frequency content resolved from both methods. Again a good agreement between soundscapes (a) and CLEAN output (b) is noted. The frequency content of the resolved infrasound sources between both is complementary. Both show a broad frequency distribution during the austral winter (July), including the finding of lower frequencies. The frequency distribution during the austral summer (January) is more narrow.

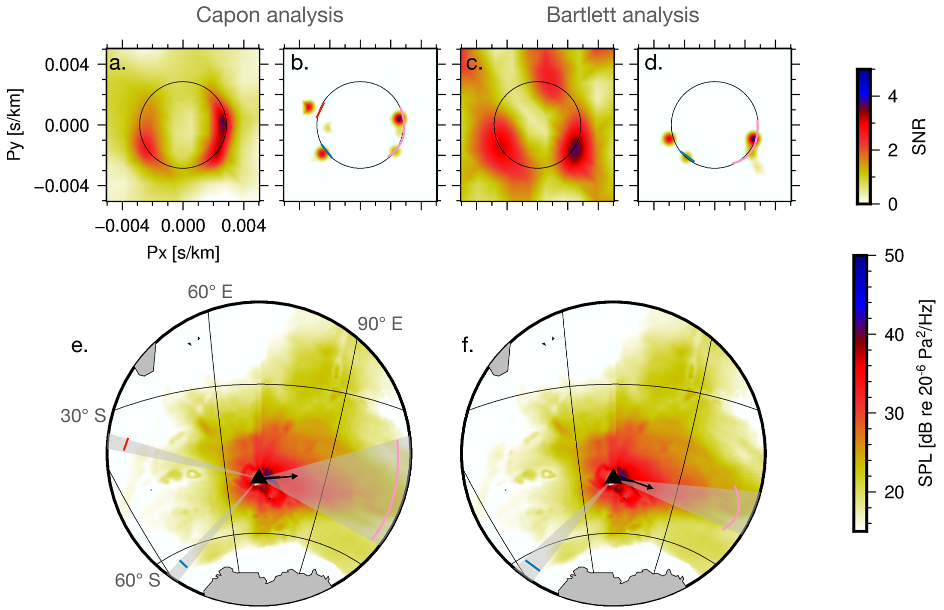

Figure 5.12: *A comparison between beamforming results and synthetic soundscape for 2015 October 01 at 0 UTC. (a) and (b) show the f/k spectra of the initial Capon beamforming result and the result after applying CLEAN. (c) and (d) show a similar analysis based on Bartlett beamforming. (e) and (f) present the corresponding soundscape. The direction of the dominant source contribution from beamforming (black arrow), and the CLEAN results (grey cones) are highlighted within the soundscapes.*

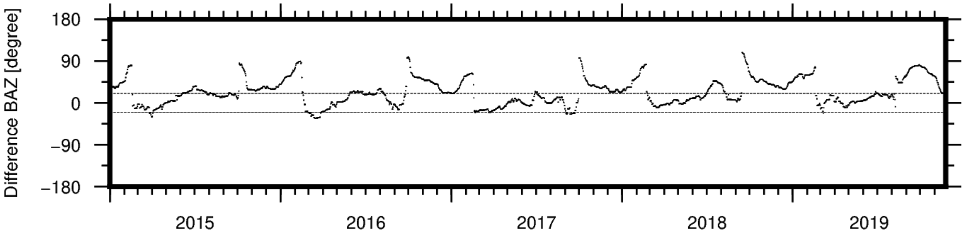

Figure 5.13: *Comparison plot between the most dominant back azimuth direction resolved by the time-domain Fisher analysis (Figure 5.7) and the soundscape reconstructions (Figure 5.10). During the austral winter, there is a good agreement between model and observation. During the equinox and austral summer, the agreement decreases.*

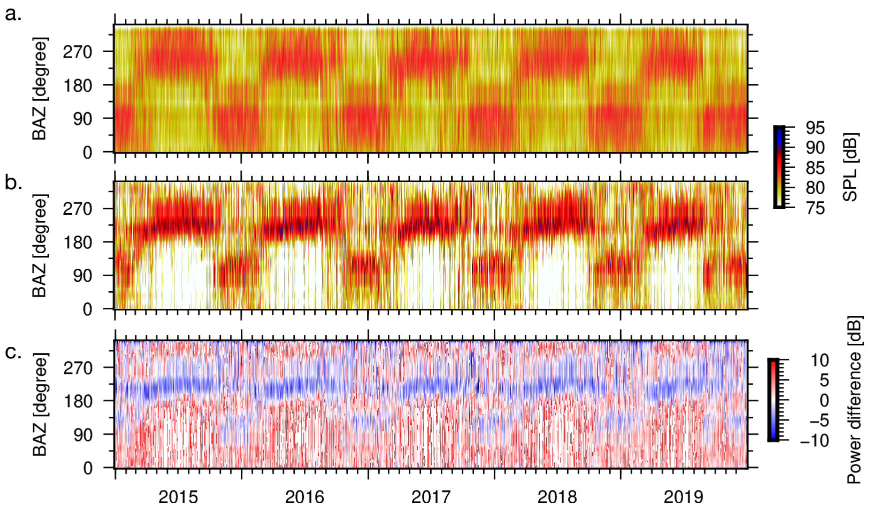

Figure 5.14: *Comparison between directional synthetic soundscapes (a) and CLEAN observations (b). The panels show the SPL and back azimuth direction resolved from the soundscapes and CLEAN beamforming, where panel (c) shows a direct comparison between both in SPL.*

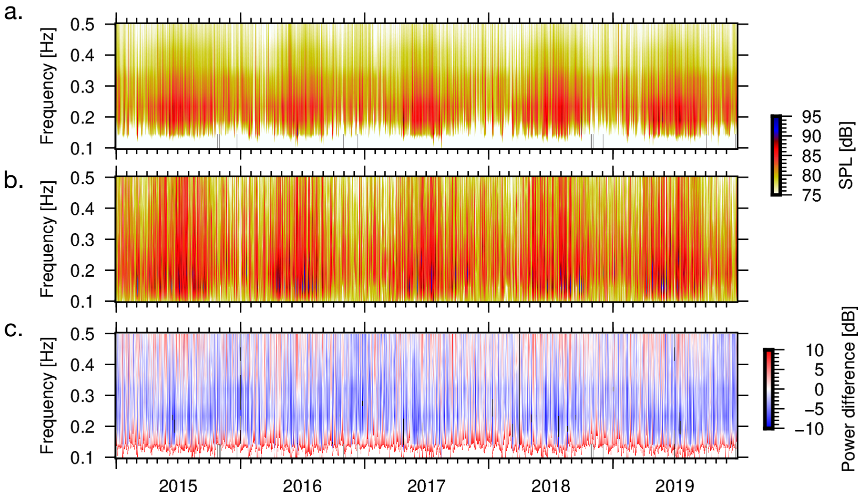

Figure 5.15: *Comparison between the frequency content resolved from the synthetic soundscapes (a) and the CLEAN beamforming (b). Panel (c) shows a direct comparison between frequency content of both expressed in SPL.*

5.7 Discussion and Conclusion

In this study, a climatology analysis of I23FR has been performed. This array is one of the microbarometer arrays of the IMS and provides real-time monitoring of the atmosphere [Marty, 2019]. The array is located at the Kerguelen Islands, positioned around the Indian and Southern ocean boundaries. Since the array experiences high ambient noise levels [Brown *et al.*, 2014], it is often excluded from scientific studies. The climatology analysis presented in this study improves the general knowledge regarding the infrasonic wavefield received by the array. Various methods have been introduced and applied to unravel and characterize the wavefield into its individual components. The performed analysis is essential for the understanding of the infrasonic wavefield. The dominant source contribution is characterized as microbaroms, thanks to the frequency and amplitude signature [Campus and Christie, 2010]. Microbarom source regions are large areas from the perspective of distant arrays. The microbarom source component within the infrasonic wavefield has been analysed using observations and synthetic soundscapes. Microbaroms are often classified as ambient noise and may mask infrasonic signals of interest. A further understanding of the ambient noise field therefore comes to the benefit of infrasonic monitoring of nuclear tests and natural hazards.

Microbarom observations are analysed over five years using I23FR infrasound data by I23FR (2015-2020). Insight into the statistical distribution of microbarometer pressure spectra in terms of PPSDs is discussed in section 5.4. These PPSDs contain both coherent infrasound as well as wind noise spectra. The microbarom peak can clearly be distinguished. The local noise conditions are high, relative to the global high and low noise curves [Brown *et al.*, 2014]. However, the difference in local noise conditions between the array elements is similar regardless of the wind direction and strength (Figure 5.4). This analysis does not express anything about the ability to resolve infrasonic signals but can measure local noise consistency over the array. Similar noise conditions between array elements are essential when applying array processing routines, which typically rely on similar ambient noise conditions on the various array elements and a highly correlated infrasound signal.

Moreover, the infrasonic wavefield has been separated into coherent and incoherent parts by applying beamforming. Two beamforming methods (i.e. time-domain Fisher detection and frequency-domain CLEAN beamforming), have been applied to estimate the directivity and speed of the incoming coherent infrasonic wave front. Although the microbarom source regions seem close to the array (Figure 5.8 and 5.12), the sources can still be considered to be in the acoustic far field and therefore can be described by a superposition of plane waves. As a consequence, the CLEAN methodology as described by chapter 3 is still appropriate. CLEAN beamforming is a post-processing method on conventional data processing techniques (i.e. Capon beamforming). CLEAN iteratively deconvolves the array response of the most dominant source contribution from the data. The ability to resolve multiple microbarom sources therefore depends on the array response (Figure 5.1)). CLEAN divides the 'diffuse' Capon spectrum (Figure 5.12-a) into multiple point sources in the slowness domain (Figure 5.12-b, i.e. parametrized by azimuth and apparent velocity). In the case of microbarom processing, these point sources represent 'pseudo-microbarom point sources'. The point sources follow a Gaussian point spread function (PSF) described in Gal *et al.* [2016] and chapter 3. The diffuse Capon spectrum is therefore divided into microbarom source contributions. The width of the PSFs is user-defined and the functions serve merely as a tool to represent the separated source contributions in the slowness space. Whenever the initial f/k spectrum has a lower resolution, CLEAN will not separate the various microbarom contributions into these PSFs. Nevertheless, the representation of microbarom source regions as pseudo-microbarom point sources is merely an approximation, since microbarom sources are in reality spread out source regions. Microbarom classification as point sources suggests there is no correlation between two neighbouring sources (especially since the source region is relatively close to the array). Within section 5.6, the first initiation of a non-point source microbarom analysis has been presented by dividing the CLEAN outcome into directional cones.

Besides the analysis of microbarom observations, the climatology involves the reconstruction of omnidirectional soundscapes from the perspective of I23FR (chapter 4). Section 5.5 describes the soundscapes and how to interpret results obtained from them. From the soundscapes, it stands out that the most dominant microbarom source regions are relatively close to the island (Figures 5.8 and 5.11), which may be the reason that the microbaroms are resolved clearly despite the very high wind noise levels. The microbarom signals are therefore significantly less affected by atmospheric propagation effects. A direct comparison between the dominant source contributions from soundscape simulations and observations is presented in section 5.6. Within this section, a comparison method between soundscapes and CLEAN observations have been introduced and presented (Figure 5.14 and 5.15). The 'cone' partition transforms the resolved microbarom point source contributions of the beamforming detectors into microbarom source regions.

Although the comparison shows similarities in direction and frequency content, there is a notable SPL difference between observations and soundscapes. Within this study, the soundscapes only account for the theoretical contribution of microbaroms between 0.069-1.095 Hz. Additional source contributions within this frequency range are not taken into account. Furthermore, the beamforming outcome is affected due to the effects of incoherent noise within the recordings.

Moreover, within the reconstruction of the soundscapes, the transmission loss from each position in the grid to the infrasound array location at Kerguelen island is computed using an empirical relation [Le Pichon *et al.*, 2012; Tailpied *et al.*, 2016]. This class of empirical propagation loss functions is derived as a functional fit to transmission loss curves computed using the PE method. This model can be used to approximate the losses due to propagation in a stratospheric duct, but is inappropriate to quantify losses due to tropospheric and thermospheric ducting. Furthermore, cross-winds are not taken into account by applying this propagation model. These winds influence the propagation conditions [Smets and Evers, 2014*a*; Assink *et al.*, 2018; Blixt *et al.*, 2019], which may explain the differences in dominant source angle between observations and soundscapes (Figure 5.13). The use of formal propagation models requires atmospheric specifications from the ground to the upper atmosphere. As upper atmospheric specifications are typically limited to climatologies, this has implications for the accuracy of thermospheric returns [Assink *et al.*, 2012; Drob, 2019].

Nonetheless, the comparison between soundscapes and observations is promising. The soundscapes are generated from an initial 2DFD file that contains 30 frequency steps (0.0345-0.5476 Hz), which results in a soundscape reconstruction for propagating microbaroms ranging between 0.069-1.095 Hz. Based on the comparisons, it can be concluded that soundscapes give a good insight into the contribution of microbaroms within the infrasonic wavefield. Moreover, soundscapes can also be used for spectral analysis of the source regions. From the frequency analysis of both the soundscapes and observations, it follows that the microbarom signals are contained in a broad frequency range spanning from 0.1 to 0.5 Hz during the austral winter. Figure 5.16 shows the central frequency content of the various microbarom source regions extracted from the soundscapes during one day of the austral summer and winter. The dominant microbarom source direction for the different periods (Figure 5.6, 2015 January 01 and 2015 July 01) is highlighted as a cone, whereas the remaining source regions are made transparent. The initial microbarom source model of the soundscapes is based on Waxler *et al.* [2007], which account for the effects of bathymetry. Therefore, the bathymetry features [GEBCO, 2020] are highlighted within the figure by the grey contour lines. Spectral analyses of the microbarom source regions provide insights into the frequency signature of the global ambient noise field [Campus and Christie, 2010; Marty, 2019]. The microbarom source peak is typically estimated to be at 0.2 Hz. However, within this study it has been shown that the microbarom frequency range is shifting seasonally. Knowing the frequency signature of the microbarom source regions enables to distinguish between different source regions, and specifically characterize and identify these. Implementing the operational 2DFD model of the ECMWF, with 36 frequency steps (0.0345-0.9695 Hz) and 36 directions, will provided additional insight into the higher frequency signature (0.069-1.939 Hz).

The climatology analysis has addressed the differences between soundscapes and observations, which is essential for future improvements of the detection algorithms and soundscape reconstructions. Moreover, the combination of observations and soundscapes may enhance the filtering of microbarom source contributions within the infrasonic wavefield. In conclusion, this new knowledge contributes to a better verification of the CTBT and better applicability of infrasound as a remote sensing technique for the upper atmosphere [Donn and Rind, 1972; Smets, 2018]. The climatology analysis as performed within this paper can act as guidance. The analysis is modular and can be applied to any infrasound station or place on earth. Moreover, the analysis could play a role in the installation of future infrasound arrays. The soundscapes provide insights into the expected microbarom exposure at (future) infrasound arrays.

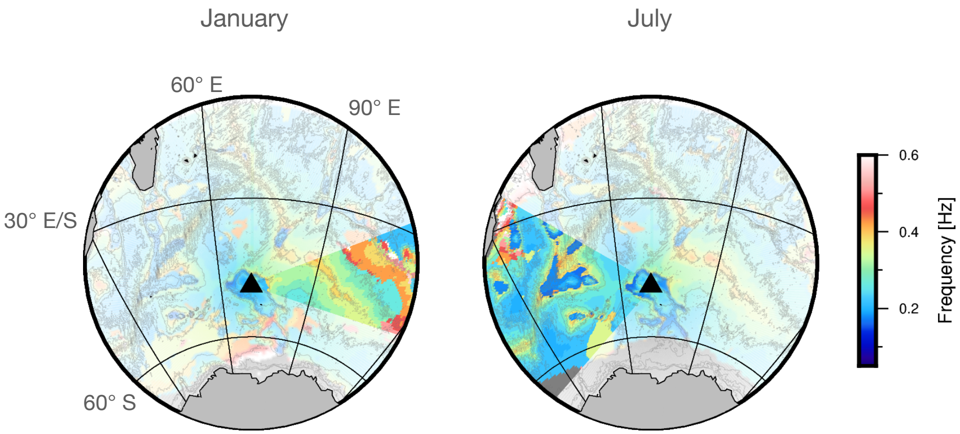

Figure 5.16: *Spatial frequency analysis of two synthetic soundscapes during austral summer (a, 2015 January 01) and winter (b, 2015 July 01). The grey overlayed contour lines within the panels indicate the bathymetry from GEBCO 2020 [GEBCO, 2020]. The cone indicates the dominant microbarom source direction at 2015 January 01 and 2015 July 01, respectively.*

6

Conclusions and recommendations

Religion is a culture of faith; science is a culture of doubt.

Richard P. Feynman

In this final chapter, the conclusions of the previous chapters will be summarised, and recommendations will be given for future research.

6.1 Conclusions

This dissertation contributes to developing methods to characterise and identify the ambient infrasonic noise field (i.e., microbaroms) by presenting novel methods for: measuring, processing and modelling infrasound. Knowledge regarding the infrasonic wavefield is of great interest for a better verification of the CTBT and applicability of infrasound as a remote sensing technique for the upper atmosphere. Understanding the ambient noise field is needed to identify sources of interest like nuclear-test explosions. The signals of such sources can be hidden by ambient noise or masked by other, more dominant, noise signals. Especially low-yield atmospheric and underground explosions are likely to be masked by microbaroms [Bedard *et al.*, 2000; Haak and Evers, 2002; Golden *et al.*, 2012]. Sparse infrasound sensor arrays and most infrasound processing tools limit the ability to distinguish interfering infrasound sources. In this dissertation, it has been shown how the infrasonic wavefield can be unravelled into contributions of noise and several sources. As such, sources like nuclear-test explosions can be enhanced and extracted from the complex wavefield. The ambient infrasonic noise field has been unravelled in four consecutive stages.

Firstly, a new approach for monitoring the infrasonic wavefield, and concurrently measuring the influence of the atmosphere has been addressed. Cost-efficient sensor technology has been implemented and applied to complement existing sensor networks. The use of such sensor platforms enables to increase the number of stations in an economical way. Moreover, it allows an increase of spatial resolution and mobile deployments. The applied sensor technology within this thesis is known to be less accurate than existing high-fidelity equipment. However, rapid innovation processes will lead to an increase of sensor resolution, which is beneficial for the spatial resolution and accuracy of a measurement. Chapter 2 shows how MEMS accelerometers have improved over two years of research and development. Platforms, as described within this dissertation, complement scientific studies and will lead to the application of interdisciplinary studies. Chapter 4 demonstrates how cost-efficient sensor platforms, the INFRA-EAR, have provided new insights in the microbarom wavefield within the Southern Ocean, which has lead to the reconstruction of microbarom soundscapes.

Secondly, this thesis presents various data processing techniques, which have been applied on infrasonic data. Within chapter 3, CLEAN beamforming has been introduced. The CLEAN algorithm iteratively removes the most dominant source contribution from the f/k spectrum by including the array response and deconvolving the f/k spectrum with it. Therefore, this algorithm distinguishes multiple source contributions within overlapping time and frequency segments besides the most dominant source. This way of data processing enables to charaterize the incoming wavefield and decompose it into various source contributions (i.e., divide signals based on apparent velocity, frequency, back azimuth).

Thirdly, a method has been introduced for the reconstruction of ambient synthetic infrasoundscapes. The soundscapes account for all omnidirectional microbarom source regions in the vicinity (~ 5000 km) of an infrasound sensor. The initial input is any 2DFD ocean-wave model for the calculation of the microbarom source regions. Long-range propagation is accounted for by applying a range and time-dependent atmospheric and propagation model based on PE [Le Pichon *et al.*, 2012; Tailpied *et al.*, 2016]. The reconstructed soundscapes are directly compared with in-situ (the INFRA-EAR, chapter 2) and remote microbarom observations (I23FR Kerguelen Island, chapter 5). From the comparison, it has been concluded that the soundscapes are in agreement with these observations. Previously, only a few studies have considered evanescent microbaroms, which are only detectable directly above the microbarom source regions. Within this study, the evanescent microbarom component has been recorded for the first time by the INFRA-EAR. The theoretical and observed evanescent microbarom component has been analysed and compared with the synthetic reconstructed evanescent contribution.

Fourthly, a climatology study has been performed in which the methodologies described in chapters 3 and 4 are used in concert. The study presents a comparison between the infrasonic model and observational data. The outcome states that the soundscapes (chapter 4) are a valuable first approach. There is a good agreement between observed and modelled source back azimuth and frequency. However, the amplitude difference between model and observations suffers due to the lack of vertical resolution within the long-range propagation model, and uncertainties within the microbarom source model (e.g., limited ocean-wave model resolution). Moreover, it has been shown that a comparison between microbarom observations and soundscapes have to be performed omnidirectionally. The entire microbarom source field contributes and influences the total acoustic power of the infrasonic wavefield, which consists of multiple sources.

■ Conclusions from chapter 2 on Atmospheric monitoring techniques

The monitoring principle of atmospheric pressure perturbations, infrasonic waves, is explained in chapter 2. Within this chapter, the INFRA- and Multi-EAR are introduced, two cost-efficient multidisciplinary sensor platforms. Both platforms concurrently measure various geophysical parameters (i.e., barometric pressure, infrasound, accelerations, GPS, wind, temperature, humidity). Within chapter 2, the design, development and calibration of the platforms are explained. The applied sensor technology is based on digital Micro-electromechanical systems (MEMS). These MEMS are small single-chip sensors that combine electrical and mechanical components and have low energy consumption. Moreover, there is rapid development and improvement on these sensors in terms of sensitivity, resolution, accuracy and robustness while being cost-efficient.

Although the MEMS are not as accurate as high-fidelity equipment, the provided sensor platforms complement existing high-fidelity geophysical sensor networks. This study shows that, as long as the MEMS are well-calibrated, they perform in agreement with the reference sensors. Therefore, they can provide observations during remote or rapid deployments (e.g., albatrosses, weather towers and balloons).

■ Conclusions from chapter 3 on Data processing techniques

Beamforming can be applied as a data processing technique to separate the coherent and incoherent parts of the infrasonic wavefield. In addition, beamforming enables resolving the wavefront amplitude, back azimuth, frequency, and apparent velocity while impinging an infrasound array. Within chapter 3, various beamforming methods are introduced and theoretically derived. The chapter includes synthetic and real data examples to present the outcome and performances of the methods. A selection of high-resolution beamforming methods have been compared, with particular attention to the classical beamforming methods of Bartlett, Capon and MUSIC.

Besides the general introduction to beamforming, the chapter addresses CLEAN beamforming. CLEAN is a post-processing method to resolve multiple spatial distributed sources within overlapping time and frequency segments. Other beamforming algorithms often only identify the most dominant source. However, the ability to resolve and distinguish between multiple sources is crucial for fully unravelling the infrasonic wavefield.

The enhanced beamforming resolution of CLEAN improves the ability to resolve multiple microbarom sources. In addition, decomposed microbarom observations can be helpful in the assessment of microbarom source models [Waxler *et al.* [2007]; chapter 4; chapter 5] as well as in the remote sensing of the middle and upper atmosphere for which microbarom signals have been used in previous research [Donn and Rind, 1972; Smets, 2018]. Besides the application to infrasound arrays, the algorithm can improve the detection ratio of arrays with unfavorable array responses because of a limited number of sensors.

■ Conclusions from chapter 4 on infrasonic soundscapes

In chapter 4, a reconstruction method for infrasonic soundscapes has been presented. These soundscapes use as initial source model the deterministic microbarom source model by Waxler *et al.* [2007]. The empirical propagation model of Le Pichon *et al.* [2012] and Tailpied *et al.* [2016] is used to accounted for long-range propagation. Both model inputs (ERA5 HRES 2DFD reanalysis ocean-wave model and ERA5 HRES atmospheric reanalysis model) have been interpolated over a stereographic polar grid, with an infrasound sensor as polar position. Soundscapes have been generated and are compared within this chapter with in-situ infrasound observations by the INFRA-EAR (chapter 2) and remote infrasound observations by I23FR (chapter 5). Soundscapes give insight into how much various source regions contribute to the total acoustic power measured in the microbarom band. Earlier studies have been limited to analysing normalised microbarom amplitudes, i.e. no absolute microbarom power values. Furthermore, earlier work focused on the maximum contribution of a specific region. However, all omnidirectional source contributions within the ambient noise field contribute to infrasound observations and thus need to be considered within the synthetic soundscape reconstruction. Previously, only a few studies have considered evanescent microbaroms, which are only detectable directly above the microbarom source regions. Within this study, the evanescent microbarom component has been recorded for the first time by the INFRA-EAR. The theoretical and observed evanescent microbarom component has been analysed and compared with the synthetic reconstructed evanescent contribution.

Furthermore, this chapter addresses the comparison of soundscapes while using different initial microbarom source models (i.e., Waxler and Gilbert [2006] and Waxler *et al.* [2007], which assume a finite and infinite ocean depth, respectively). The integrated SPL has been determined for the frequency range of 0.2-0.35 Hz for both infrasound observation and ambient soundscape. The in-situ measurements of the INFRA-EAR occur directly above the microbarom source region. According to De Carlo *et al.* [2020*a*] it is therefore relevant to account for the near-vertical propagation of the propagating microbaroms [Waxler *et al.*, 2007; De Carlo *et al.*, 2020*a*]. Near-vertical propagation of propagating microbaroms, however, is not applicable to distant ground-based IMS arrays, because these are not refracted in the atmosphere and not observed at long ranges. Therefore there is no need to include finite-depth ocean effects within these soundscapes [De Carlo *et al.*, 2020*a*].

In addition, spatial and frequency analyses of the ambient soundscapes are performed, which shows that the microbarom source regions cluster around bathymetry. Moreover, there is an amplitude increase around these features. Nonetheless, the observations by the INFRA-EAR include overlap of evanescent and propagating microbaroms within the frequency range of 0.1-0.3 Hz. For a sufficient comparison between soundscapes and observations, and the effect of near-vertical propagation effects, the observations should not include the evanescent microbarom component (i.e., stratospheric scientific balloon measurements [Bowman *et al.*, 2015])

■ Conclusions from chapter 5 on the climatology study

In this study, a climatology of microbarom signals at I23FR has been performed over five years of data (2015 - 2020). This array is one of the microbarometer arrays of the IMS and provides real-time measurements of the infrasonic wavefield as well as basic meteorological parameters [Marty, 2019]. The array is located at the Kerguelen Islands, an island within the Southern Ocean, and is part of the IMS for the verification of the CTBT. The climatology analysis addresses the expected ambient noise levels, propagation paths, and potential sources within the vicinity of an infrasound sensor ($\sim$ 5000+ km). Time and frequency domain beamforming methods (chapter 3) have been applied to analyse the infrasonic wavefield from the I23FR observations. Soundscapes (chapter 4) are computed and compared with beamform results.

The climatology analysis addresses the differences between soundscapes and observations, which is essential for future detection algorithms and soundscape reconstructions. Understanding the full wavefield allows for extracting the different sources like continuous ambient noise and deterministic transient signals like those from, e.g., nuclear tests and volcanos. In conclusion, this new knowledge contributes to a better verification of the

CTBT and better applicability off infrasound as a remote sensing technique for the upper atmosphere [Donn and Rind, 1972; Smets, 2018]. The analysis as performed within this chapter should be repeated for all IMS arrays and other operational microbarometer arrays in order to map the background infrasonic wavefield. Doing so, deterministic transient signals of sources of interest can be uniquely identified even if hidden in the noise (i.e., at SNR < 1).

6.2 Recommendations and outlook

As shown within this dissertation, various infrasound sources occur within overlapping frequency and time segments. Often the most dominant source contribution is resolved by conventional array processing techniques for the detection and characterization of infrasonic events. The infrasound sensors and models, however, contain more information. It is therefore of importance to consider consider all (noise) sources contributing the observed complex wavefield.

■ Cost-efficient modernisation of sensor networks

The famous Dutch proverb "Meten is weten" (to measure is to know) was once coined by Dutch Nobel laureate Kamerlingh Onnes and is still a famous saying today. To advance our understanding of the infrasonic wavefield, increasing the spatial sampling of both infrasound and the ambient meteorological conditions is essential. Chapter 2 introduces cost-efficient multidisciplinary sensor platforms, which concurrently measure infrasound, accelerations, and meteorological conditions. Typical geophysical measurement platforms still provide logging solutions for a single parameter due to different community standards and the higher cost rate per added sensor. The joint analysis of multiple geophysical parameters benefits studies and real-time monitoring of natural hazards.

The INFRA-EAR was designed, and has been used, as biologger for the Wandering Albatross. Chapter 4 describes how the data has been used to create a reconstruction method for infrasonic soundscapes. The Multi-EAR is partly ready for integration within field campaigns, or existing monitoring network. E-Surfmar is the first collaborative partners of the Multi-EAR. E-Surfmar is part of EUMETNET (European Meteorological Service Network) and led by Marijn de Haij (KNMI-RDWD). Within the E-Surfmar a barometer comparison has been performed. Pressure is the most important parameter measured at sea for Numerical Weather Prediction. National Meteorological Services (NMS) such as KNMI are used to equip voluntary observing ships with high level standard barometers, with a low uncertainty and drift. However, the sources of uncertainties on pressure measurements on a ship are numerous (e.g., changing height of barometer, wind effects, waves, air conditioning). Barometer prices vary between tens to several thousands of euros. Therefore it is worth wile to test, and compare, various barometers in a calibration lab, as well as in real conditions. Inter-comparison will show the measurement quality, robustness, and cost/benefit ratio over longer periods of deployment. The study will focus on digital barometers that can easily be integrated in the TurboWin+ software, on which Automatic Pressure Report solutions are already available for some NMS.

Although the MEMS sensors are not as accurate as high-fidelity equipment, it has been shown that this sensor technology can be used within scientific monitoring campaigns. Moreover, MEMS technology is improving rapidly. Therefore, it is expected that these sensors will improve significantly over the coming years [D'Alessandro *et al.*, 2014]. Furthermore, MEMS are cost-efficient. The application of sensor arrays on one platform will allow for output summation, which improves the SNR. In addition, one high-cost high-fidelity sensor can be complemented with a large number cost-efficient sensors. The high-fidelity sensor can then be used for calibration while the large number of cost-efficient sensors contributes into higher resolution in the spatial and temporal domain. As such, the absolute value measured by the cost-efficient sensor is not of interest, but its relative value. The deployment of cost-efficient sensor platforms can therefore lead to higher temporal and spatial resolution monitoring of the infrasonic wavefield.

Moreover, the presented sensor platforms require low-voltage and are relatively small in dimension. Mobile measurement campaigns are enabled thanks to such platforms. The power supply can either be provided by an external power supply or a solar panel. Therefore the possible implementations of mobile, cost-efficient sensor platforms are many. Equipped scientific balloons and drones will enable atmospheric altitude measurements or infrasonic measurements directly above the sources (e.g., volcanos, earthquakes, oceans, waterfalls). Marine buoys with sensor platforms will provide insights into the infrasonic wavefield in the middle of the ocean (as shown in chapter 4), and can be used by oceanographers for monitoring the sea-state. The existing meteorological sensor network may increase its spatial resolution by the implementation of cost-efficient sensor technology, which will lead to a better comparison (and later validation) of the weather models. In general, current high-fidelity sensor and sensor network often suffer from under sampling parameters or vector fields in the spatial and temporal domain. The addition of cost-efficient sensors can strongly increase both the spatial and temporal resolution and as such the characterisation of wavefields and scalar parameters.

■ Application of soundscapes

The use of mobile sensor platforms, and the ability to resolve multiple infrasonic sources within overlapping time and frequency segments, have enabled new insights into infrasonic ambient noise. Based on microbarom observations, a reconstruction method has been developed for microbarom soundscapes based on an initial microbarom source model and an empirical atmospheric propagation model.

There is a good agreement between source back azimuth and frequency content. The amplitude, however, between soundscapes and observations differ. The empirical formulation of sound propagation by Le Pichon *et al.* [2012] and Tailpied *et al.* [2016] is modelled along the great circle path from source to the receiver only, neglecting out-of-plane propagation effects. This model can be used to approximate propagation losses in atmospheres with a dual (stratospheric-thermospheric) duct and neglects tropospheric ducting. A different approach could involve using a 3-D ray-theory model cast in spherical coordinates [Smets, 2018; Blom, 2019] to quantify propagation losses, a normal modes model, or a full-wave propagation model. The use of formal propagation models requires atmospheric specifications from the ground to the upper atmosphere. As upper atmospheric specifications are typically limited to climatologies, this has implications for the accuracy of thermospheric returns [Assink, 2012; Drob, 2019]. Therefore, it is recommended to investigate a follow-up on the PE propagation model by Tailpied *et al.* [2016], which solves the long-range propagation assumptions, before addressing significant changes in the initial microbarom source model.

Nevertheless, it has been shown within chapter 5 that the soundscapes provide insight into the microbarom source contributions around an infrasound array. It is recommended that this analysis is carried out for infrasound arrays worldwide, including those within the IMS infrasound network, to understand the microbarom contributions to the observations better. Moreover, within this dissertation, the soundscapes are generated for microbarom signals. The infrasonic wavefield, however, consists of more source signals. It is therefore recommended to investigate the reconstruction of soundscapes based on other infrasonic sources.

■ Beamforming uncertainties

Within chapter 3 of this dissertation, various data processing techniques are introduced and implemented. Most infrasound processing routines are designed to only detect the dominant infrasonic signal in a given time segment and frequency band. Nevertheless, various beamform techniques exist in the literature that allow for the detection of signals from multiple spatially distributed sources [Viberg and Krim, 1997; Rost and Thomas, 2002]. The ability to detect and classify interfering sources relies on the beamform resolution as quantified by the array response, determined by the beamform technique and the array layout. Ideally, the array response consists of one lobe, the main lobe. The peak of the main lobe determines the resolution and is favourably a delta function. The shape of the main lobe determines a main circular lobe corresponds to an isotropic response in which the array is equally sensitive to all directions. A low beamform resolution could make the array incapable of estimating wavefront parameters accurately in situations where there are either one or multiple sources in the vicinity of the array.

The enhanced beamforming resolution of CLEAN improves the capabilities of infrasound as a monitoring technique. This benefits from infrasonic monitoring of nuclear tests and natural hazards, such as volcanoes, earthquakes, and hurricanes.

Nevertheless, such deconvolution method for array response optimization are not always taken into account. The main lobe's sharpness and shape have not been compensated within beamforming algorithms. Neele and Snieder [1991] and Dost [1987] have introduced and implemented a data-driven and manual correction factor to shape the array response towards delta function, respectively. However, the application of such correcting factors biases the remainder of the f/k spectrum, resulting in more dominant side lobes. It is therefore recommended to investigate an algorithm that accounts for the artefacts caused by the array design. Such a correction algorithm depends on the parameters of the signals of interest (e.g., back azimuth, apparent velocity, frequency) and the array design. Such an optimisation algorithm should result in a dynamic and changing algorithm over various source contribution within different time segments. The array response will be optimised towards a delta function shaped response without generating side lobes.

Moreover, the Fourier transform applied to the data (frequency-domain beamforming) can possibly smear the infrasonic source contributions within the time-domain recordings. Averbuch [2021] stated that the short-time Fourier-transform (STFT), often used as the basis for advanced signal processing techniques, can present the time-domain recordings into a smeared frequency spectrum, due to the inexact phase information in some time-frequency elements. Therefore, an STFT may bias the data processing before the application of any beamforming technique. Averbuch [2021] re-introduces the reassigned spectrogram (RS) to compromise the artefacts made by the STFT. It was shown that the RS can provide a more exact time-frequency representation of deterministic signals and significantly improves beamforming results. Nonetheless, the RS is not robust, like the STFT. The application of the RS is therefore not always favourable. It is recommended to investigate the use of STFT and RS, to generate a robust Fourier transform without smearing the frequency spectrum.

Furthermore, the introduced beamforming techniques in chapter 3 do not present statistical uncertainties. Olson and Szuberla [2004] introduced a method to determine the statistical confidence in estimates of the direction and velocity of signals impinging infrasound arrays. However, this method does not present multi-paths and multiple spatially distributed source effects within the infrasonic wavefield. An extension of the method proposed by Olson and Szuberla [2004] for CLEAN beamforming is recommended.

In addition, beamforming methods resolve sources contributions and represent the frequency, apparent velocity, and back azimuth content of this source as a point source from the perspective of an array. Although CLEAN beamforming enables to resolve multiple source contributions, these are still represented as point sources with a Gaussian distribution. Whenever CLEAN resolves a contribution outside an earlier classified source, a new source contribution is added. Microbarom source regions are known to be large and dynamic areas (chapter 4). It is, therefore, reasonable to state that the CLEAN algorithm may classify various point sources that originate from the same microbarom source region.

Figure 6.1 represents a theoretical case study. In this case, the CLEAN algorithm resolves and classifies multiple source contributions (Figure 6.1-a). The Gaussian source distribution determined using the CLEAN algorithm is symbolized by the orange circles, where the red cross represents the centre. The yellow contour lines symbolize the initial source area. From where the microbarom signals have propagated, the source area is characterized within (Figure 6.1-b). This source region is dynamic and large and has higher and lower intensity areas. Although the CLEAN algorithm classifies multiple point sources (black crosses) into three Gaussian distributed point sources, in practice, all the resolved contributions add to one source area with varying source intensities (Figure 6.1-c).

Within section 5.5, a post-processing method has been applied to the CLEAN beamforming results. Here the beamforming outcomes are clustered within 10° Gaussian cones. The classification of a microbarom source within the CLEAN algorithm, as proposed in chapter 3, is based on a Gaussian distribution. When the algorithm resolves a source signal, it is compared to earlier resolved sources and added a new source signal if it does not match earlier source content. However, due to this approach, microbaroms are classified as 'point sources'. These point sources may correspond to the same microbarom source region. It is therefore recommended to apply a post-processing analysis to the CLEAN outcome, in order to define source regions instead of source points. This can either be done by the use of a gap measure (e.g., SORTE, section 3.3.2) or an image-processing technique (e.g., the Hough transform [Averbuch *et al.*, 2018]). Such applications indicate the correlation between the resolved point-sources, and therefore may distinguish the various microbarom source regions.

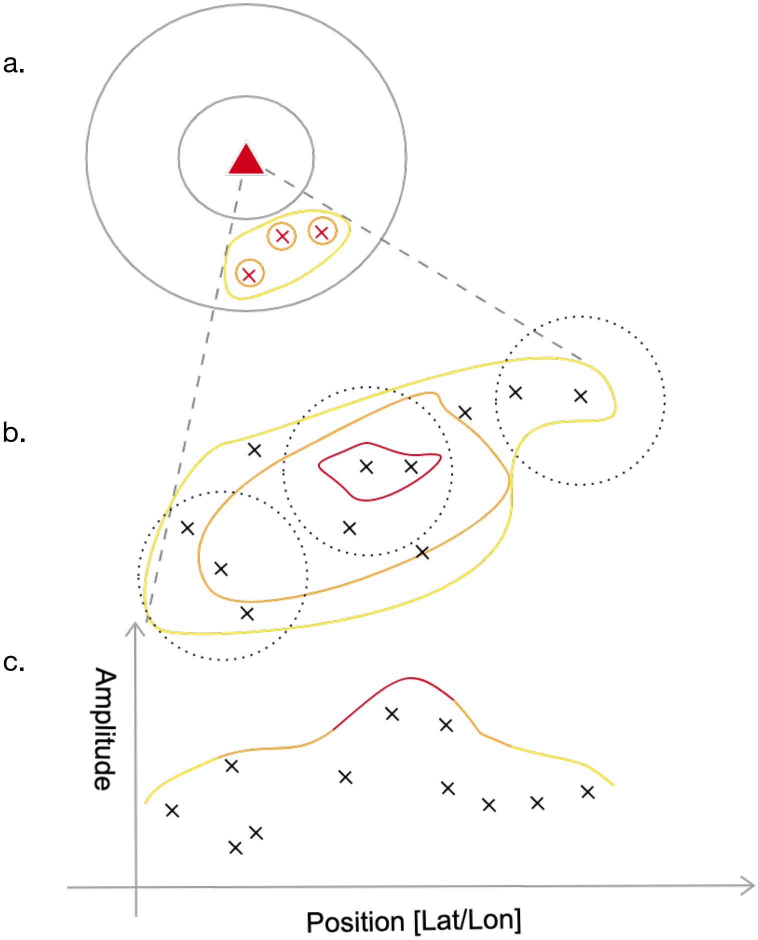

Figure 6.1: *A schematic overview of distinguishing various parts of a microbarom source region from the perspective of an infrasound array (red triangle). (a) The theoretical outcome of the CLEAN beamforming algorithm (chapter 3). The grey circles indicate the applied slowness grid of the beamforming algorithm. The yellow area is the initial outcome of the Capon/Bartlett beamformer. The orange circles indicate the Gaussian source distribution of the resolved point sources (red crosses). (b) Shows the conceptional corresponding microbarom source region within a soundscape. The yellow, orange, and red contour lines indicate the source intensities within the area. The grey crosses are the iterative sources resolved by the CLEAN algorithm. Whereas the dotted circles indicate the pseudo point sources. (c) The analysis of the source region in perspective of amplitude and position. The resolved CLEAN sources are highlighted within this figure.*

■ Decomposing of microbarom source contributions

As follow-up, the application of the various presented high-resolution tools in concert can potentially be used to decompose ambient noise contributions from the infrasonic wavefield. Synthetic microbarom soundscapes provide information regarding the expected source contributions of microbaroms within the wavefield. Adopting the temporal and spatial information from the soundscapes enables characterising individual components from the CLEAN beamforming analysis. A deconvolution function can be generated based on the input of both model and observations. A pre-defined deconvolution of the microbarom source contributions from the data will suppress the microbarom source contributions within the wavefield and increase the SNR of the signals of interest. As such, the decomposing of microbarom source contributions is based on both frequency and wavenumber (f/k).

As a case study, a synthetic data example has been created. A meteor from outer space has been simulated to enter the atmosphere at 50°E/50°S on 22-04-2019 around 2200UTC. The most nearby positioned IMS infrasound array is I23FR. This dissertation has shown that I23FR experiences extreme local noise conditions while resolving microbarom signals. Synthetic soundscapes (Figure 6.2-a) indicate the dominant microbarom source direction, amplitude, and frequency content over two days around the synthetic event has been obtained. These parameters are used to generate synthetic waveforms for the elements of I23FR (Figure 6.2)-b). The waveforms include continuous microbarom source signals ($\sim 300^\circ$ BAZ) and a transient meteor event ($\sim 250^\circ$ BAZ). Figure 6.2-c shows the integrated spatial microbarom soundscape for I23FR (triangle) during the meteor arrival (star). Panel (d) indicates the outcome of the CLEAN analysis on the synthetic waveforms. The algorithm has resolved both the microbarom and transient source.

Combining the soundscapes and the CLEAN analysis generates double-sided information regarding the microbaroms used to characterise them. Such information allows for the estimation of an expected array response of the microbarom source component. Deconvolution of this microbarom response from the data (Equation 3.4.1) will generate a first approximation of spatial decomposition of microbaroms. Panel (e) presents the outcome of the CLEAN algorithm after the microbarom source component has been characterised and decomposed from the data.

It is recommended that such applications of decomposing techniques are further investigated in future studies. Nevertheless, fundamental improvements to the analysis can already be highlighted. Although there is a good agreement in the resolved directionality of the microbaroms between model and observations, the model is less accurate due to the empirical propagation model. Future steps will need to compute a propagation model that includes the tropospheric propagation paths and out-of-plane propagation. Such a model may improve the agreement in directionality and amplitude between soundscapes and observations.

Moreover, the apparent velocity of the infrasonic signal at an infrasound array is not resolved from the soundscapes. The comparison between model and observations is therefore limited to frequency, amplitude, and back azimuth. The apparent velocity is strongly dependent on ducting conditions within the propagation path between source and receiver. Therefore this can be estimated if the direction is known.

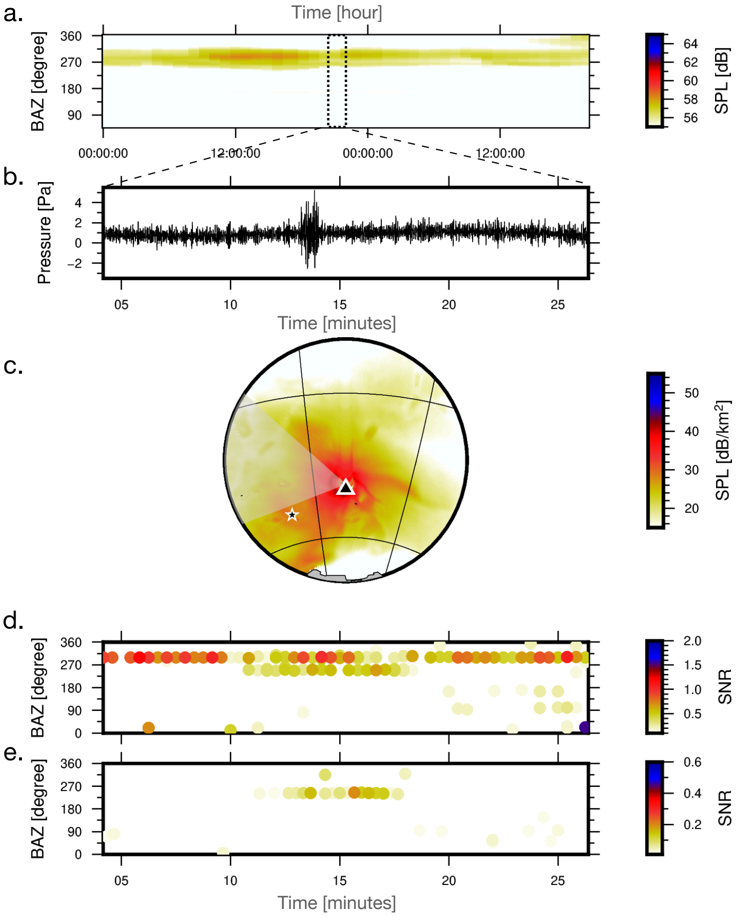

Figure 6.2: *Decomposing microbarom source contributions from the infrasonic wavefield. (a) Spectrogram of the microbarom source contribution as a function of time and back azimuth. (b) A synthetic waveform, consisting of microbarom signals with the signature obtained from panel (a) and a transient source at 14 min after the start of the trace. (c) The synthetic microbarom soundscape at the time of the transient event. The triangle indicates the infrasound array location, and the star the source location of the transient. The transparent cone indicates the microbarom source region, as shown in panel (a). (d) The CLEAN beamforming outcome of the transient event. The microbarom signal is resolved at 300 degrees back azimuth. The transient is resolved from 11 until 17 minutes of the trace due to the window size of the beamformer. (e) Shows the CLEAN result after the microbarom signals are decomposed from the data. The decomposing of microbarom signals is based on the information of the synthetic soundscapes combined with the CLEAN outputs.*

A

Derivation of the infrasonic wave equation

The derivation of the acoustic wave equation follows the fundamental equations of fluid dynamics: the conservation of mass, conservation of momentum, in addition to a constitution relation or equation of state. From these equations, the linear equation of the perturbation method will be derived [Brekovskikh, 1973; Gossard and Hooke, 1975; Wapenaar, 2014; Pierce, 2019]. Subdividing the linear perturbation method will lead to the derivation of the linear wave equation, which is computationally efficient to resolve small perturbations. Large perturbations, however, can not be solved by the linear perturbation method. Within this appendix, the fundamental conservation laws and the perturbation method are introduced and elementary derived. A thorough derivation can be found within literature (e.g., Brekovskikh [1973]; Gossard and Hooke [1975]; Assink [2012]; Wapenaar [2014]; Pierce [2019]).

A.1 Conservation of Mass

For the derivation of the conservation of mass, consider a fluid in motion with particles moving in space ($\vec{r}(x, y, z)$) at a specific time (t) with a dependent velocity ($\vec{v}(\vec{r}, t)$). The volume density of the mass is assumed to be depended on space and time ($\rho(\vec{r}, t)$). A fixed volume (V) inside the fluid is enclosed a surface (S) with an outward pointing normal vector ($\vec{n}$) [Welty *et al.*, 2020].

The law of conservation states that the time rate of change of mass in V is equal to the incoming mass flux through S, increased with the time rate of mass injection:

$$\frac{\partial}{\partial t}\int_V \rho \, dV = -\oint_S \rho\vec{v}\cdot\vec{n}\, dS + \frac{\partial}{\partial t}\int_V i_m \, dV \tag{A.1.1}$$

where $i_m(\vec{r}, t)$ represents the volume density of mass injection. Applying the theorem of Gauss to equation A.1.1 results in:

$$\int_V \frac{\partial \rho}{\partial t}\, dV = -\int_V \nabla\cdot(\rho\vec{v})\, dV + \int_V \frac{\partial i_m}{\partial t}\, dV \tag{A.1.2}$$

Since this holds for any volume (V), the non-linear equation of continuity can be written:

$$\frac{\partial \rho}{\partial t} + \nabla \cdot (\rho \vec{v}) = \frac{\partial i_m}{\partial t} \tag{A.1.3}$$

A.2 Conservation of Momentum

When deriving the conservation of momentum, the same volume (V) with an enclosed surface (S) and field variables are considered. This law states that the rate of change of momentum of the particles in V is equal to the incoming momentum flux through S, increased with the resultant force acting on the particles in V (Newton's second law):

$$\frac{\partial}{\partial t} \int_V \rho \vec{v} \, dV = - \oint_S (\rho \vec{v}) \vec{v} \cdot \vec{n} \, dS + \vec{F}(V) \tag{A.2.1}$$

where

$$F(V) = - \oint_S p \vec{n} \, dS + \int_V \vec{f} \, dV \tag{A.2.2}$$

here $p(\vec{r}, t)$ denotes pressure and $\vec{f}(\vec{r}, t)$ the volume density of the external forces.

Applying the theorem of Gauss to Eq. A.2.1 results in:

$$\int_V \frac{\partial (\rho \vec{v})}{\partial t} \, dV = - \int_V \left[\vec{v} \nabla \cdot (\rho \vec{v}) + (\rho \vec{v} \cdot \nabla) \vec{v} \right] dV - \int_V \nabla p \, dV + \int_V \vec{f} \, dV \tag{A.2.3}$$

Again this holds for any given volumes, and thus Eq. A.2.3 can be re-written as the non-linear equation of motion

$$\frac{\partial (\rho \vec{v})}{\partial t} + \vec{v} \nabla \cdot (\rho \vec{v}) + (\rho \vec{v} \cdot \nabla) \vec{v} = - \nabla p + \vec{f} \tag{A.2.4}$$

A.3 Equation of State

In addition to the conservation of mass and momentum, an equation of state is needed that relates the various physical quantities.

Consider the fluid volume as an ideal gas. The pressure p, volume density ρ, and temperature T are mutually dependent. By combining the three fundamental gas laws (Charles law, Boyle's law, Gay-Lussac's law), the air volume can be described by the ideal gas law:

$$pV = MRT \tag{A.3.1}$$

where M is the molar mass of a given gas, $R = R^*/M$ represents the specific gas constant, with $R^* = 8.314\text{J kg}^{-1}\text{mol}^{-1}$ being the ideal gas constant.

Commonly the pressure and density of an atmospheric air volume is scaled to dry air in the ideal gas law by a virtual temperature. The equation of state expresses that the pressure, density, and temperature of a fluid are mutually dependent. The most general, and non-linear, representation of the equation of state is:

$$X(p, \rho, T) = 0 \tag{A.3.2}$$

Assuming that the compression and rarefaction (Figure 1.1-a) of a wave motion occurs adiabatic, and thus heat exchanges are neglected, the adiabatic speed of sound c_T at constant entropy E_s can be expressed by the equation of state as [Zemansky, 1968]:

$$c_T^2 = \left(\frac{\partial P}{\partial \rho}\right)_{E_s} \tag{A.3.3}$$

Equation A.3.3 relates the propagation speed to the medium's compressibility and density, which can be related to the isentropic bulk modulus or stiffness coefficient $K \leq 0$. For an ideal gas the bulk modulus can be expressed as:

$$K = \gamma P \tag{A.3.4}$$

where $\gamma = C_p/C_v$ represents the ratio of heat capacity at constant pressure to the heat capacity at constant volume. Expressing equation A.3.3 in terms of the isentropic bulk modulus, the equation of state becomes:

$$c_T^2 = \frac{K}{\rho} \tag{A.3.5}$$

which is known as the Newton-Laplace equation. Substituting equation A.3.4 into A.3.5 yields the adiabatic speed of sound for an ideal gas, as formulated in section 1.3.

A.4 Perturbation method

Applying the assumptions of the perturbation method (Chapter 1, equation 1.0.4) on the basic conservation laws will result in the linear equations of state:

$$\overline{p}\Big(1 + \frac{p'}{\overline{p}}\Big)\overline{\rho}^{-\gamma}\Big(1 + \frac{\rho'}{\overline{\rho}}\Big)^{-\gamma} = \overline{p}\overline{\rho}^{-\gamma} \tag{A.4.1}$$

In general the wave velocity $\vec{v}(\vec{r}, t)$ represents the actual traveling velocity superimposed by the constant flow of the basic state. Within the linearisation of the basic consevration laws, it is assumed that the only the particle velocity of the travelling waves are represented by the velocity vector. Therefore the linear equation of the conservation of mas becomes:

$$\frac{1}{\overline{p}}\frac{\partial p'}{\partial t} + \nabla \cdot \vec{v} = \frac{1}{\overline{p}}\frac{\partial i_m}{\partial t} \tag{A.4.2}$$

Similarly, the linear equation of motion can be derived:

$$\overline{\rho}\frac{\partial \vec{v}}{\partial t} + \nabla p' = \vec{f} \tag{A.4.3}$$

Combining the perturbation method and the linear equation of motion results in a subdivision of various classes of wave motions [Gossard and Hooke, 1975]:

$$\overline{\rho}\left(\overset{(1)}{\frac{\partial \vec{v}'}{\partial t}} + \overset{(2)}{\overline{\vec{v}} \cdot \nabla \vec{v}'}\right) + \overset{(3)}{\nabla p'} - \overset{(4)}{\rho' g} + \overset{(5)}{2\overline{\rho}\Omega \times \vec{v}'} = 0 \tag{A.4.4}$$

This gives a convenient overview of the theoretical perturbation equation. Table A.1 list the various atmospheric oscillations and the corresponding terms of importance corresponding to equation A.4.4.

1	2	3	4	5	
x	x	x			Sound waves
	x	x	x	x	Lee waves
	x			x	Rossby waves

Table A.1: *Various atmospheric oscillations and the corresponding terms of importance corresponding to equation A4.4.*

A.5 Sound waves

Using the assumptions for acoustic waves (chapter 1), and keeping only first-order terms, the equation of motion (equation A.4.4) can be expressed as:

$$\frac{d\vec{v}^{'}}{dt} + \big(\vec{v}^{'} \cdot \nabla\big)\overline{\vec{v}} = -\frac{1}{\overline{\rho}}\nabla p^{'} \tag{A.5.1}$$

where $d/dt(= \partial/\partial t + \overline{\vec{v}} \cdot \nabla)$ is the material derivative, and $(\vec{v}^{'} \cdot \nabla)\overline{\vec{v}}(= v_z^{'} d\overline{\vec{v}}/dx)$ is the wind-shear term.

Since adiabatic processes and a lossless atmosphere is assumed, the entropy is stated to be constant (equation A.3.3). An increment of the entropy can be expressed by following Wilson [1957]:

$$dE_s = C_p\frac{dT}{T} - R\frac{dp}{p} \tag{A.5.2}$$

Integrating this expression with the combination of equations A.3.3 and A.3.5 results in the equation of state for acoustic waves:

$$\big(\frac{\partial}{\partial t} + \vec{v} \cdot \nabla\big)p = c^2\big(\frac{\partial}{\partial t} + \vec{v} \cdot \nabla\big)\rho = 0 \tag{A.5.3}$$

Combining this equation of state (equation A.5.3) with the equation of motion (equation A.5.1) yields:

$$\frac{1}{c^2}\big(\frac{\partial}{\partial t} + \vec{v} \cdot \nabla\big)p + \rho\nabla \cdot \vec{v} = 0 \tag{A.5.4}$$

By keeping the first order terms, and adapting that $(\overline{v} \cdot \nabla)\overline{p} = 0$, this becomes:

$$\frac{1}{c^2}\frac{dp^{'}}{dt} + \overline{\rho}\nabla \cdot \vec{v}^{'} = 0 \tag{A.5.5}$$

By assuming a layered medium with flow, and combining the divergence of equation A.5.1, the material derivative of equation A.5.5, and subtracting these from eachother result into:

$$\frac{d}{dt}\left(\frac{1}{\overline{\rho}c^2}\frac{dp^{'}}{dt}\right) + \frac{d}{dt}\nabla \cdot \vec{v}^{'} - \nabla \cdot \frac{d\vec{v}^{'}}{dt} - \frac{d\overline{v_z}}{dz} \cdot \nabla v_z^{'} - \nabla \cdot \left(\frac{1}{\overline{\rho}}\nabla p^{'}\right) = 0 \tag{A.5.6}$$

It can be shown that:

$$\frac{d}{dt}\nabla \cdot \vec{v}^{'} - \nabla \cdot \frac{d\vec{v}^{'}}{dt} = -\frac{d\overline{v_z}}{dz}\cdot \tag{A.5.7}$$

which results that equation A.5.6 can be re-written as:

$$\frac{d}{dt}\big(\frac{1}{\overline{\rho}c^2}\frac{dp^{'}}{dt}\big) - 2\frac{d\overline{v_z}}{dz}\cdot\nabla\vec{v}^{'} - \nabla\cdot\big(\frac{1}{\overline{\rho}}\nabla p^{'}\big) = 0 \qquad \text{(A.5.8)}$$

By taking the material derivative and express $dv_z^{'}/dt$ using equation A.5.1. The acoustic wave equation in a moving layered medium can be expressed as:

$$\frac{d}{dt}\Big[\frac{d}{dt}\big(\frac{1}{\overline{\rho}c^2}\frac{dp^{'}}{dt}\big) - \nabla\cdot\big(\frac{1}{\overline{\rho}}\nabla p^{'}\big)\Big] + 2\big(\frac{d\overline{v}_z}{dz}\cdot\nabla\big)\big(\frac{1}{\overline{\rho}}\frac{\partial p^{'}}{\partial z}\big) = 0 \qquad \text{(A.5.9)}$$

where $d\overline{v}_z/dz$ represents the effects of wind-shear on the propagation of acoustic waves. However, for infrasonic frequencies the wind-shear is neglatible. Therefore the acoustic wave equation for infrasonic waves in a moving layered medium becomes:

$$\frac{1}{c^2}\frac{d^2p^{'}}{dt^2} - \overline{\rho}\nabla\cdot\big(\frac{1}{\overline{\rho}}\nabla p^{'}\big) = 0 \qquad \text{(A.5.10)}$$

This is a homogeneous derivation, followed from Brekhovskikh and Godin [1999]. It has neglected the presence of acoustic sources, which are represented at the right side of the equation. The acoustic wave equation in a moving layer (equation A.5.10) can be simplified by assuming an effective sound speed [Assink, 2012], which simplifies the following operator:

$$\frac{1}{c}\Big(\frac{\partial}{\partial t} + \overline{\vec{v}_z}\cdot\nabla\Big)^2 \qquad \text{(A.5.11)}$$

By assuming harmonic time behavior an horizontal plane waves, this can be re-written as:

$$\frac{1}{c^2}\Big(-i\omega + i\vec{k}_z\cdot\overline{\vec{v}_z}\Big)^2 \qquad \text{(A.5.12)}$$

For small angles and in-plane propagation, $\vec{k}_z \approx \frac{\omega}{c}\widehat{k_z}$. Applying this approximation, equation A.5.12 becomes:

$$\frac{\omega}{c}\Big[1-\frac{\overline{\vec{v}_z}\cdot\widehat{k_z}}{c}\Big] \approx \frac{\omega}{c+\overline{\vec{v}_z}\cdot\widehat{k_z}} \equiv \frac{\omega}{c_{\text{eff}}} \qquad \text{(A.5.13)}$$

where $\overline{\vec{v}_z}\cdot\widehat{k_z}$ represents the wind in the direction of propagation, and $\frac{\overline{\vec{v}_z}}{c}$ the Mach number. By neglecting the Mach term, the Helmholtz equation for effective sound approximation becomes:

$$\Big[\nabla_z^2 + \overline{\rho}\frac{\partial}{\partial z}\frac{1}{\overline{\rho}}\frac{\partial}{\partial z} + \frac{\omega^2}{c_{\text{eff}}^2}\Big]\widehat{p^{'}}(r,z) = 0 \qquad \text{(A.5.14)}$$

where $\widehat{p^{'}}$ is related to $p^{'}$ through the Fourier transform. Within equation A.5.14, the adiabatic speed of sound is assumes small propagation angles, in-plane propagation, low Mach numbers, and accounts for refractive wind effects. Infrasound propagation does not exceed 15 degrees propagation angles, the cross-wind effects are negligible, and the infrasound Mach numbers are low. Therefore, the assumptions for equation A.5.14 hold for infrasound.

Bibliography

Aki, Keiiti and Paul G Richards (2002). *Quantitative seismology.*

Albarbar, A, Abdellatef Badri, Jyoti K Sinha and A Starr (2009). Performance evaluation of mems accelerometers. *Measurement* **42**(5), 790–795.

Alcoverro, Benoit and Alexis Le Pichon (2005). Design and optimization of a noise reduction system for infrasonic measurements using elements with low acoustic impedance. *The Journal of the Acoustical Society of America* **117**(4), 1717–1727.

All-Sensors (2019). Technical Report DLVR Series Low Voltage Digital Pressure Sensors. https://www.allsensors.com/datasheets/DS-0300_Rev_E.pdf.

Anderson, Jacob F, Jeffrey B Johnson, Daniel C Bowman and Timothy J Ronan (2018). The gem infrasound logger and custom-built instrumentation. *Seismological Research Letters* **89**(1), 153–164.

ANSYS (n.d.). Ansys academic research mechanical, release 18.1.

Anthony, Robert E, Adam T Ringler, David C Wilson and Emily Wolin (2019). Do low-cost seismographs perform well enough for your network? an overview of laboratory tests and field observations of the osop raspberry shake 4d. *Seismological Research Letters* **90**(1), 219–228.

Ardhuin, Fabrice, Lucia Gualtieri and Eleonore Stutzmann (2015). How ocean waves rock the earth: Two mechanisms explain microseisms with periods 3 to 300 s. *Geophysical Research Letters* **42**(3), 765–772.

Assink, JD, R Waxler and D Drob (2012). On the sensitivity of infrasonic traveltimes in the equatorial region to the atmospheric tides. *Journal of Geophysical Research: Atmospheres.*

Assink, JD, R Waxler, P Smets and LG Evers (2014). Bidirectional infrasonic ducts associated with sudden stratospheric warming events. *Journal of Geophysical Research: Atmospheres* **119**(3), 1140–1153.

Assink, Jelle D (2012). Infrasound as upper atmospheric monitor. *Ph. D. Thesis.*

Assink, Jelle, Gil Averbuch, Shahar Shani-Kadmiel, Pieter Smets and Läslo Evers (2018). A seismo-acoustic analysis of the 2017 north korean nuclear test. *Seismological Research Letters* **89**(6), 2025–2033.

Assink, Jelle, Pieter Smets, Omar Marcillo, Cornelis Weemstra, Jean-Marie Lalande, Roger Waxler and Läslo Evers (2019). Advances in infrasonic remote sensing methods. In: *Infrasound Monitoring for Atmospheric Studies*. pp. 605–632. Springer.

Averbuch, Gil (2021). The spectrogram, method of reassignment, and frequency-domain beamforming. *The Journal of the Acoustical Society of America* **149**(2), 747–757.

Averbuch, Gil, Jelle D Assink and Läslo G Evers (2020). Long-range atmospheric infrasound propagation from subsurface sources. *The Journal of the Acoustical Society of America* **147**(2), 1264–1274.

Averbuch, Gil, Jelle D Assink, Pieter SM Smets and Läslo G Evers (2018). Extracting low signal-to-noise ratio events with the hough transform from sparse array data. *Geophysics* **83**(3), WC43–WC51.

Backus, Milo, John Burg, Dick Baldwin and Ed Bryan (1964). Wide-band extraction of mantle p waves from ambient noise. *Geophysics* **29**(5), 672–692.

Bacmeister, Julio T, Stephen D Eckermann, Paul A Newman, Leslie Lait, K Roland Chan, Max Loewenstein, Michael H Proffitt and Bruce L Gary (1996). Stratospheric horizontal wavenumber spectra of winds, potential temperature, and atmospheric tracers observed by high-altitude aircraft. *Journal of Geophysical Research: Atmospheres* **101**(D5), 9441–9470.

Bartlett, MS (1948). Smoothing periodograms from time-series with continuous spectra. *Nature* **161**(4096), 686.

Bedard, Alfred, Thomas Georges et al. (2000). Atmospheric infrasound. *Acoustics Australia* **28**(2), 47–52.

Billingsley, John and R Kinns (1976). The acoustic telescope. *Journal of Sound and Vibration* **48**(4), 485–510.

Blanc, Elisabeth, Lars Ceranna, Alain Hauchecorne, A Charlton-Perez, Emanuele Marchetti, Läslo Gerardus Evers, Tormod Kvaerna, J Lastovicka, Lars Eliasson, Norma B Crosby et al. (2018). Toward an improved representation of middle atmospheric dynamics thanks to the arise project. *Surveys in geophysics* **39**(2), 171–225.

Blixt, Erik Mårten, Sven Peter Näsholm, Steven J Gibbons, Läslo G Evers, Andrew J Charlton-Perez, Yvan J Orsolini and Tormod Kværna (2019). Estimating tropospheric and stratospheric winds using infrasound from explosions. *The Journal of the Acoustical Society of America* **146**(2), 973–982.

Blom, Philip (2019). Modeling infrasonic propagation through a spherical atmospheric layer - analysis of the stratospheric pair. *The Journal of the Acoustical Society of America* **145**(4), 2198–2208.

Bowman and Lees (2018). Upper atmosphere heating from ocean-generated acoustic wave energy. *Geophysical Research Letters* **45**(10), 5144–5150.

Bowman, Daniel C and Jonathan M Lees (2015). Infrasound in the middle stratosphere measured with a free-flying acoustic array. *Geophysical Research Letters* **42**(22), 10–010.

Bowman, Daniel C, C Scott Johnson, Rachana A Gupta, Jacob Anderson, Jonathan M Lees, Douglas Patrick Drob and Dennis Phillips (2015). High altitude infrasound measurements using balloon-borne arrays. In: *AGU Fall Meeting Abstracts*. Vol. 2015. pp. S54B–06.

Bracewell, Ronald Newbold and Ronald N Bracewell (1986). *The Fourier transform and its applications*. Vol. 31999. McGraw-Hill New York.

Brachet, Nicolas, David Brown, Ronan Le Bras, Yves Cansi, Pierrick Mialle and John Coyne (2010). Monitoring the earth's atmosphere with the global ims infrasound network. In: *Infrasound monitoring for atmospheric studies*. pp. 77–118. Springer.

Brekhovskikh, Leonid M and Oleg A Godin (1999). Wave propagation in a range dependent waveguide. In: *Acoustics of Layered Media II*. pp. 243–360. Springer.

Brekovskikh, LM (1973). Waves in layered media academic, new york, 1960, chap. 1. 31 ba auld. *Acoustic Fields and Waves in Solids*.

Brown, David, Lars Ceranna, Mark Prior, Pierrick Mialle and Ronan J Le Bras (2014). The idc seismic, hydroacoustic and infrasound global low and high noise models. *Pure and Applied Geophysics* **171**(3-5), 361–375.

Brown, Peter (2013). A preliminary report on the chelyabinsk fireball/airburst. *J. Int. Meteor Organ.* **41**, 22.

Burridge, R (1971). The acoustics of pipe arrays. *Geophysical Journal International* **26**(1-4), 53–69.

Campus, P and DR Christie (2010). Worldwide observations of infrasonic waves. In: *Infrasound monitoring for atmospheric studies*. pp. 185–234. Springer.

Capon, Jack (1969). High-resolution frequency-wavenumber spectrum analysis. *Proceedings of the IEEE* **57**(8), 1408–1418.

Ceranna, Lars, Robin Matoza, Patrick Hupe, Alexis Le Pichon and Matthieu Landès (2019). Systematic array processing of a decade of global ims infrasound data. In: *Infrasound monitoring for atmospheric studies*. pp. 471–482. Springer.

Christie, DR and P Campus (2010). The ims infrasound network: Design and establishment of infrasound stations. In: *Infrasound monitoring for atmospheric studies*. pp. 29–75. Springer.

Chunchuzov, Igor and Sergey Kulichkov (2019). Internal gravity wave perturbations and their impacts on infrasound propagation in the atmosphere. In: *Infrasound Monitoring for Atmospheric Studies*. pp. 551–590. Springer.

Clark, BG (1980). An efficient implementation of the algorithm'clean'. *Astronomy and Astrophysics* **89**, 377.

Clay, Thomas A, Rocío Joo, Henri Weimerskirch, Richard A Phillips, Olivier Den Ouden, Mathieu Basille, Susana Clusella-Trullas, Jelle D Assink and Samantha C Patrick (2020). Sex-specific effects of wind on the flight decisions of a sexually dimorphic soaring bird. *Journal of Animal Ecology* **89**(8), 1811–1823.

Cornes, Richard C, Marieke Dirksen and Raymond Sluiter (2020). Correcting citizen-science air temperature measurements across the netherlands for short wave radiation bias. *Meteorological Applications* **27**(1), e1814.

D'Alessandro, Antonino, Dario Luzio and Giuseppe D'Anna (2014). Urban mems based seismic network for post-earthquakes rapid disaster assessment.. *Advances in Geosciences*.

De Bree, Hans-Elias et al. (2003). The microflown: An acoustic particle velocity sensor. *Acoustics Australia* **31**(3), 91–94.

De Bruijn, Evert IF, Fred C Bosveld, Siebren de Haan and Bert G Heusinkveld (2020). Measuring low-altitude winds with a hot-air balloon and their validation with cabauw tower observations. *Journal of Atmospheric and Oceanic Technology* **37**(2), 263–277.

De Carlo, M, Fabrice Ardhuin and A Le Pichon (2020*a*). Atmospheric infrasound generation by ocean waves in finite depth: unified theory and application to radiation patterns. *Geophysical Journal International* **221**(1), 569–585.

De Carlo, M, P Hupe, A Le Pichon, L Ceranna and F Ardhuin (2020*b*). Global microbarom patterns: a first confirmation of the theory for source and propagation. *Geophysical Research Letters* p. e2020GL090163.

Donn, WL and D Rind (1972). Microbaroms and the temperature and wind of the upper atmosphere. *Journal of the Atmospheric Sciences* **29**(1), 156–172.

Dost, Bernard (1987). The NARS array: a seismic experiment in western Europe. PhD thesis. Instituut voor Aardwetenschappen RUU.

Drob, Douglas (2019). Meteorology, climatology, and upper atmospheric composition for infrasound propagation modeling. In: *Infrasound Monitoring for Atmospheric Studies*. pp. 485–508. Springer.

Drob, Douglas P, JM Picone and M Garcés (2003). Global morphology of infrasound propagation. *Journal of Geophysical Research: Atmospheres.*

ECMWF (2008). Part vii: Ecmwf wave model ifs documentation-cy33r1 operational implementation 3 june 2008 part vii: Ecmwf wave model. Technical report. Technical Report June, The European Centre for Medium-Range Weather Forecast, Reading, United Kingdom.

ECMWF (2016). Changes in ecmwf model. Technical report. The European Centre for Medium-Range Weather Forecast, Reading, United Kingdom.

ECMWF (2017). Era5 reanalysis.

Edwards, Wayne N and David N Green (2012). Effect of interarray elevation differences on infrasound beamforming. *Geophysical Journal International* **190**(1), 335–346.

Emerson (2021). Technical Report SMA cable. https://docs.rs-online.com/8c8d/0900766b8142afa4.pdf.

EUSCIENCE-HUB (2021). EU SCIENCE HUB; PVGIS. https://ec.europa.eu/jrc/en/PVGIS/docs/usermanual.

Evers and Haak (2007). Infrasonic forerunners: Exceptionally fast acoustic phases. *Geophysical research letters.*

Evers, Läslo G (2008). The inaudible symphony: on the detection and source identification of atmospheric infrasound. PhD thesis. TU Delft, Delft University of Technology.

Evers, Läslo Gerardus and Heinrich Wilhelm Haak (2000). *The Deelen Infrasound Array: on the detection and identification of infrasound.* Koninklijk Nederlands Meteorologisch Instituut.

Evers, LG, DN Green, NW Young and M Snellen (2013). Remote hydroacoustic sensing of large icebergs in the southern indian ocean: Implications for iceberg monitoring. *Geophysical research letters* **40**(17), 4694–4699.

Fang, Zhen, Zhan Zhao, Lidong Du, Jiangang Zhang, Cheng Pang and Daoqu Geng (2010). A new portable micro weather station. In: *2010 IEEE 5th International Conference on Nano/Micro Engineered and Molecular Systems*. IEEE. pp. 379–382.

FIBOX (2021). Technical Report Large Casing. https://docs.rs-online.com/3dd9/0900766b80f255a2.pdf.

Fisher, RA (1948). Statistical methods for research workers. new york: Hafner, 1948. *Google Scholar.*

Formlabs (n.d.). Technical Report Formlabs 3D printer. https://formlabs.com/3d-printers/form-3/.

Gabrielson, Thomas B (2011). In situ calibration of atmospheric-infrasound sensors including the effects of wind-noise-reduction pipe systems. *The Journal of the Acoustical Society of America* **130**(3), 1154–1163.

Gal, M, AM Reading, SP Ellingsen, KD Koper, R Burlacu and SJ Gibbons (2016). Deconvolution enhanced direction of arrival estimation using one-and three-component seismic arrays applied to ocean induced microseisms. *Geophysical Journal International* **206**(1), 345–359.

Garcia-Marti, Irene, Marjin de Haij, Jan Willem Noteboom, Gerard van der Schrier and Cees de Valk (2019). Using volunteered weather observations to explore urban and regional weather patterns in the netherlands. *AGUFM* **2019**, IN22A–08.

Garrett, Michael A (2013). Radio astronomy transformed: Aperture arrays - past, present and future. In: *2013 Africon*. IEEE. pp. 1–5.

GEBCO (2020). Gebco 2020 grid.

Golden, Paul, Petru Negraru and Jesse Howard (2012). Infrasound studies for yield estimation of he explosions. Technical report. SOUTHERN METHODIST UNIV DALLAS TX.

Gore-TEX (2020). Technical Report Gore TEX air vents. https://www.gore.com/products/gore-protective-vents-for-lighting-enclosures.

Gossard, Earl E and William H Hooke (1975). Waves in the atmosphere: atmospheric infrasound and gravity waves-their generation and propagation. *AtSc*.

Grangeon, Jacques and Philippe Lesage (2019). A robust, low-cost and well-calibrated infrasound sensor for volcano monitoring. *Journal of Volcanology and Geothermal Research* **387**, 106668.

Green, David N (2015). The spatial coherence structure of infrasonic waves: analysis of data from international monitoring system arrays. *Geophysical Journal International* **201**(1), 377–389.

Green, DN, RS Matoza, J Vergoz and A Le Pichon (2012). Infrasonic propagation from the 2010 eyjafjallajökull eruption: Investigating the influence of stratospheric solar tides. *Journal of Geophysical Research: Atmospheres*.

Grimmett, Doug, Randall Plate and Jason Goad (2019). Measuring infrasound from the maritime environment. In: *Infrasound Monitoring for Atmospheric Studies*. pp. 173–206. Springer.

Haak, Hein and Läslo Evers (2002). Infrasound as a tool for ctbt verification. *Verification Yearbook* pp. 208–221.

Haak, Heinrich Wilhelm and GJ De Wilde (1996). *Microbarograph systems for the infrasonic detection of nuclear explosions*. Royal Netherlands Meteorological Institute, Seismology Division.

Haiden, T, Martin Janousek, J Bidlot, R Buizza, L Ferranti, F Prates and Frédéric Vitart (2018). *Evaluation of ECMWF forecasts, including the 2018 upgrade*. European Centre for Medium Range Weather Forecasts.

Han, Mee Lan, Jin Lee, Ah Reum Kang, Sungwook Kang, Jung Kyu Park and Huy Kang Kim (2015). A statistical-based anomaly detection method for connected cars in internet of things environment. In: *International Conference on Internet of Vehicles*. Springer. pp. 89–97.

Harjes, HP and M Henger (1973). Array-seismologie. *Zeitschrift für Geophysik* **39**, 865–905.

Hasselmann, K (1963). A statistical analysis of the generation of microseisms. *Reviews of Geophysics* **1**(2), 177–210.

Hetzer, Claus H, Kenneth E Gilbert, Roger Waxler and Carrick L Talmadge (2010). Generation of microbaroms by deep-ocean hurricanes. In: *Infrasound Monitoring for Atmospheric Studies*. pp. 249–262. Springer.

Högbom, JA (1974). Aperture synthesis with a non-regular distribution of interferometer baselines. *Astronomy and Astrophysics Supplement Series* **15**, 417.

Homeijer, B, D Lazaroff, D Milligan, R Alley, J Wu, M Szepesi, B Bicknell, Z Zhang, RG Walmsley and PG Hartwell (2011). Hewlett packard's seismic grade mems accelerometer. In: *2011 IEEE 24th International Conference on Micro Electro Mechanical Systems*. IEEE. pp. 585–588.

Homeijer, Brian D, Donald J Milligan and Charles R Hutt (2014). A brief test of the hewlett-packard mems seismic accelerometer. *US Geological Survey Open-file Report*.

Hons, MS, RR Stewart, DC Lawton, MB Bertram and G Hauer (2008). Field data comparisons of mems accelerometers and analog geophones. *The Leading Edge* **27**(7), 896–903.

Huang, Qing-An, Ming Qin, Zhongping Zhang, Minxin Zhou, Lei Gu, Hao Zhu, Desheng Hu, Zhikun Hu, Gaobin Xu and Zutao Liu (2003). Weather station on a chip. In: *SENSORS, 2003 IEEE*. Vol. 2. IEEE. pp. 1106–1113.

Hupe, Patrick (2019). Global infrasound observations and their relation to atmospheric tides and mountain waves.

Husebye, ES and BO Ruud (1989). Array seismology - past, present and future developments. *Observatory Seismology* pp. 123–153.

Jacob, Renju Thomas, Zohra Aziz Ali Manjiyani et al. (2014). Development of mems based 3-axis accelerometer for hand movement monitoring. *International Journal of Computer Science and Engineering Communications* **2**(1), 87–92.

Jansky, Karl G (1932). Directional studies of atmospherics at high frequencies. *Proceedings of the Institute of Radio Engineers* **20**(12), 1920–1932.

Johari, Houri (2003). Development of mems sensors for measurements of pressure, relative humidity, and temperature.

KNMI (1993). Netherlands Seismic and Acoustic Network. Royal Netherlands Meteorological Institute (KNMI), Other/Seismic Network. 10.21944/e970fd34-23b9-3411-b366-e4f72877d2c5.

Krishnamoorthy, Siddharth, Daniel C Bowman, Attila Komjathy, Michael T Pauken and James A Cutts (2020). Origin and mitigation of wind noise on balloon-borne infrasound microbarometers. *The Journal of the Acoustical Society of America* **148**(4), 2361–2370.

Laine, Jerome and Denis Mougenot (2007). Benefits of mems based seismic accelerometers for oil exploration. In: *TRANSDUCERS 2007-2007 International Solid-State Sensors, Actuators and Microsystems Conference*. IEEE. pp. 1473–1477.

Lammel, Gerhard (2015). The future of mems sensors in our connected world. In: *2015 28th IEEE International Conference on Micro Electro Mechanical Systems (MEMS)*. IEEE. pp. 61–64.

Landes, Matthieu, Lars Ceranna, Alexis Le Pichon and Robin S Matoza (2012). Localization of microbarom sources using the ims infrasound network. *Journal of Geophysical Research: Atmospheres*.

Le Pichon, A, L Ceranna and J Vergoz (2012). Incorporating numerical modeling into estimates of the detection capability of the ims infrasound network. *Journal of Geophysical Research: Atmospheres*.

Levy, Gad and Robert A Brown (1991). Southern hemisphere synoptic weather from a satellite scatterometer. *Monthly weather review* **119**(12), 2803–2813.

Linx-Technologies (2021). Technical Report Linx antenna. https://docs.rs-online.com/85aa/A700000007484028.pdf.

Longuet-Higgins, Michael Selwyn (1950). A theory of the origin of microseisms. *Philosophical Transactions of the Royal Society of London A: Mathematical, Physical and Engineering Sciences* **243**(857), 1–35.

Ma, Rong-Hua, Yu-Hsiang Wang and Chia-Yen Lee (2011). Wireless remote weather monitoring system based on mems technologies. *Sensors* **11**(3), 2715–2727.

Manobianco, John and David A Short (2001). On the utility of airborne mems for improving meteorological analysis and forecasting. In: *Conference on Modeling and Simulation of Microsystems.* pp. 342–345.

Marcillo, Omar, Jeffrey B Johnson and Darren Hart (2012). Implementation, characterization, and evaluation of an inexpensive low-power low-noise infrasound sensor based on a micromachined differential pressure transducer and a mechanical filter. *Journal of Atmospheric and Oceanic Technology* **29**(9), 1275–1284.

Marlton, Graeme, Andrew Charlton-Perez, Giles Harrison and Christopher Lee (2019). Calculating atmospheric gravity wave parameters from infrasound measurements. In: *Infrasound Monitoring for Atmospheric Studies.* pp. 701–719. Springer.

Marty, Julien (2019). The ims infrasound network: current status and technological developments. In: *Infrasound Monitoring for Atmospheric Studies.* pp. 3–62. Springer.

Marty, Julien, Stéphane Denis, Thomas Gabrielson, Milton Garcés and David Brown (2017). Comparison and validation of acoustic response models for wind noise reduction pipe arrays. *Journal of Atmospheric and Oceanic Technology* **34**(2), 401–414.

Matoza, Robin S, Matthieu Landès, Alexis Le Pichon, Lars Ceranna and David Brown (2013). Coherent ambient infrasound recorded by the international monitoring system. *Geophysical research letters* **40**(2), 429–433.

McKee, Kathleen, Cassandra M Smith, Kevin Reath, Eveanjelene Snee, Sean Maher, Robin S Matoza, Simon Carn, Diana C Roman, Larry Mastin, Kyle Anderson et al. (2021). Evaluating the state-of-the-art in remote volcanic eruption characterization part ii: Ulawun volcano, papua new guinea. *Journal of Volcanology and Geothermal Research* p. 107381.

McNamara, Daniel E and Raymond P Buland (2004). Ambient noise levels in the continental united states. *Bulletin of the seismological society of America* **94**(4), 1517–1527.

Melton, Ben S and Leslie F Bailey (1957). Multiple signal correlators. *Geophysics* **22**(3), 565–588.

Mentink, Johan H and Läslo G Evers (2011). Frequency response and design parameters for differential microbarometers. *The Journal of the Acoustical Society of America* **130**(1), 33–41.

Merchant, B John (2015). Hyperion 5113/gp infrasound sensor evaluation. *Sandia Report SAND2015–7075, Sandia National Laboratories.*

Merchant, B John and Darren M Hart (2011). Component evaluation testing and analysis algorithms. *Sandia National Laboratories Technical Report No. SAND2011-8265.*

Michel, Ulf et al. (2006). History of acoustic beamforming. In: *Berlin Beamforming Conference, Berlin, Germany, Nov.* Citeseer. pp. 21–22.

Milligan, Donald J, Brian D Homeijer and Robert G Walmsley (2011). An ultra-low noise mems accelerometer for seismic imaging. In: *SENSORS, 2011 IEEE.* IEEE. pp. 1281–1284.

NASA (2021). NASA TRL definitions. https://www.nasa.gov/pdf/458490main_TRL_Definitions.pdf.

Neele, Filip and Roel Snieder (1991). Are long-period body wave coda caused by lateral heterogeneity?. *Geophysical Journal International* **107**(1), 131–153.

Nief, G, N Olivier, S Olivier and A Hue (2017). New optical microbarometer. In: *AGU Fall Meeting Abstracts*. Vol. 2017. pp. A21A–2150.

Nief, Guillaume, Carrick Talmadge, Jeff Rothman and Thomas Gabrielson (2019). New generations of infrasound sensors: technological developments and calibration. In: *Infrasound Monitoring for Atmospheric Studies*. pp. 63–89. Springer.

Nishimura, Ryouichi, Zhenglie Cui and Yôiti Suzuki (2019). Portable infrasound monitoring device with multiple mems pressure sensors. In: *International Congress on Acoustics (ICA)*. pp. 1498–1505.

Olson, JV and CAL Szuberla (2004). The least squares estimation of the azimuth and velocity of plane waves. *Inframatics* **6**, 8–12.

Pain, Herbert John and Robert T Beyer (1993). The physics of vibrations and waves.

Panel, Data Buoy Cooperation (2005). Reference guide to the gts sub-system of the argos processing system. revision 1.6.

Park, Joseph, Milton Garcés, David Fee and Geno Pawlak (2008). Collective bubble oscillations as a component of surf infrasound. *The Journal of the Acoustical Society of America* **123**(5), 2506–2512.

Peterson, Jon R (1993). Observations and modeling of seismic background noise. Technical report. US Geological Survey.

Pierce, Allan D (2019). *Acoustics: an introduction to its physical principles and applications*. Springer.

Poler, Guerman, Raphaël F Garcia, Daniel C Bowman and Léo Martire (2020). Infrasound and gravity waves over the andes observed by a pressure sensor on board a stratospheric balloon. *Journal of Geophysical Research: Atmospheres* **125**(6), e2019JD031565.

Ponceau, D and L Bosca (2010). Low-noise broadband microbarometers. In: *Infrasound monitoring for atmospheric studies*. pp. 119–140. Springer.

Raspberry-Pi (2018). Technical report raspberry pi model 3b+. https://static.raspberrypi.org/files/product-briefs/Raspberry-Pi-Model-Bplus-Product-Brief.pdf.

RaspberryShake (2021). RPi- Shake Metadata - instrument response files. `https://manual.raspberryshake.org/metadata.html#id3`. Online; accessed 2021.

Raspet, Richard, Jiao Yu and Jeremy Webster (2008). Low frequency wind noise contributions in measurement microphones. *The Journal of the Acoustical Society of America* **123**(3), 1260–1269.

Raspet, Richard, John-Paul Abbott, Jeremy Webster, Jiao Yu, Carrick Talmadge, Kirkpatrick Alberts II, Sandra Collier and John Noble (2019). New systems for wind noise reduction for infrasonic measurements. In: *Infrasound Monitoring for Atmospheric Studies*. pp. 91–124. Springer.

RBOOM (2017). Specifications for: Raspberry Boom (RBOOM) and 'Shake and Boom' (RS-BOOM). https://manual.raspberryshake.org/_downloads/SpecificationsforBoom_SnB.pdf.

RF-LoRa (2021). Technical Report LoRa Telecommunication. https://www.rfsolutions.co.uk/downloads/1623417611DS-RFLoRa-7.pdf.

Richardson, Philip L, Ewan D Wakefield and Richard A Phillips (2018). Flight speed and performance of the wandering albatross with respect to wind. *Movement ecology* **6**(1), 1–15.

Richiardone, Renzo (1993). The transfer function of a differential microbarometer. *Journal of Atmospheric and Oceanic Technology* **10**(4), 624–628.

Rost, Sebastian and Christine Thomas (2002). Array seismology: Methods and applications. *Reviews of geophysics.*

Schmidt, Ralph (1986). Multiple emitter location and signal parameter estimation. *IEEE transactions on antennas and propagation* **34**(3), 276–280.

Schneider (2021). Technical Report Small Casing. http://www.farnell.com/datasheets/2334261.pdf.

Schweitzer, Johannes, Jan Fyen, Svein Mykkeltveit, Tormod Kværna and P Bormann (2002). Seismic arrays. *IASPEI new manual of seismological observatory practice* p. 52.

Sensirion (2021). Technical Report SHT8x temperature/humidity sensor. https://nl.mouser.com/datasheet/2/682/Sensirion_03222021_Datasheet_SHT85-2237633.pdf.

Shani-Kadmiel, Shahar, Jelle D Assink, Pieter SM Smets and Läslo G Evers (2018). Seismoacoustic coupled signals from earthquakes in central italy: Epicentral and secondary sources of infrasound. *Geophysical Research Letters* **45**(1), 427–435.

Shumway, Robert H (1971). On detecting a signal in n stationarily correlated noise series. *Technometrics* **13**(3), 499–519.

Sijtsma, Pieter (2007). Clean based on spatial source coherence. *International journal of aeroacoustics* **6**(4), 357–374.

Šindelářová, Tereza, Marine De Carlo, Csenge Czanik, Daniela Ghica, Michal Kozubek, Kateřina Podolská, Jiří Baše, Jaroslav Chum and Ulrike Mitterbauer (2021). Infrasound signature of the post-tropical storm ophelia at the central and eastern european infrasound network. *Journal of Atmospheric and Solar-Terrestrial Physics* **217**, 105603.

Slad, George W and B John Merchant (2016). Chaparral model 60 infrasound sensor evaluation. *Technical Report* pp. SAND2016–1902.

Sleeman, Reinoud, Arie Van Wettum and Jeannot Trampert (2006). Three-channel correlation analysis: A new technique to measure instrumental noise of digitizers and seismic sensors. *Bulletin of the Seismological Society of America* **96**(1), 258–271.

Smart, Eugene and Edward A Flinn (1971). Fast frequency-wavenumber analysis and fisher signal detection in real-time infrasonic array data processing. *Geophysical journal international* **26**(1-4), 279–284.

Smets, P. S. M. and L. G. Evers (2014*a*). The life cycle of a sudden stratospheric warming from infrasonic ambient noise observations. *Journal of Geophysical Research: Atmospheres* **119**(21), 12,084–12,099.

Smets, P.S.M. (2018). Infrasound and the dynamical stratosphere: A new application for operational weather and climate prediction. *Delft University of Technology.*

Smets, PSM and LG Evers (2014*b*). The life cycle of a sudden stratospheric warming from infrasonic ambient noise observations. *Journal of Geophysical Research: Atmospheres* **119**(21), 12–084.

Smink, Madelon ME, Jelle D Assink, Fred C Bosveld, Pieter SM Smets and Läslo G Evers (2019). A three-dimensional array for the study of infrasound propagation through the atmospheric boundary layer. *Journal of Geophysical Research: Atmospheres* **124**(16), 9299–9313.

Speller, Kevin E and Duli Yu (2004). A low-noise mems accelerometer for unattended ground sensor applications. In: *Unattended/Unmanned Ground, Ocean, and Air Sensor Technologies and Applications VI.* Vol. 5417. International Society for Optics and Photonics. pp. 63–72.

Steinhart, John S and Stanley R Hart (1968). Calibration curves for thermistors. In: *Deep Sea Research and Oceanographic Abstracts*. Vol. 15. Elsevier. pp. 497–503.

STElectronics (2021). Technical Report LIS3DH MEMS sensor. file:///Users/olivierdenouden/Downloads/lis3dh.pdf.

Stettner, Felix Benedikt (2018). Infrasound data analysis of signals produced by greenlandic glaciers. Master's thesis. Utrecht University.

STMicroelectronics (2020*a*). Technical Report STMicroelectronics LPS33HW. https://www.st.com/resource/en/datasheet/lps33hw.pdf.

STMicroelectronics (2020*b*). Technical Report STMicroelectronics LSM303. https://www.st.com/resource/en/datasheet/DM00027543.pdf.

Strachey, R (1888). On the air waves and sounds caused by the eruption of krakatoa in august 1883. krakatau 1883 (published 1983). ed. by t. simkin and rs fiske.

SuperiorSensor-Technology (2021). Technical Report Superior Sensor Technology SP210. https://nl.mouser.com/datasheet/2/962/DS_0002B_SP_Series-1923489.pdf.

Sutherland, Louis C and Henry E Bass (2004). Atmospheric absorption in the atmosphere up to 160 km. *The Journal of the Acoustical Society of America* **115**(3), 1012–1032.

Szuberla, Curt AL and John V Olson (2004). Uncertainties associated with parameter estimation in atmospheric infrasound arrays. *The Journal of the Acoustical Society of America* **115**(1), 253–258.

Szuberla, Curt AL, John V Olson and Kenneth M Arnoult (2009). Explosion localization via infrasound. *The Journal of the Acoustical Society of America* **126**(5), EL112–EL116.

Tailpied, Dorianne, Alexis Le Pichon, Emanuele Marchetti, Jelle Assink and Sylvie Vergniolle (2016). Assessing and optimizing the performance of infrasound networks to monitor volcanic eruptions. *Geophysical Journal International* p. ggw400.

TDK (2018). Technical Report TDK NTC element G1540. https://www.tdk-electronics.tdk.com/en/530384/products/product-catalog/sensors-and-sensor-systems/ntc-temperature-measurement-sensors/ntc-elements-epcos.

TDK (2021). Technical Report ICS-40300 microphone. https://3cfeqx1hf82y3xcoull08ihx-wpengine.netdna-ssl.com/wp-content/uploads/2019/02/DS-ICS-40300-00-v1.3.pdf.

Texim-Europe (2020). Technical Report Texim Europe GNS2301. http://www.texim-europe.com/promotion/820/gns2301_datasheet_v02_te.pdf.

Vergoz, Julien, Alexis Le Pichon and Christophe Millet (2019). The antares explosion observed by the usarray: an unprecedented collection of infrasound phases recorded from the same event. In: *Infrasound Monitoring for Atmospheric Studies*. pp. 349–386. Springer.

Viberg, Mats and H Krim (1997). Two decades of array signal processing. In: *Proc. 31st Asilomar Conf. Sig., Syst., Comput., Pacific Grove, CA*.

Voltaic (2020*a*). Technical Report 9W, 6V, Solar panel. https://voltaicsystems.com/9-watt-panel/.

Voltaic (2020*b*). Technical Report V75 Battery Pack. https://voltaicsystems.com/v75/.

Vorobeva, E., M. De Carlo, A. Le Pichon, P. J. Espy and S. P. Näsholm (2020). Microbarom radiation and propagation model assessment using infrasound recordings: a vespagram-based approach. *Annales Geophysicae Discussions* **2020**, 1–22.

Walker, Kristoffer T and Michael AH Hedlin (2010). A review of wind-noise reduction methodologies. In: *Infrasound monitoring for atmospheric studies*. pp. 141–182. Springer.

Wapenaar, Cornelis Pieter Arie (2014). *Elastic wave field extrapolation: Redatuming of single-and multi-component seismic data*. Elsevier.

Washburn, Edward W (1921). The dynamics of capillary flow. *Physical review* **17**(3), 273.

Waxler, R, KE Gilbert, CL Talmadge and C Hetzer (2007). The effects of finite depth of the ocean on microbarom signals. In: *8th International Conference on Theoretical and Computational Acoustics (ICTCA), Crete, Greece.*

Waxler, Roger and Jelle Assink (2019). Propagation modeling through realistic atmosphere and benchmarking. In: *Infrasound Monitoring for Atmospheric Studies*. pp. 509–549. Springer.

Waxler, Roger and Kenneth E Gilbert (2006). The radiation of atmospheric microbaroms by ocean waves. *The Journal of the Acoustical Society of America* **119**(5), 2651–2664.

Welch, Peter (1967). The use of fast fourier transform for the estimation of power spectra: a method based on time averaging over short, modified periodograms. *IEEE Transactions on audio and electroacoustics* **15**(2), 70–73.

Welty, James, Gregory L Rorrer and David G Foster (2020). *Fundamentals of momentum, heat, and mass transfer*. John Wiley & Sons.

Wessel, P, JF Luis, L Uieda, R Scharroo, F Wobbe, WHF Smith and D Tian (2019). The generic mapping tools version 6. *Geochemistry, Geophysics, Geosystems* **20**(11), 5556–5564.

Wilson, Alan Herries (1957). Thermodynamics and statistical mechanics. *Thermodynamics and statistical mechanics.*

Wyngaard, J and B Kosovic (1994). Similarity of structure-function parameters in the stably stratified boundary layer. *Boundary-Layer Meteorology* **71**(3), 277–296.

Zemansky, MW (1968). Heat and thermodynamics mcgraw-hill book coy. *New York.*

Zeyl, Jeffrey N, Olivier den Ouden, Christine Köppl, Jelle Assink, Jakob Christensen-Dalsgaard, Samantha C Patrick and Susana Clusella-Trullas (2020). Infrasonic hearing in birds: a review of audiometry and hypothesized structure–function relationships. *Biological Reviews.*

Zirpel, Martin, Wim Kraan and Peter-Paul Mastboom (1978). *Operationele versterkers: een verzameling schakelingen en formules voor de toepassing van operationele versterkers*. Kluwer.

Zou, Xudong, Pradyumna Thiruvenkatanathan and Ashwin A Seshia (2014). A seismic-grade resonant mems accelerometer. *Journal of Microelectromechanical Systems* **23**(4), 768–770.

List of symbols and abbreviations

Symbols

The principal symbols used are alphabetically listed. Symbols formed by adding overbars, primes or indices are not listed separately. An overhead arrow indicates vector quantities.

Symbol	**Description**	**Units**
$A(x)$	Acoustic attenuation	dB
a_i	Diameter	m
$\vec{a}$	Steering vector	-
α	Thermal diffusivity	m^2/s
c	Speed of sound	m/s
c_{app}	Apparent velocity	m/s
c_{eff}	The effective sound speed	m/s
$c_{\text{eff,ratio}}$	The effective sound speed ratio	-
c_T	Adiabatic sound speed	m/s
C	Cross-spectral density matrix	-
C_d	Diaphragm sensitivity KNMI mini-MB	m^{4}s^{2}kg^{-1}
C_p	Heat capacity at constant pressure	J/K
C_v	Heat capacity at constant volume	J/K
$\overline{C}_j$	Corrected capacity KNMI mini-MB	V/Pa
C_{Ω_j}	Thermistor constants	Farad
δ_t	Thermal penetration depth	m
D	Theoretical response	Pa - degree
D_{bath}	Ocean depth (Bathymetry)	m
D_m	Average diameter WNRS	m
D_{MUSIC}	Number of sources	-
E	Statistical expectation	-

Symbol	Description	Units
E_s	Entropy	J/K
ϵ	Array resolution vs error variance	-
η	Air viscosity	μPa s
f	Frequency	Hz
$\vec{f}$	Volume density of external forces	Newton
$\bar{f}$	Transition frequency gas constant	Hz
$f^{'}$	Volume flux	m^3/s/m^2
f_0	Monochromatic wave frequency	Hz
f_a	Acoustic cut-off frequency	3.3 mHz
f_l	Low-frequency cut-off	Hz
f_w	Ocean wave frequency	Hz
f_{WNRS}	First resonance peak WNRS	Hz
$\vec{F}$	External forces	Newton
F_{Fisher}	Fisher ratio	-
F_w	Distribution of wave variance	Hz
$\overline{F}_w$	Integral of sea mean energy spectrum	
g	Gravitational force	m/s^2
G	Fourier transformed recording	Pa
G_p	Propagation factor	-
γ_{iso}	Isothermal gas constant	1
γ_{adi}	Adiabatic gas constant	1.4
$\bar{\gamma}$	Transition value gas constant	-
$\mathcal{H}$	Hasselmann integral	-
i_m	Volume density of mass injection	ρ
I	Electrical current	Ampere
l_i	Length	m
$\vec{I}$	Sound intensity	W/m^2
J_j	j^{th} order Bessel function	-
k	Wavenumber	-
K	Bulk modulus	GPa
κ_c	Thermal conductivity	Wm$^{[}$ − 3K^{-1}
λ	Wavelength	m
λ_{nc}	The non-centrality parameter	SNR - F
λ_w	Accoustic wavelength	m
Λ	Heat capacity correction factor	-
M	Molar mass	-
$\vec{n}$	Normal vector	-
N	Number of array elements	-
ω	Angular frequency	Hz
Ω	Coriolis force	g
p	Sound pressure	Pa

Symbol	**Description**	**Units**
$p^{'}$	Acoustic pressure difference	Pa
$\vec{p}$	Slowness vector	s/m
P_{atm}	Atmospheric pressure	Pa
$\mathcal{P}_1$	Evanescent acoustic power	Pa
$\mathcal{P}_2$	Propagatting acoustic power	Pa
$\mathcal{P}_{av}$	Average Acoustic power	Pa
ϕ	Fraction of removed power	%
ϕ_t	Inclination angle	degree
ϕ_w	Ocean wave direction	degree
L	Number of snapshots within one sample window	-
L_j	Length	m
q_m	Rounding factor	-
q_N	Optimum array element weight Neele and Snieder	-
q_v	Volumetric airflow	m^3/s
r	Position in space	m
R	Specific gas constant	J kg^{-1} mol^{-1}
R^*	Ideal gas constant	8.314J kg^{-1} mol^{-1}
R_d	Specific gas constant for dry air	
R_j	Electrical resistance KNMI mini-MB	$\text{kgm}^{-4}\text{s}^{-1}$
R_Ω	Thermistor Resistance valeu	Ohm
$\mathcal{R}$	Reflection coefficient	-
ρ	Density	$\text{kgm}^{[} - 3$
S	Surface of Volume V	m
t	Time	sec
t_m	model time	seconds
T	Temperature	$^\circ C$
T_s	Number of Sample points	-
τ_j	Time constants	s
θ	Back azimuth	degree
U	Electrical voltage	Volt
v	Particle speed	m/s
V	Volume	m^3
$V(f)$	MUSIC noise subspace	-
V_j	Volume KNMI mini-MB	m^3
w	Beamform weight factor	-
w_{cross}	Cross wind	m/s
w_{uv}	Wind speed in direction of propagation	m/s
xi	Sea state	SWH - m
Z	Number of adjacent frequencies	–

Abbreviations

2DFD	Two-dimensional wave spectra
4D-Var	Four-dimensional variational data assimilation
ADC	Analog-Digital-Converter
Beidou	Chinese navigational system
CAD	Computer aided design
CTBT	Comprehensive Nuclear-Test-Ban Treaty
CTBTO	Comprehensive Nuclear-Test-Ban Treaty Organization
dB	Decibel
DLVR	Digital Low Voltage Range differential pressure sensor
ECMWF	European Centre for Medium-Range Weather Forecasts
EDA	Ten-member ensemble atmosphere model
ERA5	ECMWF reanalysis model
FIR	Finite impulse response
Galileo	European navigational system
GLONASS	Russian navigational system
GMT	Generic Mapping Tools
GPIO	General-Purpose Input/Output
GPS	Global Positioning System
GTS	Global Telecommunication System
HRES	High-resolution atmosphere model
HRES-WAM	High-resolution ocean wave model
Hz	Hertz
I2C	Inter-Integrated Circuit
IMS	International Monitoring System
IMU	Inertial measurement unit
INFRA-EAR	Infrasound and Environmental Atmospheric data Recorder
KNMI	Royal Netherlands Meteorological Institute
MAE	Mean absolute error
MB	Mega bytes
MEMS	Micro-electromechanical Systems
Mini-MB	KNMI mini-microbarometer
Multi-EAR	Multi Earth and Atmospheric data Recorder
NHNM	New High Noise Model
PCB	Printed Circuit Board
PE	Parabolic Equation
PPSD	Probabilistic Power Spectral Density
PSD	Power Spectral Density
PSF	Point spread function
R&D	Research and development
RF	Relative frequency
RPi	Raspberry Pi

RS	Reassigned spectrogram
SFTF	Short-time Fourier-transform
SLA	Stereolithography 3D printing
SMA	SubMiniature version A
SNR	Signal to noise ratio
SPI	Serial Peripheral Interface
SPL	Sound pressure level
SWH	Significant Wave Height
TRL	Technology Readiness Level
UART	Universal Asynchronous Receiver Transmitter
UTC	Universal Time Coordinated
WNRS	Wind Noise Reduction System response
WAN	Wireless wide area network
WMO	World Meteorological Organization
WOW	Weather Observations Website

Curriculum Vitæ

Olivier Frederik Constantinus den Ouden

21-08-1994	Wythenshaw, Manchester, UK.

Education

1998–2006	Primary school St. Antoniusschool, Kortenhoef [NL].
2006–2012	Secondary school A. Roland Holst College, Hilversum [NL].
2012–2015	B.Sc. Applied Earth Science Delft University of Technology, Delft [NL]. *Minor:* Vienna University of Technology, Vienna [AT]. *Thesis:* Testing of novel deformation strategies for optimising fracture network connectivity *Supervisor:* Dr. A. Barnhoorn *Committee:* Prof. Dr. G. Bertotti ir. W. Verwaal
2015–2017	M.Sc. Applied Geophysics IDEA League. (TU Delft [NL], ETH Zürich [CH], RWTH Aachen [GE]) *Thesis:* Localization of Ocean Seismic Noise *Supervisor:* Dr. ir. P.S.M. Smets (KNMI/TU Delft) *Committee* Prof. Dr. L.G. Evers (KNMI/TU Delft) Prof. Dr. ir. E.C. Slob (TU Delft) Prof. Dr. F. Wellmann (RWTH Aachen)

Professional Experience

Oct. 2017 – Sept. 2021	Geophysicist at the Royal Netherlands Meteorological Institute (KNMI) Research on the Human Frontier Science project (HFSP) SeaBirdSound, a collaboration between the University of Liverpool, University of Florida, Stellenbosch University, and the KNMI (RGY0072/2017) Research on infrasound generation and observation, for the Dutch Ministry of Economic affairs and Climate Policy (KEM-31).
Sept. 2021 –	R&D Engineer at the Royal Netherlands Aerospace Centre (NLR)

Awards

2020	Ministry of Infrastructure and Water Management *Awarded the 'Stimulering en Innovatiefonds'* My research proposal on further development of low-cost multidisciplinary sensor platforms for monitoring of geophysical hazards got awarded by the internal jury of the Ministry of IenW, led by Gijs van Schouwenburg.
2020	Delft University of Technology *Awarded the 'Innovation research grant'* My research proposal on further development of low-cost multidisciplinary sensor platforms for monitoring of geophysical hazards got awarded by Auke Barnhoorn, Associate Professor at the DUT.

List of publications

■ Peer-reviewed first author publications of this thesis

- **den Ouden, O.F.C.**, Assink, J.D., Smets, P.S.M., Shani-Kadmiel, S., Averbuch, G., Evers, L.G. (2020), *CLEAN beamforming for the enhanced detection of multiple infrasonic sources*, Geophysical Journal International, Volume 221. DOI: 10.1093/gji/ggaa010
  Chapter 3 of this thesis
- **den Ouden, O.F.C.**, Assink, J.D., Oudshoorn, C.D., Filippi, D., Evers, L.G. (2021), *The INFRA-EAR: a low-cost mobile multidisciplinary measurement platform for monitoring geophysical parameters*, Atmospheric Measurement Techniques, Volume 14. DOI: 10.5194/amt-14-3301-2021
  Chapter 2 of this thesis
- **den Ouden, O.F.C.**, Smets, P.S.M., Assink, J.D., Evers, L.G. (2021), *A bird's-eye view on ambient infrasonic soundscapes*,Geophysical Research Letters, Volume 48. DOI: 10.1029/2021GL094555
  Chapter 4 of this thesis
- Assink & **den Ouden**, and co-authors (2021), *Infrasound as a cue for seabird navigation*, Frontiers in Ecology and Evolution, Volume 9. DOI: 10.3389/fevo.2021.740027
  Chapter 1 of this thesis
- **den Ouden, O.F.C.**, Assink, J.D., Smets, P.S.M., Evers, L.G. (2022), *A climatology of microbarom detections at the Kerguelen Islands: unravelling the ambient noise wavefield*. Geophysical Journal International, Volume 229. DOI: 10.1093/gji/ggab535
  Chapter 5 of this thesis

Note that minor changes have been introduced to make the text consistent with the other chapters.

■ Full publication record

- Assink, J.D., Nusselder, R., White, K., **den Ouden, O.F.C.**, de Graaff, E., Nieuwenhuizen, E. (2021), *Methods for the assessment of low-frequency noise from mining activities in the Netherlands*, Institute of Noise Control Engineering.

- Clay, T., Joo, R., Weimerskirch, H., Philips, R., **den Ouden, O.F.C.**, Basille, M., Clusella Trullas, S., Assink, J.D., , Patrick S.C., Clusella-Trullas, S. (2020), *Sex-specific effects of wind on the flight decisions of a sexually-dimorphic soaring bird*, Journal of Animal Ecology.

- Lecocq, T., and co-authors (**den Ouden, O.F.C.**) (2020), *Global quieting of high frequency seismic noise due to COVID-19 pandemic lockdown measures*, Science.

- Zeyl, J.N., **den Ouden, O.F.C.**, Köppl, C. Assink, J.D., Christensen Dalsgaard, J., Patrick S.C., Clusella Trullas, S. (2020), *Infrasonic hearing in birds: a review of audiometry and hypothesized structure function relationships*, Biological Reviews.